

Ultrafast tangential micro-mixers for the study of biochemical reactions on the microsecond time scale

Mitic, Sandra

DOI

[10.4233/uuid:03bc62aa-c046-417d-82d6-ef8d51d9a965](https://doi.org/10.4233/uuid:03bc62aa-c046-417d-82d6-ef8d51d9a965)

Publication date

2016

Document Version

Final published version

Citation (APA)

Mitic, S. (2016). *Ultrafast tangential micro-mixers for the study of biochemical reactions on the microsecond time scale*. [Dissertation (TU Delft), Delft University of Technology]. <https://doi.org/10.4233/uuid:03bc62aa-c046-417d-82d6-ef8d51d9a965>

Important note

To cite this publication, please use the final published version (if applicable). Please check the document version above.

Copyright

Other than for strictly personal use, it is not permitted to download, forward or distribute the text or part of it, without the consent of the author(s) and/or copyright holder(s), unless the work is under an open content license such as Creative Commons.

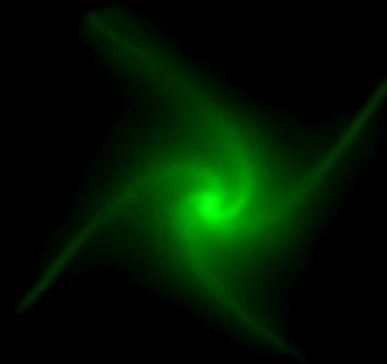
Takedown policy

Please contact us and provide details if you believe this document breaches copyrights. We will remove access to the work immediately and investigate your claim.

Ultrafast tangential micro-mixers for the study of biochemical reactions on the microsecond time scale

Sandra Mitić

Ultrafast tangential micro-mixers for the study of biochemical reactions on the microsecond time scale



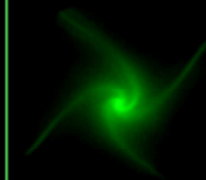
Sandra Mitić

Invitation

Public defence of PhD thesis entitled:

Ultrafast tangential micro-mixers
for the study of
biochemical reactions
on the microsecond time scale

by Sandra Mitić



Monday September 19th, 2016
at 10:00 hr
in the Frans van Hasseltroom
of the Aula of TU Delft,
Mekelweg 5, Delft.

A short presentation of this work
will proceed the defence at 9:30 hr

After the ceremony you are
cordially invited to accompany me
for a reception in the Aula
and lunch at 12:30 hr
in the Botanical Garden
Poortlandplein 6, Delft

sanmit88@gmail.com

Ultrafast tangential micro-mixers for the study of biochemical reactions on the microsecond time scale

PROEFSCHRIFT

ter verkrijging van de graad van doctor
aan de Technische Universiteit Delft,
op gezag van de Rector Magnificus prof. ir. K.C.A.M. Luyben,
voorzitter van het College voor Promoties,
in het openbaar te verdedigen op
19 september, 2016, om 10 uur

door

Sandra MITIĆ

Master of Science in Technology, University of Belgrade, Serbia
geboren te Belgrado, Joegoslavië

This dissertation has been approved by the
promotors: Prof.dr. S. de Vries† and Prof.dr. W.R. Hagen

Composition of the doctoral committee:

Rector Magnificus	chairman
Prof.dr. Simon de Vries†	Delft University of Technology
Prof.dr. W.R. Hagen	Delft University of Technology

Independent members:

Dr.ir. D. Jacobs	DSM Delft
Prof.dr. A.J. Pierik	Technical University Kaiserslautern
Prof.dr.ir. A. van den Berg	Technical University Twente
Dr. P.L. Hagedoorn	Technical University Delft
Prof.dr. I.W.C.E. Arends	Delft University of Technology
Prof.dr. U. Hanefeld	Delft University of Technology



The studies presented in this thesis were performed at the Department of Biotechnology, Delft University of Technology., The Netherlands.
The research was supported by the NanoNed (project TAC.6380).

Copyright © 2016 Sandra Mitić All rights reserved.

Printed by: Ipskamp Printing, Enschede.

Cover design: Sandra Mitić.

Inverted microscope image of fluorescence appearance due to deprotonation of HPTS recorded in the optically transparent vortex chamber of the four-jet tangential ABAB glass-silicon mixer

ISBN: 978-94-0280316-7

An electronic version of this dissertation is available at [TU Delft Repository](#).

To my family and in memoriam of Simon

Contents

Summary		1
Samenvatting		3
Chapter 1	Introduction and thesis outline	5
Chapter 2	Rapid mixing techniques for the study of enzyme catalysis	19
Chapter 3	Design of turbulent tangential micro-mixers that mix liquids on the nanosecond time scale	55
Chapter 4	Design and characterization of a continuous flow ultra-fast mixing instrument for the study of transient (bio)chemical reactions by optical spectroscopy	81
Chapter 5	An optically improved continuous flow ultra-fast mixing instrument for the study of transient intermediates	111
Chapter 6	Conclusions and outlook	129
Curriculum vitae		133
List of Publications		
Acknowledgments		134

Summary

Detailed understanding of chemical and enzyme catalysis constitutes a main focus of current biochemical research. Fundamental insight in how (bio)catalysts function, requires knowledge of their three dimensional structure and a wide range of time resolved experiments that monitor the reaction progress. The ultimate aim is the determination of the molecular structure of transition and transient states during the chemical bond-breaking and bond-making step that occurs as part of the overall reaction. Chemists claim to have observed transient or transition states with lifetimes as short as 100-500 femtoseconds. Single steps in enzyme catalysis are usually slower than this, although electron transfer and proton transfer can occur in picoseconds or nanoseconds, respectively. The movements of protein domains which are critical to drive enzyme catalysis because they directly promote the breaking and reforming of chemical bonds, occur at a longer time scale of $\sim 0.1-1 \mu\text{s}$. This time range can thus be regarded as the fastest in which formation of enzyme catalytic intermediates occur or protein domains can fold into the native structure of the active enzyme.

To study catalytic mechanisms of enzymes and chemical reactions in detail, the reaction should be initiated so rapidly that the subsequent formation and decay of all reaction intermediates can in fact be detected. Even the fastest present-day continuous-flow mixing equipment is too slow ($\sim 45 \mu\text{s}$) to monitor the very beginning of enzyme catalysis. In order to design a general kinetic instrument with a much shorter dead-time to mix reactants and observe the reaction progress both the mixer and observation cell need to be miniaturized to micrometer dimensions ($\sim 100 \mu\text{m}$) while maintaining high mixing efficiency and good optical quality. This thesis deals with the design and development of a new kinetic instrument that can perform, observe and detail, on the μs time scale, the catalytic mechanism of enzymes, in particular those of the oxidoreductases.

Chapter 2 provides a review of turbulent, laminar continuous, and stopped-flow rapid mixing instrumentation as well as rapid freeze-quenching and microsecond freeze-quenching/sampling methodologies. The specific design features of mixers and rapid mixing instruments are discussed in relation to the various spectroscopic analyses methods.

In **Chapter 3** new types of turbulent tangential micro-mixers were designed and characterized for their mixing and unwanted pre-mixing characteristics. The results show that it is possible to completely mix two reactants within 160 ns, which is at least 50-times faster than estimated for other micro-mixing devices. The **Chapter 3** further provides several general guidelines to the design of fast mixers.

Based on the design principles outlined in **Chapter 3**, in **Chapter 4** a continuous flow ultra-fast mixing device has been developed with a greatly improved time resolution indicated by the mixing and observation dead-time of $3.8 \pm 0.3 \mu\text{s}$. This instrument contains a four-jet tangential micro-mixer that completely mixes two liquids within $3.5 \mu\text{s}$. The mixer is integrated with a long cylindrical capillary flow-cell enabling the recording of UV-Vis or fluorescence spectra between 300-700 nm using a sensitive CCD camera. In the kinetic mode of the instrument, each UV-Vis spectrum

corresponds to a different reaction time that is determined by the distance between the mixer and a pixel of the CCD chip and the fluid flow rate. The reaction progress can be monitored in steps of 318 ns for approximately 600 μ s.

In **Chapter 5** improvements in flow-cell design and optical performance of the ultra-fast mixing instrument described in **Chapter 4** are described without affecting the short dead-time of 3.8 μ s. The rectangular instead of cylindrical flow cell contains a ~30 mm long channel of 70 ± 5 μ m height, constructed from two parallel sheets of silver foil with 109 μ m thickness that also acts as an effective shield for stray light. This arrangement enables recording of spectral intensities that are linear up to at least 3.5 Absorbance units. The new instrument was used to study protein refolding of denatured horse heart cytochrome *c*. After a very rapid initial phase ($\tau = 4.7$ μ s), which has not been reported previously, partial refolding proceeds with time constants of 83 μ s and 345 μ s. Using singular value decomposition the complete spectra of three folding intermediates were determined. The instrument enables study of (bio)chemical reactions on the microsecond time scale including protein folding.

Samenvatting

De studie van chemische en enzymatische katalyse vormt een belangrijk aandachtsgebied binnen het huidige biochemisch onderzoek. Fundamenteel inzicht in de wijze waarop (bio)katalysatoren werken, vereist kennis van hun driedimensionale structuur gekoppeld aan talrijke tijdsopgeloste experimenten waarin de voortgang van de reactie wordt vastgelegd. Het uiteindelijke doel vormt de bepaling van de moleculaire structuur van de overgangstoestand en van of tijdelijke intermediären tijdens de reactie waarin de chemische bindingen worden gebroken en gemaakt. Volgens chemici kunnen overgangstoestanden en tijdelijke intermediären bestudeerd worden met een levensduur van slechts 100-500 femtoseconden. De snelste stappen in enzymgekatalyseerde reacties hebben in de regel een langere levensduur, maar toch kunnen elektron- en protonoverdrachtsreacties plaatsvinden op een tijdsschaal van respectievelijk picoseconden of nanoseconden. De beweging van domeinen binnen enzymen is van belang om de chemische reactie te bewerkstelligen, omdat hierdoor chemische bindingen kunnen worden gebroken en opnieuw kunnen worden gevormd; deze bewegingen kunnen plaatsvinden op een tijdsschaal van of $\sim 0.1-1 \mu\text{s}$. Met andere woorden, dit is de kortste tijdsschaal waarop katalytische intermediären gevormd kunnen worden of eiwitdomeinen zich kunnen vouwen tot de native structuur van het actieve enzym.

Teneinde het katalytisch werkingsmechanisme van enzymen en chemische reacties te kunnen ontrafelen zal men de reactie zo snel moeten kunnen starten opdat alle daaropvolgende reactiestappen kunnen worden vastgelegd. Zelfs de snelste continuous-flow mengapparatuur die heden ten dage beschikbaar is, en een dode tijd heeft van $\sim 45 \mu\text{s}$, is te traag om de allereerste enzymatische (of chemische) reactiestappen te kunnen observeren. Het ontwerp van een algemeen kinetisch instrument met een veel kortere dode tijd om reactanten te kunnen mengen en observeren, vereist miniaturisering van de meng- en meetapparatuur tot een schaalgrootte van $\sim 100 \mu\text{m}$, terwijl tegelijkertijd de efficiency van menging behouden blijft en de signaal-ruis verhouding van de optische detector om de reactie te kunnen volgen voldoende hoog is. In dit proefschrift wordt het ontwerp en de totstandbrenging van dergelijk nieuwe kinetische apparatuur beschreven om het katalytisch werkingsmechanisme van enzymen, in het bijzonder van oxidoreductases, te kunnen bestuderen op de tijdsschaal van microseconden.

Hoofdstuk 2 is een overzichtsartikel waarin turbulente, laminaire continuous-flow en stopped-flow instrumenten worden beschreven alsmede verschillende snelle freeze-quench methoden. Aan bod komt verder welke de specifieke ontwerp factoren zijn voor snelle mixers en hoe deze mixers geïntegreerd kunnen worden in opstellingen om verschillende specifieke spectroscopische analyses te kunnen uitvoeren.

In **Hoofdstuk 3** wordt het ontwerp van nieuwe typen turbulente tangential micro-mixers beschreven, welke worden getest op hun ongewenst voormengingsvermogen en hun gewenst menggedrag. De analyses tonen aan dat het mogelijk blijkt om twee reactanten compleet te mengen binnen 160 ns, hetgeen minstens 50-maal sneller is dan geschat voor andere micro-mixers. De resultaten stellen ons in staat om een aantal algemene regels voor het ontwerp van snelle mixers op te stellen.

Op grond van de ontwerpregels in **Hoofdstuk 3** wordt in **Hoofdstuk 4** een continuous-flow ultra-fast meng- meetinstrument beschreven met een totale dode tijd van $3.8 \pm 0.3 \mu\text{s}$ voor menging en observatie, hetgeen een significante verbetering in dode tijd vertegenwoordigt. De vier-jet tangentiële micro-mixer mengt de reactanten in $3.5 \mu\text{s}$ en is gekoppeld aan een lange cilindrische capillaire flow-cel waarin UV-Vis of fluorescentie spectra kunnen worden opgenomen van 300-700 nm met behulp van een gevoelige CCD camera. In de kinetiek modus van het apparaat correspondeert elk UV-Vis spectrum met een andere reactietijd, welke wordt bepaald door de afstand tussen de mixer en de positie van de pixel van de CCD camera en de lineaire stroomsnelheid van de vloeistof met de gemengde reactanten. Daardoor is het mogelijk om de reactie te volgen met een tijdsresolutie van 318 ns gedurende ongeveer $600 \mu\text{s}$.

In **Hoofdstuk 5** zijn verbeteringen aangebracht in de ultrasnelle meng-meetopstelling die beschreven is in **Hoofdstuk 4**. In plaats van een cilindrische cuvet, wordt nu gebruik gemaakt van een rechthoekige cuvet, ~ 30 mm in lengte en $70 \pm 5 \mu\text{m}$ breed. Deze cuvet/flow-cel is vervaardigd uit twee parallelle plaatjes zilverfolie ($109 \mu\text{m}$ dik hetgeen correspondeert met de optische weglengte). De plaatjes zilverfolie dienen tevens als afscherming van strooilicht, waardoor de spectrometer lineair is tot minstens 3.5 Absorptie eenheden. Met deze nieuwe opstelling is de hervouwing van gedenatureerd cytochrome *c* uit paardenhart bestudeerd. Na een zeer snelle initiële fase met $\tau = 4.5 \mu\text{s}$ die niet eerder geobserveerd is, vervolgt de gedeeltelijke vouwing met tijdsconstanten van $83 \mu\text{s}$ en $345 \mu\text{s}$. Met behulp van singuliere waarden ontbinding zijn de volledige spectra van drie vouwingsintermediären bepaald. In zijn huidige vorm is het met dit nieuwe meng- meetinstrument mogelijk om chemische en biochemische reacties alsmede eiwitvouwing te bestuderen op een tijdsschaal van enkele microseconden.

Chapter 1

Introduction and thesis outline

1. Background

1.1 Enzymes

The great majority of biochemical conversions in a cell need the help of biocatalysts to enhance the rate of the reaction in order to enable and to sustain life. The cell's biocatalysts are enzymes, a chain of amino acids joined through peptide bonds. Enzymes fold into intricate and precise, but dynamical, three-dimensional structures that are essential to their function, and may employ a wide range of organic or inorganic ('metal ion') co-factors or co-enzymes, which, in addition to the greater chemical variety of amino acids, may explain their greater catalytic variety. It is therefore no surprise that enzymes are involved in all metabolic pathways.

Present day computational methods are not sufficiently accurate to reliably predict 3D-structures from the 1D amino-acid sequences of enzymes¹. Moreover, the associated functions of enzymes cannot be predicted *a priori* from the primary sequences. An important reason for this failure is that bond angles and bond lengths of thousands of atoms need to be known with enormous precision – within 1-2 degrees and within 10-20 pm, respectively – in order to correctly account for example for the large local electrostatic gradients that generally govern binding of substrates and subsequent catalysis. Hence research on biocatalysts in general or enzymes in particular, Enzymology, has a strong experimental character. Enzymology covers among other things studies on: the subunit structure and composition of enzymes, subunit folding and their spatial arrangement, co-factor identity, the 3D-structure and the catalytic mechanism. This thesis deals with the development of new general methods to observe in detail on the shortest possible time scale (microseconds) the catalytic mechanism of enzymes, in particular those of the oxidoreductase family of enzymes.

1.2 Oxidoreductases, general electron transfer characteristics

Oxidoreductases are enzymes catalyzing electron or hydride transfer reactions. Because neither the electron nor the hydride ions are free species in solution, oxidoreductases need at least two substrates (**Eq. 1**), an electron (hydride) donor (D_{red}) and acceptor (A_{ox}):



Oxidoreductases usually follow a Ping-Pong mechanism. Although tyrosin, tryptophan, cysteine and seleno-cysteine are redox active amino acids, oxidoreductases often contain additional cofactors that enhance electron transfer rates and/or enable complex redox chemistry². The most common organic cofactors are flavin, heme and nicotinamide; inorganic co-factors may contain one or more 3d, 4d

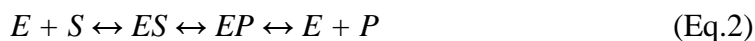
or 5d transition elements (V, Mn, Fe, Co, Ni, Cu, Mo, W). Enzymes carrying metal-ions, not necessarily redox active metals but also Mg, Ca or Zn, are often called metallo-enzymes. The different metal-ions give rise to an enormous variety of catalytic centers including redox centers. Iron-sulphur centers may consist of 1, 2, 3, 4, 7 or 8 iron atoms, copper centers of 1, 2, 3 or 4 Cu-atoms. In addition, there are mono- and di-nuclear iron centers, mixed metal centers (Fe-Ni in hydrogenases, V or Mo with Fe in nitrogenases) and Mo- or W-pterin co-factors. Furthermore, some redox enzymes contain several of these redox centers to enable electron transfer over large distances (10-15 nm) within a single enzyme^{3,4}.

Electron transfer between enzymes is called electron transport. Electron transport in respiratory chains is carried out by a variety of benzo- or naphthoquinones anchored to the membrane by an isoprenoid side chain consisting of five to twelve isoprene units (ubi- and menaquinones) and by a diverse class of small electron shuttles such as cytochrome *c*, blue copper proteins, rubredoxines, several types of ferredoxins and the [4Fe-4S]-containing HIPIP⁵.

Redox enzymes are not essentially different from other enzymes regarding their structure but often contain multiple redox centers or active sites. The various interactions between amino acids, between co-factor and amino acids (His, Met, Cys, Tyr, Glu, Asp, Gln, Asn, Lys, N-terminal NH₃, C-terminal carboxylate and backbone amide carbonyl oxygen or α -amine) and between substrate and active site comprise electrostatic interactions (25-50 kJ mol⁻¹), hydrogen bonding (2.0-7.5 kJ mol⁻¹ between uncharged donor/acceptor pairs, 12-25 kJ mol⁻¹ between charged pairs) and Van der Waals interactions (6-8 kJ mol⁻¹). The great number of hydrogen bonds and van der Waals interactions contribute mainly to the stability of the enzyme, the enzyme-co-factor and the enzyme-substrate complex whereas electrostatic interactions and specific hydrogen bonding patterns are more prominent in biocatalysis, promoting bond breaking and bond formation.

1.3 Oxido-reductases, functional considerations

The minimal catalytic cycle of an enzyme consists of the binding of a single substrate, the formation of a single product followed by product release, all of which may be reversible (**Eq. 2**):



In practice, however, substrate binding (and product release) may be far more complex, including exchange of solvent water, conformational rearrangement of the enzyme (induced-fit) and/or the substrate (product). Also the pure catalytic step – $ES \leftrightarrow EP$ – usually comprises several bond making and bond breaking events integrated with enzyme conformational changes including changes in hydrogen-bond interactions, protonation states and hence in local and global electrostatic interactions¹.

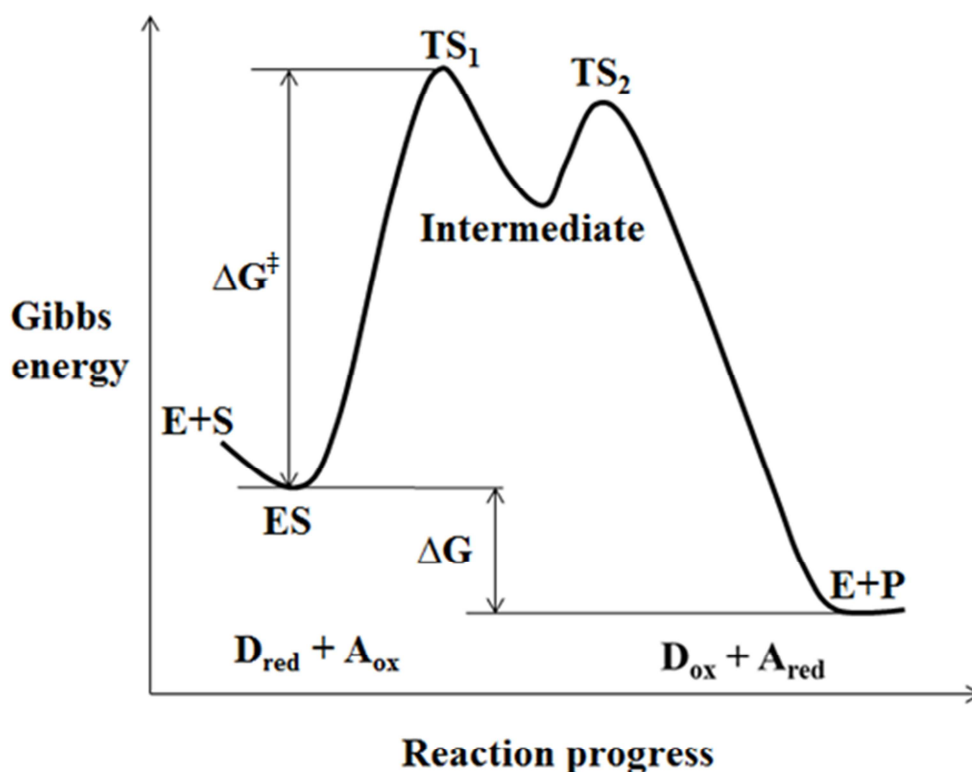


Figure 1. Transition state occurs at the peaks of the energy profile of a reaction (TS_1 and TS_2), and metastable, transient intermediates occupy the troughs.

Transition-state theory provides a simple framework for a qualitative assessment of chemical and enzyme catalysed rates⁶. The transition state corresponds to the state with the highest energy in the reaction coordinate diagram (**Fig. 1**). In the transition state, chemical bonds are in the process of being made and broken, and it represents the most unstable species (with an estimated lifetime of 100-500 fs⁷ in the reaction pathway. Therefore, these states populate to very small amounts, which prevents accurate determination of their structure. In contrast, (metastable or transient) intermediates, whose bonds are fully formed, occupy the (relative) minima in the diagram, have a longer lifetime, populate correspondingly higher and are easier to trap and characterize. The theory assumes that the reaction rate is controlled by decomposition of an activated transition-state complex, and that the transition-state is in thermodynamic equilibrium with the reactants ground state. In this way and for an unimolecular reaction, the concentration of the transition state can be calculated from the difference in Gibbs free energy between the transition state, S^\ddagger , and the ground state, S , that is ΔG^\ddagger .

$$[S^\ddagger] = [S] \cdot K^\ddagger = [S] \cdot e^{-\frac{\Delta G^\ddagger}{RT}} \quad (\text{Eq. 3})$$

Where K^\ddagger is equilibrium constant for formation of the transition-state complex from reactant, R is the gas constant, and T is the temperature^{1,6,8}. The frequency at which the transition-state complex decomposes to give product is the same as the vibrational frequency of the bond that is breaking:

$$\nu = \frac{k_B \cdot T}{h} \sim 6.1 \times 10^{12} \text{ s}^{-1} \text{ or } \frac{1}{\nu} \sim 164 \text{ fs at } 20^\circ\text{C} \quad (\text{Eq. 4})$$

where k_B is the Boltzmann constant and h Planck's constant.

Thus, the rate of decomposition of S is given by:

$$k = \frac{-d[S]}{dt} = \nu \cdot [S^\ddagger] = \left(\frac{k_B \cdot T}{h}\right) \cdot [S] \cdot e^{-\frac{\Delta G^\ddagger}{RT}} \quad (\text{Eq. 5})$$

The first order rate constant for the decomposition of S is given by:

$$k = \left(\frac{k_B \cdot T}{h}\right) \cdot e^{-\frac{\Delta G^\ddagger}{RT}} \quad (\text{Eq. 6})$$

The rate is dependent on ΔG^\ddagger and not on the driving force ΔG (see also **Fig. 1**). The value of ΔG^\ddagger or the activation energy when the Arrhenius equation is used, is determined experimentally by measuring the reaction rate over a wide temperature range. In order to calculate ΔG^\ddagger accurately ($\pm 5 \text{ kJ mol}^{-1}$ or a rate that is accurate to within a factor of ~ 10 -50), the structure of the transition state needs to be known with high precision which rarely is the case. Since enzymes speed up a reaction essentially by lowering ΔG^\ddagger , the value of ΔG^\ddagger is not a unique function of the reactants only, but in addition dependent on the properties of the surrounding medium such as the enzyme's active site. Since structures of true transition states of enzymes have not yet been determined, calculated rates for enzyme catalyzed reactions are easily off by a factor of ~ 1000 ($\sim 15 \text{ kJ mol}^{-1}$).

However, calculated rates for outer-sphere (pure) electron transfer using the Marcus theory are more accurate ($\sim 5 \text{ kJ mol}^{-1}$), and are therefore, predicted quite well⁹, within a factor of 10. The Marcus theory describes the rate of electron transfer from a reduced electron donor (D_{red}) to an initially oxidized acceptor (A_{ox}):

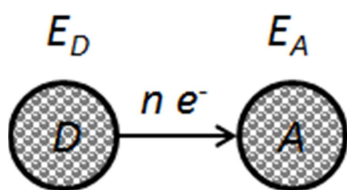


Figure 2. Electron transfer between cofactor D and A.

The rate of the overall reaction depends on the difference between the midpoint potentials E_D and E_A (the thermodynamic driving force), and on the distance between two cofactors, D and A (**Fig. 2**). Marcus theory provides a way to understand why cofactors involved in transferring electrons are often found to be arranged at distances $< 15 \text{ \AA}$.

If the metal ion in a complex is oxidized or reduced, its charge and size will change. In addition, water molecules around the complex will rearrange their orientation and distance. Most of these changes are slow and will limit the reaction rate. This rearrangement is associated with the reorganization energy. For the overall reaction between D and A , all these changes can be put together into a single 'reaction

coordinate', and plotted versus the Gibbs free energy as function of this coordinate (**Fig. 1**). For a redox reaction, $\Delta G = -nF(E_A - E_D)$, where F is the Faraday constant in C mol^{-1} , ΔG is in J mol^{-1} and E in J C^{-1} . As **Fig. 1** indicates, the maximum is the transition state, and the rate of the reaction depends on random fluctuations (temperature) that take the reaction coordinate across this maximum: $k \sim \exp(-\Delta G^\ddagger/RT)$. The energy plot can be extended by assuming that both the initial state ($D_{red} + A_{ox}$) and final state ($D_{ox} + A_{red}$) are simple harmonic oscillators, giving a parabolic dependence of the energy on deviation from the equilibrium reaction coordinate (**Fig. 3**):

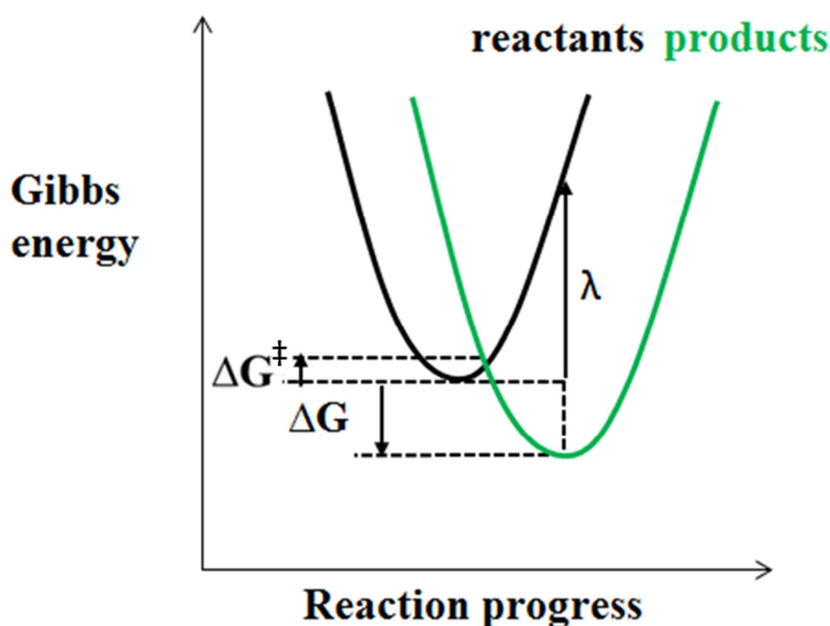


Figure 3. Parabolic dependence of the energy of reactants (—) and products (—).

The crossing point of the parabolas represents the transition state. The reorganization energy, λ , is defined as the energy required to change the geometry of the reactants into that of the products without actually transferring electrons and can be determined directly from **Fig. 3**.

A wavefunction of a free electron on a redox center is (de)localized in all directions. The tail of the wavefunction extends to an adjacent redox center, and the 'protein medium' between the two centers enables tunneling of the electron with a rate that decreases exponentially with distance. The maximum tunneling rate of room temperature electron transfer, k_{max} (in s^{-1}) is given by following equation:

$$k_{max} = 10^{13} \exp\{-\beta(R - R_o)\} [\text{s}^{-1}] \quad (\text{Eq. 7})$$

and is experimentally determined at $\sim 10^{13} \text{ s}^{-1}$ when R , the edge-to-edge distance between redox centers is as short as possible at van der Waals contact ($R_o = 3.6 \text{ \AA}$)^{10,11}. This maximal rate is similar to the value of $6.1 \cdot 10^{12} \text{ s}^{-1}$ quoted in **Eq. 4**. The rate decreases with increasing R or β , where β is proportional to the square root of barrier height. As a first approximation, β depends on the average density of protein atoms in the volume between redox centers D and A , and the highest density (smallest

β) is obtained with a chain of covalently bound atoms all the way between D and A . For tunneling of electrons through a chain of σ -bonded carbon, $\beta = 0.9 \text{ \AA}^{-1}$. A conjugated (π -bonded) chain of atoms between D and A has $\beta = 0$ and it forms a conduction wire. In proteins, the medium in between the cofactors contains many atoms from the peptide. This means that small stretches of vacuum, hydrogen bonds, σ -bonds and π -bonds can be found. Thus, the electron tunneling rate, k , through a protein medium (β is between 0.8 and 1.4 \AA^{-1} for most proteins) is much faster than tunneling through vacuum ($\beta = 2.8 \text{ \AA}^{-1}$) and is given by the generic equation:

$$\log k = 13 - 0.6(R - 3.6) - 3.1(\Delta G + \lambda)^2 / \lambda \quad (\text{Eq. 8})$$

where ΔG is the driving force, the difference in redox potentials between cofactors (in eV) and λ (in eV) the reorganization energy¹¹. The maximum rate occurs when $\Delta G = -\lambda$. Thus when $\Delta G > -\lambda$, which is designated as the inverted regime, the rate is actually smaller than the maximal rate. In most proteins, the distances between cofactors are found to be $\leq 14 \text{ \AA}$ (1.4 nm) and transfer over longer distances always involves a chain of several cofactors. Although most cofactors in a chain appear to have similar potential, in many natural electron transfer proteins such as hydrogenase or nitrate reductase the midpoint potential of one of the redox centers in the chain is much lower or higher than that of the surrounding cofactors¹¹. Although steps that are energetically uphill, are relatively slow and thus considered unfavorable for fast electron transfer, the close proximity of redox centers in most natural systems compensates for the unfavorable thermodynamics and these electron transfers ($\sim \mu\text{s}$) are still much faster than catalytic turnover ($\sim \text{ms}$) of the redox enzyme and thus not rate limiting for function.

In conclusion, calculated rates for pure electron transfer using the Marcus theory can be predicted quite well compared to reactions involving bond making and bond breaking because the activation energy is a simple expression of ΔG and λ .

2. Pre-steady state kinetic techniques

2.1 Introduction

The relation between enzyme function and protein (dynamic) structure is of great interest in biochemistry. To study catalytic mechanisms of enzymes and chemical reactions in detail, the reaction should be initiated so rapidly that the subsequent formation and decay of all reaction intermediates could be detected. The pre-steady kinetics of enzymes can be monitored by a great variety of spectroscopic techniques, which provide electronic and/or true structures of intermediates: UV-Vis spectroscopy, Fluorescence, Circular Dichroism, Fouriertransform IR, Electron Paramagnetic Resonance (EPR), Resonance Raman spectroscopy, Nuclear Magnetic Resonance (NMR) etc. Nowadays a variety of different pre-steady state instrumental techniques are used to rapidly initiate a reaction: direct photoflash, release of a caged compound by a photoflash, flow-flash, pressure jump, temperature jump, stopped-flow, continuous-flow, rapid quenched-flow, rapid freeze-quenching, microsecond-freeze hyperquenching and continuous flow hydrodynamic focusing^{7,12-29}.

2.2 Chemical relaxation techniques

Rapid reactions have been studied with chemical relaxation (single turnover) techniques where the enzyme and substrate are usually premixed and at a state of equilibrium^{10,14-18}. The reaction system is disturbed from its state of equilibrium by a sudden change of an external parameter, such as temperature, pressure or a pulse of light from a laser. Hereafter the system relaxes (readjusts itself) either to a new equilibrium state or returns to the original equilibrium state through a series of intermediate steps. The laser flash may induce 'natural' photochemical reactions such as electron transfer in plant and bacterial photosynthetic systems. In the caged compound technique one of the substrates is an inactive photo-labile substrate-analogue ('caged compound') that is converted by a pulse of light into a true substrate ready to react without need for mixing³⁰⁻³². In particular, when the caged compound is already bound to the enzyme before the light pulse, the reaction between enzyme and substrate is potentially very fast, and limited only by the kinetics of the photochemistry. Alternatively, a laser may rapidly change the temperature of the enzyme/substrate mixture, which subsequently evolves to a new equilibrium at the higher temperature. The advance of femtosecond pulse-probe laser flash photolysis methods has made it possible to trap and characterize very short-lived transient intermediates (if not transition states)⁷. Although, the time resolution of the relaxation techniques is superior to that of the mixing techniques^{7,12-16}, the majority of these studies have focused on small molecules only. Moreover, chemical relaxation methods require equilibrium conditions at the start of the experiment, which is not always possible to achieve or in the case of complex (serial) reactions, not wanted.

2.3 The rapid mixing techniques

Mixing reactants followed by spectroscopic observation of the mixture on (sub)-microsecond time scales, presents an important technological barrier. In spite of their limitation in time resolution, the mixing techniques have a more general and wider field of application than the relaxation techniques. To determine the kinetics of processes that are not driven by light, rapid mixing of two or more reactants is the most versatile and common method of initiating (bio)chemical reactions. The time resolution of fast mixing devices offer opportunities to study enzyme and/or chemical catalytic mechanisms in detail and to follow the time progress of (bio)chemical reactions far from equilibrium in transient regions where most likely intermediate states can be accumulated and detected. To do so successfully, a mixing instrument should be able to do both, initiate the reaction by ultra-fast mixing of two or more reactants e.g. enzyme and substrate, and enable monitoring of formation and decay of all reaction intermediates. Although usually very high enzymes concentrations (up to ~mM) are required to monitor rapid reactions at acceptable signal-to-noise ratios, rapid mixing techniques are of prime interest to determine biochemical and biophysical properties of enzyme catalytic intermediates. Regarding chemical synthesis, short mixing times of the reactants with respect to the timescale of the reaction might prevent the formation of chemical side reactions improving chemical purity and yield.

2.4 The mixing efficiency

The mixing efficiency of a mixing device depends on the dimensionless Reynolds number, Re , a criterion of whether fluid flow is absolutely steady (streamlined, or laminar) or the average steady with (small) unsteady fluctuations (turbulent) and it's defined as the ratio of inertial forces to viscous forces in a fluid flow. Whenever Re is less than about 2000, flow in a pipe is generally laminar, whereas, at values greater than 2000, the turbulent flow regime begins³³. Actually, the transition between laminar and turbulent flow does not occur at a specific value of Re but sets on in a range between 1000 to 2000 extending to between 3000 and 5000. The transition from laminar to turbulent flow in a pipe depends on the product of the mass density of the fluid ρ (1000 kg m⁻³ for water), v , the average velocity of flow (m s⁻¹ in a channel) and l , a characteristic length (traveled length of fluid, or hydraulic diameter of a channel in m) divided by η , the dynamic viscosity of the solutions (10⁻³ kg m⁻¹ s⁻¹ for water at 20°C). The Reynolds number Re is given by:

$$Re = \frac{\rho \cdot v \cdot l}{\eta} \quad (\text{Eq. 9})$$

According to the equation ρ and η are relatively constant in aqueous solution and the instrumental mixing time depends mainly on the mixer's geometry and dimensions (width, depth and length of the channel) and on the flow rate. Therefore, to achieve rapid and complete turbulent mixing in a minimal period of time requires high flow rates, relatively small channel dimensions (<100 μm) and a sufficiently high Re . When high concentrations of enzyme are required, the increase in viscosity of the solutions may cause a decrease of Re below ~ 2000 , which is often insufficient for complete mixing. The viscosity also increases with decreasing temperatures, in particular when cryo-solvents (glycerol or ethylene glycol) are used to perform kinetics at sub-zero temperatures. To maintain high flow rates of viscous solutions a powerful hydraulic/pneumatic drive-ram system is needed or HPLC pumps with a 40 MPa pressure limit^{23-25,33-35}. High flow velocities require large amounts of samples and lead to pressure (ΔP) build-up according to Bernoulli's velocity/dynamic pressure equation:

$$\Delta P = 0.5 \cdot \rho \cdot (< v >)^2 \quad (\text{Eq.10})$$

2.5 The turbulent mixing techniques

The majority of rapid mixing devices rely on turbulent mixing. Turbulence is an efficient mechanism to disperse the solutions into sufficiently small volume elements, so-called turbulent eddies. The small size of the eddies enables fast diffusion of the reactants over very short distances and constitutes the final step in mixing. Mixers of various designs that enable efficient turbulent mixing have been constructed over approximately the last hundred years and range from simple T- or Y-mixers to more complex geometries, such as multiple-jet tangential mixers^{23-26,34-48}. Mixers, with channel and bore dimensions smaller than one millimetre, so-called micro-mixers, date back some fifty years, e.g. the Berger ball mixer. The co-axial type micro-mixers were first introduced some forty years ago. Micro-mixers with dimensions of

approximately 100 μm or smaller, produced in particular for so-called Lab-on-a-chip applications, have been introduced in the last two decades.

The various types of mixers might be integrated with an optical observation cell as in the stopped-flow apparatus (SF, usually with millimeter dimensions) and in continuous-flow instruments (CF, dimensions of $\sim 250 \mu\text{m}$), allowing monitoring of the reaction by a great variety of optical spectroscopic methods at a single wavelength and/or at multiple wavelengths simultaneously³⁵.

The total dead-time of a mixing device in which kinetic changes are monitored by e.g. optical spectroscopy is determined by the mixing time and the residence time of the mixed reactants in the dead volume, i.e. the volume between the point of mixing and area of observation. Both, the mixing time and residence time, decrease with smaller dimensions of the compartments, hence increasing the (linear) flow rates. In micro-mixers, owing to their smaller dimensions, linear flow rates need to be higher than in the larger mixers in order to obtain Re above $\sim >2000$ needed for turbulent mixing and rapid completion of mixing.

The most commonly used kinetic techniques such as the stopped-flow, continuous-flow and freeze-quench techniques are further detailed in **Chapter 2**.

3. Background and aim of the thesis

Determination of the molecular identity of transition and transient states is the key to understanding chemical and enzyme catalysis. This thesis deals with the development of new (bio)chemical kinetic analysis tools to observe and detail, on the shortest possible time scale, the catalytic mechanism of enzymes, in particular those of the oxidoreductases. Ideally a pre-steady-state kinetic study would be capable of capturing each bond breaking and bond making step that occurs as part of the overall reaction. Individual steps in enzyme catalysis may proceed on the sub-picosecond time scale such as light-driven electron transfer in photochemical reaction centers. Rotations of aromatic amino-acid side chains, proton transfer and hydride transfer occur in the nanoseconds. Movements of the main chain or (small) protein domains take place at the time scale of ~ 0.1 -1 μs , as determined by NMR and Time Resolved X-ray diffraction experiments^{16,53-55}. The movements of protein domains are critical to drive enzyme catalysis because they directly promote the breaking and remaking of chemical bonds. In some cases, the characteristic enzyme motions that occur during catalysis were shown to be already present in the free enzyme with frequencies corresponding to the catalytic turnover rate. Motions are localized not only to the active site but also take place in the wide dynamic network distant from the active site⁵⁷. Protein folding may occur at the same time scale as catalysis. A number of small proteins and domains were shown to undergo two-state folding/unfolding transitions with relaxation times as short as a few microseconds. For example, the engineered 35-residue subdomain of the chicken villin headpiece has a folding rate of $0.7 \mu\text{s}^{-1}$, ref.⁵³. The protein folding rate limit is estimated both empirically and theoretically to be $\sim (N/100 \mu\text{s})^{-1}$, where N is the number of residues in the polypeptide chain⁵³. A time scale of 0.1 μs - 1 μs for the fastest catalytic steps appears in agreement with the enzyme binding rate constant of $k_{\text{on}} \sim 10^{9-10} \text{ M}^{-1} \text{ s}^{-1}$ for the fastest enzymes for a physiological substrate concentration of $\sim 1\text{mM}$.

In the light of the analysis above, our aim is to develop (bio)chemical kinetic analyses tools that can monitor reactions that occur on the μs time scale, which appears to be the time scale for formation of enzyme catalytic intermediates. The dead-time of current continuous-flow mixing equipment is impressive but yet too slow ($\sim 45 \mu\text{s}$) to study the very onset of catalysis by enzymes. In order to design an instrument capable of mixing reactants and observing the reaction progress on the microsecond time scale both the mixer and observation cell had to be miniaturized ($\sim 100 \mu\text{m}$) while maintaining high mixing efficiency and satisfactory optical quality to enable pre-steady state kinetic analyses.

4. Outline of the thesis

Chapter 2 gives an overview of the current rapid mixing devices. In **Chapter 3** new types of turbulent micro-mixers are designed and tested regarding their true mixing times providing routes to design mixers capable of mixing liquids within a few hundred nanoseconds. **Chapter 4** describes the construction and testing of a new Ultra-Fast turbulent mixing instrument. The device enables monitoring of (bio)chemical reactions by optical spectroscopy and has a dead-time of $3.8 \mu\text{s}$. In **Chapter 5** improvements in flow-cell design and optical performance of the ultra-fast mixing instrument are described.

References

1. Fersht, A. Structure and Mechanism in Protein Science. *A Guide to Enzyme Catalysis and Protein Folding*. W. H. Freeman and Company, NY, 1999.
2. The Biological Chemistry of the Elements. *The Inorganic Chemistry of Life* by R.J.P. Williams and J.R.R. Frausto da Silva, Clarendon Press, New York, 1996.
3. Sazanov, L. A.; Hinchliffe, P. Structure of the Hydrophilic Domain of Respiratory Complex I from *Thermus thermophilus*. *Science*, 2006, 311, 1430-1436.
4. Iverson, T. M.; Luna-Chavez, C.; Cecchini, G.; Rees, D. C. Structure of the *Escherichia coli* fumarate reductase respiratory complex. *Science*, 1999, 284, 5422, 1961-6.
5. Richardson, D. J. Bacterial respiration: a flexible process for a changing environment, *Microbiology*, 2000, 146, 551-571.
6. Kraut, J. How do enzymes work? *Science*, 1988, 242.
7. Zewail, A. H. Femtochemistry: Atomic-Scale Dynamics of the Chemical Bond. *The Journal of Physical Chemistry A*, 2000, 104, 5660-5694.
8. Lienhard, G. E. Enzymatic catalysis and transition-state theory. *Science*, 1973, 180, 149-154.
9. Marcus, R. A.; Sutin, N. Electron transfers in chemistry and biology. *Biochimica et Biophysica Acta*, 1985, 811, 265-322.
10. Page, C. C.; Moser, C. C.; Chen, X.; Dutton, P. L. Natural engineering principles of electron tunneling in biological oxidation-reduction. *Nature*, 1999, 402.
11. Page, C. C.; Moser, C. C.; Chen, X.; Dutton, P. L. Mechanism for electron transfer within and between proteins. *Current Opinion in Chemical Biology*, 2003, 7, 551-556.
12. Ma, H.; Wan, C.; Zewail, A. H. Ultrafast T-jump in water: studies of conformation and reaction dynamics at the thermal limit. *Journal of the American Chemical Society*, 2006, 128, 6338-6340.
13. Ren, Z.; Perman, B.; Srajer, V.; Teng, T. Y.; Pradervand, C.; Bourgeois, D.; Schotte, F.; Ursby, T.; Kort, R.; Wulff, M.; Moffat, K. A molecular movie at 1.8 Å resolution displays the photocycle of photoactive yellow protein, a eubacterial blue-light receptor, from nanoseconds to seconds. *Biochemistry*, 2001, 40, 13788-13801.
14. Chance, B.; Saronio, C.; Leigh, J.S. Jr. Functional intermediates in the reaction of membrane-bound cytochrome oxidase with oxygen. *Journal of Biological Chemistry*, 1975, 250, 9226-9237.
15. Adelroth, P.; Karpefors, M.; Gilderson, G.; Tomson, F. L.; Gennis, R. B.; Brzezinski, P. Proton transfer from glutamate 286 determines the transition rates between oxygen intermediates in cytochrome c oxidase. *Biochimica et Biophysica Acta*, 2000, 1459, 533-539.
16. Jacob, M.; Holtermann, G.; Perl, D.; Reinstein, J.; Schindler, T.; Geeves, M. A.; Schmid, F. X. Microsecond folding of the cold shock protein measured by a pressure-jump technique. *Biochemistry*, 1999, 38, 2882-2891.
17. Regenfuss, P.; Clegg, R. M.; Fulwyler, M. J.; Barrantes, F. J.; Jovin, T. M. Mixing liquids in microseconds. *Review of Scientific Instruments*, 1985, 56, 283-290.
18. Roder, H.; Maki, K.; Cheng, H. Early events in protein folding explored by rapid mixing methods. *Chemical Reviews*, 2006, 106, 1836-1861.
19. Shastry, M. C.; Luck, S. D.; Roder, H. A continuous-flow capillary mixing method to monitor reactions on the microsecond time scale. *Biophysical Journal*, 1998, 74, 2714-2721.
20. Cherepanov, A. V.; De Vries†, S. Microsecond freeze-hyperquenching: development of a new ultrafast micro-mixing and sampling technology and application to enzyme catalysis. *Biochimica et Biophysica Acta*, 2004, 1656, 1-31.
21. Wiertz, F. G. M. Electron transfer and proton pumping pathways in cytochrome aa3. *PhD Thesis*, Delft University of Technology, Delft, The Netherlands, 2007.
22. Wiertz, F. G.; Richter, O. M.; Ludwig, B.; de Vries†, S. Kinetic resolution of a tryptophan-radical intermediate in the reaction cycle of *Paracoccus denitrificans* cytochrome c oxidase. *Journal of Biological Chemistry*, 2007, 282, 31580-31591.
23. Ballou, D. P.; Palmer, G. A. Practical rapid quenching instrument for the study of reaction mechanisms by electron paramagnetic resonance spectroscopy. *Analytical Chemistry*, 1974, 46, 1248-1253.
24. Chance, B. The Stopped-flow Method and Chemical Intermediates in Enzyme Reactions - A Personal Essay. *Photosynthesis Research*, 2004, 80, 387-400.

25. Hertzog, D. E.; Ivorra, B.; Mohammadi, B.; Bakajin, O.; Santiago, J. G. Optimization of a Microfluidic Mixer for Studying Protein Folding Kinetics. *Analytical Chemistry*, 2006, 78, 4299-4306.
26. Hertzog, D. E.; Michalet, X.; Jäger, M.; Kong, X.; Santiago, J. G.; Weiss, S.; Bakajin, O. Femtomole Mixer for Microsecond Kinetic Studies of Protein Folding. *Analytical Chemistry*, 2004, 76, 7169-7178.
27. Knight, J. B.; Vishwanath, A.; Brody, J. P.; Austin, R. H. Hydrodynamic Focusing on a Silicon Chip: Mixing Nanoliters in Microseconds. *Physical Review Letters*, 1998, 80, 3863-3866.
28. Yao, S.; Bakajin, O. Improvements in Mixing Time and Mixing Uniformity in Devices Designed for Studies of Protein Folding Kinetics. *Analytical Chemistry*, 2007, 79, 5753-5759.
29. Pabitt, S. A.; Hagen, S. J. Laminar-flow fluid mixer for fast fluorescence kinetics studies. *Biophysical Journal*, 2002, 83, 2872-2878.
30. Caged Compounds. *Methods in Enzymology*, Academic Press, 1998, 291.
31. Choi, J.; Terazima, M. Photoreaction of caged ATP studied by the time-resolved transient grating method. *Photochemical and Photobiological Sciences*, 2003, 2, 767-773.
32. Giovannardi, S.; Lando, L.; Peres, A. Flash Photolysis of Caged Compounds: Casting Light on Physiological Processes. *News in Physiological Sciences*, 1998, 13, 251-255.
33. Avila, K.; Moxey, D.; de Lozar, A.; Avila, M.; Barkley, D.; Hof, B. The Onset of Turbulence in Pipe Flow, *Science*, 2011, 333, 6039, 192-196.
34. de Vries†, S. Freeze-Quench Kinetics in *Encyclopedia of Inorganic Chemistry*. John Wiley & Sons, Ltd., 2007, 125-142.
35. Mitic, S.; de Vries†, S. Rapid Mixing Techniques for the Study of Enzyme Catalysis. Part of the online *Comprehensive Biophysics* (BIPH 00127) book, Elsevier, 2012.
36. Ballou, D. P. Freeze-quench and chemical-quench techniques. *Methods in Enzymology*, 1978, 54, 85-93.
37. Berger, R. L. Some problems concerning mixers and detectors for stopped flow kinetic studies. *Biophysical Journal*, 1978, 24, 2-20.
38. Berger, R. L.; Balko, B.; Chapman, H. F. High resolution mixer for the study of the kinetics of rapid reactions in solution. *Review of Scientific Instruments*, 1968, 39, 493-498.
39. Chance, B. *Journal of the Franklin Institute*, 1940, 229, 737-740.
40. Cherepanov, A.; de Vries†, S. bo3 oxidase studied by ultrafast mixing and freeze-quenching in the microsecond time domain. (Abstract oral presentation) in 6th *European Conference on Biological Inorganic Chemistry* (EuroBIC), 2002, p 35, July 29 - August 3, Lund, Sweden.
41. de Vries†, S.; Albracht, S. P.; Berden, J. A.; Slater, E. C. The pathway of electrons through QH2:cytochrome c oxidoreductase studied by pre-steady-state kinetics. *Biochimica et Biophysica Acta*, 1982, 681, 41-53.
42. de Vries†, S.; van Hoek, A. N.; Berden, J. A. The oxidation-reduction kinetics of cytochromes b, c1 and c in initially fully reduced mitochondrial membranes are in agreement with the Q-cycle hypothesis. *Biochimica et Biophysica Acta*, 1988, 935, 208-216.
43. Grigoryants, V. M.; Veselov, A. V.; Scholes, C. P. Variable velocity liquid flow EPR applied to submillisecond protein folding. *Biophysical Journal*, 2000, 78, 2702-2708.
44. Hartridge, H.; Roughton, F. J. W. The velocity with which carbon monoxide displaces oxygen from combination with haemoglobin. *I. Proc Royal Soc London, series B Biol Sci*, 1923, 94, 336-367.
45. Neltchev, V. Z.; Detchev, G. D.; Boyadjiev, L. A. Mixing device for investigating the kinetics of rapid reactions in solutions. *Journal of Physics E: Scientific Instruments*, 1970.
46. Paeng, K.; Paeng, I.; Kincaid, J. Time-resolved resonance raman spectroscopy using a fast mixing device. *Analytical Sciences*, 1994, 10, 157-159.
47. Roder, H.; Maki, K.; Latypov, R. F.; Cheng, H.; Shastry, M. C. R. Early events in protein folding explored by rapid mixing methods. *WILEY-VCH Verlag GmbH & Co. KGaA, Weinheim*, 2005, Vol. Part I.
48. Tanaka, M.; Matsuura, K.; Yoshioka, S.; Takahashi, S.; Ishimori, K.; Hori, H.; Morishima, I. Activation of Hydrogen Peroxide in Horseradish Peroxidase Occurs within approximately 200 micro s Observed by a New Freeze-Quench Device. *Biophysical Journal*, 2003, 84, 1998-2004.
49. Tang, J.; Gai, F. A millisecond infrared stopped-flow apparatus. *Applied Spectroscopy*, 2006, 60, 1477-1481.

50. White, A. J.; Drabble, K.; Wharton, C. W. A stopped-flow apparatus for infrared spectroscopy of aqueous solutions. *Biochemical Journal*, 1995, 306, 843-849.
51. Roughton, F. J. W. The kinetic's of haemoglobin IV - General methods and theoretical basis for the reactions with carbon monoxide. *Proceedings of the Royal Society (London)*, 1934, 115B, 451-464.
52. Majumdar, Z. K.; Sutin, J. D. B.; Clegg, R. M. Microfabricated continuous-flow, turbulent, microsecond mixer. *Review of Scientific Instruments*, 2005, 76, 1-11.
53. Kubelka, J.; Chiu, T.; Davies, D. R.; Eaton, W. A.; Hofrichter. J. Sub-microsecond Protein Folding, *Journal of Molecular Biology*, 2006, 359, 546-553.
54. Watt, E. D.; Shimada, H.; Kovrigin, E. L.; Loria, J. P. The mechanism of rate-limiting motions in enzyme function. *PNAS*, 2007, 104, 29, 11981-11986.
55. Eisenmesser, E. Z.; Millet, O.; Labeikovsky, W.; Korzhnev, D. M.; Wolf-Watz, M.; Bosco, D. A.; Skalicky, J. J.; Kay, L. E.; Kern, D. Intrinsic dynamics of en enzyme underlies catalysis. *Nature*, 2005, 438

Chapter 2

Rapid mixing techniques for the study of enzyme catalysis

Sandra Mitić and Simon de Vries†

Adapted from: Comprehensive Biophysics, Academic Press, Oxford, UK,
2012, 514-532

1. Abstract

Rapid-mixing techniques are applied to delineate enzyme and/or chemical catalytic mechanisms in detail. To do so successfully, mixing of the reactants must be sufficiently fast to cover the pre-steady state time domain in which transient intermediates are formed. The pre-steady kinetics of enzymes can be monitored by a great variety of spectroscopic techniques, which provide electronic and sometimes true structures of intermediates: UV-Vis spectroscopy, Fluorescence, Circular Dichroism, Fourier Transform IR, Electron Paramagnetic Resonance, Electron Nuclear Double Resonance spectroscopy, Electron Spin Echo Envelope Modulation, Mossbauer spectroscopy, Resonance Raman spectroscopy, Nuclear Magnetic Resonance or X-ray absorption spectroscopy.

This chapter details various aspects of turbulent, laminar continuous, and stopped-flow rapid mixing instrumentation as well as rapid freeze-quenching and microsecond freeze-quenching/sampling methodologies. The specific design features of mixers and rapid mixing instruments are discussed in relation to the various spectroscopic analyses methods.

Glossary

CCD, Charged Coupled Device
CD, Circular Dichroism
CF, Continuous Flow
ENDOR, Electron Nuclear Double Resonance
EPR, Electron Paramagnetic Resonance
ESEEM, Electron Spin Echo Envelope Modulation
EXAFS, Extended X-ray Absorption Fine Structure
FTIR, Fourier Transform InfraRed
MAS-NMR, Magic-Angle Spinning Nuclear Magnetic Resonance
MCD, Magnetic Circular Dichroism
MHQ, Microsecond freeze-HyperQuenching
RFQ, Rapid Freeze Quench
SF, Stopped Flow
XAS, X-ray Absorption Spectroscopy

d , channel diameter or diffusion path length (m)

D , diffusion constant ($\text{m}^2 \text{s}^{-1}$)

Re , Reynolds number (dimensionless)

$t_{(diff)}$, diffusion time (s)

$\langle v \rangle$, the average linear flow velocity (m s^{-1})

ρ , solvent density (kg m^{-3})

η , dynamic viscosity ($\text{kg m}^{-1} \text{s}^{-1}$)

τ_a , total sample-ageing time (s)

τ_m , mixing time (s)

τ_t , sample-transport time (s)

τ_c , cryofixation time (s)

2. Background

2.1 Introduction

Enzymology is the branch of biochemistry aiming to understand how enzymes work through the relationship between structure and function, and how they fold into their native state. To understand enzyme catalytic mechanisms in-depth one must perform a series of steady state and pre-steady state kinetic experiments and determine the precise 3D-structure of the enzyme. The techniques of pre-steady state kinetic experiments are described in this review. Enzymology is a multidisciplinary research field and integrates areas of biochemistry, microbiology, molecular biology, molecular genetics and biophysics. The core of enzymology consists of the development of reliable activity assays, (over)expression and purification, steady-state kinetic characterization and an initial basic structural characterization, which may include determination of subunit structure, molecular mass, prosthetic group content, co-factor requirement, and post-translational modifications. More detailed structural and mechanistic characterizations often require comparison of the WT with mutants and specifically labelled enzymes. In addition to the academic interest, understanding enzyme catalytic mechanisms is essential for the successful application of enzymes in industrial processes and for the development of enzyme inhibitors, which constitute a major segment of all existing drugs (~50-60%).

The literature dealing with the determination of enzyme catalytic mechanisms is enormous spanning biocatalysts as well as chemo-catalyst. A selected set of textbooks and original articles is included to help the reader on his or her way¹⁻²⁴.

2.2 Steady-state kinetics

Steady-state kinetic analyses serve to determine reaction rates, reaction rate constants and the rate law of chemical or enzyme catalysed reactions. Under steady state conditions, the enzyme performs repeated turnovers. The equation for the simplest enzyme mechanism, which applies to bio and chemo-catalysts, is given by



Solving the steady-state rate equation for this mechanism yields the Michaelis-Menten equation (assuming $\frac{dES}{dt}$ is constant and $[S] \gg [E]$) shown in **Eq. 2**:

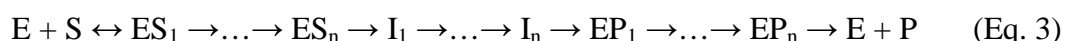
$$V = \frac{V_{max} \cdot [S]}{K_M + [S]} = \frac{k_{cat} \cdot [E] \cdot [S]}{K_M + [S]} \quad (\text{Eq. 2})$$

In **Eqs. 1** and **2** E , S and P denote enzyme, substrate and product concentrations, respectively, and further $V = -\frac{dS}{dt} = \frac{dP}{dt}$; $V_{max} = k_{cat} \cdot [E]$ and $K_M = \frac{(k_{-1} + k_{cat})}{k_1}$. Steady-state kinetic experiments in which $[S]$ is varied show a change from pseudo-first order kinetics at low $[S]$ to zero-order at high $[S]$. These analyses provide values for V_{max} or k_{cat} corresponding to the enzyme's maximal rate of turnover and also for

K_M , defined as the $[S]$ at which the rate is half-maximal. Although K_M is often associated with the binding affinity of the enzyme for its substrate, this is true only when $k_{cat} \ll k_{-1}$. The quotient k_{cat}/K_M is called the specificity constant and has the dimensions of a second order reaction-rate constant ($M^{-1} s^{-1}$). The specificity constant defines the minimal value for k_1 , the rate of substrate binding, i.e. $k_1 > k_{cat}/K_M$. The specificity constant is a rational means to distinguish between the specificities of different substrates for an enzyme, and provides a much better criterion for substrate selectivity than simply comparing the various V_{max} or K_M values.

The strength of the steady-state kinetic approach is its relative simplicity regarding experimentation and derivation of the expression of the overall rate equation. The steady-state approach enables, for example, facile discrimination between Ping-Pong kinetics and Ternary Complex formation, or between the binding of one or two of the same substrates yielding hyperbolic or sigmoidal relations between reaction rate and $[S]$, respectively. Experimental variation of pH, ionic strength, temperature, pressure, solvents and the use of inhibitors is easy and already provides mechanistic insight, which might be deepened by the application of isotopically labelled substrates or generation of site-specific mutant enzymes^{8,10,17}.

However, the major shortcoming of the steady-state kinetic method is that many enzymes show substrate saturation kinetics described by the Michaelis-Menten equation, which is therefore not very informative. By merely studying the overall reaction, the obtained information is biased towards the characteristics of the slowest step in the reaction path, obscuring the characteristics of other faster reaction steps. No matter how complex the reaction sequence of an enzyme, one will almost always be able to determine an apparent V_{max} and K_M . However, for multi-step reactions, these parameters are complex functions of many rate constants, and although the experimental value of V_{max} will still signify the maximal turnover of the enzyme under a specific set of conditions, the physico-chemical meaning of K_M remains unclear. In practice, even the simplest single substrate enzyme catalytic cycle will consist of several intermediate steps (I_1, I_n):



The initial bimolecular binding or docking of substrate (ES_1 , the so-called Michaelis complex) is represented in **Eq. 3**. An ‘induced fit mechanism’ is represented by the sequence ES_2 to ES_n . The chemical conversion of substrate into bound product generally involves a number of intermediate steps (I_1 – EP_1). Product release returns the free enzyme, which is ready for the next turnover. Product release is often slow and may follow a series of enzyme conformational changes induced by the bound product (up to EP_n), in a way similar to the changes induced by the binding of substrate. Additional substrates increase the complexity of the reaction by introducing more bimolecular steps. Some of the intermediates may bind/release H^+ or OH^- , which, like the binding of substrate is also a bimolecular reaction. The presence of intermediates that bind H^+ or OH^- can be detected by performing experiments over a wide pH range.

The individual or elementary steps in the mechanism of **Eq. 3** are necessarily faster and often much faster than the overall reaction. The first order rate constants are

generally between $\sim 10^1 \text{ s}^{-1}$ and $\sim 10^6 \text{ s}^{-1}$ (but may be 10^{12} s^{-1} in the case of electron transfer) while the second order or bimolecular rate constants range between $\sim 10^4$ and $\sim 10^{10} \text{ M}^{-1} \text{ s}^{-1}$. To solve enzyme catalytic mechanisms, the simplest, steady-state kinetic analyses do not suffice and the experimental toolbox has to be extended to pre-steady state kinetic methods.

2.3 Pre-steady state kinetics

Pre-steady state kinetic studies aim to resolve in time each individual step in a catalytic reaction sequence. In pre-steady state experiments, enzyme and substrate are very rapidly mixed and changes in the state of the enzyme are monitored over time. When possible, changes of substrate and product concentrations are also monitored. During catalysis, the optical, magnetic, vibrational and structural properties of the enzyme, substrate and product may change, which enables spectroscopic detection of transient intermediate states. Commonly used spectroscopic methods in kinetic mixing instruments are UV-Vis, Fluorescence and CD spectroscopy, while specialized instruments have been designed to enable FTIR, EPR EXAFS or NMR spectroscopy. The frozen powder samples obtained by the rapid freeze-quench techniques can be analysed by low-temperature UV-Vis, EPR, ESEEM, ENDOR, and EXAFS, resonance Raman or Mossbauer spectroscopy.

In most pre-steady state analyses, the experiment is carried out in such a way that the enzyme can perform a single turnover only. This allows intermediates to accumulate from zero concentration and subsequently breakdown completely without reaching their steady-state concentrations. A true intermediate is defined as one that is formed and broken down faster than the steady-state turnover rate of the enzyme. Detection of all intermediates is possible only when the mixing of the reactants and the observation are much faster than the turnover rate of the enzyme and much faster than the fastest step in the reaction sequence. There is no guarantee, in practice, that each individual intermediate can indeed be observed, since an intermediate may be 'spectroscopically silent' or sparsely populated below the instrumental detection limit. The latter may be the result of a very short lifetime, caused by a much greater rate of breakdown than rate of formation.

The substrate-binding step in **Eq. 3** can in principle be made faster than any other step in the reaction sequence, because it is the only bimolecular reaction. All other steps occur at first-order rates, which are sensitive to sample conditions (temperature, buffer, pH, etc.). Ideally, the pre-steady state experiment is performed at the highest possible $[S]$, so that at $t = 0$, all enzyme is in the state ES_1 , which subsequently decays with a series of characteristic rate constants. This experimental approach works best for enzymes for which product release is slow, so that the high $[S]$ will not induce a second turnover, or a steady-state kinetic behaviour of the intermediates.

In so-called *relaxation* (single turnover) pre-steady state experiments, the enzyme and substrate are usually premixed and at a state of equilibrium. By suddenly disturbing the equilibrium, for example by a pulse of light from a laser, the system will return to its initial equilibrium or to a new equilibrium state. The laser flash may induce 'natural' photochemical reactions such as electron transfer in plant and bacterial photosynthetic systems. In another type of relaxation pre-steady state experiment, ES_1

(Eq. 3) may be formed from a photo-labile substrate-analogue ('caged compound') that is converted into a true substrate upon a pulse of light, obviating the need for rapid mixing²⁵⁻²⁷. In particular, when the caged compound is already bound to the enzyme before the light pulse, the reaction between E and S will be very fast, and limited only by the kinetics of the photochemistry, which can be slow. Alternatively, a laser may rapidly change the temperature of the enzyme/substrate mixture, which subsequently evolves to a new equilibrium at the higher temperature. Similarly, an equilibrated system may be subjected to a sudden change in pressure. As **Table 1** shows, the time resolution of the *relaxation* techniques is superior to that of the mixing techniques, which is mainly due to the advent of sub-femtosecond lasers²⁴. The mixing of liquids and subsequent spectroscopic observation of the mixture on a μs or shorter time-scale presents an important technological barrier. In spite of their time limitation, the mixing techniques offer a wider range of applications than the relaxation techniques. Today a variety of different pre-steady state mixing instruments is used in studies of biochemical or chemical systems such as stopped-flow, continuous-flow, rapid quenched-flow, rapid freeze-quenching and microsecond-freeze hyperquenching.

Table 1. Dead-times of various pre-steady state kinetic techniques

Pre-steady state kinetic techniques	Instrumental dead-time*
Turbulent Flow Mixing Techniques	
Continuous-flow (minimal mixing time) ³⁹	15 μs
Capillary micro-mixers ^{23,39,41}	45 μs
Microsecond Freeze-HyperQuenching (MHQ) ^{16,45,46}	75 μs
Chemical Quenching ²³	60 μs /1 ms
Rapid Freeze-Quenching (RFQ) ²⁸	5 ms
Stopped-flow ⁶²	0.5 ms
Diffusive Flow Mixing Techniques	
Continuous-flow hydrodynamic focusing ^{51-55, *}	1-500 μs
Relaxation techniques	
Laser Flash Photolysis (shortest pulse) ²⁴	< 1 fs
Photochemistry ²⁴	5 fs
Pulse-probe (e.g. photosynthesis) ²⁴	100 fs
Temperature jump ¹¹¹	5 ps
Time resolved X-ray diffraction ¹¹⁰	200 ps
Caged compounds/Flow-Flash ^{112,113}	1 ns
Pressure-jump ¹¹⁴	50 μs

*see **section 4.5** for a discussion on the dead-times

The King-Altman method is a well-established and easily applicable method to derive steady-state rate equations for both simple and complex enzyme mechanisms^{10,17}. The derived equations generally provide quantitative fits to the experimental data. Quantitative analysis of pre-steady state kinetic data requires analytical integration of the rate equation in order to describe the substrate, intermediate and product concentrations as a function of time. However, analytical integration of the fully reversible Michaelis-Menten equation or of the three component reaction $A \leftrightarrow B \leftrightarrow C$ already presents a formidable challenge. The mathematical expression is

greatly simplified when one or more reaction steps are (quasi-) irreversible or when a relatively stable intermediate is formed. When all reactions are treated as irreversible (**Eq. 3**), the analytical expressions describing the kinetics of the intermediate states become progressively more complex in relation to the number of intermediates. However, the numerical solution for an infinite series of reactions as in **Eq. 3** requires a short computer programming procedure. The equations of the type $\frac{-dES_1}{dt} = k_1 \cdot [ES_1] \dots \frac{dES_n}{dt} = k_n \cdot [ES_n]$ are repeatedly integrated to give the desired quantitative time dependent concentration information.

3. The design of rapid mixers

3.1 Turbulent mixing

The ideal mixing device should, under turbulent flow conditions, enable complete mixing over very short distances by uniformly dispersing the reactants to the molecular level. Diffusion and collision of the reactants constitute the basic steps in mixing, after which the reaction proceeds. Turbulence enables the solutions to break-up into very small volume elements known as turbulent eddies. Smaller turbulent eddies yield shorter diffusion distances and hence faster mixing. Various mixers that enable efficient turbulent mixing have been designed over the years. The most commonly used mixers are the simple T-mixers (SF UV-Vis and RFQ), multiple-jet tangential mixers (SF UV-Vis/FTIR and RFQ), the Berger ball mixer (SF UV-Vis/EPR/FTIR) and the co-axial type mixers such as the ball mixer used in the capillary micro-mixers (CF UV-Vis/EPR) (**Figs. 1, 2, 8 and 9 and Table 2**)^{3,16,23,28-45}.

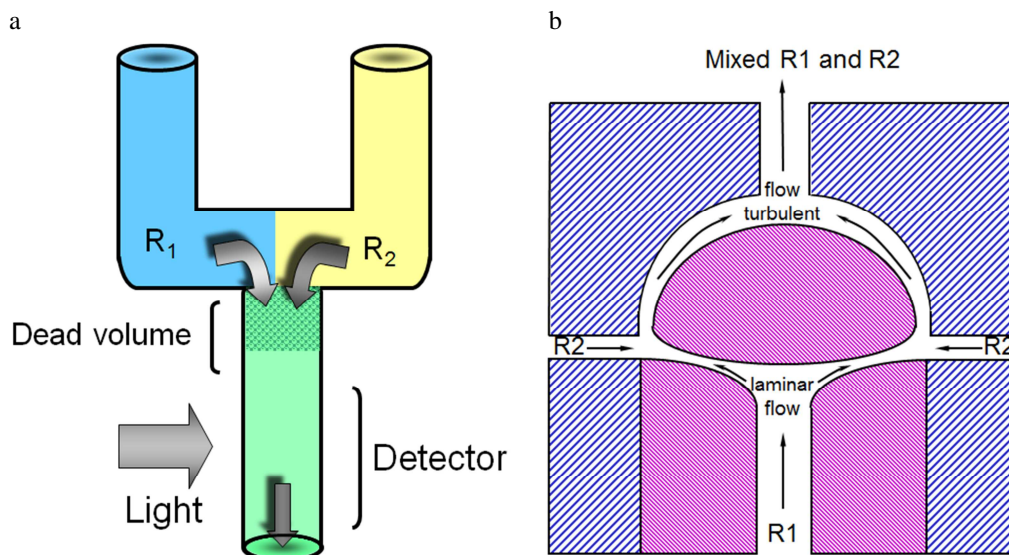


Figure 1. (a) Commonly used T-mixer in stopped-flow devices. Channel bores are usually ~0.5-2 mm, but only 60 μm in the T-mixer used for MHQ⁴². The figure is adapted from de Vries† 2007¹⁹. (b) Berger ball mixer used in stopped-flow devices. R₁ and R₂ denote reactant 1 and reactant 2, respectively. The drawing is after Berger 1968³⁰.

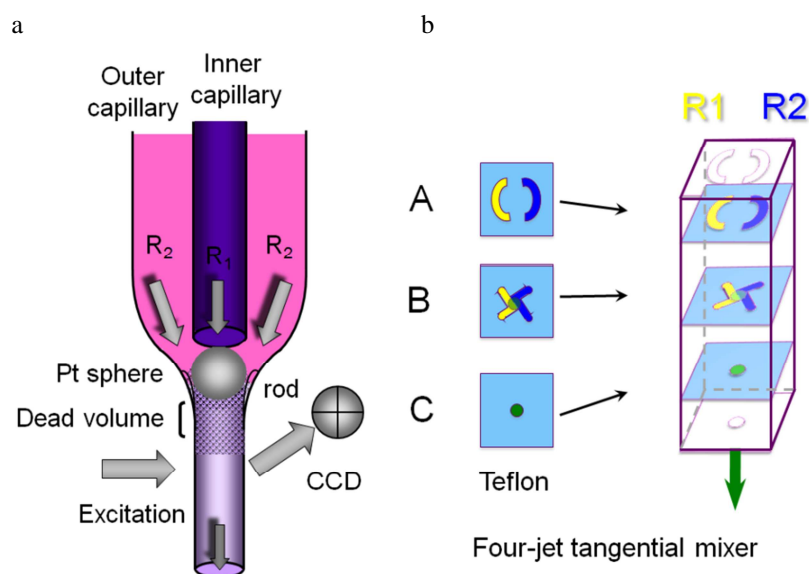


Figure 2. (a) Capillary ball micro-mixer used in continuous-flow devices. Approximate dimensions are 0.15 mm and 4 mm for the inner- and outer-capillaries, respectively and 0.25 mm for the observation cell. The drawing is adapted from de Vries† 2007¹⁹. (b) Schematic drawing of the four-jet-tangential mixer used in stopped-flow and rapid freeze-quench devices. The complete mixer is built by pressing the three (Teflon) gaskets A, B and C on top of each other (as in the right part of the figure, see also **Fig. 8**). The four-jet tangential mixer can easily be extended to a multiple stream mixer. See text, **Fig. 8** and original papers for further details. R_1 and R_2 denote reactant 1 and reactant 2, respectively.

Table 2. Technical properties of various Continuous-flow rapid mixing devices and comparison with commercial Stopped-flow apparatus*

Technical properties	Continuous-flow		Stopped-flow
	Shastry et al. ⁴¹	Majumdar et al. ⁸⁰	Commercial SF
Type of mixer	quartz capillary mixer	turbulent micro-mixer	T-mixer, Berger ball
Reactant driving system	pneumatic drive ram	double syringe pumps	pneumatic drive ram or stepper motor
Path length of the optical cell	250 μm	Observation in free jet	2 mm fluorescence 10 mm absorbance
Mixing volume	~ 10 nL	~ 5 nL	30 μL
Channel or orifice diameter (μm)	250	70	2,000
Re in mixing chamber or in orifice	30,000	5,500	40,000
Maximum back pressure (ΔP , MPa)	1.0	>7.0 bar	0.2-1.0
Maximum flow rate	40 mL min^{-1}	>30 mL min^{-1}	50 mL s^{-1}
Linear flow rate in channel or jet (m s^{-1})	>10 in flow cell	79	20
Mixing dead-time (μs)	15	10	600
Total instrumental dead-time (μs)	45-100	14-20	500-2000

*Calculations of Re and ΔP are based on $\rho = 10^3 \text{ kg m}^{-3}$ and $\eta = 10^{-3} \text{ kg m}^{-1} \text{ s}^{-1}$

The efficiency of mixing depends on the dimensionless Reynolds number, Re , used to characterize different flow regimes. Laminar flow, characterized by a smooth, constant fluid motion, occurs at $Re < \sim 2000$ for flow through pipes, where viscous

forces are dominant. Turbulent flow occurs at $Re > \sim 2000$ for pipe flow and is dominated by inertial forces, according to equation:

$$Re = \frac{\rho \cdot v \cdot d}{\eta} \quad (\text{Eq. 4})$$

In **Eq. 4**, ρ is the density of the solvent (equal to 1000 kg m^{-3} for water at 20°C), $\langle v \rangle$ the linear average flow velocity of the liquid (m s^{-1} in a channel), d the hydraulic diameter of a channel (in m) and η the dynamic viscosity (equal to $10^{-3} \text{ kg m}^{-1} \text{ s}^{-1}$ for water at 20°C). The values for ρ and η are relatively constant in aqueous solution and the instrumental mixing time depends mainly on the mixer's geometry and dimensions (width, depth and length of the channel) and on the flow rate. Consequently, in order to achieve rapid and efficient mixing with turbulent flow ($Re > 2000$ - 2500), in a minimal period of time, high flow rates are required as well as relatively large channel dimensions ($d > 100 \mu\text{m}$). High flow velocities require large amounts of energy to be delivered by the drive-ram systems. The high fluid flow velocities can cause cavitation, which occurs when the pressure of the liquid falls below its vapor pressure leading to evaporation. The vapor bubbles resulting from cavitation are detrimental for optical analyses. High flow velocities also lead to pressure (ΔP) build-up according to Bernoulli's velocity/dynamic pressure equation:

$$\Delta P = 0.5 \cdot \rho \cdot (\langle v \rangle)^2 \quad (\text{Eq. 5})$$

At high concentrations of reactants, the mixing efficiency and/or rate of mixing may decrease due to the increase of the viscosity of the solutions. As a consequence Re may fall below ~ 2000 resulting in incomplete mixing. The viscosity also increases with decreasing temperatures, in particular when cryo-solvents (glycerol or ethylene glycol) are used to perform kinetics at sub-zero temperatures. To maintain high flow rates of viscous solutions a powerful drive-ram system is needed such as a hydraulic or pneumatic ram. Regular HPLC pumps capable of providing 40 MPa of pressure may also be sufficient^{16,19,45,46}. The air pressure of regular drive-ram systems of commercial SF instruments (operating up to 1 MPa) may, however, be too low to deal with viscous solutions as encountered in RFQ experiments, but a powerful stepper-motor will do.

3.2 Laminar flow mixing

Mixing under laminar flow conditions will occur rapidly when the distance over which fluids have to be diffusively mixed is very small. Laminar flow mixing is a good alternative to turbulent mixing especially when one has limited amounts of reagents. As a result of rapid developments in the fields of micro- and nano-machining and lithography, micro-mixers with flow channels as small as $1 \mu\text{m}$ or even smaller have been manufactured. The diffusion time for solutes (t_{diff}) is given by **Eq. 6**:

$$t_{diff} = \frac{d^2}{2 \cdot D} \quad (\text{Eq. 6})$$

The diffusion time, t_{diff} is proportional to the square of the distance or the channel diameter, d over which molecules have to diffuse. For a small molecule with diffusion

constant: $D \sim 10^{-9} \text{ m}^2 \text{ s}^{-1}$ the diffusion time is $\sim 500 \text{ } \mu\text{s}$ for a channel of $1 \text{ } \mu\text{m}$. Thus, by decreasing the diffusion distance, the mixing-diffusion time becomes shorter. Based on this principle, different types of diffusive mixers have been developed, such as the glass-silicon-glass mixer (SF FTIR) and the LIGA (lithography, electroplating and molding) structured stainless-steel mixer (SF FTIR)⁴⁷⁻⁴⁹. These laminar-flow systems require small sample volumes, and low flow rates of a few nL s^{-1} , which is ideal for the study of expensive biochemical samples. The operating pressure is very close to ambient.

Hydrodynamic focusing represents a recent development to employ diffusive micro-mixers with minimal amounts of sample consumption. Through specific solvent delivery and mixer geometries, a liquid flow is squeezed or 'hydrodynamically focused' into a thin stream, reducing the diffusion distance to 50-100 nm and yielding a diffusive mixing time in the microsecond time range⁵⁰⁻⁵⁵. However, the slow onset of mixing may result in true dead-times that might in fact be longer, on the order of $\sim 500 \text{ } \mu\text{s}$ ⁵⁵. See also **Paragraph 4.5** for a discussion on the reported mixing times.

3.3 Mixers and dead-times

Figs. 1 and 2 show the most commonly used mixers. The T-mixers are the simplest and most classical types of mixers (**Fig. 1a**). At the point where the two fluids collide, the mixing is initiated but generally not complete. Mixing is completed within a short distance just downstream (dead volume), in the region between the initial collision point of the two fluids and the observation chamber. The total dead-time of a stopped-flow apparatus with a T-mixer corresponds approximately to the time needed to fill the dead volume region and the observation chamber. This dead-time depends on the linear flow rate in the system and can be decreased by increasing the flow rate, which, however, increases the pressure. The dead-times achieved by commercial stopped-flow devices ($\sim 1\text{-}2 \text{ ms}$) are often limited by the pressure the SF instrument can withstand. In miniaturized stopped-flow cells, less time is spent filling the observation cell, which results in dead-times of $\sim 0.5\text{-}0.7 \text{ ms}$ (**Table 2**).

In the Berger four-jet ball mixer (**Fig. 1b**), the mixing of two solutions is driven by turbulence as the solutions flow at high velocities around a sphere³⁰. Behind the sphere, the solutions enter a zone of high turbulence where they are completely dispersed into small volume elements resulting in complete mixing within $100 \text{ } \mu\text{s}$. Mixing is rapid because diffusion occurs over very short distances. The design of the co-axial capillary mixer (**Fig. 2a**) is based on the concept of the Berger-ball mixer³⁹. Co-axial mixers consist of an inner and an outer coaxial glass capillary, which form the mixing chamber together with a small ($50\text{-}250 \text{ } \mu\text{m}$) platinum sphere placed at their junction and at the conical end of the outer capillary. The two solutions run parallel through co-axially positioned capillaries over a short distance towards the sphere. At this stage, the two solutions do not mix because of the low Re . Mixing occurs in the small opening ($5\text{-}10 \text{ } \mu\text{m}$ wide) between the sphere and the outer capillary wall. The rapid flow of the solutions around the sphere ($\sim 100 \text{ m s}^{-1}$) produces a small area of high turbulence ($Re \sim 30,000$) and the reagents are mixed behind the sphere within $10 \text{ } \mu\text{s}$ (**Table 2**). Without the sphere, the channel dimensions and flow rates would yield a calculated Re of ~ 1500 , insufficient for rapid and complete mixing. The capillary micro-mixers have proven to be fast and versatile mixing devices. The great

advantage of the capillary micro-mixers is the short dead-time while operating at low pressures.

Four-jet tangential mixers (**Figs. 2b, 8 and 9**) are used in stopped-flow instruments but more commonly in RFQ and miniaturized MHQ (**Figs. 8 and 9**)^{16,28,34,44-46,56,57}. The four-jet tangential mixer used in SF and RFQ instruments consists of three parts (**Fig. 2b**). On top lies a thin gasket with two half-moon holes, each for one reactant. The liquid stream of each half-moon channel is divided into two in the relatively thick gasket containing the four-jet pattern. Here the liquid flows from the side to the centre ('the pre-mixing chamber') and is subsequently forced downward through a small hole in the centre of a thin gasket. In this last gasket the actual mixing occurs. The mixing time in this mixing chamber is ~50 μs (**Table 5**). The three gaskets are pressed together firmly in a mixer body to prevent solvent leakage (see also **Figs. 2b, 8 and 9**). In practice the four-jet tangential mixers are capable of mixing concentrated protein solutions more effectively than T-mixers. It is possible that the presence of the angular momentum of the flow helps to accomplish this.

3.4 The stopped-flow method

The first turbulent-mixing instrument that was faster than manual mixing was described by Hartridge and Roughton in 1923⁵⁸. The dead-time of this continuous-flow instrument was ~10 ms and improved to ~2 ms in 1930⁵⁹⁻⁶¹. The two reactants are efficiently mixed using a modified Rolls-Royce carburettor made of brass. The approach is based on the principle of alternating multi-stream mixing of reactants by a four-jet tangential mixer. The mixed reactants enter a flow observation tube and the reaction progress is monitored perpendicular to the flow tube at various points. By knowing the flow rate, the distance can be translated into reaction time. The high flow rates require large sample volumes for experimentation.

The stopped-flow technique, introduced by Roughton in 1934 was greatly improved by Britton Chance in 1940^{31,61,62}. It is currently the most frequently used method for the pre-steady state enzyme kinetics studies because of its sample economy, improvement in time resolution, and wide dynamic time range. In the commercial stopped-flow systems (**Fig. 3 and Table 2**), small volumes of the two reactants, e.g. enzyme and substrate, are simultaneously forced by a fast drive-ram system (a pneumatic actuator or stepper motor) into a high efficiency mixer to initiate the reaction. High flow rates of approximately 5-15 mL s^{-1} and relatively large channel diameters of 1-2 mm ensure turbulent flow conditions ($Re > 5000$, **Table 2**). The volume of the mixed reactants displaces the previous content of the relatively large observation flow cell (40 μL cuvette, dimensions 2 mm x 2 mm x 10 mm). The volume injected is limited by the volume set by the (emptied) stop syringe. When the volume of the stop syringe is filled, the plunger hits a block, causing the flow to be stopped 'instantaneously'. This volume of the stop syringe is set so that just prior to stopping, a steady state flow has been achieved. To prevent having any contamination of the previous experiment in the mixing chamber, the volume of the stop syringe is two to three times that of the volume of mixer and flow cell (~100 μl). The mixed solution that enters the flow cell is ~1-2 ms old, which corresponds to the dead-time of the stopped-flow device.

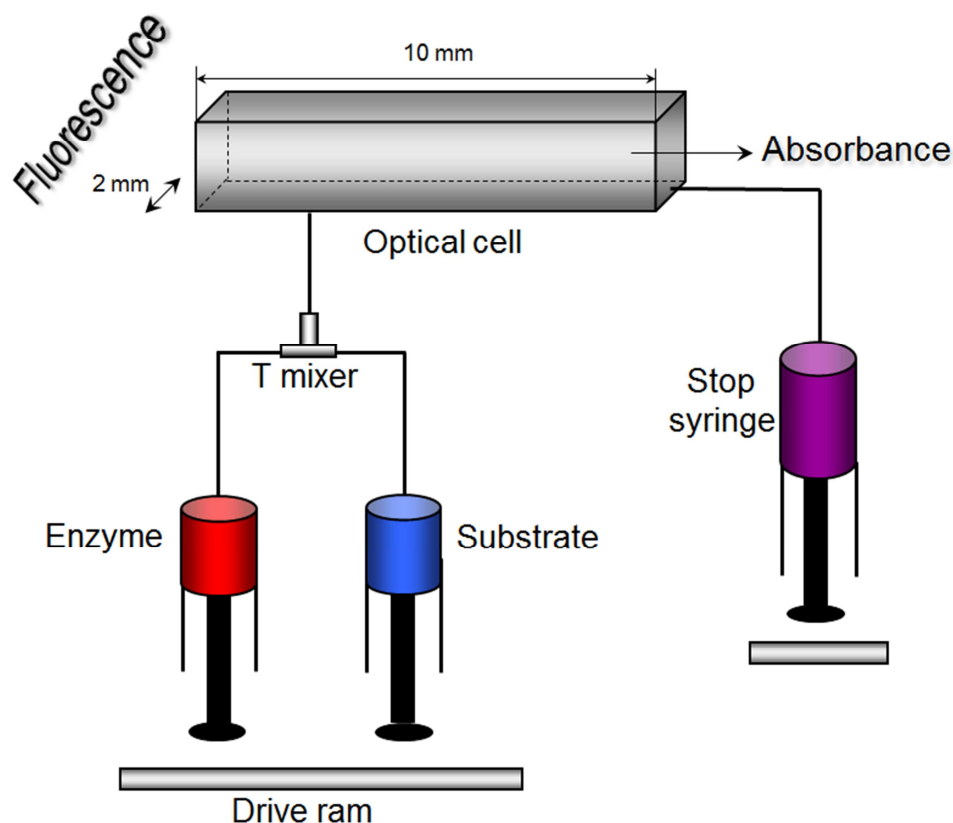


Figure 3. Schematic diagram of the Stopped-Flow apparatus. When the stop syringe is omitted the same setup can be used in the continuous-flow mode. Common dimensions of the optical cell are ~ 2 mm \times 2 mm \times 10 mm.

Mixing options for the stopped-flow technique include multi-mixing (also known as double- or sequential-mixing) where more than two reactants are mixed in two or more consecutive mixing steps. Moreover, for applications where only very small quantities of reactants are available, variable ratio mixing using syringes of different sizes is preferable. In stepper-motor driven stopped-flow devices, variable mixing ratios can be obtained by programming different motor speeds for each syringe. Most stopped-flow equipment operates over a wide temperature range (-80 to $+50^\circ\text{C}$).

To monitor the reaction progress, the contents of the observation cell are illuminated by a light source and the change in optical properties (absorbance, fluorescence, circular dichroism) is monitored in real time either from the moment when the mixed reactants enter the observation cell (using a pre-trigger) or when initiated by the stop of the stop syringe. Improvement in the time resolution (to ~ 0.5 ms) came recently with miniaturization of the observation cell by several stopped-flow manufactures.

Since the first introduction of the stopped-flow method, its field of application has expanded enormously. Present date stopped-flow devices are well-suited to deal with a great variety of non-aqueous solvents and enable anaerobic experiments, studies at sub-zero temperatures, at very high temperatures^{63,64}. High-pressure stopped-flow instruments have been developed that operate at 200 MPa (2-3 ms dead-time) to study protein (un)folding²⁵. In addition, stopped-flow instruments have been designed that

enable fluorescence lifetime measurements, FTIR (dead-times of 5-100 ms), NMR, EPR, and EXAFS analyses^{35,43,44,48,49,56,57,63,65-79}.

3.5 Continuous-flow instruments

Continuous flow methods are used in pre-steady state enzyme kinetic studies and kinetic studies of protein folding. In the continuous flow experiment two or more fluids are continuously forced at high flow rates through a mixer where they are completely mixed under turbulent flow conditions. The progress of the reaction is then observed at different times under steady-state flow conditions at several distances from the mixer along the flow cell. Monitoring of the reaction is most commonly performed by fluorescence or UV-Vis absorbance spectroscopy. The dead-time of continuous-flow instruments is considerably shorter than of the stopped-flow apparatus, however, the consumption of reagents is much higher²³. Reduction of sample amount became possible with advances in mixer design and detection methods. These advancements made it possible to achieve efficient, ultra-fast mixing and to acquire a complete kinetic profile in a few seconds.

In 1985, Regenfuss et al. introduced a continuous-flow capillary jet mixer where the principle of co-axial mixing was combined with the Berger ball mixer (**Figs. 1b** and **2a**)^{29,30,39}. The original design of the co-axial ball mixer or capillary micro-mixer by Regenfuss et al. was impractical because it was delicate and difficult to manufacture, and the progress of the reaction had to be monitored in an unstable, free-flowing jet by measuring fluorescence emission at various distances downstream from the mixer⁴¹. Continuous-flow experiments involving a free-flowing jet, in general, encounter difficulties due to instability of the jet and optical scattering artefacts⁸⁰.

Shastri et al. have successfully overcome the limitations of the Regenfuss continuous-flow capillary mixing apparatus by replacing the glass with a more sophisticated quartz capillary mixer with a fused-silica fluorescence observation flow cell, and a custom-made partially opaque absorbance flow cell, both of which have 0.25 mm path length^{23,41}. The design was further improved by integrating a digital camera with a UV-coated CCD detector into the detection system, which covers almost the entire UV-Vis spectral region (200-1000 nm) (**Fig. 2a**). The mixing time of 15 μ s and the dead-time of 45 ± 5 μ s of this mixing apparatus made it possible, for example, to study the kinetics of the early stages of protein folding by recording either the fluorescence profile or the transmittance/absorbance spectra along the whole length of the observation cell (10-15 mm) starting from the dead-time to about 2 ms.

4. Specialized stopped-flow and continuous-flow instruments

4.1 Stopped-flow FTIR

Fourier transform infrared spectroscopy coupled to the stopped-flow is a technique of particular interest because it provides direct structural and kinetic information on proteins in their native state in aqueous solution or in membranes. For example, secondary structures in proteins can be analyzed from the characteristic amide I bands around 1650 cm^{-1} or the binding of diatomic gases to metal centers can be probed using isotopes. Water, the natural solvent for many biological

macromolecules, has a strong absorbance at 1643 cm^{-1} that overlaps with the spectral areas that provide the corresponding protein structural information. To achieve good signal/noise ratios in the amide I region with protein solutions in water, the influence of water has to be minimized by decreasing the IR cell path length below $10\text{ }\mu\text{m}$ ⁴⁹. The alternative is to work with concentrated ($\sim\text{mM}$ range) protein solutions in deuterated water so that IR cuvettes with long path lengths of $25\text{ }\mu\text{m}$ up to $100\text{ }\mu\text{m}$ can be used to increase the S/N ratio^{43,44,48}. **Table 3** shows some technical properties of various infrared stopped-flow instruments and a comparison with the commercial stopped-flow apparatus.

The design of an IR cuvette coupled to the stopped-flow system is accompanied with several technical problems. The flow resistance of the thin cell increases with the inverse cube of the path length, which results in a high pressure build-up. Even a slight pressure variation can induce noticeable changes in the path length and thus in apparent IR-signal intensities. This problem can be resolved by using a more robust sealed cell of small internal volume, with thicker (4 mm) CaF_2 walls and with a fast relaxation time, τ_r , - the time required for the cell to relax from the pressurized to its depressurized path length when the flow is stopped⁴⁹. Therefore, the IR cell has to be of high mechanical stability and maintain a constant path length because even relatively low flow rates of $\sim 3\text{ mL min}^{-1}$ lead to high pressure drops in the cell⁴⁹. High flow rates are often a requirement for efficient turbulent mixing of aqueous solutions, in particular, when working with concentrated viscous proteins. In this respect, the design of an SF-FTIR apparatus that operates at reduced flow rates and low pressures enabling fast mixing by diffusion was a very constructive development^{48,49}. Moreover, in order to avoid high pressure fluctuations, while decreasing the dead volume and preventing formation of air bubbles, the stopped-flow apparatus was equipped with HPLC components, rather than a drive-ram system. **Fig. 4** shows the diagram of the FTIR stopped-flow apparatus designed by Masuch⁴⁴.

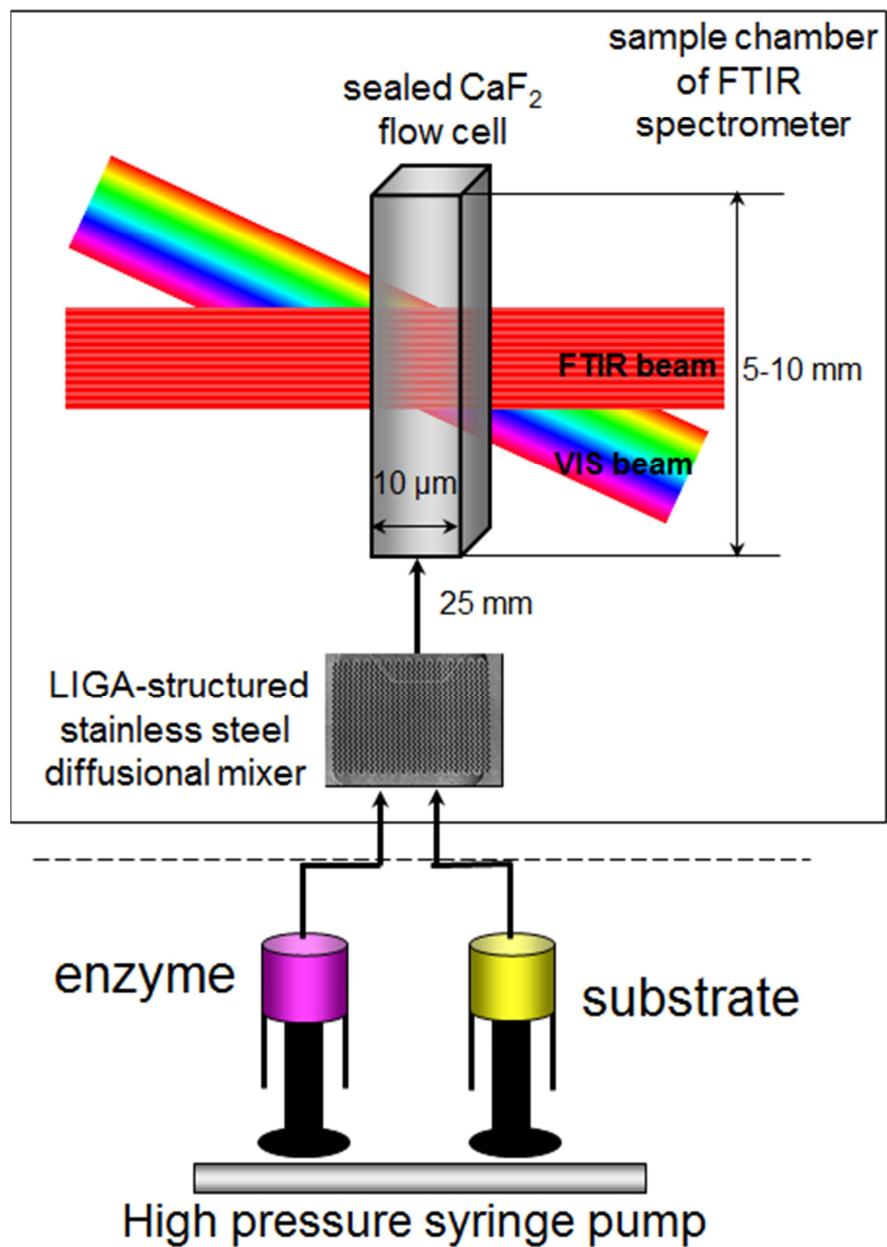


Figure 4. Schematic drawing of the Fourier Transform Infrared stopped-flow instrument. The figure has been redrawn after Masuch and Moss 2003⁴⁹.

Table 3. Technical properties of various Infrared Stopped-Flow instruments and comparison with commercial Stopped-Flow apparatus

Technical properties	Stopped-flow				
	Commercial SF	Infrared			
		White et al. ⁴⁴	Kakuta et al. ⁴⁸	Tang and Gai ⁴³	Masuch and Moss ⁴⁹
Scanning speed (resolution)		4 s ⁻¹ (2 cm ⁻¹)	4 s ⁻¹	50 ns MIR diode laser	30 ms (4 cm ⁻¹)
Type of mixer	T-mixer	six-jet turbulent mixer	glass-silicon-glass diffusive mixer	Berger ball mixer	LIGA-structured stainless-steel diffusional mixer
Reactant driving system	pneumatic drive ram or stepper motor	pneumatic drive ram operating at 0.55 MPa	double syringe pump	stepper motor	single high-pressure syringe pump
Path length of the optical cell	2 mm fluorescence 10 mm absorbance	50 μm	25 μm	100 μm	<10 μm
Max. back pressure	200-800 KPa	19 MPa in the drive system			3.5 MPa mixer 10 MPa flow cell
Max. flow rate	50 mL s ⁻¹		0.83 μL s ⁻¹	2-3 mL s ⁻¹	0.05 mL s ⁻¹
Volume of the optical cell	40 μL	10 μL 1cmx 2cmx 50mm		15 μL	0.7 μL
Total instrumental dead-time	0.5-2 ms	40 ms	> 1.4 s	5.7 ms	90/120 ms

The time resolution of the stopped-flow IR devices is also determined by the scanning rate of the Fourier transform interferometer, and the mechanical movement of the mirror. Scanning rates are typically 100 s⁻¹ at 8 cm⁻¹ spectral resolution, but a rate of 25 s⁻¹ at 2 cm⁻¹ is needed to resolve overlapping bands characteristic of specific conformers of enzyme-bound ligands. Depending on the SF-FTIR apparatus used, the time resolution may vary, but is roughly in the range from 40 to 90 ms (**Table 3**)^{44,49}. Scan averaging is used to achieve higher time resolution and improve the signal-to-noise (S/N) ratio at the cost of large quantities of reagents.

By designing an IR detection system equipped with a mid-infrared diode (MIR) laser and a mercury cadmium telluride detector (MCD #41), Tang and Gai greatly improved the dead-time of the stopped-flow IR apparatus to 6-15 ms, which was dependent on the flow rates and limited by the mixing time only⁴³. By using a quantum cascade (QC) MIR laser, both the time resolution (~6-10 ms) and the S/N ratio of the stopped-flow IR instrument can be slightly improved because a QC laser provides more power, enables broader tunability, and is more stable than the commonly used MIR.

4.2 High-pressure stopped-flow and temperature-jump stopped-flow instruments

Pressure and temperature are both thermodynamic parameters. Changes in temperature simultaneously perturb both volume and internal energy while pressure changes contribute to a change in volume and temperature of a system. The equations that describe the dependence of reaction rates on pressure or volume are analogous to the Arrhenius equation, which links reaction rates to temperature. Furthermore, pressure effects are governed by Le Chatelier's principle, which states that a system at equilibrium subjected to a stress, will shift its equilibrium in order to minimize the effect of that stress, for example, by an increase in pressure⁶⁷. Therefore, both pressure and

temperature are powerful tools in the study of the stability and dynamics of proteins and for the study of protein-ligand (substrate) interactions. They affect the interaction between solvent and chemical groups on the protein surface, substrate binding, enzyme stability and activity by perturbing the enzyme's active site. In addition, high pressure (and/or temperature) causes changes in the native protein conformation, which eventually leads to protein denaturation. The volume increase upon denaturation can be assessed from the effect of pressure. Pressures of 100-200 MPa are sufficient to cause (the onset of) dissociation of oligomeric proteins and protein complexes, whereas small monomeric proteins are usually denaturated in the pressure range from 400 to 800 MPa⁶⁷. Careful selection of buffers that are insensitive to pressure and have minimal ionization volumes are recommended to distinguish pressure effects from changes in pH.

The volume of a protein in solution is determined by three contributions: 1) the intrinsic volume composed of the volume of all individual atoms, 2) the void volume that is represented by the volume of internal cavities within the protein due to the imperfect packing of amino acid residues and which is the most compressible volume and 3) the solvation volume that is due to interactions of chemical groups on the surface of the protein with the solvent⁶⁶. Solvation includes the interaction between water molecules and the apolar domains, dissociation of substrate, breaking of ionic salt linkages, charge transfer interactions as well as the stacking of aromatic residues⁸¹. Only the second and the third contributions to the volume of proteins are usually significant in determining pressure dependent changes in structure and activity. The void volume contributes positively and the solvation volume contributes negatively to the total volume change when going from low to high pressures. Denaturation is accompanied by a large increase in solvation, yet an overall decrease in molar volume.

High-pressure stopped-flow (HPSF) instruments facilitate the study of a great number of enzyme reactions at elevated pressures and low and/or high temperatures (**Table 4**). Experiments at low temperature are not only desirable because the reaction rates decrease, thus enabling detection of transient enzyme-substrate intermediates, but also because protein denaturation can be avoided. Even a moderate pressure increase can lead to enzyme inactivation without a clearly discernable change in the protein's secondary structure. Such slight perturbations in the active site of an enzyme can be analyzed by HPSF experiments.

Table 4. Technical properties of Temperature- and Pressure-jump Stopped-Flow instruments

Technical properties	Stopped-flow				
	T jump	P jump	High P, wide T range		
	Kintses et al. ⁶⁴	Hui Bon Hoa et al. ⁶⁶	Bugnon et al. ⁵⁷	Balny et al. ⁵⁶	Hui Bon Hoa et al. ⁶³
Type of mixer	T-mixer		4-jet tangential mixer	2-jet tangential mixer	
Max. flow rate	18 mL s ⁻¹			1 mL s ⁻¹	
Path length of the optical cell			2 mm fluorescence 10 mm absorbance	10 mm	5 mm
Volume of the optical cell	25 µL		40 µL	30 µL	400 µL
Pressure range		P jump ±20 MPa	200 MPa	200 MPa	100-800 MPa
Temperature Range	T jump of 60°C		-40 to +100°C	-20 to +30°C	-40 to +30°C
Total instrumental dead-time	0.9 ms	< 3 ms	< 2 ms	20/50/100 ms	seconds

One of the first high-pressure systems called the ‘optical bomb’ was designed by Hui Bon Hoa in 1982³. This instrument was easily incorporated into conventional spectrophotometers and could handle pressures as high as 700 MPa, and was capable of absorbance and fluorescence detection between -40°C to +30°C. The main components of the system were a high-pressure chamber (equipped with 10 mm thick sapphire windows and immersed in a thermostat bath containing liquid ethanol, silicon oil or n-pentane), Bridgman’s high-pressure seals, a metallic transducer for monitoring the pressure and a high-pressure generator. An optical sample cell, made from a special quartz square tube (5 mm path length, 400 µL in volume), sealed by a flexible Teflon membrane was mounted inside the pressure chamber. Dry nitrogen gas was used to prevent ice formation at the windows or the sample cell. Even though the sample cell could be pre-cooled and rapidly closed prior to the mixing experiments, the instrumental dead-time was quite long, in the minute time range. In this case the dead-time comprises the time to fill the sample cell with mixed solutions and closing the cell.

A subsequent high-pressure system designed by Balny was a modification of the ‘optical bomb’ described above and could only operate in UV-Vis absorbance mode^{56,65}. The instrument can handle pressures and temperatures in the range of 10⁻⁴ MPa to 200 MPa and -20°C to +30°C, respectively. The instrumental dead-time was greatly improved to 20, 50 and 100 ms in water at 20°C, in 40% ethylene glycol/water at 20°C and at -15°C, respectively. The improvements included a rapid optical detection system and maintenance of thermal and pressure homogeneity in the high pressure-bomb by housing of the stopped-flow apparatus (equipped with the two-jet tangential turbulent mixer) inside the bomb⁵⁶. To avoid possible metal-ion sample contamination, the sample cuvette (2 mm x 10 mm) was made from glass or plastic. One of the key design elements of an HPSF system that is capable of operating at low temperature, is the choice of the liquid pressure transmitter (silicon oil), since it must be transparent in the UV-Vis spectral region, be noncorrosive, be inert towards biological compounds and must remain fluid under high pressure and low temperature conditions.

The developments of stopped-flow instruments at the end of the last century made it possible to study fast enzyme reactions over wide temperature and wavelength ranges between -40°C and $+100^{\circ}\text{C}$ and 220-850 nm, respectively, and at pressures up to 200 MPa⁵⁷. The modern HPSF system can be used with various solvents, and is capable of recording simultaneously in absorbance and fluorescence modes. This HPSF system can be easily integrated into a conventional ambient pressure setup by using light guides. The dead-time of the setup (time needed for the reacting components to travel from the 4-jet tangential mixer to the observation cell) was <2 ms in aqueous solution, up to 200 MPa and at room temperature. The observation cell (2 mm x 2 mm x 10 mm) has 2 mm and 10 mm path lengths in fluorescence and absorbance modes, respectively.

Pressure and temperature-jump techniques are suitable methods to reveal mechanistic details of enzyme reactions. An apparatus able to produce 20 MPa changes in pressure with a dead-time of <3 ms was designed by Hui Bon Hua⁶⁶. The basic principle is to apply a pressure jump by quickly applying an excess of pressure via a pneumatic valve to a system at equilibrium and to monitor the rate at which the system reaches the new equilibrium state. In contrast, the novel temperature-jump stopped-flow (T-jump SF) technique enables one to study enzyme reactions at extremely high temperatures, even above the denaturation temperature, provided that the reaction rates exceed those of the denaturation process itself^{66,82}. The mechanism of an enzyme reaction can be resolved in greater detail if the temperature dependencies of the various individual reaction steps are different. Furthermore, T-jump SF is helpful to determine the relation between protein (un)folding and temperature over a wide range of temperatures. With this apparatus (**Fig. 5**) single and double mixing experiments can be performed. In the case of single mixing experiments, the heat-sensitive enzyme and the heat-stable substrate are first equilibrated at room temperature. The reactants are then rapidly pushed from the two syringes. The substrate is quickly heated to a temperature well above the reaction temperature by passing it through a heating loop on its way to the mixer. When the enzyme and the heated reactant meet in the mixing chamber the reaction temperature is established. Very high temperature jumps of 60°C can be achieved almost instantly by applying the double or sequential mixing technique. After the first stopped-flow push of the drive ram system, the substrate is preheated in the heating loop (up to a temperature of 90°C) and mixed with the heat-sensitive enzyme. On their way to the second mixer, the reactants come to thermal equilibrium by flowing through a delay line during which time the enzyme should not denature. After the second stopped-flow push, the reacting solution is heated to its final temperature when it makes contact with the hot buffer of the second mixer. Since the rapid T-jump occurs simultaneously with the mixing of reactants, there is no additional increment to the instrumental dead-time (1 ms) due to the T-jump. This strategy allows enzymes to be characterized in much wider temperature ranges and consequently Arrhenius and van 't Hoff plots can be determined in broader temperature ranges too.

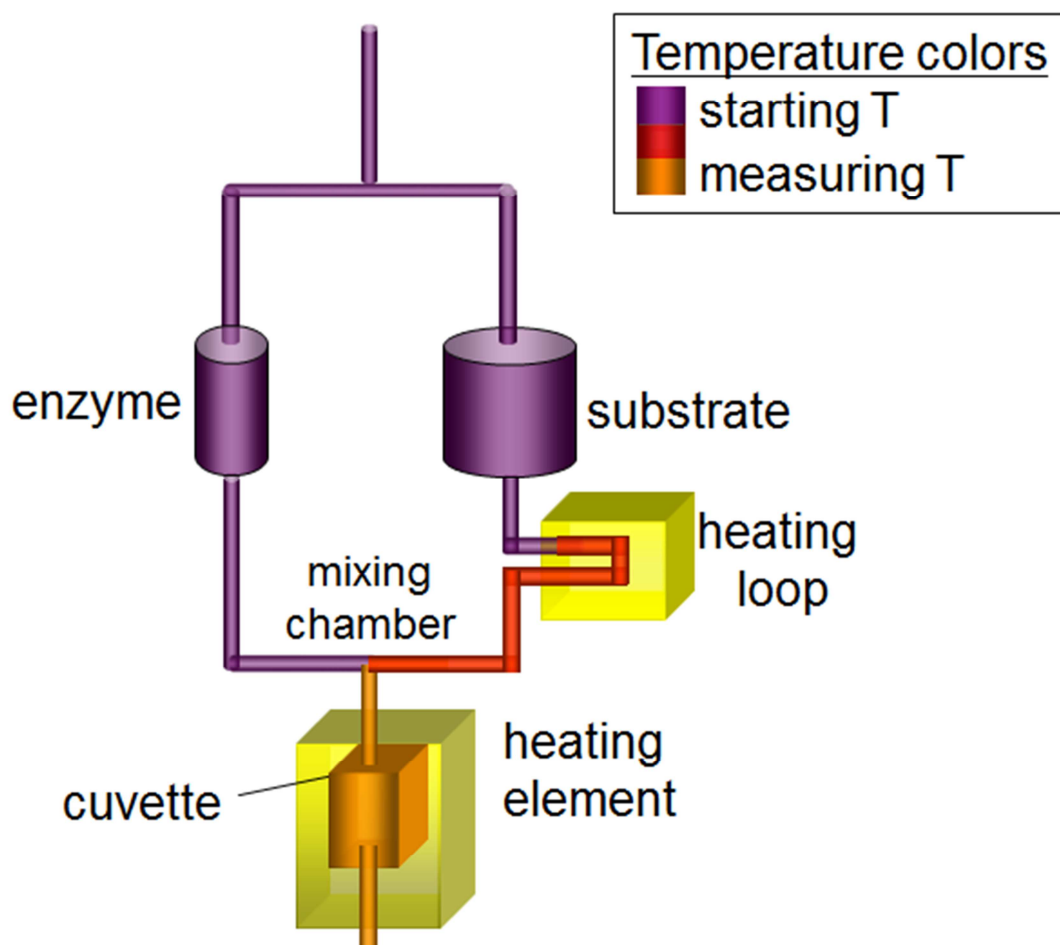


Figure 5. Schematic representation of the Temperature-jump stopped-flow instrument. The approximate volume of the cuvette is 25 μL . The figure is drawn after Kintses et al. 2006⁶⁴.

4.3 Continuous-flow EPR and stopped-flow EPR

EPR spectroscopy can usually be performed at room temperature when monitoring radicals, as opposed to transition metal ions, which must be monitored at lower temperatures. A continuous-flow aqueous sample cell for X-band EPR spectroscopy has been commercially available for a long time. This aqueous sample cell setup has a dead-time of ~ 5 ms and an improved modified version has an estimated dead-time of ~ 1 ms; both setups are suitable for kinetic studies on radical systems⁸³. Continuous flow systems are, however, very uneconomical in terms of reagents.

The first stopped-flow EPR instrument was reported in 1980 using a four-jet tangential mixer⁷⁵. The dead-time was only ~ 1 ms owing to the large flow velocities. However, the vigorous stop of the liquid flow produced strong mechanical shocks of the finely tuned resonant cavity (microphonics), which resulted in large artificial peaks in the EPR spectrum, limiting the kinetics analyses⁷⁵. Two developments have greatly improved the performance of continuous-flow and stopped-flow EPR devices. One is the use of stepper motors to drive the syringes containing the reactants. The second one is in the cavity design. The new instruments use a so-called loop-gap or dielectric ring resonator.

The continuous-flow EPR device described by the Scholes group has a sophisticated aqueous sample cell which enabled the kinetic resolution of the rapid refolding of spin-labelled iso-1-cytochrome *c* with a time resolution of 150 μ s. The aqueous sample cell is based on the continuous-flow capillary mixer^{35,41,77}. The major disadvantage of this system remains the uneconomical use of protein (~1 mL at ~0.5mM for one experiment), in spite of the very small detection volume of only ~ 0.5 μ L. EPR spectroscopy at room temperature in aqueous solution is rather insensitive requiring high concentrations of sample. The practical consequence is that the low population of native transient radicals which accumulate to <10% usually fall below the detection threshold, thereby limiting the main biochemical applications of EPR to spinlabel-modified proteins. The study of native transient radicals is facilitated by the RFQ and MHQ instruments.

A sophisticated stopped-flow EPR setup was recently reported, which builds further on the continuous-flow device described the Scholes group that incorporates a loop-gap resonator and stepper motors⁷⁶. The device has a hard-stop valve and is built in a compact way to minimize microphonics. Mixing is achieved with a small Berger ball mixer with a total dead-time of 330 μ s. The full technical details, which deal to a great extent with the optimization for EPR studies, have not been included in this review. Further details are provided by Lassman et al., who gives a detailed historical overview of the development of continuous-flow and stopped-flow EPR equipment⁷⁶.

4.4 Other stopped-flow techniques

Stopped-flow NMR instruments were first constructed in the 1970s⁷³. The key to producing the short dead-time is to position the mixer and observation cell close together. The mixer components usually disturb the magnetic field homogeneity hampering reliable data acquisition. As a consequence the mixer is placed outside the magnetic field coils. Most instruments have dead-times of 100-200 ms, but the best apparatus has a total dead-time of approximately 15 ms⁶⁸⁻⁷³. Another miscellaneous stopped-flow technique using EXAFS detection has been described with a dead-time of ~5 ms, but no biological applications have been reported so far⁷⁸.

4.5 Hydrodynamic focusing

As a fluid flow is squeezed or 'hydrodynamically focused' into a thin stream, the diffusion distance is reduced to as little as a few nanometers, yielding diffusive mixing times in the microseconds. Hydrodynamic focusing (lamination) was first proposed by Brody et al. and has opened new avenues to achieve rapid mixing at low pressures and with minimal sample consumption⁵⁰. Hydrodynamically focused continuous-flow mixers, capable of mixing liquids within 10 ms, with sample consumption rates of nanoliters per second were developed by Knight et al. in 1998⁵³. This mixer consists of four channels (two inlet-side channels, a central inlet- and single outlet-channel), which are 10 μ m deep and wide and intersect at the center of the mixer chip (cf. **Fig. 6**). The buffer solutions from two symmetric orthogonally positioned inlet channels focus the sample solution from the center channel, which ends in a nozzle of 2 μ m, into a thin stream down to the exit channel. Once focused, this thin stream maintains its small width of less than 50 nm unless it is broadened by an increase in channel width or by diffusion into the side flow. The width of the

focused stream does not depend on the magnitude of the applied pressure, but rather on the ratio (α) of the side pressure (P_s) to the inlet pressure (P_i), $\alpha = P_s/P_i$. This ratio is, however, controlled by varying the flow rate ratios at the mixer intersection (**Fig. 6**). Hertzog et al. improved the methodology to create a device with a mixing time of $8 \mu\text{s}$ ⁵². The mixer consists of a sample stream ($60 \mu\text{m}$ wide and 9mm long) that enters the mixing chamber through a central nozzle ($\sim 1\text{-}2 \mu\text{m}$ wide) and is focused by two side supply channels ($60 \mu\text{m}$ wide and 9mm long) into a $0.11 \mu\text{m}$ thin stream down to the exit channel ($200 \mu\text{m}$ long, constant width). Moreover, the optimization of the mixer design entailed the use of small nozzle diameters and a high exit velocity (2.9m s^{-1}). The flow-rate ratios of the central and side channels of 1:100 resulted in a very short mixing time. The mixing time was decreased from $8 \mu\text{s}$ to $4 \mu\text{s}$ with only femtomoles of sample consumption by fabrication of a small nozzle at the intersection of the three inlet channels, which provides a local flow velocity increase in the region where the jet is formed⁵¹. In 2007 Yao et al. improved the mixing uniformity across the streamlines prior to the jet formation by reducing the size of the nozzle (the intersection of the three inlet channels) and by minimizing the bend of the side channel streamlines⁵⁴. By increasing the local velocity in the mixing chamber and the total flow rate of this redesigned micro-fluidics device the mixing time was reduced to $1 \pm 1 \mu\text{s}$. These micro-machined devices with very short mixing times, sensitive detection of very small amounts of fluorescent sample by confocal microscopy and very low reagent consumption constitute impressive achievements. However, the mixing times quoted by the researchers are in the authors' opinion, not realistic. The diffusion mixing time of $\sim 1 \mu\text{s}$ would correspond to diffusion lengths of $\sim 50\text{-}100 \text{nm}$, which are roughly similar to the widths of the focused streams reported⁵¹⁻⁵⁴. However, the detection methods used to assess the mixing time, fluorescence quenching by iodine of fluorescein and FRET (Foster or fluorescence resonance energy transfer) in the single-strand DNA study are not reliable to establish mixing. Both fluorescent methods work at a distance. Furthermore, the experimental iodine to fluorescein ratio was 0.5M to $10 \mu\text{M}$, which is such a high excess of the quencher that only a small amount of diffusion of the iodine would be required to quench the fluorescence. Neither method involves a direct collision between the reactants to quench the fluorescence, in contrast to all other test reactions that are employed to determine dead-times of (turbulent) mixing instruments. A better test for the determination of the dead-times of the hydrodynamic focusing instruments would be a simple acid-base reaction with the reagents in an approximate 1:1 ratio with a pH-sensitive fluorescent dye like HPTS (1-hydroxypyrene-3, 6,8-trisulfonate).

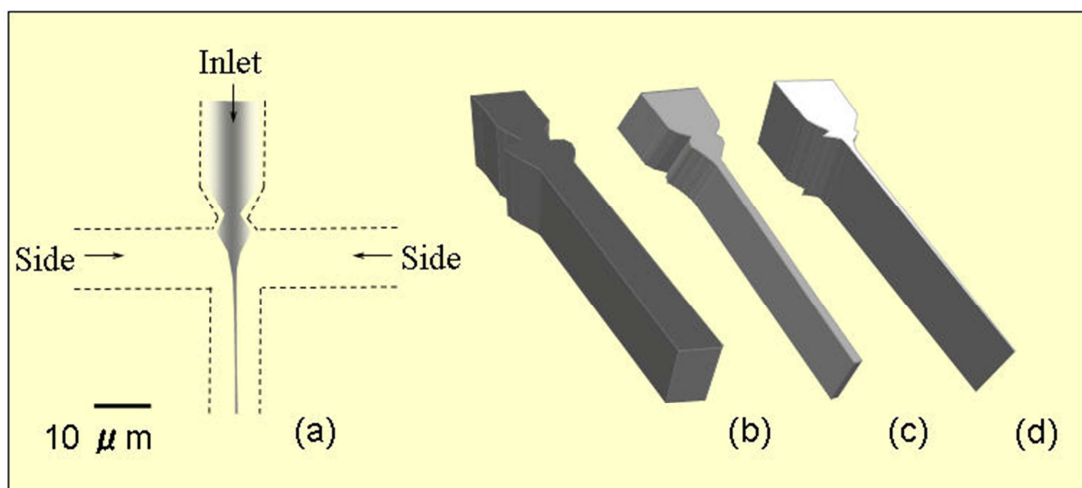


Figure 6. Continuous flow hydrodynamic focussing. (a) Hydrodynamic focusing with $Pi = 5$ psi and $\alpha = 1.1$ in the mixing region of the continuous-flow mixer. The three dimensional structure of hydrodynamically focussed streams with $Pi = 5$ psi and (b) $\alpha = 0.5$, (c) $\alpha = 1.0$ and (d) $\alpha = 1.1$. Redrawn after Figs. 1 and 2 in Knight et al. 1998⁵³.

5. Rapid freeze-quenching techniques

Rapid-mixing/rapid-freezing techniques (RFQ) were developed in the 1960s and 1970s and initiated by workers in the field of metallo-redox-enzymes.^{3,28,84-88} These researchers aimed to understand the role of transition-metal centers in enzyme catalysis for which EPR spectroscopy is of enormous value. However, EPR spectroscopy of transition metals must generally be performed at low temperatures to slow down spin relaxation, which renders the continuous-flow and stopped-flow techniques described above inadequate. In addition, EPR and several other spectroscopic methods require relatively high concentrations of proteins or enzymes, yielding solutions of high viscosity. In order to obtain $Re > \sim 2000$ a four-jet tangential mixer was designed that proved capable of mixing viscous solutions in conjunction with a more powerful sample delivery device or drive-ram system than is normally used in the stopped or continuous-flow devices.

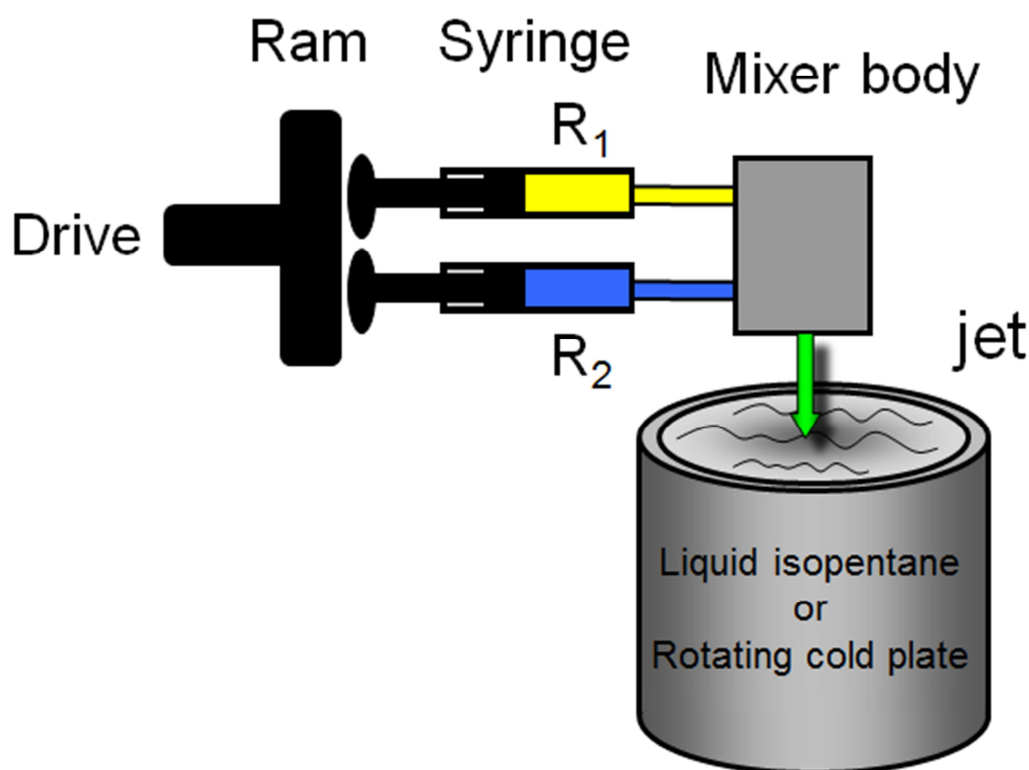


Figure 7. Basic sketch of the rapid-mixing rapid freezing setup as used in the RFQ and MHQ devices. Liquid isopentane is cooled to 130-140 K; the shortest distance between mixer body and isopentane is ~1-2 cm. In MHQ devices, rotating cold plates are often used to quench the reaction. R₁ and R₂ denote reactant 1 and reactant 2, respectively. The drawing is adapted from de Vries† 2007¹⁹.

5.1 The rapid-mixing / rapid freezing sampling technique (RFQ)

A schematic diagram of the rapid mixing/rapid freezing setup is depicted in **Fig. 7**. The instrument is commercially available and is essentially a continuous-flow system with the addition of a quenching bath filled with liquid isopentane at ~130-140 K³⁵. The construction, mixer dimensions and specifications of the RFQ have been reviewed in detail by the original designers^{3,28,84-88}. Briefly, the RFQ instrument consists of a powerful (~373 W) hydraulically, pneumatically or stepper-motor driven ram to ensure that the pistons, which are tightly sealed into the syringes, are pushed at a *constant* speed. The reactants are mixed in the mixing chamber (a four-jet tangential mixer **Fig. 8**) and subsequently enter a tube that ends in a nozzle (diameter ~0.25 mm). The mixed reactants are sprayed through the nozzle into a bath containing the cryo-medium where the reaction is rapidly quenched due to freezing. In most setups, the distance between the mixer body and the liquid isopentane is approximately 1-2 cm. In order to vary the reaction time, the length of the tubing is changed rather than the ram speed because a low ram speed will result in inadequate mixing of the viscous solutions ($Re < \sim 2000$). The shortest reaction times are obtained by omitting the tubing and mounting the nozzle directly on the mixer body (**Fig. 8**). The minimal dead-time of the RFQ is 5-7 ms^{19,28,33}. Liquid isopentane (at ~135 K) is the most commonly used cryo-medium for quenching, but liquid ethane (at ~90-120 K) can yield shorter freezing times. The advantage of liquid ethane over liquid isopentane is

that it can be pumped off under vacuum providing a solvent-free powder amenable to resonance Raman spectroscopy, for example, at low-temperatures^{89,90}.

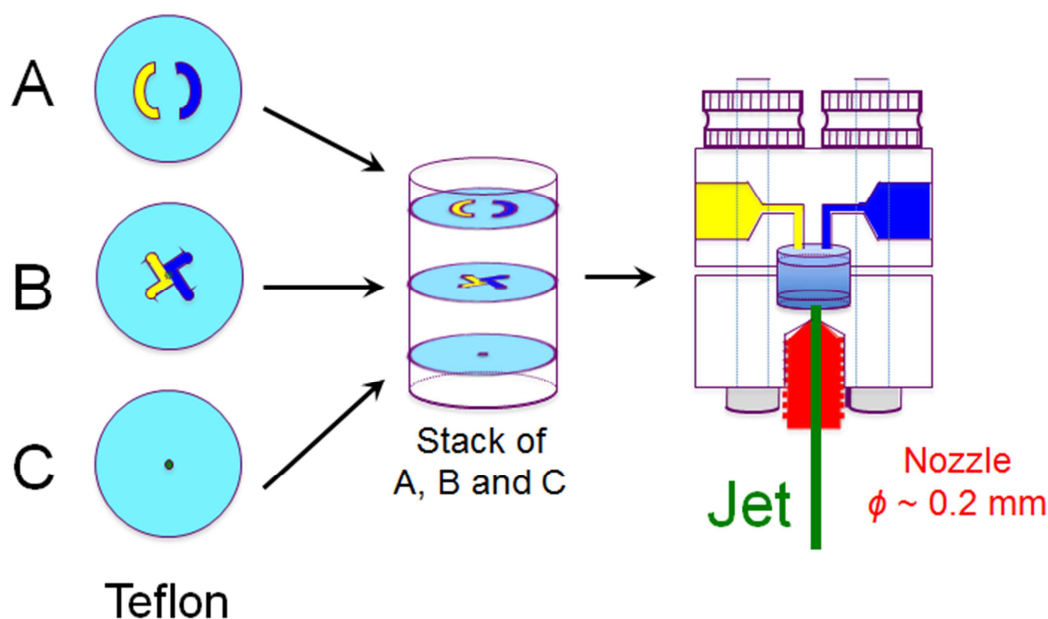


Figure 8. Ballou-Palmer four-jet tangential mixer used in Rapid Freeze Quench shown in the configuration with the shortest dead-time when the spraying nozzle is attached to the mixer body. For longer reaction times, tubings of various lengths are attached to the mixer body, ending with a spraying nozzle. The mixer body is made from Lucite. Figure redrawn from Ballou and Palmer 1974²⁸.

The cold powder that is obtained after spraying into the cryo-medium is difficult to handle because of its electrostatic nature. The static electricity can be greatly reduced by using an anti-static gun, greatly facilitating packing the powder in X-band EPR tubes. The electrostatic nature of the fine-grained powder may cause clogging and sticking to quartz or glass during sample preparation. Samples packed in EPR tubes are adequate for low-temperature UV-Vis diffuse reflectance spectroscopy, resonance Raman spectroscopy or EPR spectroscopy. However, specific devices and sample holders must be constructed for low-temperature UV-Vis spectroscopy, Q- or W-band EPR, ENDOR, ESEEM, MCD, Mossbauer spectroscopy or x-ray absorption spectroscopy (XAS or EXAFS)⁹¹⁻¹⁰⁰. In spite of this, the sampling methodologies enable one to study enzyme catalytic mechanisms by many different spectroscopic methods.

The RFQ setup (**Fig. 7**) is easily extended to a double mixing system by using three syringes plus a second mixer, similar to the sequential stopped-flow setup. The sequential mixing strategy ('push-push') enables one to study reactions in which one of the reactants is an unstable or metastable compound. Moreover, sequential mixing is used in chemical-quench instruments, which may be considered a variant of the double mixing RFQ setup¹⁰¹. In chemical-quench studies the contents of the third syringe serve to quench the reaction. The tube connecting the two mixers or delay line determines the reaction progress. The quenching media may be a highly acidic or basic solution, or a solvent in which the reaction no longer proceeds, and/or media which generates a phase separation of the reactant/products. The overall dead-time of ~2 ms is somewhat shorter than for rapid freeze quench. However, the dead-times of

60 μs for chemical quenching obtained with capillary micro-mixers described above are superior to that obtained with an RFQ-like instrument²³.

5.2 The RFQ mixers and dead-time estimation

The components of the four-jet tangential mixer used in the RFQ have been described in **Paragraph 3.3** and **Fig. 2b**. The complete mixer as constructed by Palmer and Ballou is shown in **Fig. 8**^{3,28}. The mixing time in this mixing chamber is $\sim 50 \mu\text{s}$ (**Table 5**). The three gaskets are held together in the mixer body by four long screws that are tightened until the system is free of leaks. The spraying nozzle can be screwed into the mixer body to obtain the shortest reaction times, or connected to tubing of different length to vary the reaction times. Despite the short mixing time of $\sim 50 \mu\text{s}$, the total dead-time of the RFQ instrument is 5-7 ms. The dead-time of freeze-quench instruments is usually determined using the reaction of metmyoglobin with azide, changing the initial high-spin state of the ferric heme to the low spin state, of which the kinetic parameters have been well established¹⁶. The two spin states have different non-overlapping EPR signals, and the amount of conversion at a particular time can be determined in a single sample. This technique has great advantage because the calibration of the dead-time is independent of sample packing, which can vary ± 15 -20% between different samples. In addition to EPR, the sample analysis can be done by low temperature UV-Vis spectroscopy or by resonance Raman spectroscopy^{89,90,102}.

In general, the total instrumental dead-time of the freeze-quench mixing-and-sampling procedure (both RFQ and MHQ, see below) can be divided into three steps. In the first step, the reactants are mixed with a characteristic mixing time (τ_m). In the second step, the sample is transported from the mixing chamber to the cryo-medium through a tube (of variable length) and subsequently as a free jet, giving τ_t , the sample-transport time. Finally, the sample is quickly frozen in the cryo-medium (e.g., liquid isopentane) or on a rotating cold plate (MHQ), quenching the chemical reaction, yielding τ_c , the cryofixation or quenching time^{19,103}.

The total sample-ageing time, τ_a , is expressed as the sum of three terms:

$$\tau_a = \tau_m + \tau_t + \tau_c \quad (\text{Eq. 7})$$

In the case of RFQ the τ_m is $\sim 50 \mu\text{s}$; the shortest transport distance to the cold liquid isopentane bath is 1-2 cm when the spraying nozzle is directly attached to the mixer body. At the maximal linear jet speed of $\sim 44 \text{ m s}^{-1}$ the shortest sample-transport time τ_t is 0.5-1 ms. The actual freezing time τ_c in isopentane at 135 K is 4-6 ms with a nozzle diameter of 200-250 μm ²⁸. Thus the total dead-time for the RFQ setup is τ_a 5-7 ms (**Table 5**). The rate of freezing is dependent on the nozzle diameter, the jet speed and the temperature of the quenching medium. For isopentane at 100 K the freezing time is estimated to be 8-9 ms²⁸.

Table 5. Specifications of rapid mixing devices performing at the limit to achieve the shortest dead-times.*

Technical properties	RFQ ³⁸	MHQ		
		Cherepanov and de Vries ^{†16,19,45,46}	Tanaka et al. ⁴²	Lin et al. ¹⁰²
Mixing volume	68 nL	10 pL	5.6 nL	450 pL
Exit channel diameter, μm	200	20	60	10x100 μm
Re in mixing chamber	7,000	4,000	3,000	700
Max. back pressure (ΔP , bar)	9-15	200-400	12	4
Max. flow rate (ml min^{-1})	83	4	8.4	1.2
Linear speed (m s^{-1}) in channel or jet	44	200	49	20
Mixing time	50 μs	<1 μs	40 μs	20 μs
Experimental Quenching time	4-6 ms	30-50 μs	270-450 μs ^a	96-159 μs ^a
Total instrumental Dead-time	5-7 ms	70-80 μs	~ 200 μs ~ 500 μs ^a	~ 50 μs ~ 175 μs ^a

*Calculations of Re and ΔP are based on $\rho = 10^3 \text{ kg m}^{-3}$ and $\eta = 10^{-3} \text{ kg m}^{-1} \text{ s}^{-1}$

^a Calculated by the authors of this review as described in the text

5.3 Microsecond freeze-hyperquenching (MHQ)

The dead-time of the classical RFQ methodology of 5-7 ms is too long to study fast enzyme reactions (turnover time below ~1 ms) such as the initial steps in the reactions of oxidoreductases. Over the last decade the dead-time of freeze-quench instruments has been improved to cover the microsecond time range (~100 μs). In these MHQ (Microsecond freeze-HyperQuenching) instruments the freezing is so fast that the produced cold powder is initially composed of vitrified water rather than tiny ice crystals. Key to the new instrumental devices is the use of a micro-mixer, which can be constructed by micro-machining technology. The micro-mixers that have been described are a miniaturized four-jet tangential mixer (**Fig. 9**) and a T-mixer both made from stainless-steel and a micro-fluidic mixer made from silicon^{16,42,45,46,102,104}. The silicon mixer contains alternating passages of 10, 20 and 50 μm (**Fig. 10**) that enable mixing at low Re in the non-turbulent regime (**Table 5**). The advantage of this mixer is that relatively low flow rates are needed for fast (20-25 μs) and complete mixing and that as a consequence the build-up of pressure in the system is low (**Table 5**). The mixing time in the four-jet tangential micro-mixer is <1 μs due to the small dimensions of the mixing chamber with a volume of 10 pL (**Table 5**). All three MHQ instruments use HPLC pumps for solvent delivery instead of a pneumatic or hydraulic drive-ram system as in the RFQ.

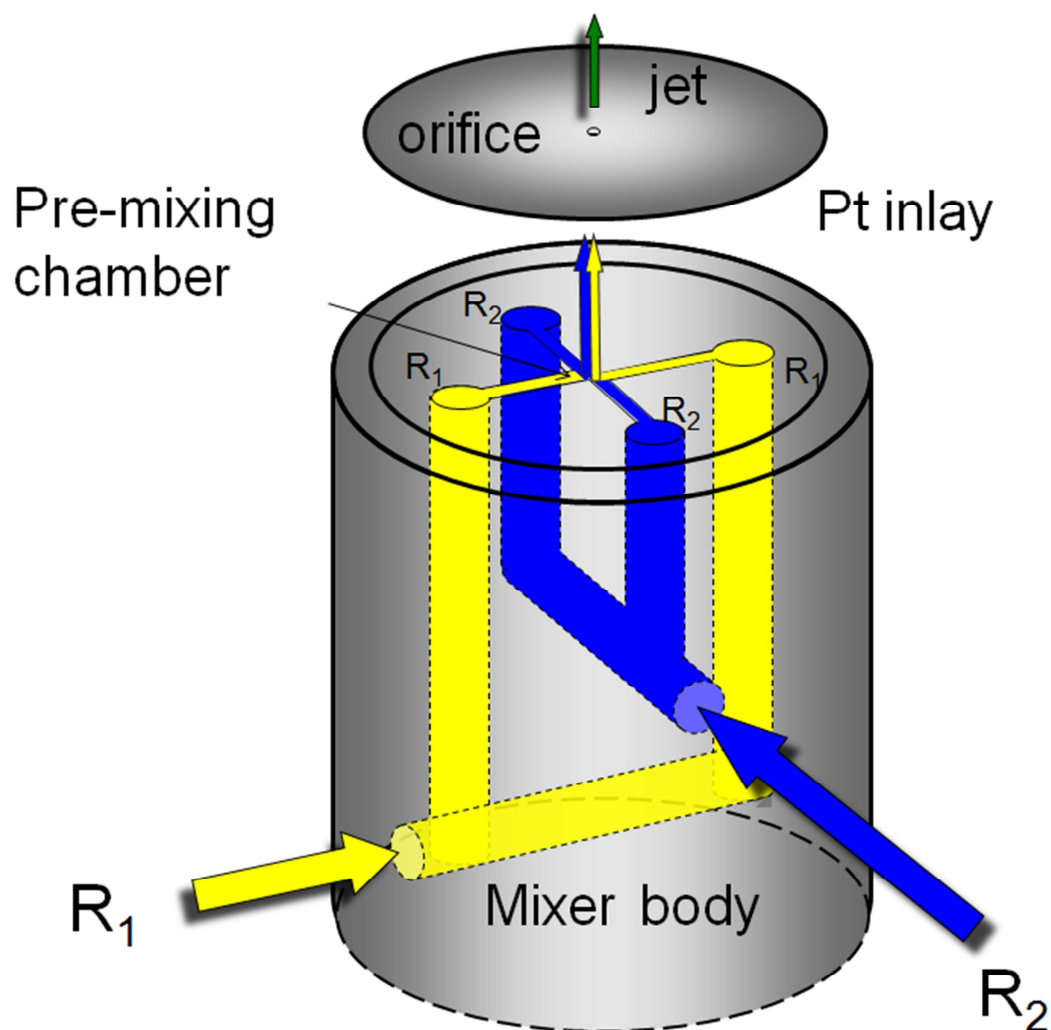


Figure 9. Schematic drawing of the four-jet tangential micro-mixer used in MHQ^{16,32,45,46}. Mixing occurs in the orifice of the *Pt* inlay (MHQ). R_1 and R_2 denote reactant 1 and reactant 2, respectively. Channels in the mixer body are 300- μm diameter, the channels leading to the pre-mixing chamber are 50-70 μm wide and deep; the orifice diameter is 20 μm . The mixed reactants of the jet are quenched in liquid isopentane or on a tungsten-coated rotating cold plate^{45,46}. The drawing is adapted from de Vries† 2007¹⁹.

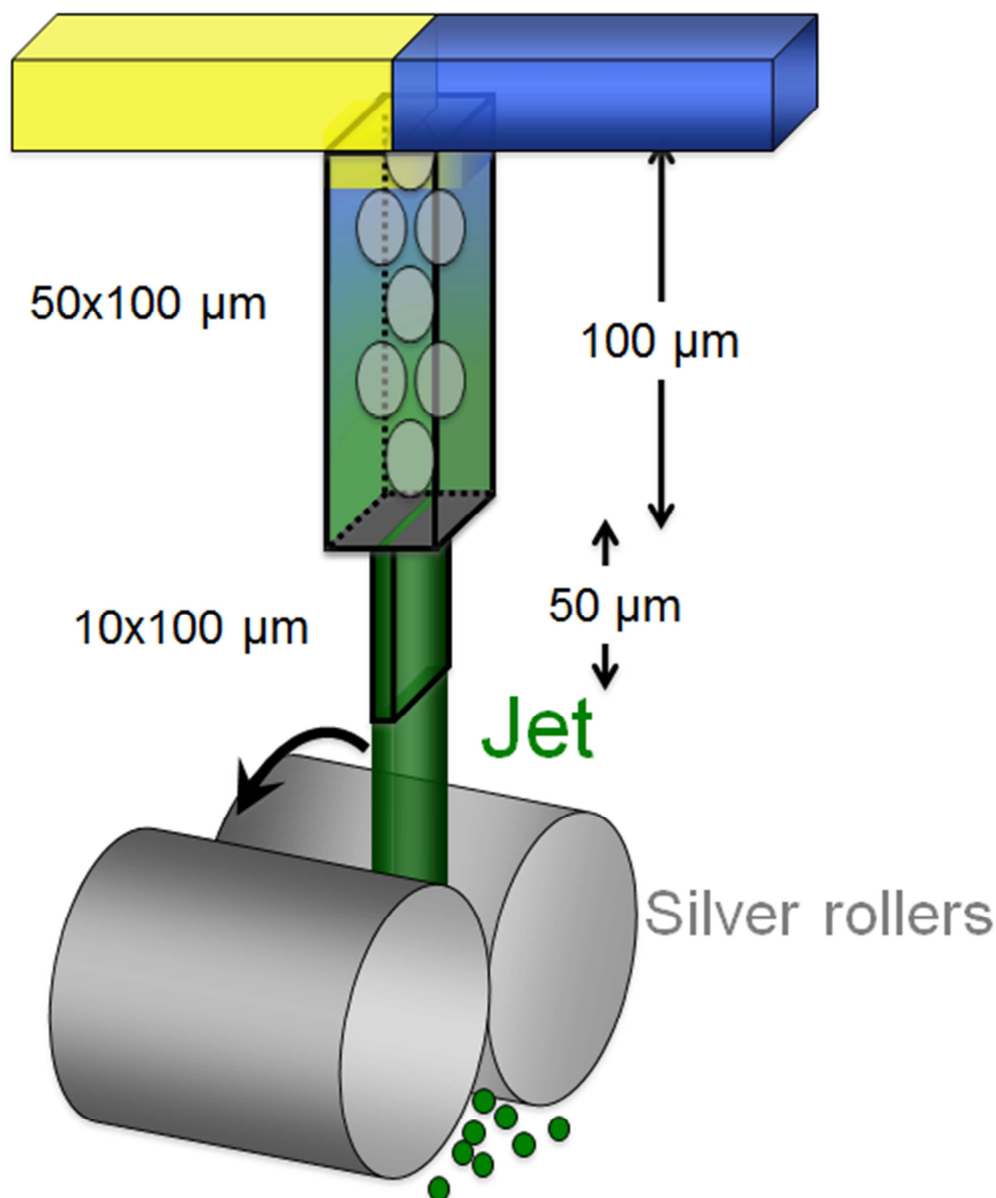


Figure 10. Silicon micro-mixer used in MHQ by Lin et al.¹⁰². The alternating passages in the upper part are drawn as ovals and create passages for the liquid stream of 10, 20 or 50 μm . The residence time in the lower part leading to the jet is 23 μs ; the shortest distance to the rapidly rotating silver (or copper) rollers is 0.5 mm. The silver rollers are immersed approximately half way in a bath of liquid nitrogen.

In spite of the miniaturization, the mixing times of the micro-mixers are not significantly better than that of the RFQ mixer, except for the four-jet tangential miniature mixer (**Table 5**). As a consequence, the speed of the jet in MHQ instruments is not significantly higher than in RFQ setups, except for the MHQ setup of Cherepanov and de Vries† (**Table 5**). All three MHQ instruments use a solid cold surface for quenching, while the MHQ setup of Cherepanov and de Vries† can also be used with liquid isopentane^{16,45,46,104}. Quenching occurs on fast rotating silver or copper wheels at 77 K in the MHQ devices of Tanaka et al. and Lin et al., respectively, while a rotating cylinder at 80 K is used in the setup of Cherepanov and de Vries†^{45,46,104}. The free jet trajectory, the distance between the mixer exit and the

cryo-medium, is minimally 6 mm for the rotating cylinder or 2 cm when isopentane is used in the MHQ device of Cherepanov and de Vries†¹⁶. This corresponds to minimal sample transport times of 30 μs and 100 μs for the rotating cold plate and isopentane quenching devices, respectively. The minimal free jet trajectory for the instruments of Tanaka et al. and Lin et al. are ~ 10 mm and only 0.5 mm, respectively, yielding minimal transport times of 200 μs and 25 μs , respectively. The sample transport times of the MHQ devices are considerably shortened with the respect to the RFQ instruments (**Table 5**).

Tanaka et al. and Lin et al. tested the dead-times of their devices with the metmyoglobin-azide reaction and concluded that these were similar to the calculated values of ~ 200 μs and ~ 50 μs from the mixing and sample transport times. However, the metmyoglobin-azide test reaction reported was performed at maximal rates of 1580 s^{-1} ($\tau \sim 630$ μs) and with such a comparatively low reaction rate, one cannot determine the dead-times quoted above reliably¹⁰². Therefore, the authors of this review consider the apparent correspondence between calculated and measured dead-time fortuitous. In addition, the calculation ignores the true freeze-quenching time, which was carefully determined at azide concentrations where the reaction with myoglobin proceeds at rates $>10.000\text{ s}^{-1}$ ¹⁶. The authors determined true freezing times of 30-40 μs using liquid isopentane and 40-50 μs using the rotating cold plate^{16,45,46}. It was further determined that the freezing time is proportional to the jet diameter, as theoretically expected^{45,46,105-107}. Thus the true freezing time of 4-6 ms for RFQ where the diameter of the jet is ~ 200 -250 μm , is in fact totally consistent with the true freezing times of 30-50 μs for a jet diameter of 20 μm for the MHQ device designed by Cherepanov and de Vries† and a total dead-time of 70-80 μs (see **Table 5**). Using the jet diameters of the micro-mixers designed by Tanaka et al. and Lin et al. the true freezing times of their MHQ instruments are calculated as 270-450 μs and 96-159 μs , respectively, yielding total instrumental dead-times of ~ 500 μs and ~ 175 μs , respectively (**Table 5**). These calculated dead-times are further consistent with the detection by the de Vries† at al. but not by Tanaka et al. or Lin et al. De Vries† at al. performed similar experiments of hitherto unknown transient tryptophan radicals in cytochrome *b*₀₃ oxidase and of a new short-lived (~ 100 μs) high-spin ferric-azide intermediate by resonance Raman spectroscopy in the reaction between metmyoglobin and azide^{16,19,89,102,104,108}.

The great advantage of the MHQ devices of Tanaka et al. and Lin et al. is the sample packing procedure. The cold powder is ground by the copper or silver wheels used for quenching to a non-electrostatic coarse powder, which is easily packed to a density of 60% in X-band EPR tubes. In contrast, in the MHQ device of Cherepanov and de Vries† the density of sample packing is only 10% for quenching in liquid isopentane and 20% for quenching on the rotating cold plate. Moreover, the packing procedure for the fine electrostatic cold powder requires special open-ended EPR tubes^{45,46,97,104,109}.

The pressures up to ~ 400 bar (40 MPa) that occur at very high flow rates (**Table 5**) may seem high, but are similar to those that occur in the French pressure cell to break open cells and do not lead, in general, to denaturation of the enzymes under study. The HPLC system that is used for the MHQ experiments shuts off at 40 MPa, is also successfully used to purify proteins and enzymes. In the author's experience, none of

the approximately twenty enzymes that have been studied denature during MHQ experiments, evidenced by the 90-100% preservation of enzyme activity determined after thawing and assaying the freeze-quenched samples.

6. Conclusions and outlook

The stopped-flow, continuous-flow and rapid-mixing/sampling freeze quench techniques have contributed enormously to our insight into the catalytic mechanisms of a wide range of enzymes despite the superior time resolution of (light-initiated) relaxation techniques. The stopped-flow and continuous-flow devices enable reactions to be monitored across wide temperature and pressure ranges by UV-Vis, fluorescence, CD, NMR, FTIR and EPR spectroscopy. To this list of the spectroscopic methods the RFQ and potentially the MHQ methodologies enable resonance Raman, Mossbauer, ENDOR, ESEEM and EXAFS spectroscopy. The rapid-mixing techniques described in this review are general and versatile and because they are easily combined with various spectroscopic techniques, applicable to the study of enzyme catalytic mechanisms. In the nearly 100 years since the development of the first rapid-flow methods, the pre-steady state kinetics of numerous enzymes have been analyzed. This has provided information on conformational-, substrate-, ligand- and protonation-state changes during catalysis in all classes of enzymes. With respect to the oxidoreductases, such studies have afforded, in addition, rates of electron transfer and oxido-reduction kinetics of heme centres, iron-sulphur centres, mono and di-iron centres, single and multiple Mn-, Fe-, Co-, Ni-, Cu-, Mo-, W-sites, amino-acid main-chain and side-chain radicals, quinone, flavin, pterin radicals et cetera.

The production of hyperquenched samples by the recently developed MHQ methods makes it possible to study enzymes and enzyme intermediate states in the (near) native state of vitrified water, as if in aqueous solution. MAS-NMR at low temperatures is a promising technique to study enzyme mechanisms¹⁰³. The application of MAS-NMR to MHQ frozen samples below the ice-glass phase transition temperature would yield a 3D-structure of a true catalytic intermediate in the native state. The structures of a series of intermediates could provide a 3D-movie that delineates the structure-function relationship of enzyme catalysis as has been done successfully in a relaxation-type experiment using time-resolved x-ray crystallography¹¹⁰.

References cited

1. Antonini, E.; Brunori, M. Hemoglobin and myoglobin in their reactions with ligands. *North-Holland Publishing Company, Amsterdam London*, **1971**, Vol. 21.
2. Lienhard, G. E. Enzymatic catalysis and transition-state theory. *Science*, **1973**, *180*, 149-154.
3. Ballou, D. P. Freeze-quench and chemical-quench techniques. *Methods in Enzymology*, **1978**, *54*, 85-93.
4. Pettersson, G. Effect of evolution on the kinetic properties of enzymes. *European Journal of Biochemistry*, **1989**, *184*, 561-566.
5. Gerstein, M.; Lesk, A. M.; Chothia, C. Structural mechanisms for domain movements in proteins. *Biochemistry*, **1994**, *33*, 6739-6749.
6. Ferguson-Miller, S.; Babcock, G. T. Heme/Copper Terminal Oxidases. *Chemical Reviews*, **1996**, *96*, 2889-2907.
7. Sono, M.; Roach, M. P.; Coulter, E. D.; Dawson, J. H. Heme-Containing Oxygenases. *Chemical Reviews*, **1996**, *96*, 2841-2888.
8. House, J. E. Principles of Chemical Kinetics. *Wm. C. Brown Publishers*, **1997**.
9. Yoshikawa, S.; Shinzawa-Itoh, K.; Nakashima, R.; Yaono, R.; Yamashita, E.; Inoue, N.; Yao, M.; Fei, M. J.; Libeu, C. P.; Mizushima, T.; Yamaguchi, H.; Tomizaki, T.; Tsukihara, T. Redox-coupled crystal structural changes in bovine heart cytochrome c oxidase. *Science*, **1998**, *280*, 1723-1729.
10. Fersht, A. Structure and Mechanism in Protein Science. A Guide to Enzyme Catalysis and Protein Folding. *W.H. Freeman and Company, NY*, **1999**.
11. Michel, H. Proton pumping by cytochrome c oxidase. *Nature* **1999**, *402*, 602-603.
12. Bruice, T. C.; Benkovic, S. J. Chemical basis for enzyme catalysis. *Biochemistry*, **2000**, *39*, 6267-6274.
13. Eisenmesser, E. Z.; Bosco, D. A.; Akke, M.; Kern, D. Enzyme dynamics during catalysis. *Science*, **2002**, *295*, 1520-1523.
14. Hammes, G. G. Multiple conformational changes in enzyme catalysis. *Biochemistry*, **2002**, *41*, 8221-8228.
15. Daniel, R. M.; Dunn, R. V.; Finney, J. L.; Smith, J. C. The role of dynamics in enzyme activity. *Annual Review of Biophysical and Biomolecular Structure*, **2003**, *32*, 69-92.
16. Cherepanov, A. V.; De Vries†, S. Microsecond freeze-hyperquenching: development of a new ultrafast micro-mixing and sampling technology and application to enzyme catalysis. *Biochimica et Biophysica Acta*, **2004**, *1656*, 1-31.
17. Cornish-Bowden, A. Fundamentals of Enzyme Kinetics. Third edition ed.. *Portland Press Ltd., London, UK*, **2004**.
18. Garcia-Viloca, M.; Gao, J.; Karplus, M.; Truhlar, D. G. How enzymes work: analysis by modern rate theory and computer simulations. *Science*, **2004**, *303*, 186-195.
19. de Vries†, S. Freeze-Quench Kinetics in Encyclopedia of Inorganic Chemistry. *John Wiley & Sons, Ltd.*, **2007**, 125-142.
20. Schramm, V. L. Enzymatic transition state theory and transition state analogue design. *Journal of Biological Chemistry*, **2007**, *282*, 28297-28300.
21. Zalatan, J. G.; Herschlag, D. The far reaches of enzymology. *Nature Chemical Biology*, **2009**, *5*, 516-520.
22. Blankenship, R. E. Molecular Mechanisms of Photosynthesis. *Blackwell, Oxford*, **2000**.
23. Roder, H.; Maki, K.; Cheng, H. Early events in protein folding explored by rapid mixing methods. *Chemical Reviews*, **2006**, *106*, 1836-1861.
24. Zewail, A. H. Femtochemistry: Atomic-Scale Dynamics of the Chemical Bond Using Ultrafast Lasers (Nobel Lecture) Copyright((c)) The Nobel Foundation 2000. We thank the Nobel Foundation, Stockholm, for permission to print this lecture. *Angewandte Chemie International Edition (English)*, **2000**, *39*, 2586-2631.
25. Caged Compounds. *Methods in Enzymology*. *Academic Press*, **1998**, Vol. 291.
26. Choi, J.; Terazima, M. Photoreaction of caged ATP studied by the time-resolved transient grating method. *Photochemical and Photobiological Sciences*, **2003**, *2*, 767-773.
27. Giovannardi, S.; Lando, L.; Peres, A. Flash Photolysis of Caged Compounds: Casting Light on Physiological Processes. *News in Physiological Sciences*, **1998**, *13*, 251-255.
28. Ballou, D. P.; Palmer, G. A. Practical rapid quenching instrument for the study of reaction mechanisms by electron paramagnetic resonance spectroscopy. *Analytical Chemistry*, **1974**, *46*, 1248-1253.

29. Berger, R. L. Some problems concerning mixers and detectors for stopped flow kinetic studies. *Biophysical Journal*, **1978**, *24*, 2-20.
30. Berger, R. L.; Balko, B.; Chapman, H. F. High resolution mixer for the study of the kinetics of rapid reactions in solution. *Review of Scientific Instruments*, **1968**, *39*, 493-498.
31. Chance, B. *Journal of the Franklin Institute*, **1940**, *229*, 737-740.
32. Cherepanov, A.; de Vries†, S. bo3 oxidase studied by ultrafast mixing and freeze-quenching in the microsecond time domain. (Abstract oral presentation) in *6th European Conference on Biological Inorganic Chemistry (EuroBIC)*, **2002**, p 35, July 29 - August 3, Lund, Sweden.
33. de Vries†, S.; Albracht, S. P.; Berden, J. A.; Slater, E. C. The pathway of electrons through QH2:cytochrome c oxidoreductase studied by pre-steady-state kinetics. *Biochimica et Biophysica Acta*, **1982**, *681*, 41-53.
34. de Vries†, S.; van Hoek, A. N.; Berden, J. A. The oxidation-reduction kinetics of cytochromes b, c1 and c in initially fully reduced mitochondrial membranes are in agreement with the Q-cycle hypothesis. *Biochimica et Biophysica Acta*, **1988**, *935*, 208-216.
35. Grigoryants, V. M.; Veselov, A. V.; Scholes, C. P. Variable velocity liquid flow EPR applied to submillisecond protein folding. *Biophysical Journal*, **2000**, *78*, 2702-2708.
36. Hartridge, H.; Roughton, F. J. W. The velocity with which carbon monoxide displaces oxygen from combination with haemoglobin. I. *Proc Royal Soc London, series B Biol Sci*, **1923**, *94*, 336-367.
37. Neltchev, V. Z.; Detchev, G. D.; Boyadjiev, L. A. Mixing device for investigating the kinetics of rapid reactions in solutions. *Journal of Physics E: Scientific Instruments*, **1970**.
38. Paeng, K.; Paeng, I.; Kincaid, J. Time-resolved resonance raman spectroscopy using a fast mixing device. *Analytical Sciences*, **1994**, *10*, 157-159.
39. Regenfuss, P.; Clegg, R. M.; Fulwyler, M. J.; Barrantes, F. J.; Jovin, T. M. Mixing liquids in microseconds. *Review of Scientific Instruments*, **1985**, *56*, 283-290.
40. Roder, H.; Maki, K.; Latypov, R. F.; Cheng, H.; Shastry, M. C. R. Early events in protein folding explored by rapid mixing methods. *WILEY-VCH Verlag GmbH & Co. KGaA, Weinheim*, **2005**, Vol. Part I.
41. Shastry, M. C.; Luck, S. D.; Roder, H. A continuous-flow capillary mixing method to monitor reactions on the microsecond time scale. *Biophysical Journal*, **1998**, *74*, 2714-2721.
42. Tanaka, M.; Matsuura, K.; Yoshioka, S.; Takahashi, S.; Ishimori, K.; Hori, H.; Morishima, I. Activation of Hydrogen Peroxide in Horseradish Peroxidase Occurs within approximately 200 micro s Observed by a New Freeze-Quench Device. *Biophysical Journal*, **2003**, *84*, 1998-2004.
43. Tang, J.; Gai, F. A millisecond infrared stopped-flow apparatus. *Applied Spectroscopy*, **2006**, *60*, 1477-1481.
44. White, A. J.; Drabble, K.; Wharton, C. W. A stopped-flow apparatus for infrared spectroscopy of aqueous solutions. *Biochemical Journal*, **1995**, *306* (Pt 3), 843-849.
45. Wiertz, F. G. M. Electron transfer and proton pumping pathways in cytochrome aa3. *PhD Thesis, Delft University of Technology, Delft, The Netherlands*, **2007**.
46. Wiertz, F. G.; Richter, O. M.; Ludwig, B.; de Vries†, S. Kinetic resolution of a tryptophan-radical intermediate in the reaction cycle of *Paracoccus denitrificans* cytochrome c oxidase. *Journal of Biological Chemistry*, **2007**, *282*, 31580-31591.
47. Ehrfeld, W.; Golbig, K.; Hessel, V.; Lowe, H.; Richter, T. Characterization of Mixing in Micro-mixers by a Test Reaction: Single Mixing Units and Mixer Arrays. *Industrial & Engineering Chemical Research*, **1999**, *38*, 1075-1082.
48. Kakuta, M.; Hinsmann, P.; Manz, A.; Lendl, B. Time-resolved Fourier transform infrared spectrometry using a microfabricated continuous flow mixer: application to protein conformation study using the example of ubiquitin. *Lab on a Chip*, **2003**, *3*, 82-85.
49. Masuch, R.; Moss, D. A. Stopped flow apparatus for time-resolved Fourier transform infrared difference spectroscopy of biological macromolecules in H2O. *Applied Spectroscopy*, **2003**, *57*, 1407-1418.
50. Brody, J. P.; Yager, P.; Goldstein, R. E.; Austin, R. H. Biotechnology at Low Reynolds Numbers. *Biophysical Journal*, **1996**, *71*, 3430-3441.
51. Hertzog, D. E.; Ivorra, B.; Mohammadi, B.; Bakajin, O.; Santiago, J. G. Optimization of a Microfluidic Mixer for Studying Protein Folding Kinetics. *Analytical Chemistry*, **2006**, *78*, 4299-4306.
52. Hertzog, D. E.; Michalet, X.; Jäger, M.; Kong, X.; Santiago, J. G.; Weiss, S.; Bakajin, O. Femtomole Mixer for Microsecond Kinetic Studies of Protein Folding. *Analytical Chemistry*, **2004**, *76*, 7169-7178.

-
53. Knight, J. B.; Vishwanath, A.; Brody, J. P.; Austin, R. H. Hydrodynamic Focusing on a Silicon Chip: Mixing Nanoliters in Microseconds. *Physical Review Letters*, **1998**, *80*, 3863-3866.
54. Yao, S.; Bakajin, O. Improvements in Mixing Time and Mixing Uniformity in Devices Designed for Studies of Protein Folding Kinetics. *Analytical Chemistry*, **2007**, *79*, 5753-5759.
55. Pabit, S. A.; Hagen, S. J. Laminar-flow fluid mixer for fast fluorescence kinetics studies. *Biophysical Journal*, **2002**, *83*, 2872-2878.
56. Balny, C.; Saldana, J. L.; Dahan, N. High-pressure stopped-flow spectrometry at low temperatures. *Analytical Biochemistry*, **1984**, *139*, 178-189.
57. Bugnon, P.; Laurency, G.; Ducommun, Y.; Sauvageat, P.-Y.; Merbach, A. E.; Ith, R.; Tschanz, R.; Doludda, M.; Bergbauer, R.; Grell, E. High-pressure stopped-flow spectrometer for kinetics studies of fast reactions by absorbance and fluorescence detection. *Analytical Chemistry*, **1996**, *68*, 3045-3049.
58. Hartridge, H.; Roughton, F. J. W. A method of measuring the velocity of very rapid chemical reactions. *Proc Royal Soc London, series A Math Phys Sci*, **1923**, *104*, 376-394.
59. Hartridge, H.; Roughton, F. J. W. Improvements in the apparatus for measuring the velocity of very rapid chemical reactions. II. *Proceedings of the Cambridge Philosophical Society*, **1927**, *XXIII*, 450-460.
60. Roughton, F. J. W. The time course of the heat effects in rapid chemical changes. I. Apparatus and methods. *Proceedings of the Royal Society (London)*, **1930**, *126A*, 439-469.
61. Roughton, F. J. W. The kinetic's of haemoglobin IV - General methods and theoretical basis for the reactions with carbon monoxide. *Proceedings of the Royal Society (London)*, **1934**, *115B*, 451-464.
62. Chance, B. The Stopped-flow Method and Chemical Intermediates in Enzyme Reactions - A Personal Essay. *Photosynthesis Research*, **2004**, *80*, 387-400.
63. Hui Bon Hoa G.; Douzou, P.; Dahan, N.; Balny, C. High-pressure spectrometry at subzero temperatures. *Analytical Biochemistry*, **1982**, *120*, 125-135.
64. Kintses, B.; Simon, Z.; Gyimesi, M.; Toth, J.; Jelinek, B.; Niedetzky, C.; Kovacs, M.; Malnasi-Csizmadia, A. Enzyme kinetics above denaturation temperature: a temperature-jump/stopped-flow apparatus. *Biophysical Journal*, **2006**, *91*, 4605-4610.
65. Balny, C.; Masson, P.; Heremans, K. High pressure effects on biological macromolecules: from structural changes to alteration of cellular processes. *Biochimica et Biophysica Acta*, **2002**, *1595*, 3-10.
66. Hui Bon Hoa, G.; McLean, M. A.; Sligar, S. G. High pressure, a tool for exploring heme protein active sites. *Biochimica et Biophysica Acta*, **2002**, *1595*, 297-308.
67. Mozhaev, V. V.; Heremans, K.; Frank, J.; Masson, P.; Balny, C. High pressure effects on protein structure and function. *Proteins*, **1996**, *24*, 81-91.
68. Frieden, C.; Hoeltzli, S. D.; Ropson, I. J. NMR and protein folding: equilibrium and stopped-flow studies. *Protein Science*, **1993**, *2*, 2007-2014.
69. Green, D. B.; Lane, J.; Wing, R.M. A Standard Session Stopped-Flow NMR Tube. *Applied Spectroscopy*, **1987**, *41*, 847-850.
70. Bhuyan, A. K.; Udgaonkar, A.K. Stopped-Flow NMR Measurement of Hydrogen Exchange Rates in Reduced Horse Cytochrome c Under Strongly Destabilizing Conditions. *PROTEINS: Structure, Function, and Genetics*, **1998**, *32:241-247* 32, 241-247.
71. Yushmanov, P. V.; Furo, I.; Stilbs, P. Micellar kinetics of a fluorosurfactant through stopped-flow NMR. *Langmuir*, **2006**, *22*, 2002-2004.
72. Hoeltzli, S. D.; Frieden, C. Stopped-flow NMR spectroscopy: real-time unfolding studies of 6-19F-tryptophan-labeled Escherichia coli dihydrofolate reductase. *Proceedings of the National Academy of Sciences (USA)*, **1995**, *92*, 9318-9322.
73. Grimaldi, J. J.; Sykes, B. D. Stopped flow fourier transform nuclear magnetic resonance spectroscopy. An application to the alpha-chymotrypsin-catalyzed hydrolysis of tert-butyl-L-phenylalanine. *Journal of the American Chemical Society*, **1975**, *97*, 273-276.
74. Hubbel, W.; Froncisz, W.; Hyde, J. Continuous and stopped-flow EPR spectrometer based on a loop gap resonator. *Review of Scientific Instruments*, **1987**, *58*, 1879-1886.
75. Klimes, N.; Lassmann, G.; Ebert, B. Time-resolved EPR spectroscopy stopped-flow EPR apparatus for biological application. *Journal of Magnetic Resonance*, **1980**, *37*, 53-59.
76. Lassmann, G.; Schmidt, P.P.; Lubitz, W. An advanced EPR stopped-flow apparatus based on a dielectric ring resonator. *Journal of Magnetic Resonance*, **2005**, *172*, 312-323.

77. Sienkiewicz, A.; daCosta Ferreira, A.; Danner, B.; Scholes, C.P. Dielectric resonator-based flow and stopped-flow EPR with rapid field scanning: a methodology for increasing kinetic information. *Journal of Magnetic Resonance*, **1999**, *136*, 137-142.
78. Inada, Y.; Hayashi, H.; Funahashi, S.; Nomura, M. Time-resolved stopped-flow x-ray absorption fine structure system using synchrotron radiation for fast reactions in solution. *Review of Scientific Instruments*, **1997**, *68*, 2973-2977.
79. George, S. J.; Allen, J. W.; Ferguson, S. J.; Thorneley, R. N. Time-resolved infrared spectroscopy reveals a stable ferric heme-NO intermediate in the reaction of *Paracoccus pantotrophus* cytochrome cd1 nitrite reductase with nitrite. *Journal of Biological Chemistry*, **2000**, *275*, 33231-33237.
80. Majumdar, Z. K.; Sutin, J. D. B.; Clegg, R. M. Microfabricated continuous-flow, turbulent, microsecond mixer. *Review of Scientific Instruments*, **2005**, *76*, 1-11.
81. Claude B.; Patrick M.; Karel H. *Frontiers in High Pressure Biochemistry and Biophysics. Elsevier*, **2002**, *1595*, 2, 1-403.
82. Desamero, R.; Rozovsky, S.; Zhadin, N.; McDermott, A.; Callender, R. Active site loop motion in triosephosphate isomerase: T-jump relaxation spectroscopy of thermal activation. *Biochemistry*, **2003**, *42*, 2941-2951.
83. Lassmann, G.; Eriksson, L.A.; Himo, F.; Lendzian, F.; Lubitz, W. Electronic Structure of a Transient Histidine Radical in Liquid Aqueous Solution: EPR Continuous-Flow Studies and Density Functional Calculations. *Journal of Physical Chemistry*, **1999**, *103A*, 1283-1290.
84. Chance, B.; Eisenhardt, R. H.; Gibson, Q. H.; Longberg-Holm, K. K.; Eds. Rapid mixing and sampling techniques in biochemistry. *Academic Press, New York*, **1964**, pp 195-203,
85. Bray, R. C. Sudden Freezing as a Technique for the Study of Rapid Reactions. *Biochemical Journal*, **1961**, *81*, 189-195.
86. Bray, R. C. Quenching by squirting into cold immiscible liquids, in *Rapid mixing and sampling techniques in biochemistry* (Chance, B.; Eisenhardt, R. H.; Gibson, Q. H.; Longberg-Holm, K. K.; Eds.). *Academic Press, New York*, **1964**, pp 195-203.
87. Palmer, G.; Beinert, H. An experimental evaluation of the Bray rapid-freezing technique, in *Rapid mixing and sampling techniques in biochemistry*. (Chance, B.; Eisenhardt, R. H.; Gibson, Q. H.; Longberg-Holm, K. K.; Eds.) *Academic Press, New York*, **1964**, pp 205-217.
88. Palmer, G.; Bray, R. C.; Beinert, H. Direct Studies on the Electron Transfer Sequence in Xanthine Oxidase by Electron Paramagnetic Resonance Spectroscopy. I. Techniques and Description of Spectra. *Journal of Biological Chemistry*, **1964**, *239*, 2657-2666.
89. Lu, S.; Wiertz, F. G. M.; de Vries†, S.; Moëne-Loccoz, P. Resonance Raman characterization of a high-spin six-coordinate iron(III) intermediate in metmyoglobin-azido complex formation trapped by microsecond freeze-hyperquenching (MHQ). *Journal of Raman Spectroscopy*, **2005**, *36*, 359-362.
90. Moëne-Loccoz, P.; Krebs, C.; Herlihy, K.; Edmondson, D. E.; Theil, E. C.; Huynh, B. H.; Loehr, T. M. The ferroxidase reaction of ferritin reveals a diferric μ -1,2 bridging peroxide intermediate in common with other O_2 -activating non-heme diiron proteins. *Biochemistry*, **1999**, *38*, 5290-5295.
91. de Vries†, S.; Albracht, S. P.; Berden, J. A.; Marres, C. A.; Slater, E. C. The effect of pH, ubiquinone depletion and myxothiazol on the reduction kinetics of the prosthetic groups of ubiquinol:cytochrome c oxidoreductase. *Biochimica et Biophysica Acta*, **1983**, *723*, 91-103.
92. Mitic, N.; Saleh, L.; Schenk, G.; Bollinger, J. M., Jr.; Solomon, E. I. Rapid-freeze-quench magnetic circular dichroism of intermediate X in ribonucleotide reductase: new structural insight. *Journal of the American Chemical Society*, **2003**, *125*, 11200-11201.
93. Ravi, N.; Bollinger, J. M.; Jr., Huynh, B. H.; Stubbe, J.; Edmondson, D. E. Mechanism of Assembly of the Tyrosyl Radical-Diiron(III) Cofactor of E. Coli Ribonucleotide Reductase: 1. Moëssbauer Characterization of the Diferric Radical Precursor. *Journal of the American Chemical Society*, **1994**, *116*, 8007-8014.
94. Riggs-Gelasco, P. J.; Shu, L.; Chen, S.; Burdi, D.; Huynh, B. H.; Que, L. Jr.; Stubbe, J. EXAFS Characterization of the Intermediate X Generated During the Assembly of the Escherichia coli Ribonucleotide Reductase R2 Diferric Tyrosyl Radical Cofactor. *Journal of the American Chemical Society*, **1998**, *120*, 849-860.
95. Ryle, M. J.; Lee, H. I.; Seefeldt, L. C.; Hoffman, B. M. Nitrogenase reduction of carbon disulfide: freeze-quench EPR and ENDOR evidence for three sequential intermediates with cluster-bound carbon moieties. *Biochemistry*, **2000**, *39*, 1114-1119.

-
96. Schunemann, V.; Jung, C.; Ternner, J.; Trautwein, A. X.; Weiss, R. Spectroscopic studies of peroxyacetic acid reaction intermediates of cytochrome P450cam and chloroperoxidase. *Journal of Inorganic Biochemistry*, **2002**, *91*, 586-596.
 97. Tsai, A. L.; Berka, V.; Kulmacz, R. J.; Wu, G.; Palmer, G. An improved sample packing device for rapid freeze-trap electron paramagnetic resonance spectroscopy kinetic measurements. *Analytical Biochemistry*, **1998**, *264*, 165-171.
 98. Willems, J.-P.; Lee, H. I.; Burdi, D.; Doan, P. E.; Stubbe, J.; Hoffman, B. M. Identification of the Protonated Oxygenic Ligands of Ribonucleotide Reductase Intermediate X by Q-Band 1,2H CW and Pulsed ENDOR. *Journal of the American Chemical Society*, **1997**, *119*, 9816-9824.
 99. Bollinger, J. M.; Jr., Tong, W. H.; Ravi, N.; Huynh, B. H.; Edmondson, D. E.; Stubbe, J. Use of rapid kinetics methods to study the assembly of the diferric-tyrosyl radical cofactor of E. coli ribonucleotide reductase. *Methods in Enzymology*, **1995**, *258*, 278-303.
 100. Burdi, D.; Sturgeon, B. E.; Tong, W. H.; Stubbe, J.; Hoffman, B. M. Rapid Freeze-Quench ENDOR of the Radical X Intermediate of Escherichia coli Ribonucleotide Reductase Using 17O₂, H₂17O, and 2H₂O. *Journal of the American Chemical Society*, **1996**, *118*, 281-282.
 101. Brenner, M. C.; Murray, C. J.; Klinman, J. P. Rapid freeze- and chemical-quench studies of dopamine beta-monooxygenase: comparison of pre-steady-state and steady-state parameters. *Biochemistry*, **1989**, *28*, 4656-4664.
 102. Lin, Y.; Gerfen, G. J.; Rousseau, D. L.; Yeh, S. R. Ultrafast microfluidic mixer and freeze-quenching device. *Analytical Chemistry*, **2003**, *75*, 5381-5386.
 103. Cherepanov, A. V.; Doroshenko, E. V.; Matysik, J.; de Vries†, S.; de Groot, H. J. The associative nature of adenylyl transfer catalyzed by T4 DNA ligase. *Proceedings of the National Academy of Sciences (USA)*, **2008**, *105*, 8563-8568.
 104. Wiertz, F. G. M.; Richter, O. M.; Cherepanov, A. V.; MacMillan, F.; Ludwig, B.; de Vries†, S. An oxo-ferryl tryptophan radical catalytic intermediate in cytochrome c and quinol oxidases trapped by microsecond freeze-hyperquenching (MHQ). *FEBS Letters*, **2004**, *575*, 127-130.
 105. Bald, W. B. On crystal size and cooling rate. *Journal of Microscopy*, **1986**, *143*, 89-102.
 106. Mayer, E. Vitrification of pure liquid water. *Journal of Microscopy*, **1985**, *140*, 3-15.
 107. Mayer, E.; Bruggeller, P. Vitrification of pure liquid water by high pressure jet freezing. *Nature*, **1982**, *298*, 715-718.
 108. Matsuura, K.; Yoshioka, S.; Takahashi, S.; Ishimori, K.; Mogi, T.; Hori, H.; Morishima, I. Dioxxygen Reduction by bo-Type Quinol Oxidase from Escherichia coli Studied by Submillisecond-Resolved Freeze-Quench EPR Spectroscopy. *BiochemistryASAP Articles*, **2004**, 1-9.
 109. Wiertz, F. G. M.; de Vries†, S. Low-temperature kinetic measurements of microsecond freeze-hyperquench (MHQ) cytochrome oxidase monitored by UV-Vis ible spectroscopy with a newly designed cuvette. *Biochemical Society Transactions*, **2006**, *34*, 136-138.
 110. Ren, Z.; Perman, B.; Srajer, V.; Teng, T. Y.; Pradervand, C.; Bourgeois, D.; Schotte, F.; Ursby, T.; Kort, R.; Wulff, M.; Moffat, K. A molecular movie at 1.8 Å resolution displays the photocycle of photoactive yellow protein, a eubacterial blue-light receptor, from nanoseconds to seconds. *Biochemistry*, **2001**, *40*, 13788-13801.
 111. Ma, H.; Wan, C.; Zewail, A. H. Ultrafast T-jump in water: studies of conformation and reaction dynamics at the thermal limit. *Journal of the American Chemical Society*, **2006**, *128*, 6338-6340.
 112. Chance, B.; Saronio, C.; Leigh, J. S., Jr. Functional intermediates in the reaction of membrane-bound cytochrome oxidase with oxygen. *Journal of Biological Chemistry*, **1975**, *250*, 9226-9237.
 113. Adelroth, P.; Karpfors, M.; Gilderson, G.; Tomson, F. L.; Gennis, R. B.; Brzezinski, P. Proton transfer from glutamate 286 determines the transition rates between oxygen intermediates in cytochrome c oxidase. *Biochimica et Biophysica Acta*, **2000**, *1459*, 533-539.
 114. Jacob, M.; Holtermann, G.; Perl, D.; Reinstein, J.; Schindler, T.; Geeves, M. A.; Schmid, F. X. Microsecond folding of the cold shock protein measured by a pressure-jump technique. *Biochemistry*, **1999**, *38*, 2882-2891.

Chapter 3

Design of turbulent tangential micro-mixers that mix liquids on the nanosecond time scale

Sandra Mitić , Jan W. van Nieuwkastele, Albert van den Berg,
Simon de Vries†

Adapted from: *Analytical Biochemistry*, 2015, 469:19-26

Abstract

Unraveling (bio)chemical reaction mechanisms and macromolecular folding pathways on the (sub)microsecond time scale is limited by the time resolution of kinetic instruments for mixing reactants and observation of the progress of the reaction. To improve the mixing time resolution, turbulent four- and two-jet tangential micro-mixers were designed and characterized for their mixing and (unwanted) premixing performances employing acid-base reactions monitored by a pH-sensitive fluorescent dye. The mixing performances of the micro-mixers were determined after the mixing chamber in a free-flowing jet. The premixing behavior in the vortex chamber was assessed in an optically transparent glass-silicon replica of a previously well-characterized stainless-steel four-jet tangential micro-mixer. At the highest flow rates, complete mixing was achieved in 160 ns with only approximately 9% premixing of the reactants. The mixing time of 160 ns is at least 50 times shorter than estimated for other fast mixing devices. Key aspects to the design of ultrafast turbulent micro-mixers are discussed. The integration of these micro-mixers with an optical flow cell would enable the study of the very onset of chemical reactions in general and of enzyme catalytic reactions in particular.

Introduction

Studies to delineate the mechanism of (bio)chemical reactions are performed in either of two different ways. A reaction can be initiated by rapidly mixing two or more reactants, or an initial equilibrium is suddenly disturbed, for example, by a short laser pulse, so-called relaxation techniques^{1,2}. Thanks to the development of the laser during the 1960s and of ultrafast lasers during the past two decades, the time resolution of relaxation techniques is below femtoseconds, enabling characterization of ultra-transient states in chemical reactions or determination of the (sub)picosecond kinetics of electron transfer in photochemically activated reaction centers of chloroplasts and photosynthetic microorganisms^{3,4}. The time resolutions for turbulent mixing and subsequent observation in stopped-flow (~0.5-1 ms^{5,6}) and continuous flow (~11-50 μ s⁷⁻⁹) mixing instruments are much lower than those for relaxation techniques. The shortest time scale for protein and RNA folding or breaking and making chemical bonds in reactions catalyzed by enzymes is 0.1 to 1 μ s^{1,2,8-14} and, thus, is not accessible with mixing techniques. Fast enzymes with kinetic phases on the (sub)microsecond time scale include many members of the oxidoreductases (e.g., catalase, cytochrome oxidases), hydrolases (e.g., acetylcholinesterase), and lyases (e.g., carbonic anhydrase) but are also found among the isomerases and ligases. In general, the reaction progress of oxidoreductases can be monitored by ultraviolet-visible (UV-Vis)¹ spectroscopy or vibrational spectroscopy at least for heme containing enzymes²; fluorescence spectroscopy is more appropriate for the study of the other classes of enzymes. To approach the time scale of 0.1 to 1 μ s experimentally, the need for mixing reactants can be obviated by the application of caged compounds, that is, photolabile substrate analogues that are premixed with the enzyme and activated on a (laser) flash of light^{1,2,15,16}. However, the study of the catalytic cycle of the great majority of enzymes requires that enzyme and substrate be rapidly mixed. A comparison of the shortest time scales of enzyme-catalyzed reactions and of the best mixing instruments indicates the need to improve the mixing time resolution of the kinetic equipment in particular to record as many transient states as possible to define the catalytic mechanism.

The first instrument with subsecond time resolution developed to mix two solutions was described in 1923 by Hartridge and Roughton. This continuous-flow instrument with its inherent high sample consumption rate employed a four-jet tangential mixer (dead-time of ~10 ms¹⁷; improved a few years later to ~2ms¹⁸) and was used to study the binding kinetics of O₂ to hemoglobin by means of UV-Vis spectroscopy. The long axis of the transparent flow tube served as the time axis; optical changes were monitored perpendicular to the long axis. The next development in time resolution (~1 ms) along with a great reduction in sample consumption was the stopped-flow instrument designed in 1940 by Chance¹⁹. The time resolution of this now widely used instrument cannot be significantly improved to below approximately 0.5 ms, in spite of miniaturization, because it is determined by the speed of arresting the fluid flow. The stopped-flow instrument allows detection of reactions by UV-Vis and fluorescence spectroscopy, circular dichroism, Fourier transform infrared, resonance Raman spectroscopy, nuclear magnetic resonance, or X-ray absorption spectroscopy². Significant improvements in mixing time resolution were achieved with the continuous-flow instruments designed in 1998 by Roder and coworkers^{7,8,20,21} and in 2007 by Takahashi's group⁹ that enable UV-Vis and fluorescence detection. The

instrument designed by Roder employed a capillary micro-mixer with smallest channel dimensions of approximately 200 μm where the flow is laminar and a *Pt* ball to mix the reactants in 10 to 15 μs by turbulent mixing. The total dead-time for observation of this instrument amounts to approximately 50 μs , which includes the mixing time, the dead volume, and the time to fill the observation chamber. In the instrument designed by Takahashi, the reagent flows are nonlaminar before mixing, which increases the mixing efficiency when the flows collide, decreasing the dead-time to approximately 11 μs . An important key to improve the mixing time resolution in these latter studies was miniaturization of the flow channels ($\sim 10 \mu\text{m}^9$), leading to smaller dead volumes and, hence, to shorter dead-times.

Micro-mixers (channels $\sim < 500 \mu\text{m}$) are mostly used in ‘Lab-on-a-chip’ devices for analytical purposes²²⁻²⁴. The use of microfabricated structures and microfluidics offers many advantages, including new functionalities, higher throughput, reduced sample consumption, shorter analysis time, and reduced operating and manufacturing costs^{23,25,26}. However, the majority of the micro-mixers used in lab-on-a-chip devices usually operate in the laminar flow regime at low Reynolds numbers (< 100) that generally limits their mixing efficiency and time resolution, in particular in the case of simple mixer geometries (T- and Y-mixers). The efficiency or degree of mixing depends on the dimensionless Reynolds number, *Re*. Rapid and complete mixing requires turbulent flow conditions to disperse the reactants to the molecular level of the solvent(s) so that the collision rate of the reactants is governed only by diffusion. The transition from laminar to turbulent flow occurs at *Re* ~ 2000 for flow in pipes²⁷, where *Re* is given by the equation

$$Re = \frac{\rho \times \langle v \rangle \times d}{\eta} \quad (\text{Eq. 1})$$

where ρ is the solvent density (equal to 1000 kg m^{-3} for water at 20 $^\circ\text{C}$), $\langle v \rangle$ is the linear average flow velocity of the liquid in a channel (m s^{-1}), d is the hydraulic diameter of the channel (m), and η is the dynamic viscosity (equal to $10^{-3} \text{ kg m}^{-1} \text{ s}^{-1}$ for water at 20 $^\circ\text{C}$). To enter the turbulent regime in micro-channels of 100 μm , linear flow rates greater than 20 m s^{-1} are required. Such high flow rates lead to a buildup of pressure (ΔP) according to Bernoulli’s velocity/dynamic pressure equation²⁸:

$$\Delta P = 0.5 \cdot \rho \cdot \langle v \rangle^2 \quad (\text{Eq. 2})$$

The calculated pressure for the turbulent regime in channels of 100 μm amounts to at least 0.2 MPa but may be as high as 0.5 to 1 MPa in practice due to wall friction and increased viscosity of concentrated solutions. Pressures greater than 0.2 MPa are much higher than those usually generated by the hydrodynamic flows in μTAS (micro total analysis system) and MEMS (micro electromechanical system) devices²⁹. High pressures require a robust design that appears to be incompatible with the majority of lab-on-a-chip devices. For these reasons, many types of micro-mixers for Lab-on-a-chip applications that operate at low hydrodynamic pressures^{23,30} while able to mix reactants in approximately 1 ms have been designed. This is achieved by introducing complex premixing geometries that generally increase the contact areas between the reactant flows²⁸⁻³⁵. For example, contact areas can be increased by splitting incoming

flows into several narrower streams that later join as described for 4-jet and 16-jet tangential mixers^{28,32}.

In hydrodynamic focusing devices, a thin stream of, for example, a protein solution is squeezed between two reagent streams^{2,36-42}. The small width and depth dimensions of the stream carrying the protein solution (~ 30 nm - 1 μ m and ~ 10 μ m, respectively) allow rapid diffusive mixing (~ 4 - 10 μ s and with a claim of only ~ 1 μ s³⁹) with the reagent with minimal protein consumption^{41,42}. Thus, protein and RNA folding intermediates that occur on a short time scale could be studied by fluorescence spectroscopy, in particular by FRET (Forster resonance energy transfer)^{41,42}.

Inspired by the developments listed above, we were interested in the design requirements for turbulent micro-mixers with mixing times in the (sub)microsecond time domain for use in real-time spectroscopic instruments for the characterization of ultra-transient intermediates. Premixing in such mixers should, in contrast to mixers used in lab-on-a-chip application, be minimized and preferably be absent because it significantly adds to the dead-time for observation. In view of this, the authors previously designed a stainless-steel turbulent four-jet tangential micro-mixer with channels of 100 μ m, enabling maximal linear flow rates of 200 m s^{-1} and maximal operating pressures of 40 MPa²⁸. This mixer was integrated in an ultrafast freeze-quench instrument that achieves a shortest dead-time of 75 μ s^{28,43,44}. In this stainless-steel micro-mixer, mixing appeared to be completed within approximately 2 μ s²⁸, which is at least five times faster than in Refs.^{7,8}. However, given a smallest mixing volume of 10 pL, the true mixing time of this stainless-steel mixer can be calculated as approximately 160 ns (cf. **Fig. 1**). Precise knowledge of the mixing time was not so important for the freeze-quench procedure because the time resolution of the setup is determined mainly by the 40 - to 50 - μ s freezing time. However, exact knowledge of the premixing and mixing behavior, which determines the total mixing time, is a prerequisite to successful integration of this or similar mixers in future ultrafast real-time optical applications^{7,8}. To validate the calculated mixing time of 160 ns, we designed several four-jet and two-jet turbulent micro-mixers that are optically transparent analogues of the stainless-steel four-jet tangential micro-mixer and determined their premixing and mixing times. The results show that mixing liquids on the nanosecond time scale is possible, and guidelines to build instruments for kinetic research with the highest possible time resolution are discussed.

Materials and methods

We previously designed a stainless-steel four-jet tangential micro-mixer (**Fig. 1**) capable of completely mixing two liquids within 2 μ s²⁸. High flow rates that generate sufficient turbulence for complete mixing of (viscous) solutions were obtained with two high-performance liquid chromatography (HPLC) pumps with a 40 -MPa pressure limit described previously^{28,43,44}. In this work, we report the properties of replicas of this stainless-steel micro-mixer with minor variations. Mixers were made from plexiglass or from glass-silicon. The stainless-steel and plexiglass micro-mixers were used to quantitatively determine the final mixing performance by measuring fluorescence appearance in a free-flowing jet. We also constructed an optically transparent glass-silicon chip with a four-jet tangential mixer to quantitatively determine the premixing profile. Each mixing setup consists of a mixer body

connected to the HPLC solvent delivery system and, as defined below, comprises a premixing chamber, a vortex chamber, and a mixing chamber. The (mixed) reactants leave the mixing chamber, which is essentially an orifice, as a free jet (see **Figs. 1** and **2**). The glass-silicon mixer did not, however, produce a stable free-flowing jet, preventing direct quantitative determination of its final mixing performance. The high flow rates used in this work require high pressures. Approximately 30% of the glass-silicon mixers remained intact at pressures up to 10 to 15 MPa. The glass-silicon chip was fabricated using standard micro-fabrication techniques with one Pyrex glass wafer and one double-sided polished silicon wafer, standard substrate cleaning steps, (three) film photoresist deposition steps and (three) photolithography steps, and a glass-silicon anodic thermal bonding step, as outlined in Ref.⁴⁵. The channel etching in the silicon was done by the dry etching Bosch process.

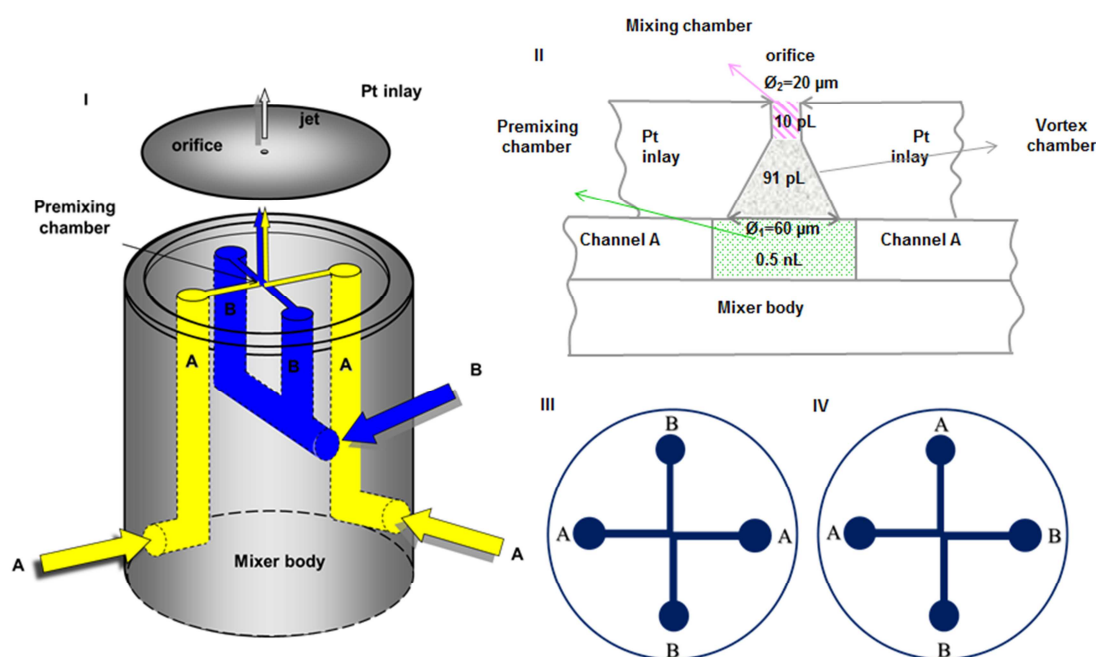


Figure 1. Schematic drawing of the four-jet tangential ABAB stainless-steel micro-mixer and its plexiglass analogues. **(I)** The stainless-steel micro-mixer. Reactants *A* and *B* enter the mixer body as shown, are subsequently split, and meet at a ‘cross’, the premixing chamber. Liquids may meet in the ABAB **(III)** or AABB **(IV)** arrangement. **(II)** After the premixing chamber, the fluids enter the vortex chamber (shown as cross section; in the AABB mixer, channel A and channel B would meet) present in the *Pt* inlay and are then forced through the orifice. The *Pt* inlay is fitted to the mixer body by a brass screw cap (not shown; see in Ref.²⁸). The channels are offset **(III, IV)**, by a full-width (stainless-steel) or two-thirds width (plexiglass) of the channel.

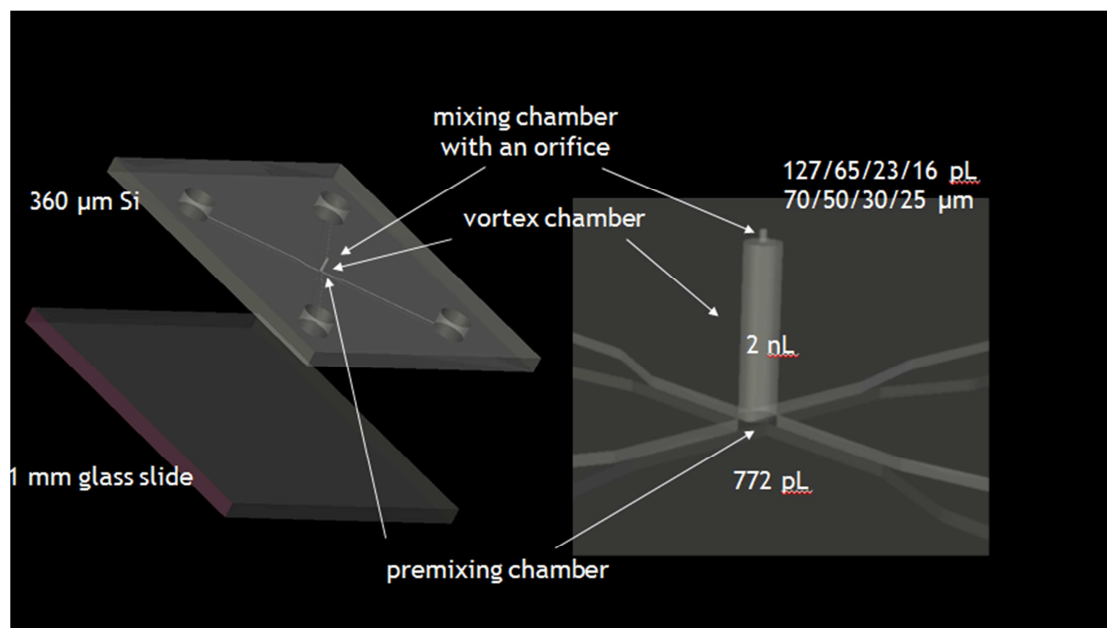


Figure 2. Design and geometry of the four-jet tangential ABAB glass-silicon micro-mixer chips with orifice diameters of 25, 30, 50, and 70 μm .

Micro-mixer designs

The schematics of the setup and dimensions of the mixers are shown in **Figs. 1** and **2** and **Table 1**. The two reactants, A and B, are delivered from sample bottles by two HPLC pumps (Schimadzu LC-20AT and Waters 515) into the mixer body as in the MHQ (microsecond freeze-hyperquenching) setup²⁸. Reactant channels are 300 μm in diameter for the four-jet tangential ABAB stainless-steel mixer and all of the plexiglass mixers or 500 μm in diameter for the four-jet tangential ABAB glass-silicon micro-mixer chips (**Fig. 2**). These wide channels narrow to micro-channels within the mixer body and meet at a cross section, the ‘premixing chamber’. The micro-channels (50, 60, or 70 μm wide and deep; see **Table 1**) are offset with respect to each other by a full-width of the channel in the four-jet tangential ABAB stainless-steel mixer, by two-thirds of the channel width in all of the plexiglass mixers, or by a half-width of the channel in the four-jet tangential ABAB glass-silicon micro-mixer chips. For example, the dimensions of the premixing chamber (in width \times width \times depth) are 100 \times 100 \times 50 μm (0.50 nL volume) for the four-jet tangential ABAB stainless-steel mixer (**Table 1**). The offset of the channels induces a vortex in which the four (or two in the case of the two-jet tangential mixer) liquid streams rotate around one another.

Table 1. Dimensions of the micro-mixers

	Type of mixer		
	Stainless-steel ^a	Plexiglass ^a	Glass silicon
Solvent inlet channel (diameter, μm)	300	500	500
Premixing chamber inlet channel (depth, width, μm)	50, 50	60, 60	70, 70
Premixing chamber (length, width, depth, μm) (volume, nL)	100, 100, 50 V = 0.50	100, 100, 60 V = 0.60	105, 105, 70 V = 0.77
Vortex chamber (diameters $\text{\O}_1\text{-}\text{\O}_2$, length, μm) (volume, nL)	Conical 60-20 x 67 V = 0.09	Conical 60-20 x 67 V = 0.09	Cylindrical 100 x 257 V = 2
Mixing chamber (diameter, length, μm) (volume, pL)	Cylindrical 20 x 33 V = 10	Cylindrical 20 x 33 V = 10	Cylindrical 25/30/50/70 x 33 V = 16, 23, 65, 127

^aThe vortex chambers and mixing chambers of the stainless-steel and plexiglass mixers are located in the Pt seal (**Figs. 1 and 2**)

After the premixing chamber, the reactants enter the ‘vortex chamber’, which is oriented perpendicularly to the plane of the channels. In the four-jet tangential ABAB stainless-steel mixer and all of the plexiglass mixers, the vortex chamber and mixing chamber are located in the Pt inlay (**Fig. 1 and Table 1**). The Pt inlay (20 μm orifice, 3 mm in outer diameter, and 100 μm thick; obtained from Baltic Preparation) also acts as a seal and is mounted on top of the channels and the premixing chamber and is fixed with a fine threaded screw cap (not shown in **Fig. 1**, but see in Ref.²⁸) to the mixer body. The shape of the Pt vortex chamber is conical, whereas the shape of the mixing chamber is cylindrical (**Fig. 1 and Table 1**). The volume of the mixing chamber is only 10 pL (**Table 1**). In the glass-silicon mixer, the vortex chamber is cylindrical and very long (257 μm) owing to the thickness of the silicon (**Table 1 and Fig. 2**). The vortex chamber of the glass-silicon mixer ends in a cylindrical mixing chamber (silicon orifice) with diameters between 25 and 70 μm (see **Supplementary Fig. 1**). In all mixers, the mixed fluids leave the orifice as a free jet. More details are provided in the **Supplementary material**.

Results and discussion

To determine the mixing efficiency of the turbulent micro-mixers, the appearance or quenching of fluorescence of 8-hydroxypyrene-1,3,6-trisulfonic acid (HPTS) in acid-base reactions was determined in a free jet (**Fig. 3 and Supplementary Section 5A**). In these experiments, a low (1.5-fold) excess of acid over base (or vice versa) was used to ensure that fluorescence quenching (or disappearance) is due to near stoichiometric encounter of H_3O^+ and OH^- , a prerequisite to assess mixing efficiency. As a result of this experimental condition, fluorescence quenching (or disappearance) or mixing efficiency can be calculated only when the reaction has progressed for more than two-thirds (**Fig. 3 and Supplementary Section 5A**). The four-jet tangential ABAB stainless-steel mixer mixes the reactants for more than 90% at $Re \sim 500$, and full mixing is obtained at $Re > 1000$ to 1500. The plexiglass analogue of this mixer and the two-jet tangential plexiglass mixer behave similarly, given the experimental error (**Fig. 3**), although full mixing by the latter mixers might require somewhat higher $Re \sim 2000$ to 2500. The four-jet AABB plexiglass mixer is less efficient, showing a maximal amount of mixing obtained at $Re > 3000$. Therefore, we conclude

that the two-jet and four-jet ABAB tangential micro-mixers with alternating reactant channels have similar mixing qualifications and that the AABB configuration performs less efficiently, presumably due to a smaller contact area between the fluid flows. The AABB mixer configuration is often used in rapid freeze-quench instruments^{1,2,46} and, thus, can easily be improved. Unfortunately, the experiment shown in **Fig. 3** could not be successfully performed with the four-jet tangential ABAB glass-silicon mixers due to difficulties of forming a stable free jet, preventing direct quantitative assessment of the mixing efficiency. However, we could confirm by eye that the jet emanating from the glass-silicon mixers is fluorescent and, hence, that the fluids are mixed for more than 66.7% (cf. the ordinate in **Fig. 3**).

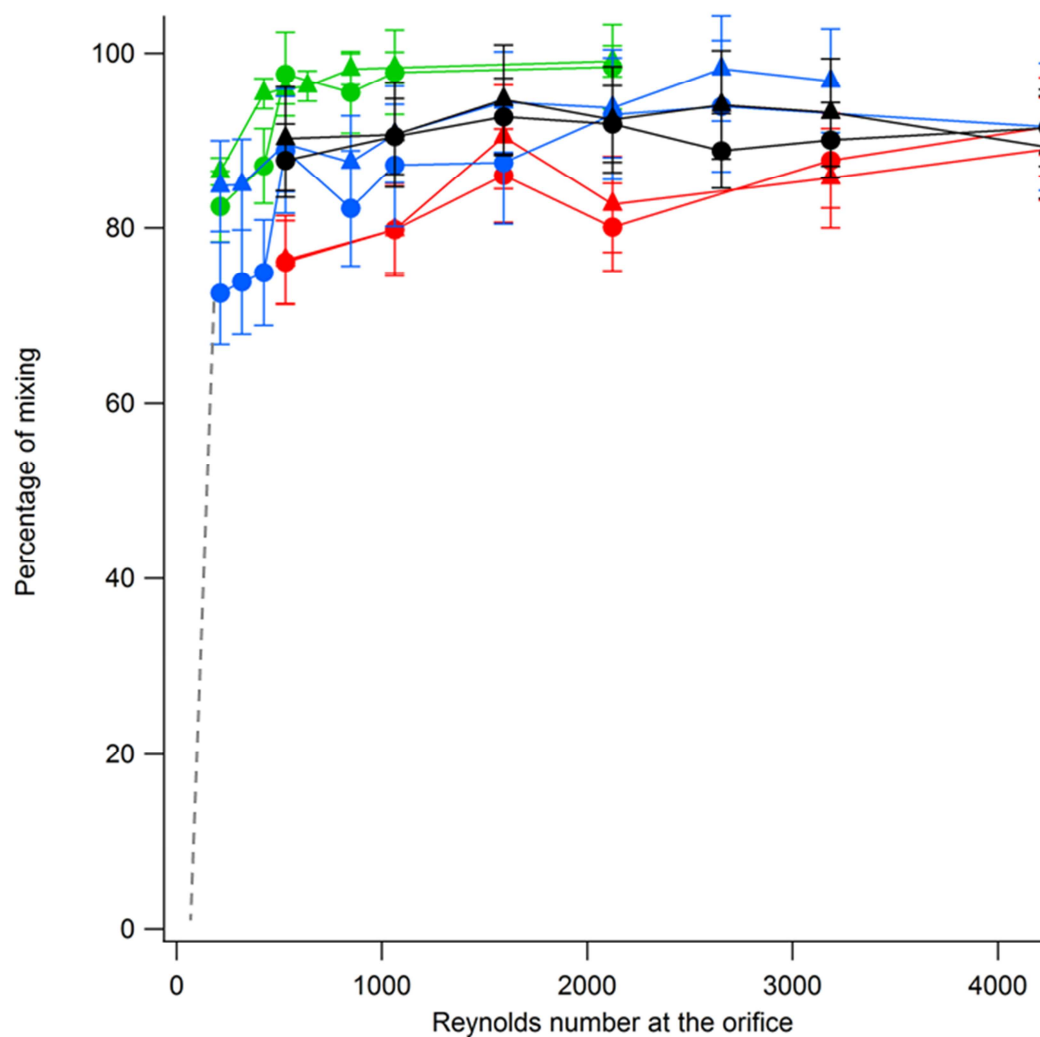


Figure 3. Percentage of mixing by tangential micro-mixers observed in a free flowing jet (20 μm diameter). Shown are the four-jet tangential ABAB stainless-steel mixer (\bullet and \blacktriangle) with fluorescence standard error values of $\pm 4.9\%$ and 1.8% , respectively, the four-jet tangential ABAB plexiglass mixer (\bullet [$\pm 8.0\%$] and \blacktriangle [$\pm 6.1\%$]), the four-jet AABB plexiglass mixer (\bullet [$\pm 6.2\%$] and \blacktriangle [$\pm 6.6\%$]), and the two-jet AB plexiglass mixer (\bullet [$\pm 4.8\%$], \blacktriangle [$\pm 6.6\%$]). Fluorescence appearance/quenching was monitored using HPTS in deprotonation (\bullet)/protonation (\blacktriangle) reactions, respectively. NaOH/HCl ratio was 15 mM/10 mM = 1.5 for deprotonation and the reverse for protonation. HPTS] = 1.5 mM. The dotted line (from zero to 66.7% fluorescence) indicates the threshold below which the percentage mixing cannot be calculated (see **Supplementary Section 5A**).

To determine the actual mixing time of the micro-mixers, one should determine whether the mixing occurs exclusively in the relatively small mixing compartment or already to some extent earlier in the larger vortex chamber and/or premixing chamber. Mixing, or rather premixing, in the vortex or premixing chamber would constitute a dead volume that would add to the total dead-time, for example, in a setup where the micro-mixers are integrated with an optical cell to monitor the kinetics of (bio)chemical reactions. To determine where and to what extent premixing occurs, fluorescence measurements were performed in the optically transparent vortex chamber of the four-jet tangential ABAB glass-silicon mixers (**Figs. 4** and **5**). In these experiments, a high (30-fold) excess of base over acid was used to determine the maximal rate of diffusion of OH⁻ across the fluid boundaries and, thus, the maximal extent of premixing in the vortex chamber. The images of the vortex chamber (diameter of 100 μm and 257 μm in length; see **Table 1** and **Fig. 2**) were recorded with the inverted microscope focused approximately halfway into the vortex chamber (see **Supplementary Fig. 3**).

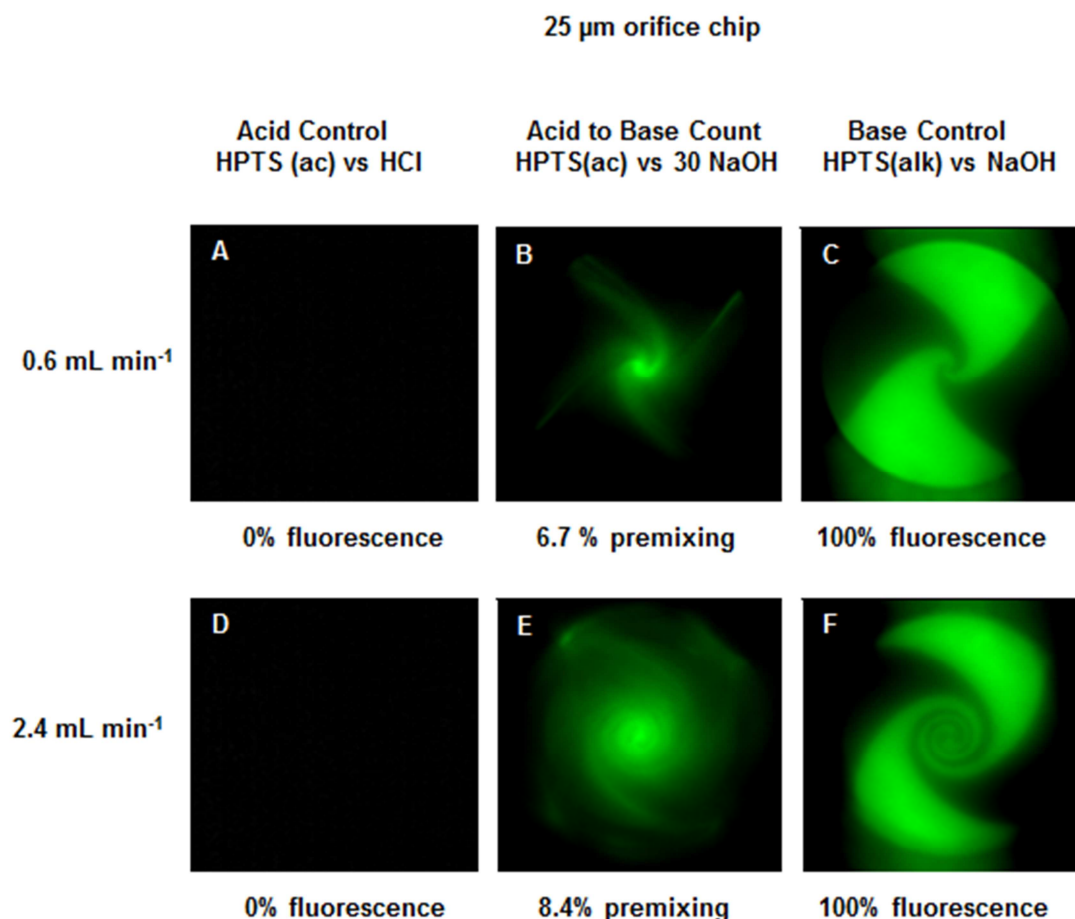


Figure 4. Determination of the amount of premixing in the vortex chamber. Fluorescence appearance due to deprotonation of HPTS was measured in the vortex chamber of the glass-silicon chip (25 μm orifice diameter) at flow rates of 0.6 mL min⁻¹ (**A-C**) and 2.4 mL min⁻¹ (**D-F**). (**A, D**) HPTS in HCl versus HCl (zero fluorescence control). (**B, E**) HPTS in HCl versus 30-fold excess NaOH. (**C, F**) HPTS in NaOH versus NaOH (100% fluorescence control). See **Supplementary Section 5** for initial and final [HCl], [NaOH] and [HPTS]. Images are 125 μm x 125 μm, the diameter of the vortex chamber is 100 μm and the microscope focus is halfway into the vortex chamber (see **Supplementary Fig. 3**).

In the very center (**Fig. 4**) or slightly off-center (**Fig. 5**), the intense fluorescence is due mainly to the mixing in the mixing chamber where the jet leaves the mixer. To determine the degree of premixing, this central fluorescence was subtracted from the total fluorescence (see **Supplementary Section 5**). The fluid flow profiles recorded for the controls (**Fig. 4C** and **F**) at low and high fluid flow rates show near irrotational and rotational flow patterns, respectively, in good agreement with calculations in Ref.²⁷. There is very little cross-boundary diffusion of the fluorescent dye. This is further confirmed in the other images of **Fig. 4**, which indicate only 6.7 to 8.4% premixing due to diffusion across the boundary. Although the mixer with a 70- μm orifice (**Fig. 5**) would require higher flow rates to produce full mixing in the mixing chamber ($\text{Re} > 2000$), the observed amount of premixing remains quite low (11.5-16.9%).

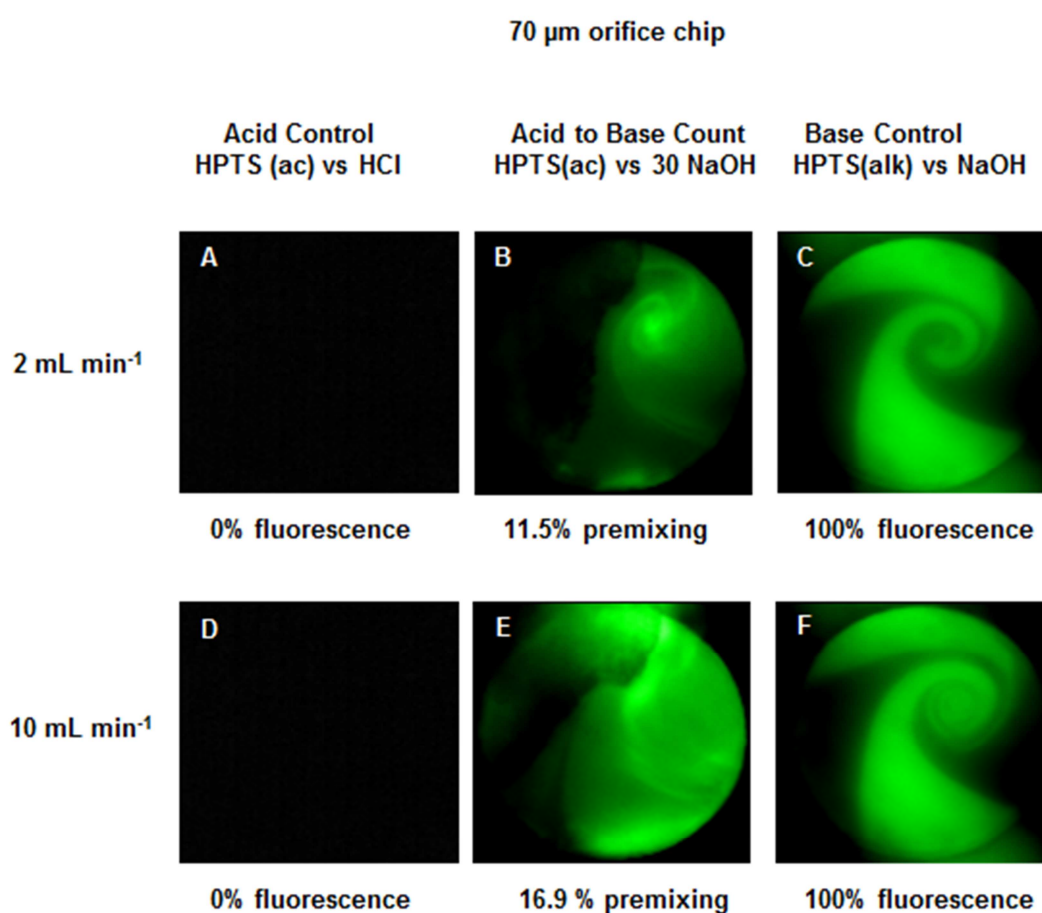


Figure 5. Determination of the amount of premixing in the vortex chamber. Fluorescence appearance due to deprotonation of HPTS was measured in the vortex chamber of the glass-silicon chip (70 μm orifice diameter) at flow rates of 2.0 mL min⁻¹ (**A-C**) and 10.0 mL min⁻¹ (**D-F**). (**A, C**) HPTS in HCl versus HCl (zero fluorescence control). (**B, E**) HPTS in HCl versus 30-fold excess NaOH. (**C, F**) HPTS in NaOH versus NaOH (100% fluorescence control). See **Supplementary Section 5** for initial and final [HCl], [NaOH] and [HPTS]. Images are 125 μm x 125 μm , the diameter of the vortex chamber is 100 μm and the microscope focus is halfway into the vortex chamber (see **Supplementary Fig. 3**).

Fig. 6 and **Supplementary Table 1** summarize the premixing behavior of the four glass-silicon mixers with different dimensions of the mixing chamber (orifices of 25, 30, 50, and 70 μm); however, note that all mixers have the same dimensions of the

vortex chamber. **Fig. 6** shows that at a given flow rate, the amount of premixing is fairly independent of the orifice diameter. The calculated Re values increase in the premixing chamber from 13 to 265, and in the vortex chamber from 27 to 531, with increasing flow rates from 0.5 to 10 mL min⁻¹. The increased Re in premixing and vortex chambers could explain why the amount of premixing increases with fluid flow rate (but apparently not for the mixer with a 50- μ m orifice for reasons currently unknown; see **Fig. 6**) even though the flow is predominantly laminar. The laminar flow regime is suggested by the approximately linear relation between fluid flow rate (and thus Re) in the vortex chamber and the percentage premixing (**Fig. 6**).

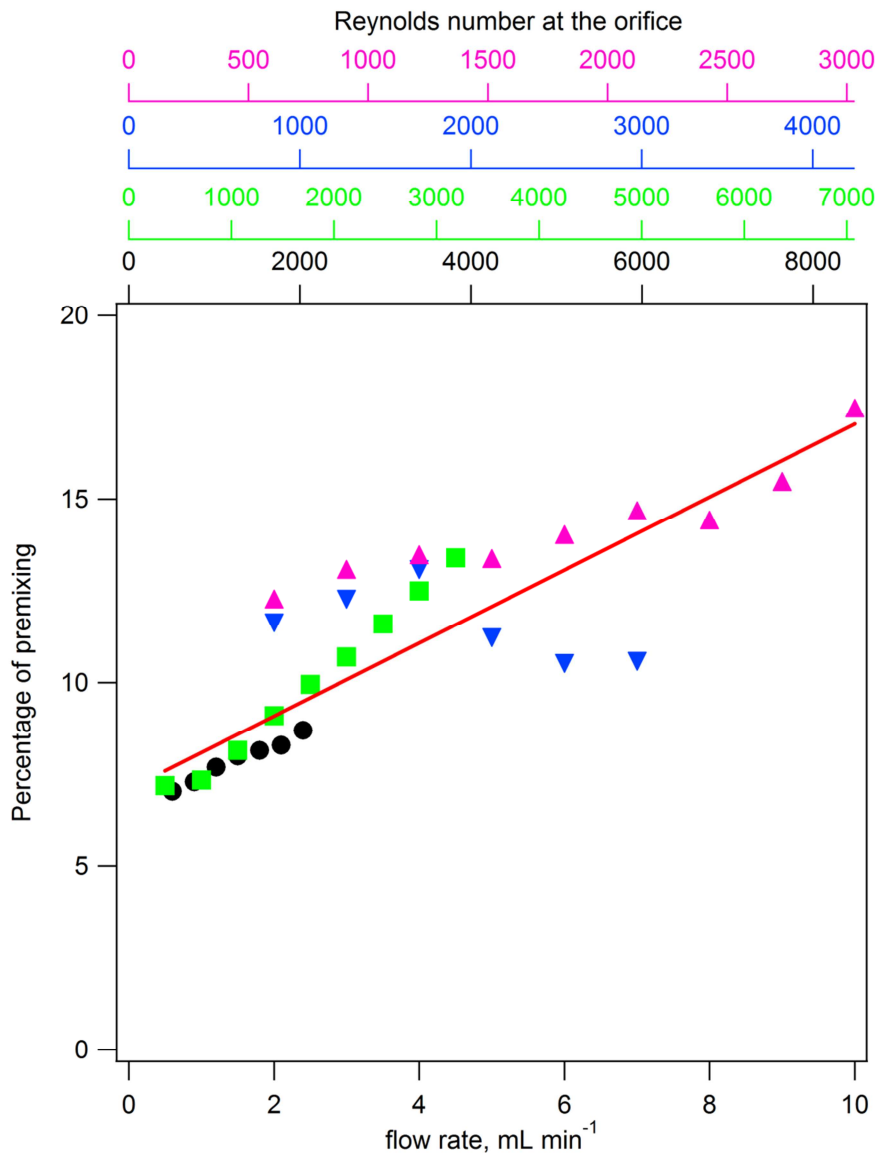


Figure 6. Percentage of premixing in the vortex chamber of the glass-silicon micro-mixers chips with orifice diameters of: 25 μ m (●); 30 μ m (■); 50 μ m (▼) and 70 μ m (▲). Experimental data of the fluorescence appearance during deprotonation of HPTS are shown as averaged values of three (two for 70 μ m) independent measurements as a function of both, flow rate and Reynolds number in the mixing chamber at the orifice, Re_{mix} . Full mixing in the orifice is at Re 1000 to 1500. The dotted straight line is a linear fit to all data points with a slope of 0.0137 (% premixing/ Re). Individual slopes are 0.0215 (25 μ m), 0.029 (30 μ m), -0.006 (50 μ m) and 0.0096 (70 μ m). Standard deviation for triplicates (duplicates) equals ± 0.04 times the measured values.

Because the geometries of the glass-silicon mixer and the stainless-steel mixer are very similar, they are expected to produce very similar mixing and premixing profiles. Thus, the onset of mixing in the glass-silicon mixers occurs at similar Re values (~ 500 - 1000 ; see **Fig. 3**) and appears complete at $Re \sim 1500$ to 2000 . **Fig. 6** indicates that at these latter Re values needed for complete mixing, the premixing amount varies from approximately 9% (for a 25- μm orifice) to 15% (for a 70- μm orifice). The low amount of premixing is a key requirement to minimize mixing dead-times.

Although the amount of premixing could not be directly determined in the stainless-steel mixer (20- μm orifice), it is possibly even lower than the approximately 9% observed for the glass-silicon mixer with the 25- μm mixing chamber (orifice) because the length of the vortex chamber is shorter (67 vs. 257 μm ; see **Fig. 1**). This implies a shorter time for diffusion of reagents across the tangential fluid boundaries and, hence, a lower degree of premixing. For the stainless-steel mixer, the shortest calculated residence time of the liquids in the vortex chamber ($V = 90$ pL, $Re \sim 417$) is 1.4 μs at the maximal flow rate of 4 ml min^{-1} ; under these same flow conditions, there is 9% or less premixing in the glass-silicon mixer (**Fig. 6**), which we assume to be true for the stainless-steel mixer in view of their similar geometries. At the flow rate of 4 ml min^{-1} , the reactants are completely mixed (**Fig. 3**), whereas the residence time in the mixing chamber of the stainless-steel mixer ($V = 10$ pL, $Re \sim 4246$) is only 160 ns. This also means that complete mixing is achieved within 160 ns. Even at flow rates of 2 ml min^{-1} ($Re \sim 2100$, where the fluids are completely mixed; see **Fig. 3**), a maximal mixing time of just approximately 310 ns is calculated with the advantage that the ambient pressure is greatly reduced (~ 4 -fold to ~ 10 MPa). Because the great majority of the glass-silicon micro-mixers were stable at pressures of 10 MPa, they can indeed be employed for large-scale production of nanosecond mixers. We further point out that the extent of premixing determined here using a pH-sensitive dye is considered an upper limit given that H^+ and OH^- diffusion constants are approximately 10 times and 5 times larger, respectively, than those of other small ions. In conclusion, the turbulent micro-mixers do completely mix liquids within 160 ns with little premixing.

Pressure buildup is a necessary consequence of the high linear fluid velocities in turbulent (micro-) mixers. The high flow rates and pressures reported here are provided by HPLC pumps that operate up to 40 MPa. The great majority of proteins are stable at these pressures⁴⁷. In our freeze-quench experiments using the same HPLC setup and stainless-steel mixer described here, we have never encountered denaturation problems and the rate constants determined at 20 to 40 MPa by us^{28,43,44,48,49} are similar to those determined by others working at ambient pressures^{5,6,8,12}. In general, oligomeric proteins start to dissociate at pressures of 100 to 200 MPa, and monomeric proteins denature at approximately four times higher pressures⁴⁷. In view of the quadratic relation between pressure and fluid flow rate (**Eq. 2**), the micro-mixers described here could be used at approximately 2-fold higher flow rates before protein denaturation sets in, potentially decreasing the mixing time to less than 100 ns.

By measuring both the premixing characteristics and mixing performance, we reason that one of the key design aspects for a micro-mixer that mixes liquids in nanoseconds

is the ABAB configuration of the four-jet tangential mixer in which the channels are offset by one-half to one channel diameter. This offset creates a vortex of four fluids that rotate around one another, which leads to a decrease in the diffusion distances and improves the mixing performance. As a result, (near) complete mixing occurs at $Re \sim 1000$ to 1500 (**Fig. 3**), which is well below the value of 2040 ± 10 for the onset of sustained turbulent flow in a pipe²⁴. Although a two-jet tangential mixer might be as efficient as a four-jet tangential mixer (**Fig. 3**), the extension to 8 or 16 tangential fluid channels leads to more or even complete premixing in the vortex chamber²⁹. This behavior is certainly suitable for lab-on-a-chip applications where a 1-ms time resolution is adequate, but not for the design of instruments with (sub)microsecond time resolution. For such devices, premixing should be prevented as much as possible. To minimize the amount of premixing, the height (or length) of the vortex chamber should be as small as possible to reduce the retention time for diffusion across the fluid boundaries. On the other hand, the diameter of the vortex chamber should be as large as possible with respect to the diameter of the mixing chamber. This will maximize the ratio of the Re values in the mixing chamber and vortex chamber and, thus, minimize premixing resulting from turbulence at the fluid boundaries. The ratio of the diameters of the mixing chamber and vortex chamber in the designs used here, three for the stainless-steel and plexiglass mixers and four for the glass-silicon mixer, yield less than 9% premixing in the vortex chamber under conditions that complete mixing occurred in the mixing chamber in nanoseconds. The future challenge is to integrate an optical cell with the micro-mixer that would allow spectroscopic observations in nanoseconds, thereby enabling study of the very onset of chemical reactions in general and of enzyme catalysis in particular.

Acknowledgments

This work was supported by NanoNed (project TAC.6380). The authors greatly acknowledge the contributions made to the designs of the plexiglass mixers by M. Langeveld (Delft University of Technology). We also are thankful to Dr. P. D. E. M. Verhaert (Delft University of Technology) for making available to us the Nikon Eclipse inverted microscope.

Appendix A. Supplementary data

Supplementary data associated with this article can be found, in the online version, at <http://dx.doi.org/10.1016/j.ab.2014.10.003> and in **Supplemental information section**.

References

1. S. de Vries†, Freeze-quench kinetics, in: R.A. Scott, C.M. Lukehart (Eds.), *Encyclopedia of Inorganic Chemistry*, John Wiley, New York, 2007, pp. 125-142.
2. S. Mitic, S. de Vries†, Rapid mixing techniques for the study of enzyme catalysis, in: E.H. Egelman (Ed.), *Comprehensive Biophysics*, Academic Press, Oxford, UK, 2012, pp. 514-532.
3. A.H. Zewail, Femtochemistry: atomic-scale dynamics of the chemical bond using ultrafast lasers [Nobel Lecture], *Angew. Chem. Int. Ed. Engl.* 39 (2000) 2586-2631.
4. R.E. Blankenship, *Molecular Mechanisms of Photosynthesis*, Blackwell, Oxford, UK, 2002.
5. P. Brissette, D.P. Ballou, V. Massey, Determination of the dead-time of a stopped-flow fluorometer, *Anal. Biochem.* 181 (1989) 234-238.
6. V.B. Borisov, E. Forte, P. Sarti, A. Giuffre, Catalytic intermediates of cytochrome bd terminal oxidase at steady-state: ferryl and oxy-ferrous species dominate, *Biochim. Biophys. Acta* 2011 (1807) 503-509.
7. M.C. Shastry, S.D. Luck, H. Roder, A continuous-flow capillary mixing method to monitor reactions on the microsecond time scale, *Biophys. J.* 74 (1998) 2714-2721.
8. H. Roder, K. Maki, H. Cheng, Early events in protein folding explored by rapid mixing methods, *Chem. Rev.* 106 (2006) 1836-1861.
9. S. Matsumoto, A. Yane, S. Nakashima, M. Hashida, M. Fujita, Y. Goto, S. Takahashi, A rapid flow mixer with 11- μ s mixing time microfabricated by a pulsed-laser ablation technique: observation of a barrier-limited collapse in cytochrome c folding, *J. Am. Chem. Soc.* 129 (2007) 3840-3841.
10. K.A. Dill, J.L. MacCallum, The protein-folding problem, 50 years on, *Science* 338 (2012) 1042-1046.
11. J. Kubelka, T.K. Chiu, D.R. Davies, W.A. Eaton, J. Hofrichter, Sub-microsecond protein folding, *J. Mol. Biol.* 359 (2006) 546-553.
12. O. Einarsdottir, C. Funatogawa, T. Soulimane, I. Szundi, Kinetic studies of the reactions of O₂ and NO with reduced *Thermus thermophilus* ba3 and bovine aa3 using photolabile carriers, *Biochim. Biophys. Acta* 2012 (1817) 672-679.
13. S.J. Chen, RNA folding: conformational statistics, folding kinetics, and ion electrostatics, *Annu. Rev. Biophys.* 37 (2008) 197-214.
14. A. Fersht, *Structure and Mechanism in Protein Science*, W. H. Freeman, New York, 1999.
15. J.N. Abelson, M.I. Simon, G. Marriott (Eds.), *Methods in Enzymology*, Vol. 291: Caged compounds, Academic Press, San Diego, 1998.
16. H.B. Gray, J.R. Winkler, Photoinduced electron transfer in ruthenium-modified cytochrome c, *Pure Appl. Chem.* 64 (1992) 1257-1262.
17. H. Hartridge, F.J.W. Roughton, A method of measuring the velocity of very rapid chemical reactions, *Proc. R. Soc. London A* 104 (1923) 376-394.
18. H. Hartridge, F.J.W. Roughton, Improvements in the apparatus for measuring the velocity of very rapid chemical reactions (part II), *Proc. Camb. Phil. Soc.* 23 (1927) 450-460.
19. B. Chance, The accelerated flow method for rapid reactions, *J. Franklin Inst.* 229 (1940) 737-766.
20. P. Regenfuss, R.M. Clegg, M.J. Fulwyler, F.J. Barrantes, T.M. Jovin, Mixing liquids in microseconds, *Rev. Sci. Instrum.* 56 (1985) 283-290.
21. Z.K. Majumdar, J.D.B. Sutin, R.M. Clegg, Microfabricated continuous-flow, turbulent, microsecond mixer, *Rev. Sci. Instrum.* 76 (2005) 1-11.
22. S.Y. Jin, Y.Z. Liu, W.Z. Wang, Z.M. Cao, H.S. Koyama, Numerical evaluation of two-fluid mixing in a swirl micro-mixer, *J. Hydrodynam. B* 18 (2006) 542-546.
23. T.T. Veenstra, T.S.J. Lammerink, M.C. Elwenspoek, A. van den Berg, Characterization method for a new diffusion mixer applicable in micro flow injection analysis systems, *J. Micromech. Microeng.* 9 (1999) 199-202.

24. C.H. Lin, C.H. Tsai, L.M. Fu, A rapid three-dimensional vortex micro-mixer utilizing self-rotation effects under low Reynolds number conditions, *J. Micromech. Microeng.* 15 (2005) 935-943.
25. K.E. Herold, A. Rasooly (Eds.), *Lab on a Chip Technology, Vol. 1: Fabrication and Microfluidics*, Caister Academic Press, Norfolk, UK, 2009.
26. A. van den Berg, T.S.J. Lammerink, *Microsystem technology*, in: A. Mans, H. Becker (Eds.), *Chemistry and Life Science, Vol. 194*, Springer, Berlin, 1998, pp. 21-49.
27. K. Avila, D. Moxey, A. de Lozar, M. Avila, D. Barkley, B. Hof, The onset of turbulence in pipe flow, *Science* 333 (2011) 192-196.
28. A.V. Cherepanov, S. de Vries†, Microsecond freeze-hyperquenching: development of a new ultrafast micro-mixing and sampling technology and application to enzyme catalysis, *Biochim. Biophys. Acta* 1656 (2004) 1-31.
29. A.A.S. Bhagat, E.T.K. Peterson, I. Papautsky, A passive planar micro-mixer with obstructions for mixing at low Reynolds numbers, *J. Micromech. Microeng.* 17 (2007) 1017-1024.
30. J.J. Chen, C.H. Chen, Investigation of swirling flows in mixing chambers, *Model. Simul. Eng.* 2011 (2011) 1-15.
31. R.H. Liu, M.A. Stremmer, K.V. Sharp, M.G. Olsen, J.G. Santiago, R.J. Adrian, H. Aref, D.J. Beebe, Passive mixing in a three-dimensional serpentine microchannel, *J. Microelectromech. Syst.* 9 (2000) 190-197.
32. S. Bohm, K. Greiner, S. de Vries†, A. van den Berg, A rapid vortex micro-mixer for studying high-speed chemical reactions, in: J.M. Ramsey, A. van den Berg (Eds.), *Micro Total Analysis System*, Kluwer, Dordrecht, Netherlands, 2001, pp. 25-27.
33. M. Kakuta, P. Hinsmann, A. Manz, B. Lendl, Time-resolved Fourier transform infrared spectrometry using a microfabricated continuous flow mixer: application to protein conformation study using the example of ubiquitin, *Lab Chip* 3 (2003) 82-85.
34. W. Ehrfeld, K. Golbig, V. Hessel, H. Lowe, T. Richter, Characterization of mixing in micro-mixers by a test reaction: single mixing units and mixer arrays, *Ind. Eng. Chem. Res.* 38 (1999) 1075-1082.
35. R. Masuch, D.A. Moss, Stopped flow apparatus for time-resolved Fourier transform infrared difference spectroscopy of biological macromolecules in H₂O, *Appl. Spectrosc.* 57 (2003) 1407-1418.
36. D.E. Hertzog, B. Ivorra, B. Mohammadi, O. Bakajin, J.G. Santiago, Optimization of a microfluidic mixer for studying protein folding kinetics, *Anal. Chem.* 78 (2006) 4299-4306.
37. D.E. Hertzog, X. Michalet, M. Jäger, X. Kong, J.G. Santiago, S. Weiss, O. Bakajin, Femtomole mixer for microsecond kinetic studies of protein folding, *Anal. Chem.* 76 (2004) 7169-7178.
38. J.B. Knight, A. Vishwanath, J.P. Brody, R.H. Austin, Hydrodynamic focusing on a silicon chip: mixing nanoliters in microseconds, *Phys. Rev. Lett.* 80 (1998) 3863-3866.
39. S. Yao, O. Bakajin, Improvements in mixing time and mixing uniformity in devices designed for studies of protein folding kinetics, *Anal. Chem.* 79 (2007) 5753-5759.
40. S.A. Pabit, S.J. Hagen, Laminar-flow fluid mixer for fast fluorescence kinetics studies, *Biophys. J.* 83 (2002) 2872-2878.
41. Y. Gambin, C. Simonnet, V. VanDelinder, A. Deniz, A. Groisman, Ultrafast microfluidic mixer with three-dimensional flow focusing for studies of biochemical kinetics, *Lab Chip* 10 (2010) 598-609.
42. S.A. Waldauer, L. Wu, S. Yao, O. Bakajin, L.J. Lapidus, Microfluidic mixers for studying protein folding, *J. Vis. Exp.* 62 (2012) e3976, <http://dx.doi.org/10.3791/3976>.
43. F.G.M. Wiertz, *Electron transfer and proton pumping pathways in cytochrome aa3* (PhD thesis), Delft University of Technology, 2007.
44. F.G. Wiertz, O.M. Richter, B. Ludwig, S. de Vries†, Kinetic resolution of a tryptophan-radical intermediate in the reaction cycle of *Paracoccus denitrificans* cytochrome c oxidase, *J. Biol. Chem.* 282 (2007) 31580-31591.
45. E.T. Carlen, J.G. Bomer, J.W. van Nieuwkastele, A. van den Berg, Silicon and glass micromachining, in: K.E. Herold, A. Rasooly (Eds.), *Lab on a Chip Technology, Vol. 1: Fabrication and Microfluidics*, Caister Academic Press, Norfolk, UK, 2009, pp. 83-114.
46. D.P. Ballou, G.A. Palmer, Practical rapid quenching instrument for the study of reaction mechanisms by electron paramagnetic resonance spectroscopy, *Anal. Chem.* 46 (1974) 1248-1253.

47. V.V. Mozhaev, K. Heremans, J. Frank, P. Masson, C. Balny, High pressure effects on protein structure and function, *Proteins* 24 (1996) 81-91.
48. K.A. Sam, M.J.F. Strampraad, S. de Vries†, S.J. Ferguson, Very early reaction intermediates detected by microsecond time scale kinetics of cytochrome cd1-catalyzed reduction of nitrite, *J. Biol. Chem.* 283 (2008) 27403-27409.
49. A. Paulus, S.H.G. Rossius, M. Dijk, S. de Vries†, An oxoferryl-porphyrin radical catalytic intermediate in cytochrome bd oxidases protects cells from the formation of reactive oxygen species, *J. Biol. Chem.* 287 (2012) 8830-8838

Supplemental Information

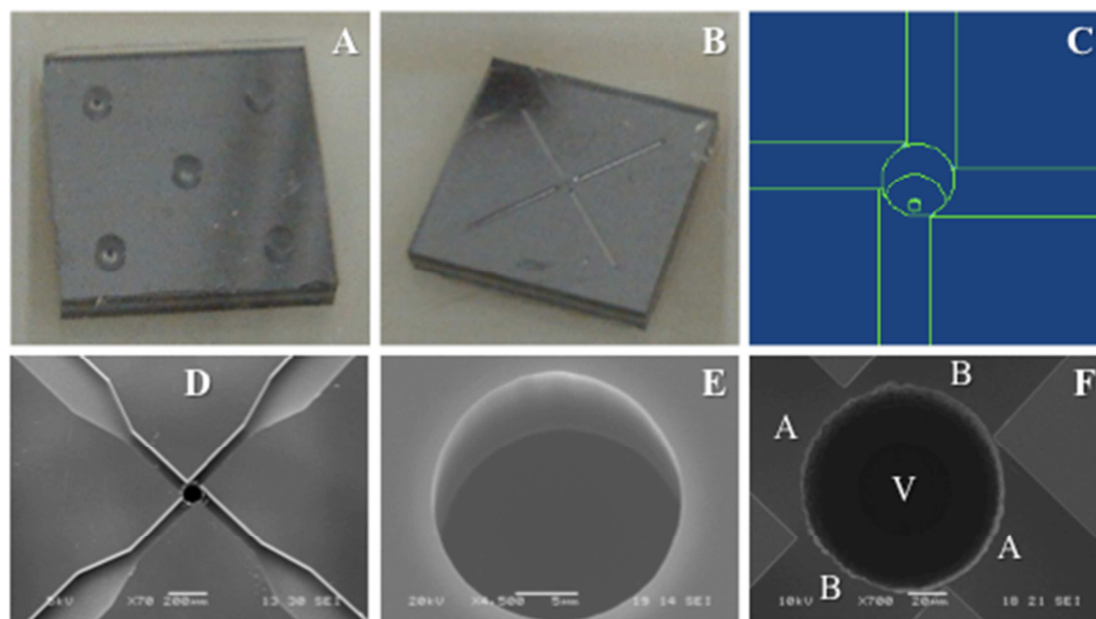
Contents

1) **Section SI 1** shows images of the chips. **Section SI 2** describes the design of the high-pressure glass-silicon chip holder, **Section SI 3** recording of fluid flow and jet flow using the fluorescent dye pyranine, **Section SI 4** shows the relation between pressure and flow rate and the analyses of the data to calculate mixing performance are described in **Section SI 5**.

2) **Sections SI 1-SI 4** contain **Supplementary Figs. 1-4**

3) **Supplementary Table 1**

4) **References**

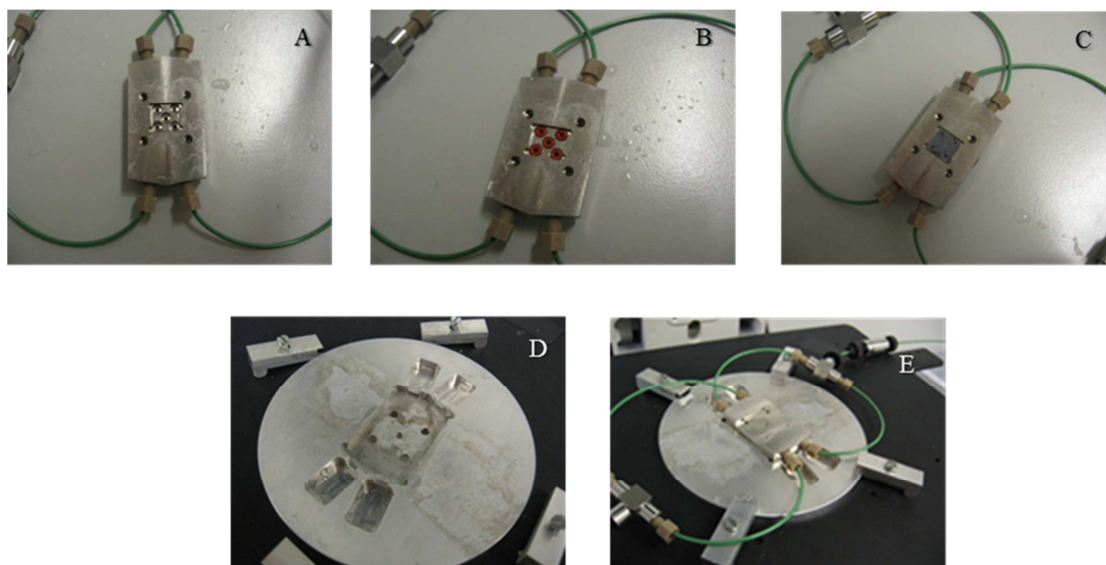
SI 1: Images of the chips

Supplementary Figure 1. Photographic images (**A**, **B**), schematic drawing (**C**) and Scanning Electron Microscope (SEM, **D-F**) images of the four-jet tangential ABAB glass-silicon micro-mixer chip. (**A**) The four inlet holes and the central outlet hole in silicon. (**B**) Bottom view of **A**, covered by a glass slide, showing four inlet holes and four inlet channels forming the premixing chamber, the latter schematically depicted in **C**. (**D**) SEM image of **B**. (**E**) the orifice (25 μm diameter) that serves as the fluid outlet channel. (**F**) The central cross section. The four ABAB inlet channels (70 μm wide, 70 μm deep) meet at the premixing chamber. The fluids flow subsequently down the vortex chamber (**V**, 100 μm diameter).

SI 2: Design of the high-pressure glass-silicon chip holder

Supplementary Fig. 2 shows a series of images as to how the glass-silicon chip is mounted into the high-pressure chip holder that can be positioned under an inverted fluorescence microscope. The stainless-steel body of the holder has four fluid inlet delivery channels at the four corners of the square chip compartment (**Supplementary Figs. 2A-C**). The central hole serves as the fluid or mixer outlet (**Supplementary Figs. 2A, B and E**). The round aluminium plate has four small rectangular recessions to hold the tubing and further a central milled compartment to clamp the body of the holder. Both the body of the chip holder and the round plate are fitted together, and secured on the plate of the inverted microscope, by four screw clamps (**Supplementary Figs. 2D and E**). To prevent solvent leak, reduce stress on the chip and prevent breaking of the chip(s) due to the high pressure in the setup, five supporting O-rings are used (**Supplementary Fig. 2B**). The viewing hole in the middle of the aluminium plate enables fluorescence measurements of the premixing and the vortex chamber (**Supplementary Fig. 2D**). To this end the high-pressure holder is positioned under an inverted fluorescence microscope (Nikon Eclipse type TE 300), equipped with an objective (CFI Plan Fluor, 40x magnification, N.A.=0.60, ELWD 2.7-3.7 mm), in such a way that the fluorescence of the HPTS dye is observed in the vortex chamber covered by the 1 mm glass slide (**Supplementary Fig. 1A**). Fluorescence was monitored using the GFP-B filter set (excitation band pass filter 460-500 nm, dichromatic mirror 505 nm and emission barrier filter 510-560 nm).

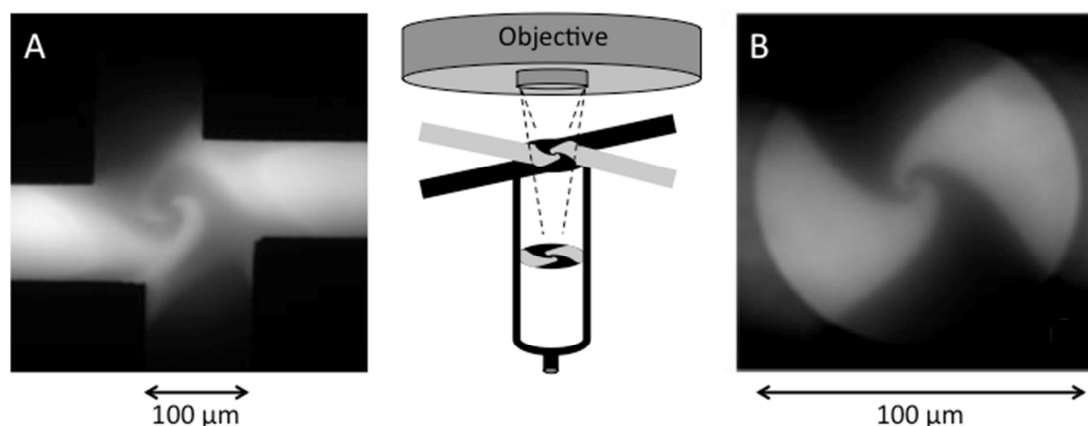
Images (**Supplementary Figs. 3, 4 and 5**) were recorded with a CCD Hamamatsu Orca C4742-95-12NRB black and white camera, 1024 x 1024 pixels, in 4 x 4 binning mode, equipped with a Nikon TV lens (0.6x magnification).



Supplementary Figure 2. Steps in mounting the glass-silicon chip onto the high-pressure chip holder positioned under the inverted fluorescence microscope. (A-C) Stainless-steel body of the chip holder equipped with (A) PEEK tubing and tubing connectors, (B) silicon O-rings and (C) the glass-silicon micro-mixer chip. (D) Round aluminium plate with cut outs for the chip and tubing connectors. (E) The glass-silicon chip [close up] mounted onto the high-pressure chip holder with four screw clamps and positioned under the inverted fluorescence microscope.

SI 3: Recording fluid flow

Images of the premixing chamber and the vortex chamber can be recorded separately with the inverted microscope focused on the premixing chamber (**Supplementary Fig. 3A**) or focused approximately halfway along the vortex chamber's length (**Supplementary Fig. 3B**). The fluorescence in the latter image (**Supplementary Fig. 3B**) is, however, that from the vortex chamber along its total length due to contributions from out-of-focus fluorescence light. Furthermore, would there be any premixing in the premixing chamber, this would show up as a light intensity above the background in the dark areas in **Supplementary Fig. 3B**. Therefore, with the focus halfway into the vortex chamber (**Figs. 4 and 5**), reliable values for total premixing (premixing in the premixing chamber, in general very small, plus premixing in the vortex chamber) could be calculated.



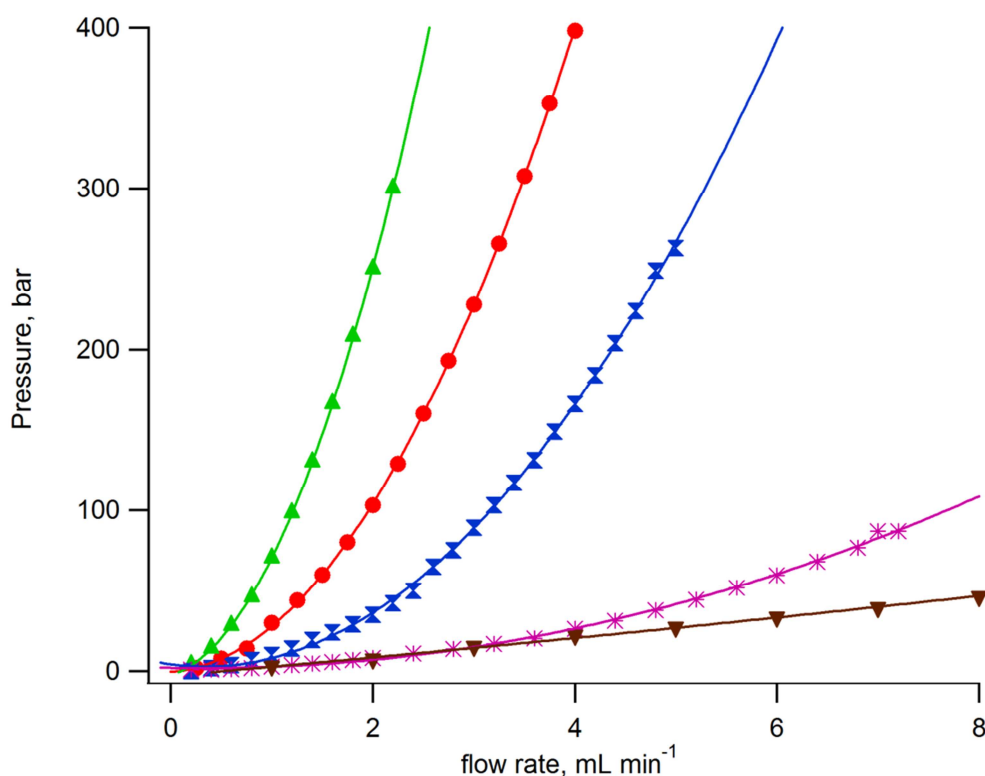
Supplementary Figure 3. Inverted Microscope images of the four-jet tangential ABAB glass-silicon micro-mixer chip (25 μm outlet hole). **(A)** The four inlet channels forming the premixing chamber (recorded with an objective of 10x magnification) with focus on the premixing chamber. **(B)** The vortex chamber (recorded with an objective of 40x magnification) with the focus halfway into the vortex chamber. The middle figure is a schematic drawing (not to scale) showing the two focal points to produce 3A and 3B. Channels A contained non-fluorescent alkaline buffer, Channels B, the same buffer plus the fluorescent HPTS.

SI 4: Relation between pressure and flow rate in the tangential stainless-steel and glass-silicon micro-mixers

Supplementary **Fig. 4** shows that with increasing flow rates the pressure in the micro-mixers increases. The pressure increase ($\Delta\Pi$) is parabolically related to the volumetric flow rate (v) according to **Supplementary Eq. 1**:

$$\Delta\Pi = a * v + b * v^2 \quad (\text{Supplementary Eq. 1})$$

In **Supplementary Eq. 1**, the linear term contains the wall friction coefficient a , and the quadratic term describes the flow through an orifice (see **Eq. 2**). The experimental values for coefficients a and b determined by fitting the experimental pressures to a parabola (**Supplementary Fig. 4**) are 3.5 and 0.2, respectively, for the glass-silicon mixer with 70 μm orifice diameter. For smaller orifice diameters, 25 μm and 20 μm , coefficients a (18.57 and 4.61) and b (54.08 and 23.83) both increase indicating a larger relative contribution by the orifice. At the maximal flow rate of 4 mL min^{-1} in the stainless-steel mixer (20 μm orifice diameter) the pressure builds up to approximately 40 MPa, while for example at the maximum flow rate of 2.2 mL min^{-1} in the glass-silicon mixer with 25 μm orifice diameter, the pressure builds up to 30 MPa.



Supplementary Figure 4. Measured (symbols) and calculated (lines) dependence between pressure and flow rate of the four-jet tangential micro-mixers. Stainless-steel mixer with 20 μm orifice diameter (—). Glass-silicon micro-mixer chip with an orifice diameter of 25 μm (—), 30 μm (—), 50 μm (—), and 70 μm (—). Lines through the data points are fitted with **Supplementary Eq. 1**.

SI 5: Data recording and data analyses

5A: Fluorescence detection in a free jet and calculation of mixing performance

Fluorescence in a free jet fluorescence was detected at an angle of 90° using a CCD camera (Andor Newton DU-940N-BU, 512 x 2048 pixels of 13.5 x 13.5 μm) covered with a long-pass 510 nm filter (ZVL0510, Optoprim Corporation, Germany). Excitation was by light of 474 nm from a Xenon arc lamp (75 Watts, Uschio) fitted to a scanning monochromator (Optical Building Blocks Corporation) that had passed an excitation GFP-B band pass filter (460-500 nm). Monochromatic light was collimated by a bi-convex lens (150 mm focal length, 50 mm diameter,) and then focused on the jet by a plano-convex lens (CSX025 UV Fused Silica Precision uncoated Cylindrical Lenses, Newport, 19 mm x 50.8 mm x 25.4 mm, width x length x focal length). Fluorescence light at 90° was collected by a second plano-convex lens (25.4 mm x 25.4 mm x 100 mm, width x length x focal length) in front of the CCD camera. The jet was imaged between 1-27.6 mm from the orifice. Every light count was recorded under identical experimental conditions, at an exposure time of 0.5 sec during which 15 images were accumulated and averaged. Images were acquired in digital form and displayed in the Andor Solis imaging program (Andor Newton CCD).

To determine the mixing efficiencies, a fast chemical reaction must be selected that is completed within the mixing dead-time of the set up. The mixing performance of the

mixers was assessed by mixing solutions of NaOH and HCl using the highly fluorescent HPTS (8-hydroxypyrene-1, 3, 6-trisulfonic acid, also known as pyranine, Invitrogen, Molecular Probes) as indicator for the pH change. The pK_a is approximately 7.3 in aqueous buffers and the protonation and deprotonation rate constants $1.8 \cdot 10^{11} \text{ M}^{-1} \text{ s}^{-1}$ and $1\text{-}2 \cdot 10^{10} \text{ M}^{-1} \text{ s}^{-1}$ (time constant of 50-100 ps), respectively^{1,2}. At the mM concentrations of HCl used first order protonation rates are between $\sim 0.25\text{-}5.5 \cdot 10^9 \text{ M}^{-1} \text{ s}^{-1}$ (time constant of $\sim 0.18\text{-}4$ ns). The control or reference images were acquired by mixing the dye in alkaline buffer with alkaline buffer presenting Base Control (100% fluorescence (I_{max})) and similarly for the Acid Control (0% fluorescence (I_{min})). To determine the percentage of mixing ($\eta_{\text{mix}\%}$) images of deprotonation and protonation of HPTS (I_{mix}) were acquired in two types of experiments: Acid to Base and Base to Acid. For the Acid to Base mixing experiment, acidic buffer (20 mM HCl + 3 mM HPTS + 30 mM NaCl) was mixed with alkaline buffer (30 mM NaOH + 50 mM NaCl) giving base/acid ratios of 1.5. Similarly, for the Base to Acid mixing experiment, alkaline buffer (20 mM NaOH + 3 mM HPTS + 30 mM NaCl) was mixed with acidic buffer (30 mM HCl + 30 mM NaCl) giving acid/base ratios of 1.5.

Since fluorescence in the jet is seen only in the Acid to Base experiment when the $[\text{OH}^-] > [\text{H}^+]$ (and the reverse for the Base to Acid experiment), mixing must be completed by at least 66.7% at the acid/base ratio of 1.5 used here. Conversely, absence of fluorescence in the jet only indicates mixing of the reactants is $< 66.7\%$. For the remaining 33.3% mixing, the fluorescence can be approximated as proportional to the fraction of the maximal fluorescence (**Supplementary Eq. 2**) since the concentration of the fluorescent dye HPTS (3 mM) is much lower than the concentration of acid + base (50 mM). The percentage of mixing ($\eta_{\text{mix}\%}$) was then calculated using the following correlation:

$$\eta_{\text{mix}\%} = 66.7 + \frac{I_{\text{mix}} - I_{\text{min}}}{I_{\text{max}} - I_{\text{min}}} \cdot 33.3 \quad (\text{Supplementary Eq. 2})$$

5B: Determination of the percentage of premixing in the four-jet tangential glass-silicon micro-mixer chip

Images of the vortex chamber of the glass-silicon chip were acquired in digital form and simultaneously displayed in the High Performance Image 32 software (Hamamatsu Orca CCD). A single series of experiments was performed at a fixed exposure time for which the light intensity was maximal for HPTS in alkaline buffer, or the reverse, minimal intensity for the dye in acidic buffer. Light counts for reference and premixing images were recorded under identical conditions at each separate flow rate, in a sequence of 20 images with 1 second intervals. The total light intensity of each recorded image was calculated by integration of the values of the pixel intensities from a corresponding .tiff image. The values of a series of 20 sequences were averaged. Controls (100% and 0% fluorescence images) were acquired as described in the experimental section. Alkaline buffer contained NaOH (10 mM), acidic buffer HCl (10 mM), and further 15 μM HPTS and 50 mM NaCl. In experiments to determine the percentage premixing (**Figs. 4 and 5**) acidic buffer (20 mM HCl + 30 μM HPTS + 50 mM NaCl) was mixed with alkaline buffer (600 mM NaOH + 50 mM NaCl) yielding a base/acid ratio of 30. The total fluorescence of the

vortex chamber contains contributions from the mixed solutions that form highly fluorescent water drops at the exit of the chip rather than a jet). To correct for this contribution, a circle at the origin of the vortex chamber with a diameter of 25 of the 100 pixels or ~6% of the area, (**Figs. 4 and 5**), was subtracted from the fluorescence count. The correction (subtraction) amounted to 16.7 %, 13.6%, 10.0% and 8.3 % of the total fluorescence for mixers with orifices of 25, 30, 50 and 70 μm , respectively. Since fluorescence in the premixing chamber is only detected when $[\text{OH}^-] > [\text{H}^+]$ fluorescence is detected from a mixing level of 3.3 % for the base/acid ratio of 30, ignoring the low concentration of HPTS (30 μM) relative to the acid + base concentrations (620 mM). **Supplementary Eq. 3** was used to calculate the percentage of premixing in **Figs. 4 and 5**.

$$\eta_{mix\%} = 3.3 + \frac{I_{mix} - I_{min}}{I_{max} - I_{min}} \cdot 96.7 \quad (\text{Supplementary Eq. 3})$$

Supplementary Table 1: Pressure dependence on the flow rate for the glass-silicon mixers with orifice diameters of 25, 30, 50 and 70 μm and for the stainless-steel mixer (20 μm). For the glass-silicon micro-mixers the amount of premixing is indicated (**Fig. 6**). The calculated Reynolds numbers for the premixing, the vortex and the mixing chambers are given (based on the dimensions in **Table 1**) as well as the fluid retention times (t_{premix} , t_{vortex} , t_{mix} , respectively). The premixing percentage could not be experimentally determined for the stainless-steel mixer (20 μm) because it is not transparent (N.A.)

orifice (μm)	V_{tot} (mL min^{-1})	Re_{premix}	Re_{vortex}	Re_{mix}	t_{premix} (μs)	t_{vortex} (μs)	t_{mix} (μs)	Premixing %	Pressure MPa
70	2.0	53	106	607	23.2	60.5	3.8	11.5	0.7
	3.0	79	159	910	15.4	40.3	2.5	12.3	1.5
	4.0	106	212	1213	11.6	30.3	1.9	12.7	2.2
	5.0	132	265	1517	9.3	24.2	1.5	12.6	2.7
	6.0	175	350	2002	7.0	18.3	1.1	13.5	3.3
	7.0	185	372	2123	6.6	17.3	1.1	13.9	3.9
	8.0	212	425	2426	5.8	15.1	1.0	14.2	4.6
	9.0	238	478	2730	5.1	13.4	0.9	14.4	5.4
	10.0	265	531	3033	4.6	12.1	0.8	16.9	6.1
50	2.0	53	106	849	23.2	60.5	1.94	11.2	0.8
	3.0	79	159	1274	15.4	40.3	1.30	12.0	1.5
	4.0	106	212	1699	11.6	30.3	1.0	12.7	2.6
	5.0	132	265	2123	9.3	24.2	0.8	11.2	4.1
	6.0	159	318	2548	7.7	20.2	0.7	10.5	6.0
	7.0	185	372	2972	6.6	17.3	0.6	10.6	8.7
30	0.5	13	27	354	92.6	242.1	2.8	7.2	0.3
	1.0	26	53	708	46.3	121.0	1.4	7.3	1.0
	1.5	40	80	1062	30.9	80.7	0.9	8.1	2.2
	2.0	53	106	1415	23.2	60.5	0.7	9.2	3.5
	2.5	66	133	1769	18.5	48.4	0.6	10.1	5.8
	3.0	79	159	2123	15.4	40.3	0.5	11.0	8.9
	3.5	93	186	2477	13.2	34.6	0.4	12.3	12.4
	4.0	106	212	2831	11.6	30.3	0.4	12.7	16.6
	4.5	119	239	3185	10.3	26.9	0.3	13.7	21.4
25	0.6	16	32	510	77.2	201.7	1.6	6.7	2.8
	0.9	24	48	764	51.5	134.5	1.1	7.0	5.8
	1.2	32	64	1019	38.6	100.9	0.8	7.5	9.8
	1.5	40	80	1274	30.9	80.7	0.7	8.1	14.8
	1.8	48	96	1529	25.7	67.2	0.5	8.2	20.8
	2.10	56	111	1783	22.1	57.6	0.5	8.3	27
	2.40	63	127	2038	19.3	50.4	0.4	8.4	36
20	0.6	31	63	636	55.0	10.0	1.1	N.A.	1.1
	0.9	47	94	955	35.5	6.4	0.71	N.A.	2.3
	1.2	63	126	1273	26.5	4.8	0.53	N.A.	4.4
	1.5	79	157	1592	21.5	3.9	0.43	N.A.	6.0
	1.8	94	189	1910	18.0	3.3	0.36	N.A.	8.5
	2.10	110	220	2228	15.1	2.7	0.3	N.A.	11.4
	2.4	126	252	2546	12.5	2.5	0.27	N.A.	14.9
	2.75	144	288	2918	11.5	2.1	0.23	N.A.	19.3
	3.0	157	315	3183	10.5	1.9	0.21	N.A.	22.8
	3.25	170	341	3448	10.0	1.8	0.20	N.A.	26.6
	3.5	183	367	3713	9.0	1.6	0.18	N.A.	30.8
	3.75	197	393	3978	8.5	1.5	0.17	N.A.	35.3
	4.0	210	420	4250	8.0	1.4	0.16	N.A.	39.8

References

1. Mojumdar SS, Mondal T, Das AK, Dey S, Bhattacharyya K (2010) Ultrafast and ultraslow proton transfer of pyranine in an ionic liquid microemulsion. *J Chem Phys* 132: 194505.
2. Spry DB, Goun A, Fayer MD (2007) Deprotonation Dynamics and Stokes Shift of Pyranine (HPTS). *J Phys Chem A* 2007, 111: 230-237.

Chapter 4

Design and characterization of a continuous flow ultra-fast mixing instrument for the study of transient (bio)chemical reactions by optical spectroscopy

Sandra Mitić and Simon de Vries†

1. Summary

A continuous flow ultra-fast mixing device has been developed with major advances in time resolution (dead-time of $3.8 \pm 0.3 \mu\text{s}$) and enabling the recording of UV-Vis spectra between 300-700 nm. The instrument employs a four-jet tangential micro-mixer that completely mixes two liquids within $3.5 \mu\text{s}$. The mixed liquids enter a high-pressure capillary flow-cell that is aligned with the long axis of a fast CCD 2048x512 chip detector. This arrangement produces one spectrum per pixel of the CCD chip and allows the simultaneous recording of ~ 1900 UV-Vis spectra in a single scan of the monochromator. In the kinetic mode of the instrument, each UV-Vis spectrum corresponds to a different reaction time that is determined by the distance between the mixer and a pixel of the CCD chip and the fluid flow rate. The reaction progress can be monitored in steps of 318 ns for approximately $600 \mu\text{s}$ at the highest flow rate. The dead-time of $3.8 \pm 0.3 \mu\text{s}$ of the mixing device was determined from the reaction between ferrocycytochrome *c* and sodium ferrihexacyanide. This newly designed ultra-fast mixing device has a 100-fold shorter mixing/observation time than the stopped-flow and is approximately 10-fold faster than current continuous-flow instruments, which, however, record optical changes at a single wavelength. This ultra-fast mixing device fills the current gap in instrumentation to study (bio)chemical reactions on the microsecond time scale and enables detailed kinetic analyses of the very onset of biocatalysis and protein folding.

2. Introduction

To study catalytic mechanisms of enzymes and chemical reactions in detail, the reaction should preferentially be initiated so rapidly that the subsequent formation and decay of all reaction intermediates can be monitored. To determine the kinetics of processes that are not driven by light, rapid mixing of two or more reactants is the most versatile and common method of initiating (bio)chemical reactions. To achieve complete mixing the majority of rapid mixing devices both rely on optimization of turbulent mixing. Turbulence is an efficient mechanism to disperse the solutions into sufficiently small volume elements, so-called turbulent eddies. The small size of the eddies enables fast diffusion of the reactants over very short distances and constitutes the final step in mixing. Mixers of various designs that enable efficient turbulent mixing have been constructed over the years and range from simple T- or Y- mixers to more complex geometries, such as multiple-jet tangential mixers, the co-axial type micro-mixers and the Berger ball mixer¹⁻²¹. The mixers might be integrated with an observation cell as in stopped-flow (SF) and continuous-flow (CF) instruments, allowing monitoring of the reaction by a great variety of spectroscopic methods²². While the SF instrument is relatively easy to construct, has a favourable sample economy and wide dynamic time range, the instrumental dead-time of ~ 1 ms is often too long to accurately determine events during the very onset of biocatalytic reactions or of protein folding and compares unfavourably with that of CF instruments (~ 50 μ s)^{5-7,15,17,23-25}. The total dead-time of a mixing device in which kinetic changes are monitored by e.g. optical spectroscopy is determined by the mixing time, the residence time of the mixed reactants in the dead volume, i.e. the volume between the point of mixing and area of observation, and finally by the time required to fill the observation chamber. Both the mixing time and residence time decrease with increasing (linear) flow rates. In micro-mixers, owing to their smaller dimensions, linear flow rates need to be higher than in the larger mixers in order to obtain Reynolds numbers above $\sim >2000$ needed for turbulent mixing and rapid completion of mixing²⁶. So, a key feature to design instruments with shorter dead-times is miniaturization of both mixer and observation compartments as has been done in set ups employing a capillary micro-mixer^{5,6,15-17}. Similarly, the microsecond freeze-hyperquenching (MHQ) instrument has been designed in which the use of a stainless-steel micro-mixer enabling very high flow rates has led to an improvement of the freeze-quenching dead-time from ~ 5 ms in 'classical' instruments^{1,4,27-33} to ~ 75 μ s^{2,21,34,35}. Miniaturization itself, the small observation compartments and the high pressures caused by the high fluid flow rates present design challenges in the fields of accurate micro-machining and instrumental sensitivity. Below we describe the design and performance of a continuous flow ultra-fast mixing device that is tightly fitted to a small high-pressure capillary optical cuvette. The instrument has a dead-time of 3.8 ± 0.3 μ s and produces good quality optical spectra enabling the study of very short-lived enzyme intermediates.

3. Results

3.1 Overview of the setup

The continuous-flow ultra-fast mixing setup (**Fig. 1**) is a home built ultra-fast mixing device that uses the same type of stainless-steel micro-mixer and reactant delivery

system (HPLC pumps) as the microsecond freeze-hyperquenching (MHQ) set up². The observation chamber is a long cylindrical cuvette - capillary flow-cell - integrated in the cuvette holder. Both micro-mixer and cuvette holder are fitted together via a *Pt* or *Cu* seal that is precisely positioned at their interface to prevent solvent leaks and joint together by four long screws to withstand pressures up to ~400 bar. The micro-mixer and cuvette holder are mounted on two independently adjustable three-axes manipulators enabling their alignment in the light path between the monochromator and the CCD camera. The CCD camera, the manipulators, the lens and the mixer-cuvette unit are all housed in a lightproof black box.

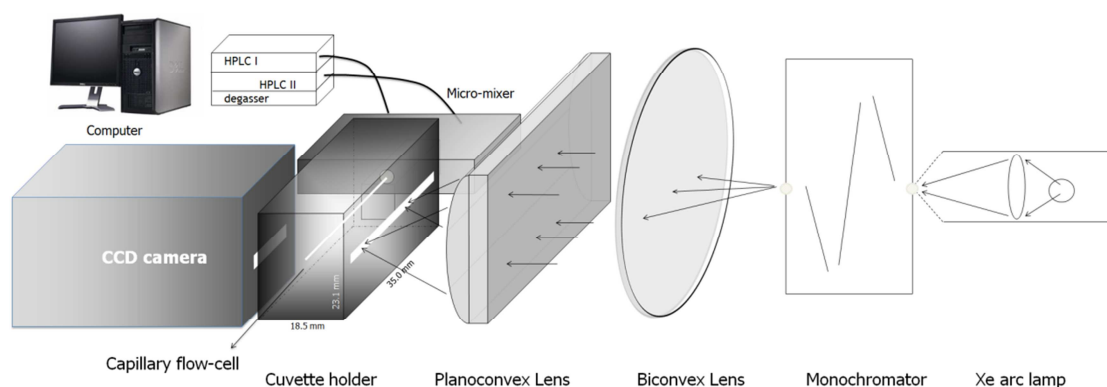


Figure 1. Schematic drawing of the continuous-flow ultra-fast mixing device integrated with the components of the UV-Vis spectrometer. Monochromatic light is produced by a horizontally placed Xenon arc lamp, fitted to a scanning monochromator. Light that is collimated by a bi-convex lens is next focused by a plano-convex lens on a slit (not shown) mounted on the plexiglass cuvette holder that contains a cylindrical capillary flow-cell that acts as the cuvette. Detection is by a CCD camera positioned directly behind the cuvette holder. The CCD camera and the scanning motor of the monochromator are synchronized by the computer. Reactants are delivered via the injection ports of two HPLC pump to the stainless-steel micro-mixer, and finally to the fused-silica flow-cell. The two three-axes manipulators to outline the various components, lens holders and the lightproof black box are omitted from the figure. The various components are not drawn to scale.

3.2 Optical components

From the optical point of view, the setup in **Fig. 1** is a scanning UV-Vis spectrometer, but instead of a rectangular cuvette it employs a 35 mm long cylindrical fused silica cuvette (100 μm path length) in which mixed reactants move away from the mixer at high linear flow rates. A fast CCD detector rather than a photomultiplier or photodiode is used to record spectra (**Fig. 2**). In a single run of the monochromator (e.g. 300-700 nm) approximately 2000 spectra are recorded by the CCD chip, one in each vertically binned pixel (z-axis, **Fig. 2**) thus corresponding to one spectrum per pixel on the y-axis. In the kinetic mode of the setup the different pixels along the y-axis of the CCD camera correspond to different reaction times (**Fig. 2**). The (reaction) time is determined by the distance between the mixer exit – recorded as ‘the 1st pixel’ – and a particular pixel, as well as by the (linear) flow rate of the liquid. At the highest flow rate of 20 mL min⁻¹ the time resolution equals 318 ns per pixel resulting in a total time span of approximately 600 μs . Calculation of the total reaction time further needs determination of the dead volume, which is calculated below from the reaction between ferrocyanide *c* and ferrihexacyanide (see also below **Section 8**).

The only optical components of the setup consist of a bi-convex collimating lens that collimates the divergent monochromatic light beam along the whole length of the cylindrical cuvette and a plano-convex lens that focuses light on the capillary flow-cell. To minimize scattering effects, two slits are mounted parallel to the optical cuvette, at opposite sides of the plexiglass holder and aligned with the 100 μm inner diameter of the fused-silica cylindrical cuvette. Both slits are fixed on the cuvette holder and mounted using a microscope equipped with a long working distance lens. The entrance slit has a 70 μm or 100 μm aperture, i.e. similar to the diameter of the cylindrical cuvette. The exit slit has a 0.25-0.29 mm aperture and faces the rectangular CCD chip of the CCD camera. In some arrangements an additional slit (0.25-0.29 mm aperture) is mounted on the plexiglass holder between plano-convex lens and the 70 μm or 100 μm aperture slit.

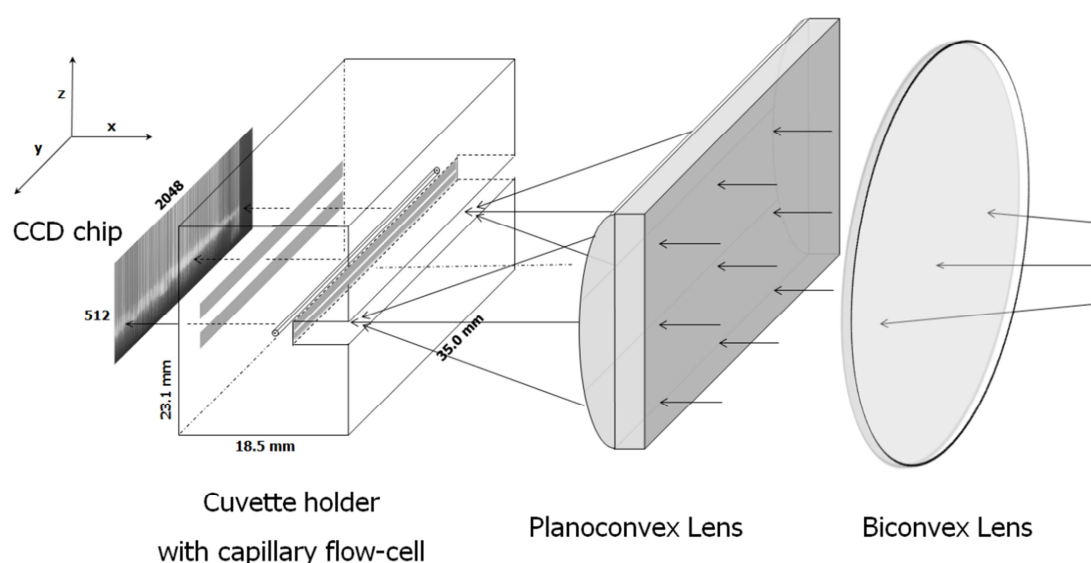


Figure 2. Schematic drawing of the lenses, the cylindrical cuvette holder and the CCD chip. Monochromatic light is collimated by a bi-convex collimating lens (150 mm focal length, 50 mm diameter) and focused on the capillary flow-cell by a plano-convex lens (100 mm focal length, 25x50 mm). The plexiglass cuvette holder is equipped with a cylindrical fused-silica cuvette (0.1 mm in inner diameter, 0.36 mm in outer diameter, 35 mm in length), and two slits: the entrance slit (0.07-0.1 mm aperture) and the exit slit (0.25 mm aperture). An additional slit (0.25 mm, not shown in the figure) may be placed between the plano-convex lens and the entrance slit. The rectangular CCD chip measures 512 pixels x 2048 pixels (height x length, each pixel being 13.5 μm x 13.5 μm). The image of the cylindrical cuvette recorded by the CCD camera in the 'Image Mode' is shown in the figure.

The optical parts of the setup such as the cylindrical cuvette, the cuvette holder and slits are micro-machined with tolerances of $\pm 5 \mu\text{m}$. In the absence of such imperfections, the CCD chip would detect only light passing through the inner diameter of the cylindrical cuvette ('sampled light', **Fig. 3**). In practice, however, imperfect machining, slight misalignments of the 70 μm or 100 μm entrance slit with the 100 μm cylindrical cuvette along the length of the cuvette and imperfect collimation may lead to uncontrollable light scattering effects (**Fig. 3**). Hence, while the optical arrangement enables light to be absorbed when passing through the solution, part of the light might bypass the solution (non-absorbed light) and/or be scattered by the round cuvette before reaching the CCD chip via the exit slit. These scattering effects are particularly visible as an apparent broadening of the capillary

flow-cell from 100 μm to 400 μm - 650 μm (30-50 vertical pixels) on the image of CCD camera (**Fig. 2**; NB: the vertical stripes on the CCD image are due to vertical streaking caused by the relatively long exposure time used for this image). Since the cuvette and the CCD chip are approximately 22 mm apart, and the image of 0.1 mm cuvette appears as 0.4 mm - 0.65 mm wide, the vertical divergence, due to light scattering from the cuvette, is approximately 0.022 (**Fig. 2**).

In order to minimize vertical divergence and to block out stray light further, only the bottom 30-50 pixels of the CCD camera (in the z-direction, **Fig. 2**) are used and accessible to light, while the rest of the CCD camera is shielded by a black cover. Data are then recorded in the so-called CROP 30 (or CROP 50) mode (and later processed by taking the average of these 30-50 pixels at each position in the y-direction), which not only speeds up the recording of data, but also selects as much as possible only the fraction of absorbed light. In spite of these measures, i.e. covering the CCD camera and a total of three slits, approximately 30% of all light reaching the CCD camera is due to stray light (see **Section 4.3**). The use of different materials (plexiglass, fused silica) might yet be another source of uncontrollable scattering effects. Given the refractive indexes of the various media light falling at angles $>66^\circ$ on the cylindrical cuvette is externally reflected (**Figs. 3** and **4**). The external reflection caused by the cylindrical shape of the cuvette and the fact that the cuvette is round rather than flat results in a reduction of the extinction coefficient (shorter mean pathway for light to be absorbed compared to a rectangular shaped cuvette) to a theoretical value of 51.4% determined by the refractive indices of the fused silica and the plexiglass (**Fig. 4**). In practice, reduction of the extinction coefficient was determined to be between 50% - 60% of the value for a rectangular cuvette.

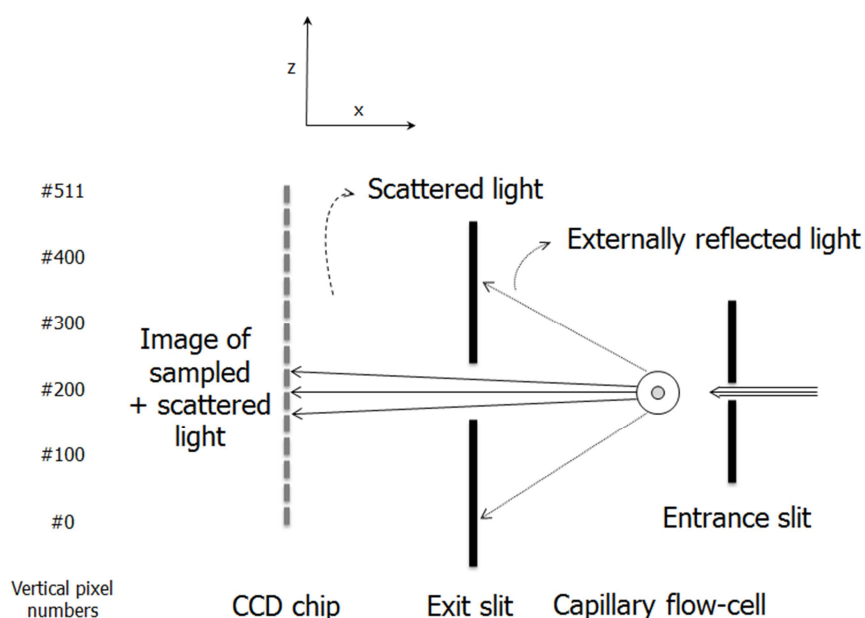


Figure 3. Side view of the optical setup highlighting the possible light paths through the cylindrical cuvette. Focused monochromatic light enters the cylindrical cuvette through the entrance slit (0.07 mm or 0.1 mm aperture has been used); at the cylindrical cuvette, part of the light is absorbed by the solution in the inner volume, another part may be scattered while light falling at angles $>66^\circ$ is externally reflected. Transmitted and scattered (non-absorbed) light passes the exit slit (0.25 mm aperture), before falling on the CCD chip producing an image as shown in **Fig. 2**.

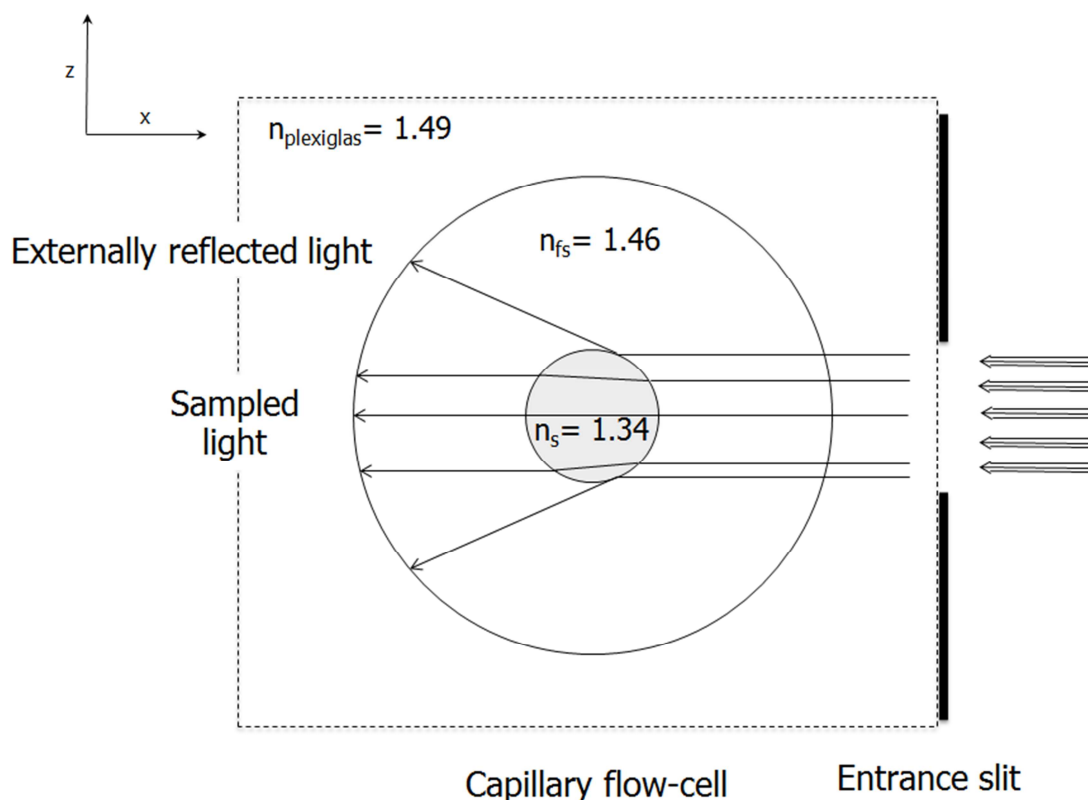


Figure 4. Enlarged side view of the light paths through different medias of the cylindrical cuvette holder. From right to left: Focused monochromatic light, entrance slit (0.07 or 0.1 mm apertures have been used), capillary flow-cell (0.1 mm in inner diameter, 0.36 mm in outer diameter), the rectangular plexiglass holder (dotted), calculated pathways of externally reflected light, sampled light. n_s , n_{fs} and $n_{plexiglass}$ are the approximate refractive indexes of the sample, fused-silica and plexiglass, respectively. Incident angles (from top to bottom) are: 66° (total external reflection angle), 30° , 0° , 30° and 45° ; the refraction angles are calculated using the refractive indexes indicated.

An important issue related to the time resolution is how well the y-axis (the time axis) is projected on the CCD chip, as the cylindrical cuvette and CCD chip are 22 mm apart. Collimation by a lens is never perfect (**Fig. 5**). With the monochromator exit slit width of 0.1 mm (the usual setting), the light intensity distribution spread approximately ± 1 pixel in the y-axis direction of the CCD chip. The peak spreading of ± 1 pixel at 0.1 or 0.2 mm slit width of the monochromator corresponds to a minimum of $\pm 0.3 \mu\text{s}$ in time at the highest possible flow rate of 20 mL min^{-1} . The divergence in the direction of the z-axis is irrelevant since the light intensity data are recorded in the so-called full vertical binning mode (FVB or CROP mode), and each column of the CCD camera is represented by a single light intensity value.

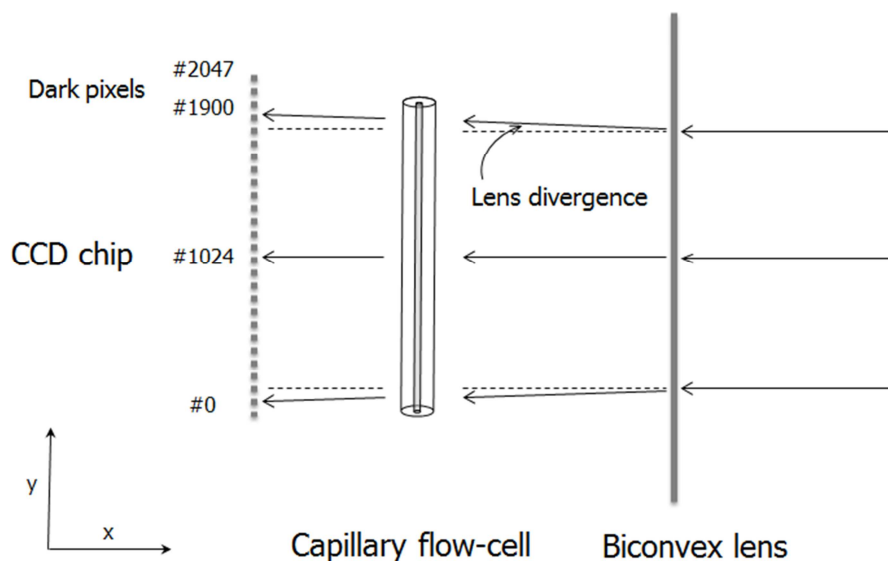


Figure 5. Top view of the light paths through the lens and the cylindrical cuvette indicating the effect of lens divergence on a collimated beam.

4. The optical performance of the UV-Vis spectrometer

4.1 Relation between absorbance and transmittance along the cylindrical flow-cell

In order to record absorbance spectra with a single beam UV-Vis spectrometer (**Fig. 1**) separate reference (I_{ref}) and sample (I_{sam}) transmission spectra are recorded and the absorbance spectrum is calculated as:

$$A = -\log \frac{I_{sam}}{I_{ref}} \quad (\text{Eq. 1})$$

Fig. 6 shows the particular transmittance profiles of reference and sample solutions in each FVB column/pixel of the CCD camera – along the whole length of the capillary flow-cell – recorded at 416 nm, the maximum of the Soret band of ferrocytochrome *c*.

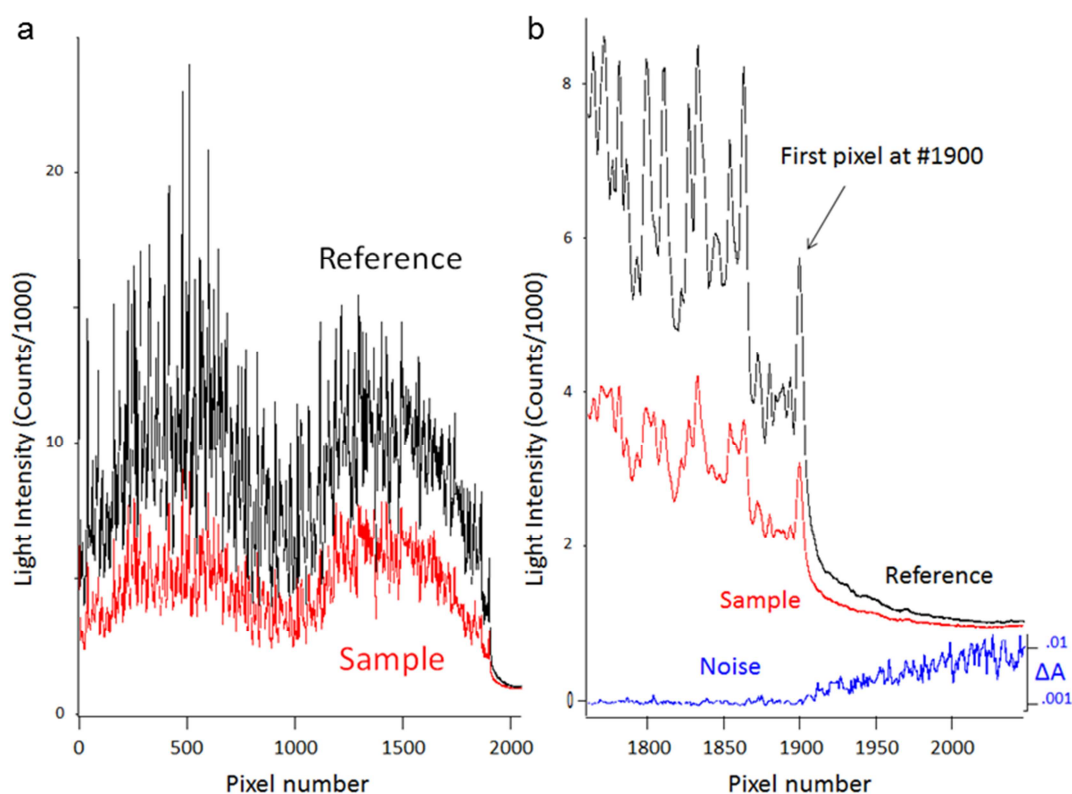


Figure 6. Non-uniform distribution of light intensity (416 nm) along the length of the cylindrical cuvette. Light intensity profiles of 20 mM phosphate buffer at pH 7.0 (—) and of 0.5 mM reduced cytochrome *c* (—) in the same buffer. (b) The blow-up of (a) highlighting the position of the first pixel, at number 1900 of the y-axis of the CCD camera. The first pixel is located at the interface of the micro-mixer and the flow-cell. Since the micro-mixer is non-transparent, the light intensity drops off sharply (by 50% in two pixels) towards the right, but not completely to zero. Pixels 1902/4–2047 are so-called dark pixels, but they nevertheless reproduce similar spectra as those observed in pixels 1900 to zero, albeit at a much higher noise due to the low light intensity (see e.g. **Fig. 8**). The increase in the noise at pixel numbers greater than 1900 from $\pm 0.001 \Delta A$ to $\sim \pm 0.01 \Delta A$ is indicated by (—) at the bottom of (b).

The light intensity along the flow-cell is seen to vary approximately threefold at 416 nm and similarly at other wavelengths (not shown). Both the reference and the sample display similar light intensity patterns, but the intensity of the latter is lower due to absorbance by ferrocyanochrome *c*. Since the law of Lambert-Beer predicts that the absorbance is independent of the light intensity (but the signal to noise ratio is not), and because Absorbance is proportional to $\log(I_{sam}/I_{ref})$, similar intensities in each pixel for the absorbance spectra are expected. **Fig. 7** shows that, contrast to expectation, the absorbance intensity (A416 and A551, the maxima of the Soret- and α -band of ferrocyanochrome *c*, respectively) also varies along the flow-cell though to a smaller extent (~ 1.5 fold) than the light intensity, while the ratio A416/A551 is more constant (variation is ~ 1.25 fold). The variation in absorbance is ascribed to small imperfections in the micro-machined 70 μm or 100 μm slit and to slight misalignments of this slit with the capillary flow-cell along its length (35 mm). Together this leads to differences in the proportion of absorbed versus non-absorbed light and hence to local (i.e. per pixel) differences in scatter (cf. **Figs. 3** and **4**). The variation in absorbance appeared to be constant for a particular alignment of the slits in respect to the flow-cell and for the position of the flow-cell plus slits in respect to

the light beam. Thus in practice the apparent differences in the absorbance can be calibrated in a manner to (re)produce the same intensity ($\pm 1\%$) in each pixel, which is sufficiently accurate to analyze kinetic data.

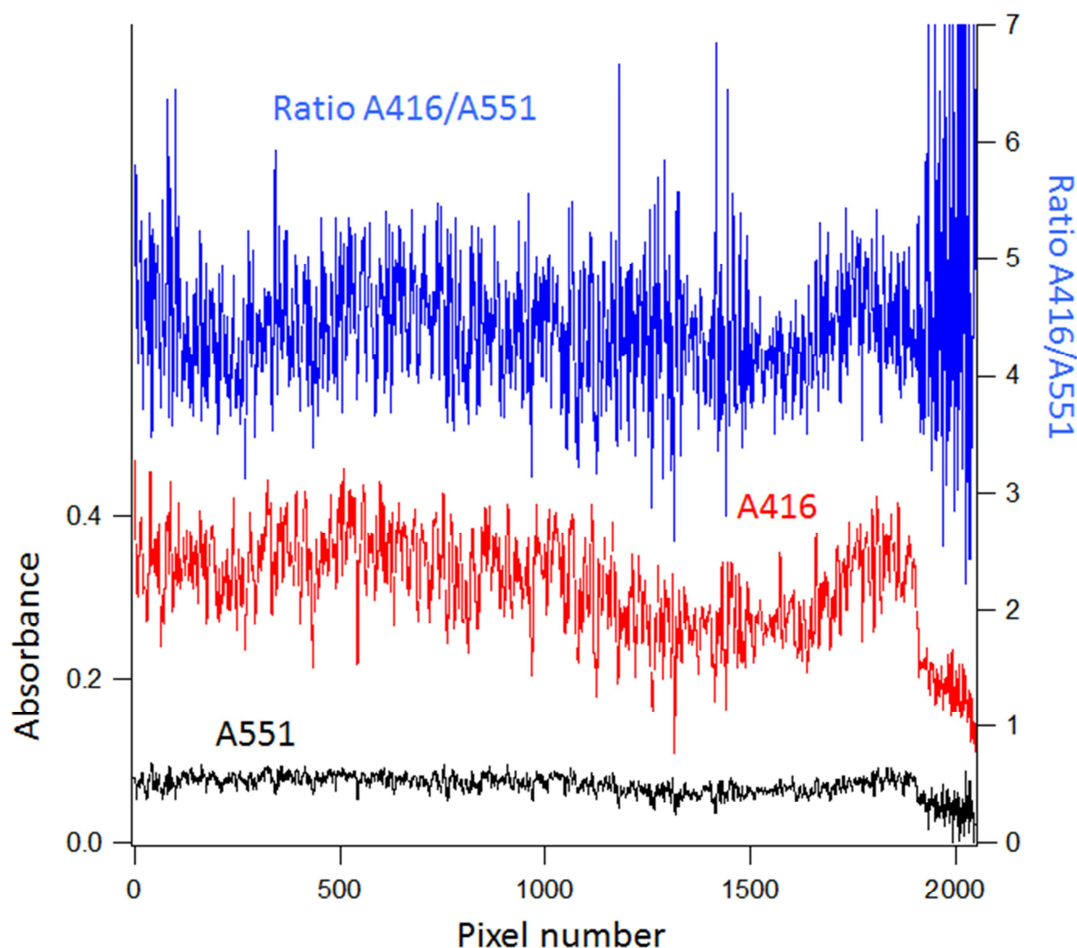


Figure 7. Non-uniform distribution of the absorbance at 416 nm (—) and 551 nm (—), and the ratio between these absorbances (—) along the length of the cylindrical cuvette. Cytochrome *c* concentration and recording is as in **Fig. 8**. Note the increase in absorbance (A416 and A551) at pixel #1900.

The sharp interface between the transparent flow-cell and the non-transparent micro-mixer is geometrically well defined (see also below **Section 6**). This interface is routinely positioned at pixel #1900 of the CCD camera (**Fig. 6b** and **Fig. 7**). To the right (pixel numbers >1900) the light intensity drops off sharply (50% in two pixels) because here the micro-mixer covers the CCD camera ‘dark pixels’. However, the light intensity does not drop to zero, and spectra are produced albeit at a much poorer signal to noise ratio (**Fig. 8**).

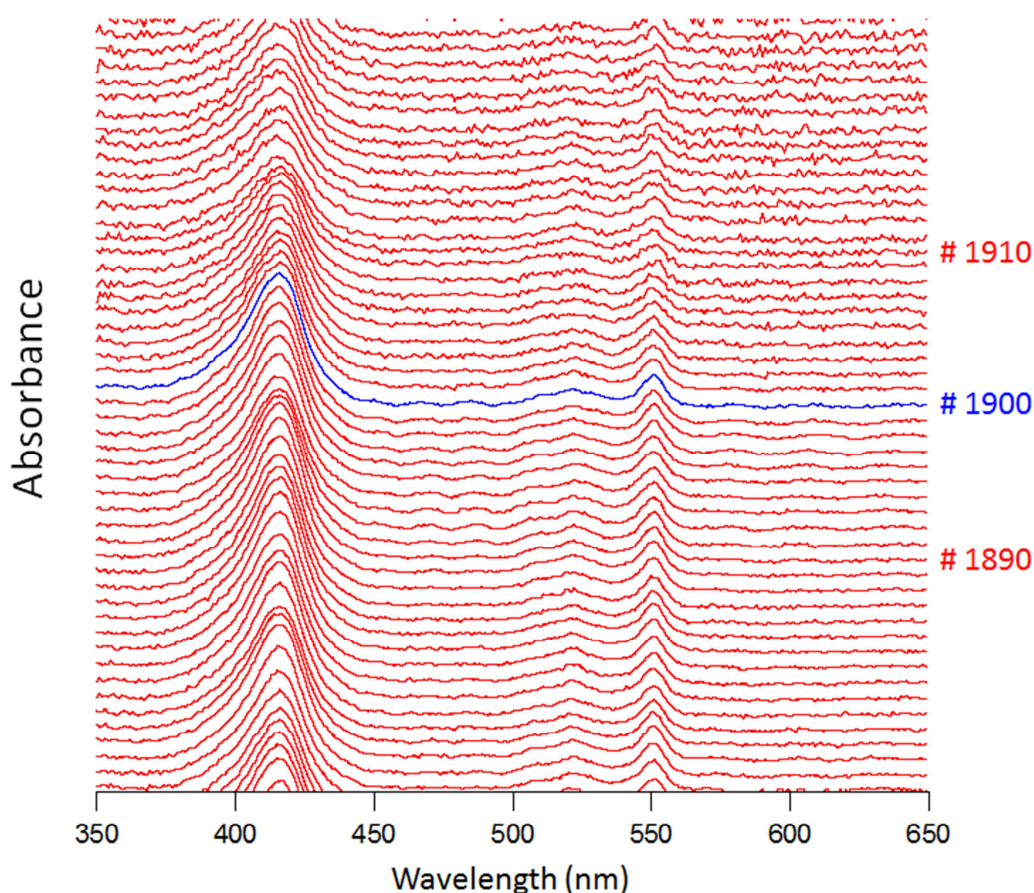


Figure 8. Absorbance spectra of ferrocyanochrome *c* (0.5 mM in 20 mM phosphate buffer pH 7.0) in individual pixels, along the capillary flow-cell, i.e. at 13.5 μm intervals - the size of a pixel of the CCD camera. BSA (10 mg ml^{-1}) in 50 mM phosphate buffer pH 7.0 served as a reference solution. Spectra were recorded at 50 nm s^{-1} with monochromator entry and exit slits at 1.0 and 0.2 mm, respectively.

The light falling on the ‘dark pixels’ has thus passed the sample solution in the capillary flow-cell, and could not be blocked by e.g. putting additional black shields around the cuvette holder. We presume that this light is reflected back and forth between the window of the CCD chip and the flow-cell. The absorbance profile (**Fig. 7**, traces A416 and A551) shows a sharp increase between pixels 1904 and 1900 (**Fig. 8**). The increase in noise is clearly visible in the ‘dark pixels’ (>1900). For kinetic measurements, it is important to know where precisely the flow-cell begins, since it is the ‘time zero’ for observation; to this ‘time zero’ the dead-time for mixing and filling the mixing chamber must be added (see **Section 8**) to obtain the total instrumental dead-time. The data in **Figs. 7** and **8** suggest that the spectra in pixels 1900-1902 represent the boundary between flow-cell and mixer and hence correspond to the first observable kinetic data points.

The (high frequency) noise in the spectra of a single pixel is approximately $\pm 0.001 \Delta A$, under the conditions of recording (a single scan at 50 nm sec^{-1} , 18.4 ms illumination time per nm, monochromator entry and exit slits at 1.0 mm and 0.2 mm, respectively). The noise is determined mainly by instabilities of the arc of the Xenon lamp and for only 10% - 15% by shot noise from the CCD camera. Once the setup has been outlined, the light intensity distribution along the flow-cell remains stable for

several hours, long enough to perform a series of kinetic measurements. The signal to noise ratios are for most pixels >50 , sufficient to perform biochemical and kinetic analyses. The volume of a single pixel corresponds to only 0.1 nL and the amount of cytochrome *c* (at 0.5 mM) to 53.0 femtomol underscoring the sensitivity of this spectrometer.

4.2 Recording absorbance spectra

The general practice to record absorbance spectra with a single beam UV-Vis spectrometer (**Fig. 1**) is to use pure buffer as the reference solution. The sample solution is then prepared by adding a dry powder or a small volume of a concentrated sample (e.g. protein) solution to the reference solution. In the UV-Vis spectrometer designed here this simple protocol failed to yield reproducible absorbance spectra (**Fig. 9a**). Sinus-like periodic absorbance signals appear at various wavelengths some of which with similar intensities as the true peaks of metmyoglobin.

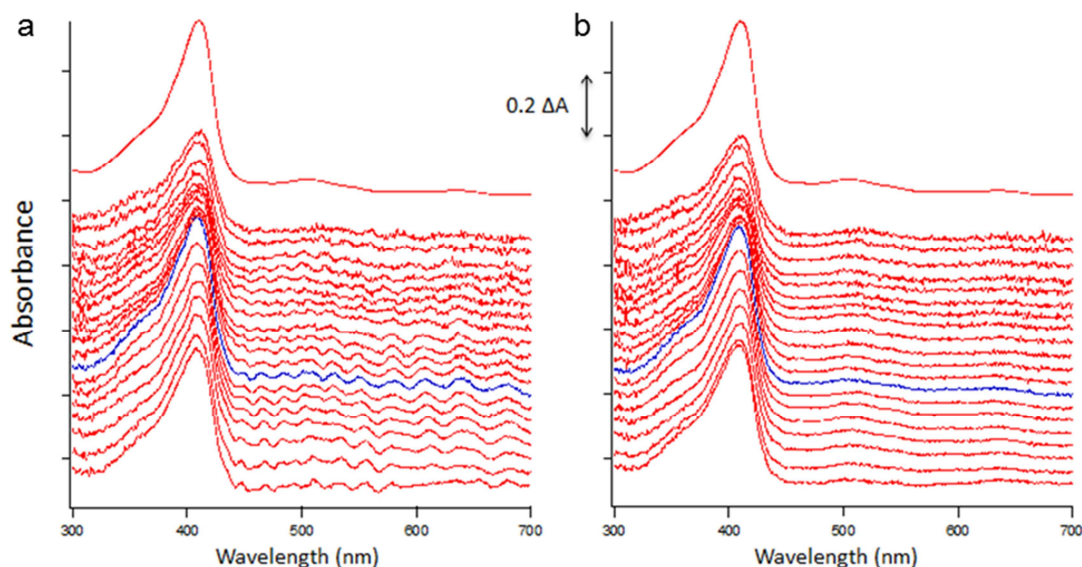


Figure 9. Absorbance spectra of 0.94 mM metmyoglobin in 20 mM potassium phosphate (pH 7.0) recorded in different pixels, i.e. at different positions along the capillary flow-cell. (—) The spectrum in pixel #1900 is approximately the first time point in kinetic experiments. (a) A buffer of 20 mM potassium phosphate (pH 7.0) served as the reference solution. (b) A buffer of 20 mM potassium phosphate (pH 7.0) with in addition 22 mg mL⁻¹ BSA served as the reference solution.

This sinus-like pattern was slightly different in each pixel as well, thus the buffer appeared not to constitute a proper reference solution. The short path length of the round flow-cell (100 μ m) necessitates the use of concentrated protein solutions, approximately 100-200 more concentrated than needed for a 10 mm rectangular cuvette. As a consequence, there is a relatively large difference between the refraction indices (Δn) or solution densities ($\Delta \rho \sim 0.001$ - 0.003) between the reference and sample solutions. This causes differences in the angular distributions of absorbed and scattered light trajectories by reference and sample solutions (see e.g. **Figs. 3** and **4**) and hence the CCD camera detects different light intensities even for two colourless solutions with different refraction indices. The differences in angular distributions of light between solutions of different densities appear more prominent in this setup than in regular spectrometers owing to the small dimensions of the slits and the small size

of the pixels of the CCD camera (one pixel is 13.5 μm x 13.5 μm). The angular distribution of light intensities is described – at least qualitatively – by a Fraunhofer scattering intensity function:

$$\frac{I_{sam}}{I_{ref}} \sim \frac{\text{sinc}^2(n_{sam} \cdot \lambda)}{\text{sinc}^2\left(\frac{n_{ref} d}{\lambda}\right)} \quad (\text{Eq. 2})$$

Herein *sinc* is the hyperbolic sine function, n_{sam} and n_{ref} the refraction indices of sample and reference solutions, respectively, and λ the wavelength of the incident light. Although this function leads to the sinus-like patterns observed (**Figs. 8** and **9**), it was in practice not possible to correct UV-Vis spectra satisfactorily with this function. Therefore an experimental approach was chosen, that is to make reference solutions with the same density/refraction index as the protein solution under study. This is a (simple) matter of trial and error. **Fig. 9b** shows that with 22 mg mL⁻¹ of the colourless protein Bovine Serum Albumine (BSA) as a reference solution for 0.94 mM metmyoglobin (16.5 mg mL⁻¹) good quality optical spectra were obtained lacking the sinus-like absorbances. In order to obtain reference and sample solutions with the same refraction index the particular BSA concentration has to be determined separately for each protein under study. Once the equivalent BSA concentration has been determined at one particular concentration of the sample protein this information can be used to prepare reference BSA solutions for different concentrations of the sample protein since the refraction indices scale in the same proportional manner.

4.3 Deviations from the law of Lambert-Beer

To test the proportionality between absorbance and concentration, as expressed by the law of Lambert-Beer, absorbance spectra of reduced cytochrome *c* were recorded in the concentration range from 0.025 mM to 2 mM with the UV-Vis spectrometer. As shown in **Fig. 10**, the absorbance appears to saturate to a maximum value of approximately 0.55 ± 0.02 AU at the highest concentrations of cytochrome *c* used, a value that corresponds to 28.5% stray light. This stray light is due to light that does not pass the capillary flow-cell that contains the cytochrome *c* solution, but nevertheless reaches the CCD camera. Machining and alignment imperfections of ± 10 μm would produce $\sim 10\%$ differences in stray-light and accounts more or less quantitatively for the observed differences of the absorbance between pixels (**Figs. 6-8**). The UV-Vis spectrometer is linear up to absorbance values of approximately 0.3 AU (**Fig. 10**). Spectra appear broadened at higher absorbance values as is particularly clear for the Soret band of ferrocytochrome *c*. The good optical quality of the spectra is evidenced by the ratio of 5.41 for the Soret- and α -band maxima at non-saturating concentrations (< 0.2 mM) ferrocytochrome *c*, the ratio found also with commercial UV-Vis spectrometers.

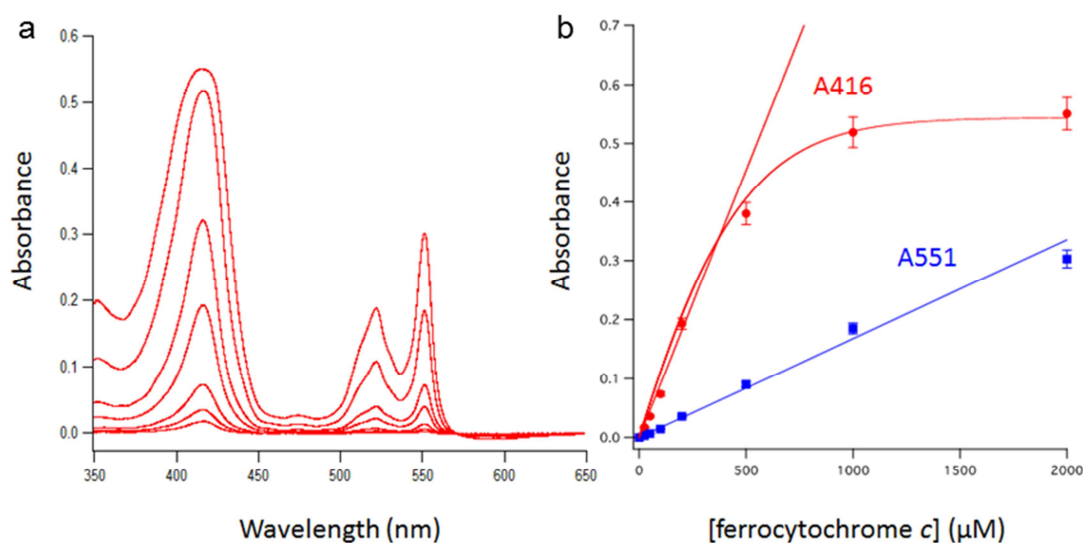


Figure 10. (a) Absorbance spectra of ferrocyanochrome *c* at various concentrations. (b) The relation between absorbance and concentration of ferrocyanochrome *c* at 416 nm (—) and 551 nm (—). The straight lines (—) are fits to the data points of the non-saturated spectra (0.2 mM). The ratio of the slopes for A416 and A551 of these lines equals 5.41, identical to the ratio of the extinction coefficients for the Soret- and α -band maxima determined in commercial UV-Vis spectrometers. Ferrocyanochrome *c* concentrations were: 0.025, 0.05, 0.1, 0.2, 0.5, 1.0 and 2.0 mM. Spectral deformations occur for absorbances >0.3 AU. The spectra are the average of the spectra recorded in pixels 0-1900, along the whole length of the flow-cell, and were put arbitrarily at zero at 630 nm.

The spectra of ferrocyanochrome *c* up to 0.20 mM (or AU 0.3) in **Fig. 10** are virtually identical to those obtained with commercial UV-Vis spectrometers using a rectangular cuvette (at concentrations below 10 μM) with the exception of the absorbance region above ~ 580 nm. The spectrum of ferrocyanochrome *c* should be flat in this region at approximately zero absorbance, but the spectrometer designed here yields a slightly curved shape. The reasons for this discrepancy are currently not understood. Control experiments with non-absorbing buffers (BSA) produced spectra with flat baselines at zero absorbance from 300 nm - 700 nm. So the effects seen with cytochrome *c* might be due to (second or higher order) grating artifacts of the monochromator.

4.4 Comparison between static absorbance spectra and spectra recorded during fluid flow

The spectra shown so far were recorded without liquid flow. For kinetic experiments the fluid in the capillary flow-cell moves at high speeds up to 40-45 m s^{-1} and at volumetric flow rate of 20 mL min^{-1} . At this high flow rate, spectra recorded under static and flow conditions appear virtually identical (**Fig. 11**).

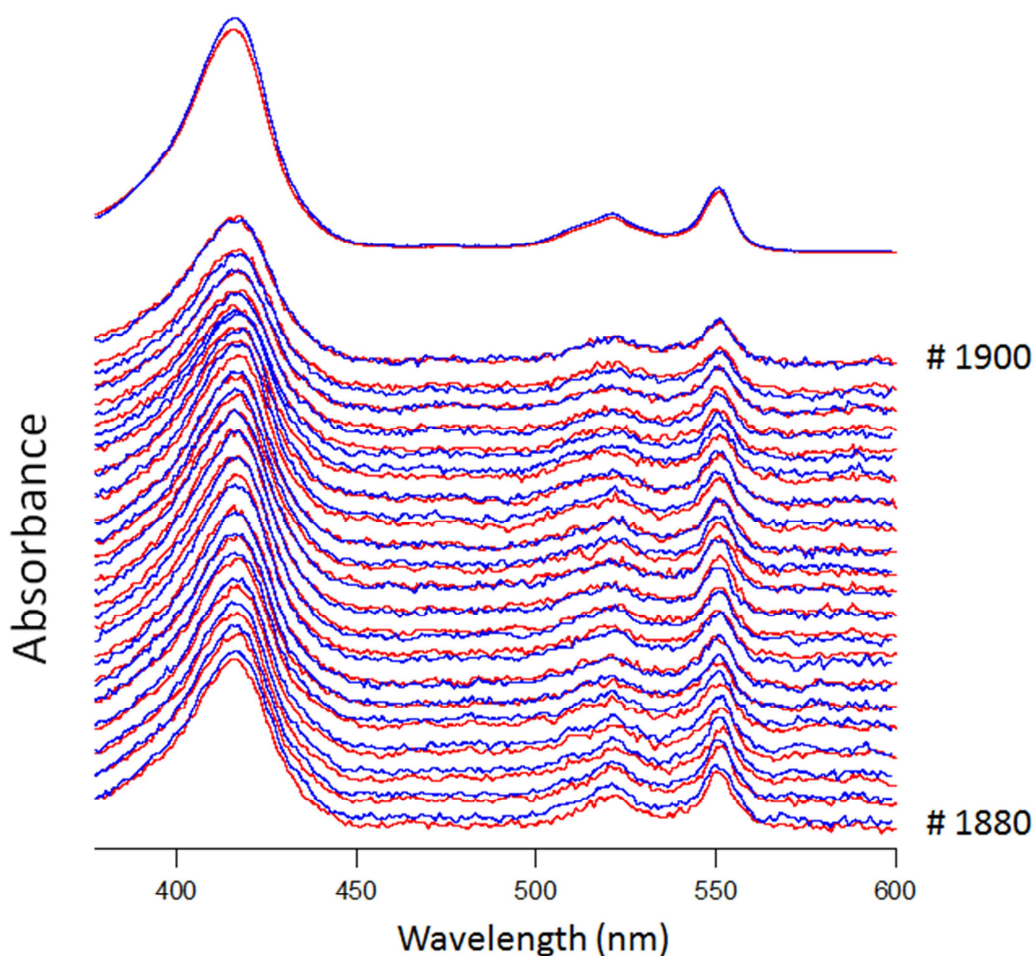


Figure 11. Absorbance spectra of ferrocyanide *c* (0.5 mM) recorded without liquid flow (—) and at a liquid flow rate of 20 mL min⁻¹ (—). The top two spectra are the average of the spectra obtained in pixels 0-1900. Spectra were recorded as in **Fig. 8**.

5. The relation between pressure and temperature and the flow rate in the continuous-flow micro-mixer

Fig. 12 shows that with increase of flow rate, both, pressure and temperature in the cylindrical cuvette increase too. The pressure increase ($\Delta\Pi$) is parabolically related to the volumetric flow rate (v) according to **Eq. 3**:

$$\Delta\Pi = a * v + b * v^2 \quad (\text{Eq. 3})$$

In **Eq. 3**, the linear term contains the wall friction coefficient a , and the quadratic term describes the flow through an orifice. Experimental values for a and b determined by fitting the experimental pressures to a parabola (**Fig. 12**) are approximately 37.01 and 8.09, respectively, indicating substantial wall friction. At the maximal flow rate of 20 mL min⁻¹ the pressure builds up to approximately 4000 PSI or 275 bar (27.5 MPa). Under these conditions, the temperature also increases to approximately 7°C higher than ambient. The increase in temperature is determined with **Eq. 4**:

$$\Delta T = \frac{0.5 \cdot \rho \cdot v^2}{c_p \cdot \rho} = \frac{\Delta \Pi}{c_p \cdot \rho} \quad (\text{Eq. 4})$$

where ρ is density of water, 1000 kg m^{-3} , v is the average flow velocity (m s^{-1}), $\Delta \Pi$ is the pressure in the cuvette (N m^{-2}) and c_p is the heat capacity of water $4186 \text{ J kg}^{-1} \text{ } ^\circ\text{C}^{-1}$.

$$\Delta T = \frac{2.85 \cdot 1010^7}{4186 \cdot 1000} = 6.8^\circ\text{C}$$

Application of **Eq. 4** yields an increase of 6.8°C at 20 mL min^{-1} in good agreement with the measurement (cf. **Fig. 12**).

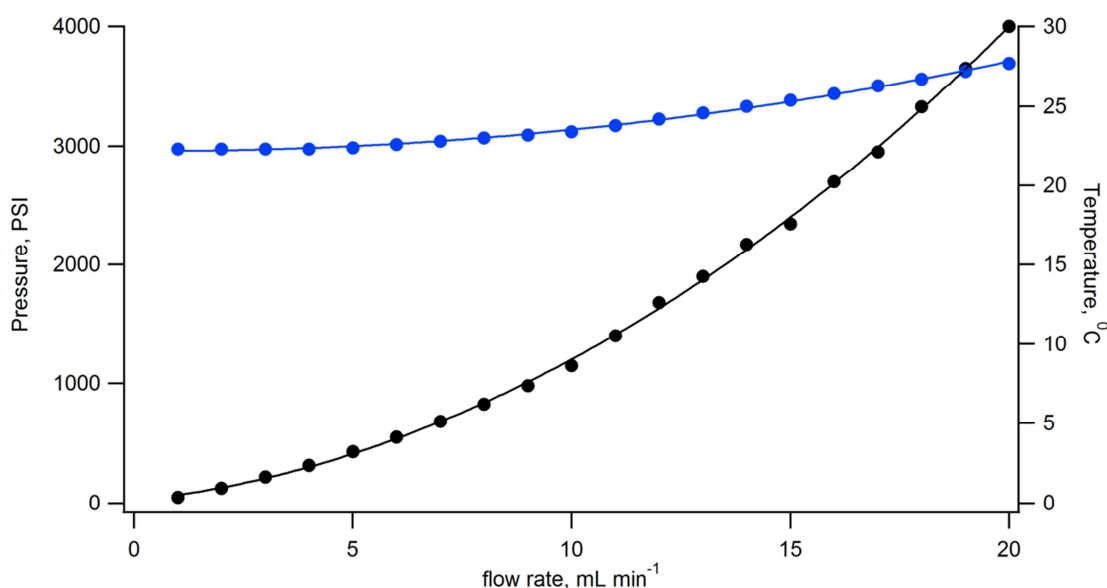


Figure 12. Parabolic dependence between pressure (—) or temperature (—) and flow rate in the cylindrical cuvette. (●) and (●) are experimental values, while (—) and (—) are fits according to **Eqs. 3** and **4**.

6. Assembly of mixing and optical components

The continuous-flow stainless-steel micro-mixer of the setup is a four-jet tangential alternating stream or ABAB micro-mixer (**Fig. 13**). Reactants are delivered by two HPLC pumps as in the MHQ setup². The micro-mixer and the cuvette holder are mounted on two independently adjustable three-axes manipulators in the light path between the monochromator and the CCD camera. The micro-mixer and the cuvette holder are separated by a *Cu* inlay (3 mm in outer diameter and 50 μm thick) that contains a hole (130 μm diameter), which is precisely positioned in front of the cylindrical cuvette by means of a *Cu* shim (5 mm in outer diameter, 3 mm in inner diameter and 25 μm thick), see **Fig. 13**. The *Cu* inlay acts both as a tight seal to prevent leaking of the reactants (at least up to 400 bar) and as the micro compartment where mixing is completed.

As **Fig. 13** indicates, each reactant enters two opposite channels (\varnothing 300 μm in diameter) before meeting at a cross section, ‘the premixing chamber’. The four micro-channels leading to the premixing chamber are 50 μm wide and deep. The four micro-

channels are offset in respect to each other by a full width of the channel to induce a vortex of the four liquid streams by which mixing is enhanced. The dimensions of the pre-mixing chamber are: $100\ \mu\text{m} \times 100\ \mu\text{m} \times 50\ \mu\text{m}$ (width \times width \times depth, $0.5\ \text{nL}$ volume). Here the reactants are premixed at relatively low Reynolds numbers, Re_{premix} . After the premixing chamber, the reactants are forced into ‘the mixing chamber’ perpendicular to the plane of the channels, i.e. into the hole in the *Cu* inlay ($130\ \mu\text{m}$ diameter, $50\ \mu\text{m}$ long or $663\ \text{pL}$ in volume). Here the linear velocity of the liquids is highest and hence also the Reynolds number, Re_{mix} leading to complete mixing. By increasing the flow rate, the residence time of the liquids in the premixing- and the mixing chamber – the dead volume – becomes shorter. The minimal residence time in the ‘dead volume’ or dead-time is obtained at the highest flow rate of $20\ \text{mL}\ \text{min}^{-1}$ (or $0.33\ \text{nL}\ \mu\text{s}^{-1}$), and is calculated as $1.5\ \mu\text{s}$ and $2.0\ \mu\text{s}$ for the premixing chamber and mixing chamber, respectively, totaling $3.5\ \mu\text{s}$. After the mixing chamber, the mixed reactants directly enter the optically transparent fused-silica cylindrical cuvette where UV-Vis measurements are made. After the cuvette the fluid flows through a wide bore flexible tubing and is finally dispensed in a waste container.

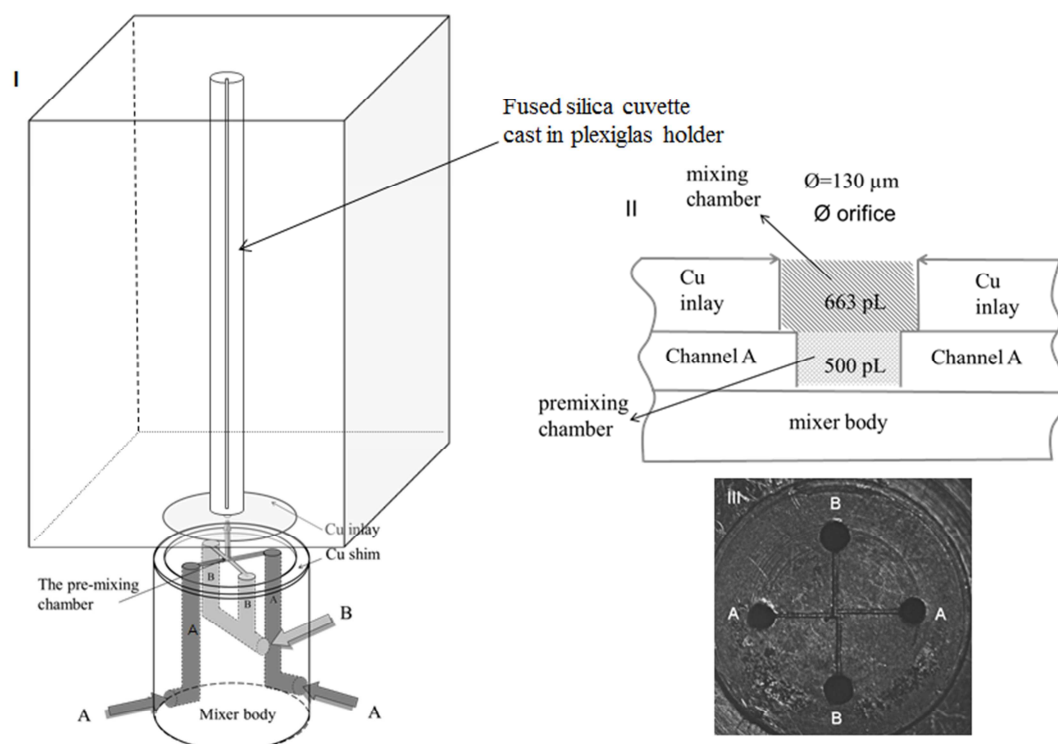


Figure 13. (I) Geometry of the four-jet tangential stainless-steel ABAB micro-mixer and the plexiglass cuvette holder equipped with a fused silica cuvette. The micro-mixer and cuvette holder are separated by a *Cu* inlay, precisely positioned with respect to one another by a *Cu* shim. The micro-mixer body and cuvette holder are held together by four long screws (not shown in the figure). Reaction components A and B enter the mixer body as indicated and subsequently flow to the four channels arranged in a cross (see III). The components are then forced through a $130\ \mu\text{m}$ wide hole (‘mixing chamber’) in the *Cu* inlay. (II) Slice through the mixer body (‘side view’) and the *Cu* inlay along two channels (A-A; B-B (not shown)). The premixing chamber is located between the mixer body and the mixing chamber. (III) Alternating ABAB channel arrangement (‘top view’) and the premixing chamber (of the dismantled mixer). The premixing chamber has dimensions of $100 \times 100 \times 50\ \mu\text{m}^3$ yielding a volume of $500\ \text{pL}$.

7. The mixing efficiency of the four-jet tangential ABAB micro-mixer

7.1 The reaction between HPTS and acidic and alkaline solutions

To determine the mixing efficiency of mixing devices, a chemical reaction must be selected that is completed within the mixing dead-time of the set up. Most suitable for this purpose are the fast protonation/deprotonation reactions with pH-sensitive dyes. HPTS (8-hydroxypyrene-1, 3, 6-trisulfonic acid, also known as pyranine) is a highly water-soluble pH-sensitive dye with a pK_a of approximately 7.3 in aqueous solution. The protonation and deprotonation rate constants are $1.8 \cdot 10^{11} \text{ M}^{-1} \text{ s}^{-1}$ and $1\text{-}2 \cdot 10^{10} \text{ M}^{-1} \text{ s}^{-1}$, respectively^{36,37}. So under our experimental conditions [H^+] or [OH^-] (~10 mM) protonation/deprotonation of HPTS occurs well within our time resolution of 318 ns per pixel at 20 mL min^{-1} fluid flow rate, and the mixing efficiency can thus be determined from the ratio of protonated versus non-protonated HPTS in the first point of observation, here called the '1st pixel'.

In alkaline solution HPTS absorbs maximally at 458 nm, whereas in acidic solutions there is no absorbance at this wavelength (**Fig. 14a**, blue). In acidic solutions the maximal absorbance is at 406 nm, a wavelength where the dye in alkaline solution has a small absorbance (**Fig. 14a**, black). The optical properties and the high protonation/deprotonation reactivity make HPTS a suitable dye to determine the mixing efficiency of the four-jet tangential micro-mixer when recording spectra between 380 nm to 500 nm along the length of the cylindrical cuvette (**Fig. 14**). Observation starts immediately after the liquids have left the *Cu* inlay and enter the cuvette.

The absorbance spectra of the protonation (Base to Acid; **Fig. 14b**, black) and deprotonation (Acid to Base; **Fig. 14b**, blue) kinetics were acquired using a 1.5 fold excess of acid over base, or the reverse, respectively. The control or reference absorbance spectra are obtained by mixing a dye in alkaline buffer with alkaline buffer and similarly for the dye in acidic buffer (**Fig. 14a**, spectra in blue and black, respectively). The percentage or degree of mixing in a Base to Acid, or Acid to Base experiment can now be determined using Two-component analysis (for details see **Material and Methods**).

Fig. 14b indicates, that at the high flow rate of 20 mL min^{-1} mixing is complete in the very first time point (318 ns after mixing in the (pre-)mixing chambers) evidenced by the appearance of only one spectral component in the 1st pixel, here pixel 1901. Either the ('acidic') 406 nm peak is visible for the Base to Acid reaction (black spectra), or the ('basic') 458 nm peak for the Acid to Base reaction (blue spectra). The residence time in the pre-mixing and mixing chambers (dead volume) at a flow rate of 20 mL min^{-1} is $3.5 \mu\text{s}$, hence mixing is completed within $3.8 \mu\text{s}$.

Fig. 15 shows kinetic traces of the Acid to Base and Base to Acid reactions calculated by the Two-component analysis method. The traces in **Fig. 15** indicate also that the mixing is completed in the first time point (pixel 1901) recorded in the capillary flow-cell. The value of coefficient *a* (the fraction of acid, black) is very close to 1 but starts from zero, while coefficient *b* (the fraction of base, blue) equals 0 but its initial value was 1 in the case of conversion of the Base to Acid form of HPTS (**Fig. 15b**).

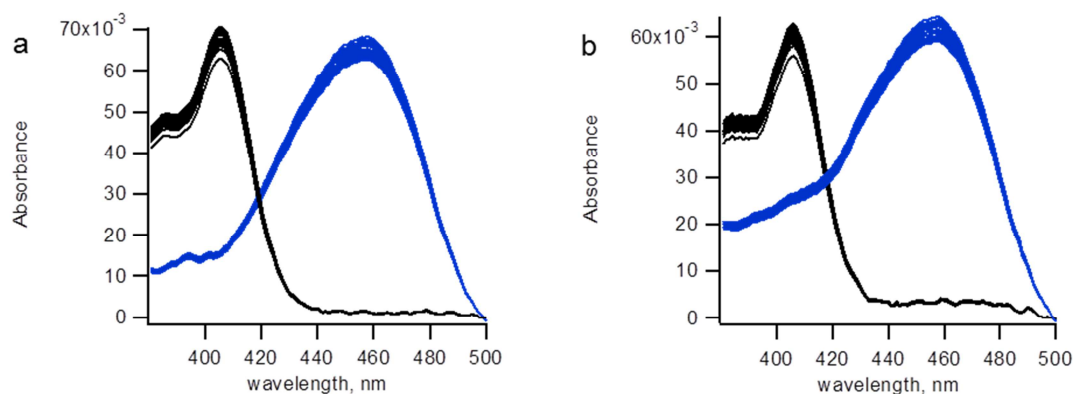


Figure 14. The absorbance spectra of HPTS dye recorded within the first 6.36 μs (20 pixels) at a liquid flow rate of 20 mL min^{-1} . (a) Base control spectra - 3 mM HPTS in 10 mM NaOH (pH 12) mixed vs 10 mM NaOH (pH 12) (-); Acid control spectra - 3 mM HPTS in 10 mM HCl (pH 2) mixed vs 10 mM HCl (pH 2) (-). (b) Kinetic traces of the Base to Acid reaction - 3 mM HPTS in 20 mM NaOH (pH 12.3) mixed vs 30 mM HCl (pH 1.52) (-) and Acid to Base reaction - 3 mM HPTS in 20 mM HCl (pH 1.7) mixed vs 30 mM NaOH (pH 12.48) (-). The final concentration of HPTS dye was 1.5 mM. To minimize the spectral effect due to the formation of salt, 30 mM NaCl was added to each solution.

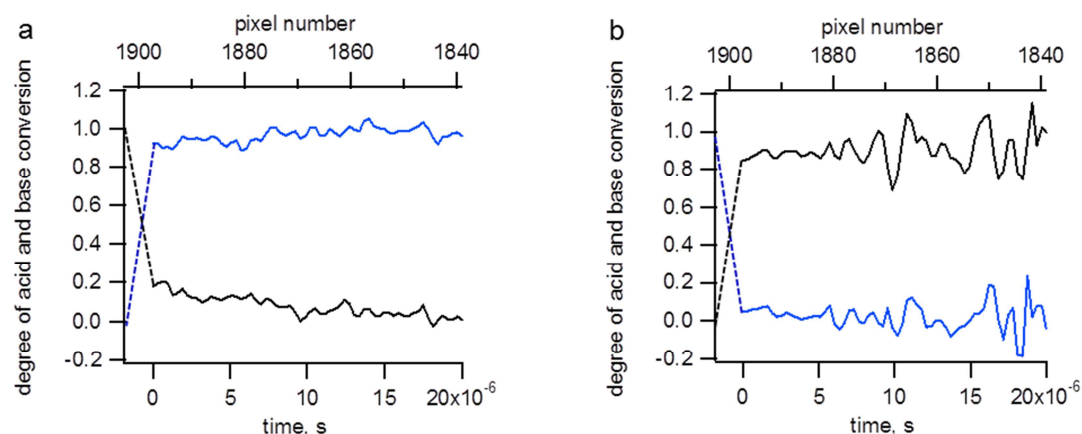


Figure 15. Kinetic traces of (a) HPTS Acid to Base reaction and (b) HPTS Base to Acid reactions determined in the first 64 pixels (20.35 μs). The spectra were analysed using Two-component analysis (see Eq. 8 in Material and Methods). The finding that coefficient a (-) and coefficient b (-) have values close to zero and one, respectively, in the first data point ('time zero') indicates complete conversion from the Acid to Base form of HPTS or the reverse. The first pixel, pixel 1901 covers the time from 0-318 ns, after mixing in the premixing and mixing chambers. The experimental conditions are the same as in Fig. 14.

7.2 Relation between Reynolds number and mixing efficiency

To determine at which Reynolds number the mixing is completed at the very first point of observation the experiment shown in Fig. 14 was repeated at flow rates between 0.5-7 mL min^{-1} using a 100 μm *Pt* instead of *Cu* inlay; the *Pt* inlay is normally used in the MHQ setup². As Fig. 16 shows, the mixing is completed already at a flow rate of approximately 5 mL min^{-1} where the calculated Re in the 100 μm *Pt* inlay orifice is 1060. This value is considerably lower than the onset of turbulence in pipe flow, which occurs at $Re = 2040$ ²⁶. That mixing is apparently complete in a pre-

turbulent regime may be due to the vortex experienced by the four tangential liquid flows that is induced by the channel offset (see **Fig. 13** and reference²).

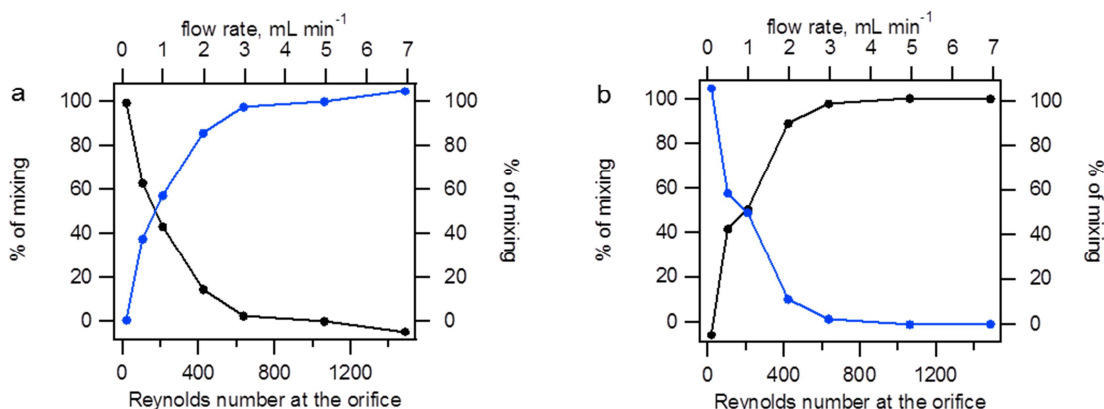
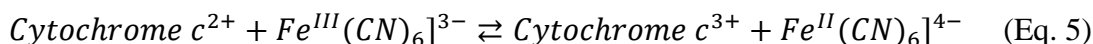


Figure 16. Percentage of mixing in the first pixel (first time point) of the cylindrical cuvette as a function of the flow rate and the Reynolds number calculated for the 100 μm Pt inlay orifice. Percentage of mixing is presented as disappearance of acid (—) and appearance of base (—) for the Acid to Base reaction (a) and as appearance of acid (—) and disappearance of base (—) for the Base to Acid reaction (b). (—●—) and (—●—) are experimental values. The experimental conditions are the same as in **Fig. 14**.

8. Calculation of the dead-time of the continuous-flow micro-mixer

To determine the dead-time of the set up, the reaction between ferrocyanochrome *c* and sodiumferrihexacyanide was studied as a model reaction:



The second order rate constant of this reaction has been determined using stopped-flow (SF) kinetic measurements³⁸. The rate constants (at pH 7) reported in the literature vary between $0.87 \times 10^7 \text{ M}^{-1} \text{ s}^{-1}$ and $1.2 \times 10^7 \text{ M}^{-1} \text{ s}^{-1}$. At concentrations of 100 mM sodiumferrihexacyanide the turnover frequency is approximately $\sim 1 \mu\text{s}$, suitable for our purposes. Given the uncertainty in the rate constants reported in the literature, which may lead to substantial errors in the dead-time determination of the set up, we determined the rate constant for the reaction ourselves by the stopped-flow method at various temperatures.

8.1 Stopped-flow kinetic measurements

The dead-time of our stopped-flow instrument is 2.5-2.6 ms, hence the reaction is completed within the dead-time already at $\sim 300 \mu\text{M}$ sodiumferrihexacyanide. To obtain reliable rate constants, the reaction was studied with excess ferrocyanochrome *c* over sodiumferricyanide under both first- and second-order conditions. In this way the concentration of sodiumferrihexacyanide can be determined accurately from the amount of oxidation of ferrous cytochrome *c*. The stopped-flow traces were analyzed from the kinetics at 550 nm (**Fig. 17**) or by Two-component analysis (**Fig. 18**). The results are shown in **Table 1**. The calculated rate constants are close to those reported in the literature, while single wavelength analysis and Two-component analysis methods agreed within approximately 10%. Since the Two-component analysis

method uses the whole spectrum for calculation rather than a single wavelength, it should be more accurate. More importantly, the rate of the reaction is found to be almost independent of temperature as might be expected when outer-sphere (pure) electron transfer is rate limiting³⁹.

Table 1. Rate constants at 0.1 M ionic strength for the reaction between ferrocyclochrome *c* and sodiumferrihexacyanide

Analysis Method	Rate constant ($\text{M}^{-1} \text{s}^{-1}$)
Stopped-flow	
550 nm peak	
19.3°C	$(0.88 \pm 0.23) \times 10^7$
34.4°C	$(0.94 \pm 0.1) \times 10^7$
Two-component analysis	
19.3°C	$(1.03 \pm 0.14) \times 10^7$
34.4°C	$(1.05 \pm 0.07) \times 10^7$
Continuous-flow set up	
27.5°C	$(0.96 \pm 0.03) \times 10^7$

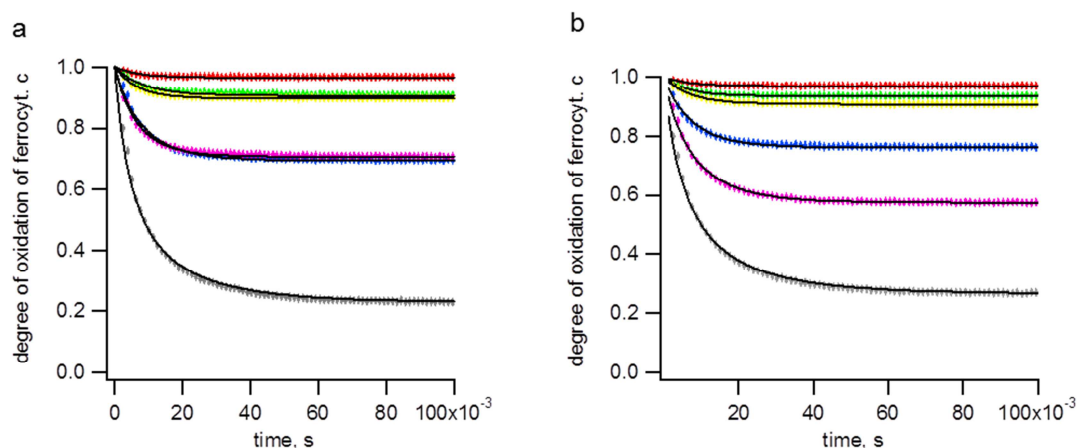


Figure 17. Stopped-flow traces of the oxidation of ferrocyclochrome *c* by sodiumferrihexacyanide calculated with two-component analysis. The fraction of reduced cytochrome *c* has been plotted (dots). (a) 19.3°C and (b) 34.4°C. Experiments were performed at 29.6 μM ferrocyclochrome *c* mixed with ferrihexacyanide in 50 mM potassium phosphate (pH 7.0): 1 μM (—); 2 μM (—); 3 μM (—); 6 μM (—); 10 μM (—) and 20 μM (—). The black lines (—) are second-order fits used to determine the rate constant of the reaction.

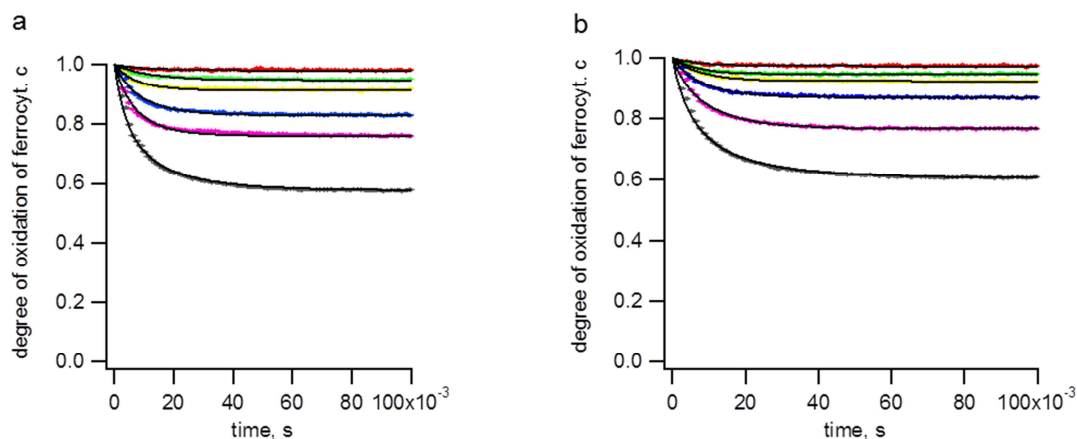


Figure 18. Stopped-flow traces of the oxidation of ferrocyclochrome *c* by sodiumferrihexacyanide monitored at 550 nm at temperatures: (a) 19.3°C and (b) 34.4°C. Experimental conditions and color coding are the same as in Fig. 17.

8.2 Kinetic measurements with the continuous-flow ultra-fast mixing instrument

To calculate the rate constant and the instrumental dead-time, the reaction was studied with excess sodium ferrihexacyanide over ferrocytochrome *c* under both first- and second-order conditions (**Fig. 19**). Analysis of the traces indicated that k_{obs} was not proportional to the concentration of ferrihexacyanide above approximately 10 mM (**Fig. 20**, black data points). Therefore, the calculated second-order rate constant (k_{2nd} , blue data, **Fig. 20**) is not constant and was found to decrease by about a factor of ten, i.e. from $\sim 10^7$ to 10^6 $M^{-1} s^{-1}$ when the concentration of ferrihexacyanide was increased from 1 mM to 100 mM. However, the increase in the concentration of oxidant leads to an increase in the ionic strength and this will reduce the rate of the reaction because it involves two oppositely charged reactants (**Eq. 5**). The oxidant ferrihexacyanide carries a high net negative charge of -3 ($Z_1=-3$) and hence the total ionic strength increases from 0.1 M to 0.7 M in the ferrihexacyanide concentration range from 1 mM to 100 mM; the phosphate buffer contributes 0.094 M to the ionic strength. The total charge of reduced cytochrome *c* is +6.5 ($Z_2=+6.5$)⁴⁰. The effect of ionic strength on the rate of electron transfer reactions is well described in the literature. **Eq. 16** in⁴⁰ was used to calculate the effect of ionic strength on the rate of electron transfer:

$$\ln k = \ln k_0 - 3.567 \cdot \left(\frac{e^{-kR_1}}{1+kR_2} + \frac{e^{-kR_2}}{1+kR_1} \right) \cdot \frac{Z_1 Z_2}{R_1 + R_2} \quad (\text{Eq. 6})$$

Herein the ionic radii R_1 and R_2 were taken as 4.5 Å and 16.6 Å for ferrihexacyanide and ferrocytochrome *c*⁴⁰. The ionic strength parameter for water, k is equal to 0.329 $\mu^{1/2} \text{Å}^{-1}$ wherein μ is the ionic strength. The rate constant at zero ionic strength is k_0 . The second-order rate constants corrected for ionic strength are plotted in **Fig. 20** (red data points and fit) and yield for 0.1 M ionic strength the value of 0.96×10^7 $M^{-1} s^{-1}$ (**Table 1**). This value is in good agreement with that obtained from the stopped-flow data and within the range of values reported in the literature.

Fig. 19b shows that the second-order fits cross at a single time point where the fraction of the reactant, ferrocytochrome *c*, equals 1.0. This time point represents the true ‘time zero’. Approximately 3.8 μs (or 12 pixels on the CCD camera) beyond this time zero, the second-order fits agree well with calculated fractions of reduced cytochrome *c*. The calculated dead-time of the instrument is thus 3.8 ± 0.3 μs . This value agrees well with the total dead volume of the micro-mixer of 1.15-1.2 nL, which is equivalent to 3.5 ± 0.1 μs at a fluid flow rate of 20 $mL \text{ min}^{-1}$. With the CCD camera outlined with the first pixel at #1900, the time zero is at pixel 1912 ± 1 , and the first part of the experimental trace that falls on the second-order fit is at pixel 1900 ± 1 , just beyond the sharp increase in light intensity of the transmission profile (see **Figs. 6-8**). The time uncertainty of ± 0.318 μs that corresponds to ± 1 pixel is in agreement with the monochromator exit slit of 0.2 mm (see **Fig. 5**). In a similar kinetic experiment as described but using 1 mm slit width, the same second-order rate constant was found, but the apparent dead-time had increased to 7 ± 2 μs (data not shown) owing to broadening of the peaks on the CCD camera.

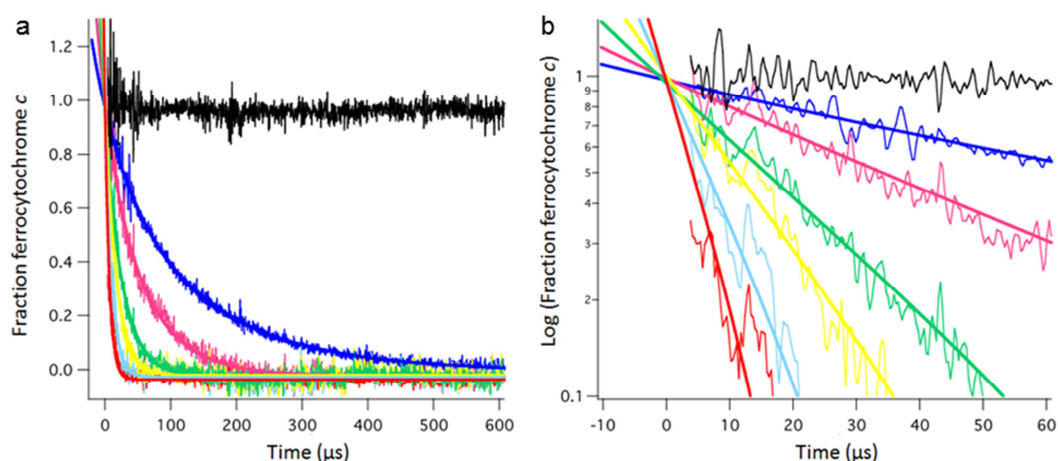


Figure 19. Kinetic traces of the reaction between ferrocyanide c (0.48 mM) and various concentrations of sodium ferrihexacyanide at 27.5°C recorded with the Continuous-flow setup. The graphs show the data after Two-component analysis as the Fraction of ferrocyanide c vs time (a) and after calculating the logarithm of this fraction (b). The buffer was 50 mM potassium phosphate (pH 7, Ionic strength is 0.1 M). Final ferrihexacyanide concentrations were: 1 mM (—), 2 mM (—), 5 mM (—), 10 mM (—), 20 mM (—) and 50 mM (—); the data obtained at 100 mM are omitted from the figure. The black line (—) is the sum of (oxidized + reduced) cytochrome c (only shown for the reaction at 2 mM sodium ferrihexacyanide), which should remain constant at 1.0. The lines through the data points (b) are second-order fits with the rate constants indicated in Fig. 20 (●). The fits all cross in a single point (± 1 pixel or 318 ns) where the fraction of reduced cytochrome c equals 1. Kinetic traces are shown from a time of 3.8 μ s (the determined dead-time). From this time onwards, the data follow the fits.

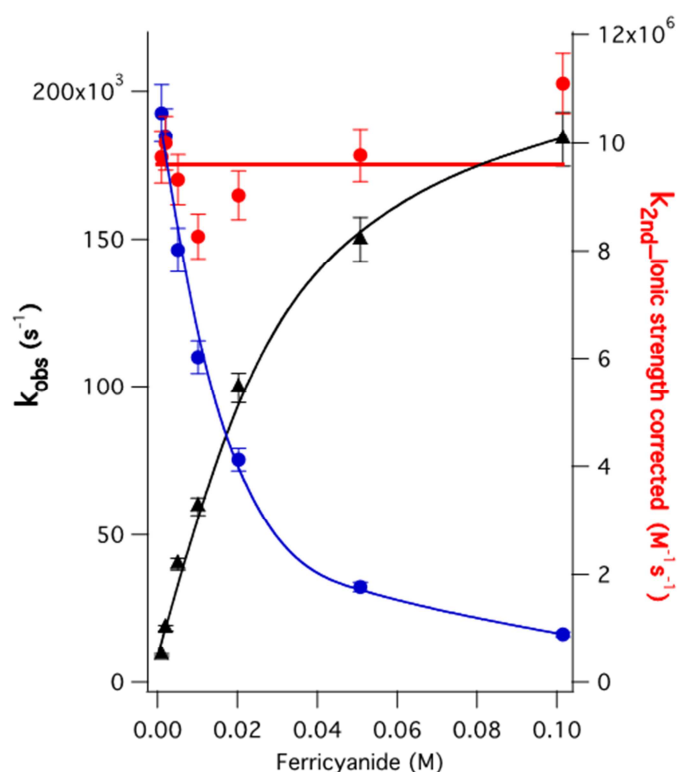


Figure 20. The effect of ionic strength caused by high concentrations of ferrihexacyanide on observed (k_{obs} , —) and calculated (k_{2nd} , —) rate constants for the reaction between 0.48 mM ferrocyanide c and sodium ferrihexacyanide. The values of the second-order rate constant corrected for ionic strength by Eq. 6 are given by (●) and fitted to a horizontal line yielding a value of $(0.96 \pm 0.1) \times 10^7\ M^{-1}\ s^{-1}$.

9. Discussion and conclusions

The test results and the kinetic experiments described here demonstrate that the newly designed continuous flow ultra-fast mixing instrument has a dead-time of $3.8 \pm 0.3 \mu\text{s}$. This dead-time is 10-20 fold shorter than any other (continuous-flow) mixing instrument in the world and represents an improvement of at least factor of 300 in time resolution over commercially available stopped-flow instruments, which achieve a dead-time of 1.5 ms at best⁴¹. The instrument produces 1900 UV-Vis spectra separated in time by only 318 ns for 600 μs at the highest flow rate of 20 mL min^{-1} . The flow rate can be reduced to approximately 5-7 mL min^{-1} with complete mixing in the first data point thus extending the time base to ~ 2 ms, overlapping with that of the stopped-flow. The optical sensitivity of the instrument is illustrated by a signal-to-noise ratio >50 of the spectra, which are recorded in a volume of only 106 pL with 10-90 femtomol of enzyme.

Turbulent mixing at high fluid flow rates imply the built up of high pressures up to ~ 400 bar. The high flow rates also lead to a temperature increase (by maximally 7°C at 20 mL min^{-1}). The current setup is not equipped with a thermostat so the reaction temperature is equal to the ambient temperature ($20\text{-}22^\circ\text{C}$) plus maximally 7°C . Although the increase in temperature relative to ambient cannot be avoided, the micro-mixer plus cuvette holder could be provided with a thermostat expanding the applications of the current setup.

Unlike stopped flow, the continuous-flow approach requires high amounts of reagents, usually at high concentrations (0.2-1 mM) to obtain sufficient optical absorbance at a path length of 100 μm . The high amount of reagents needed remains a general disadvantage of continuous-flow over stopped-flow methods. This limitation can be overcome in part by increasing the sensitivity or signal-to-noise ratio by using a light source with higher power density than used in this work. The UV-Vis spectrometer was also successfully used in either front-face or 90-degree fluorescence mode (data not shown). The latter arrangement was implemented by placing a transparent plexiglass window within the black plexiglass body (**Fig. 1**) perpendicular to the capillary flow cell.

Taken together, the specifications of the current continuous flow ultra-fast mixing setup and the experiments described here show that it is possible to study (bio)chemical reactions on the microsecond time scale filling a gap in current scientific instrumentation that relies on the mixing of reactants. The new setup enables detailed kinetic analyses of the very onset of substrate and ligand binding, biocatalysis and protein folding.

10. Materials and methods

10.1 Instrumentation and construction of the capillary flow-cell

The following parts were used in the ultrafast mixing device. The sample delivery system and stainless-steel micro-mixer were the same as used in the MHQ setup as described in². The high-speed scanning monochromator equipped with a 75 Watt Xenon short-arc light source (Ushio) was purchased from Optical Building Blocks

Corporation (OBB). It runs under Moco software program provided by OBB. The Newton DU-940N-BU CCD camera was purchased from Andor. Data are acquired with the Andor Solis imaging software, which runs the CCD detector. Fluid flow was initiated manually whereafter the CCD camera was activated. The CCD software was used to trigger the Moco program to initiate the scanning monochromator.

The two three-axes manipulators (x, y, z linear stage and the two-axis tilt and rotation stage), a plano-convex and bi-convex lens and lens holder were from Newport Corporation. The manipulators were machined to fit on top of one another and adapted to carry the micro-mixer plus cuvette holder and are used to outline the capillary flow-cell with respect to the light beam. The CCD camera is next aligned to the flow-cell. The CCD camera is mounted on a small table allowing manual translations in the x, y plane; vertical manual translations of the four supports were performed with four fine screws. The capillary fused silica flow-cell (100 μm inner diameter, 360 μm outer diameter) was from Polymicro Technologies. The various slits (70 μm , 100 μm , 250 μm) are made from brass and mounted very precisely on the cuvette holder.

The cuvette holder is made from UV transparent and black plexiglass. The capillary optical flow-cell is first glued between two UV transparent plexiglass surfaces (2.5 x 18.5 x 30 mm), one containing a U-shaped groove, the other a mirror image T-profile. To each surface a piece of black plexiglass (9 x 18.5 x 30 mm) is glued in which four holes are drilled for screws to connect to the body of the micro-mixer. The UV-transparent and black plexiglass bloc constitute the cuvette holder (**Figs. 1 and 2**). An aluminium stopper is mounted on the fluid exit of the cuvette holder to hold the capillary flow-cell in position; this stopper contains a hole (diameter of 0.2 mm) for fluid drain. On the mixer end of the cuvette holder a black plexiglass bloc (5 x 18.5 x 23 mm) with a central 5 mm hole is mounted that serves as a guide to connect the cuvette holder to the mixer body. On the light entrance side of the cuvette holder a 7-8 mm deep groove is made along its whole length up to 1 mm from the capillary flow-cell; the 70 μm or 100 μm entrance slit is positioned in the groove exactly aligned with the capillary flow-cell (**Fig. 2**). The cuvette-holder is physically connected to the micro-mixer via a disc-shaped seal of soft material of platinum or copper (50 μm or 100 μm thick). The connection is made in a leak free manner to withstand the pressures generated up to 400 bar by the fast flow of the fluids. The seal contains a single cylindrical hole of dimensions of the micro-mixer and capillary (~100-130 μm). The seal acts in practice also as the main mixing compartment. Seals with mixing volumes between 0.5-1.0 nL were used. The ends of the capillary flow-cell and the blunt ends of the plexiglass surfaces are flattened using 1 μm diamond paper to avoid solvent leaks and provide a flat surface for illumination, respectively. The various parts are machined in the laboratory's workshop. Precision outlining and construction were done with the help of a long-working distance microscope (10 cm, 15x magnification). All components are mounted on a 1.5 cm thick stainless-steel base plate. The CCD camera, cuvette holder and lenses are contained in a lightproof box.

10.2 Alignment of the setup and recording of spectra

In order to precisely outline the setup light of 474 nm was used, the maximum of the emission spectrum of the Xenon lamp and the capillary flow-cell filled with milli-Q water. The various components are outlined until the image of the flow-cell is projected approximately in the middle of the CCD camera operating in image mode. The cuvette holder is manipulated precisely parallel to the bottom of the base plate using a mini leveler and perpendicular to the light beam, i.e. to a position where the 'first pixel' has a minimum peak width. The height and tilt of the CCD camera are subsequently adjusted in respect to the image of the flow-cell so that the latter is precisely horizontally aligned with the CCD chip. Finally, the CCD camera is elevated so that the image of the flow-cell is projected on the lowest 30 (or 50) vertical pixels of the CCD chip and a cover, that acts as a permanent shutter, is placed over the front of the CCD camera so that only the lower 30 (or 50) pixels are illuminated. This arrangement in conjunction with the various slits minimizes stray light and allows recording of data in the fast CROP 30 (or 50) mode. In CROP 30 (or 50) mode the light intensity in the z-direction of 30 (or 50) vertical pixels is binned, i.e. the intensity of the vertical pixels is added, producing a single value for a pixel at a particular position of the flow-cell (y-direction or the time axis).

UV-Vis spectra from 300-800 nm or part of this spectral range were recorded with 0.1 mm or 0.2 mm monochromator exit slit and between 1-2 mm entrance slit. Kinetic data were recorded in general at 50 nm sec⁻¹ and the recording speed of the CCD camera was adjusted so that each recording cycle took 20 ms, This produces UV-Vis spectra with a data resolution of 1 nm whilst the spectral resolution determined by the exit slit was 0.35 nm or 0.7 nm (with the entrance slit at 0.1 mm or 0.2 mm, respectively). The CCD camera settings are as follows: Acquisition mode 'kinetic series', data type 'counts', frequency of 50 Hz (50 scans sec⁻¹, vertical shift speed of 14.625 μ s, pixel readout rate of 2.5 MHz, temperature of the CCD of -65⁰C, number of active pixel rows 30 (or 50), number of accumulated scans 1. This cycle time of 20 ms yields an illumination time of 18.4 ms. In particular for static measurements, slower scanning speeds may be selected or more scans accumulated, increasing the signal to noise ratio of the spectra. To obtain UV-Vis absorbance spectra separate dark count, sample and appropriate reference traces are recorded under identical alignments and settings of the CCD camera (see **Sections 3** and **4**, and the text below for further details).

10.3 Data acquisition, processing, analyses and graphical presentation of data

Spectral data are acquired with the Andor Solis imaging program. Data are collected as multi-scans in .SIF format, in general as 1 nm for one scan, each scan containing 2048 pixel data points. Processing, analysis, fitting and graphical presentation of data are performed with the software package Igor Pro v. 5.05 or 6.04 (Wavemetrics). The software was written to open Andor Solis .SIF files by Igor, to calculate and plot (2048) UV-Vis spectra and to perform kinetic analyses (see below). In order to calculate the UV-Vis spectrum, the background counts were subtracted from the light counts of sample and reference.

UV-Vis spectra were analysed using Component Analysis⁴², in particular Two-component analysis. Spectra are fitted to **Eq. 7**:

$$f(x, y) = a \cdot x + b \cdot y + c \quad (\text{Eq. 7})$$

in which x and y correspond to the one-component UV-Vis spectra, i.e. oxidized cytochrome c and reduced cytochrome c for the reaction between ferrocyanochrome c and sodiumferrihexacyanide, or, in the case of HPTS, the acid, and base forms, respectively. The coefficients a and b , which indicate the degree of conversion, vary between 0 and 1 (the maximal amount or concentration of a component); coefficient c is a vertical offset (and determined in all analyses <0.01). The three coefficients are calculated using linear regression with the starting and final component UV-Vis spectra (oxidized cytochrome c and reduced cytochrome c , or the acid and base forms of HPTS) as the input basis set. In general these basis UV-Vis spectra were recorded separately from the spectra recorded in the kinetic experiment, although in principle they could be determined to good approximation from the initial and, in particular, from the final spectra of a kinetic experiment. The advantage of using the whole spectrum for analysis rather than a single wavelength (i.e. 550 nm for cytochrome c) is that the whole spectrum contains ~ 300 spectral data points which greatly improves the reliability of the determination of the degree of conversion and similarly produces kinetic traces with much better signal-to-noise ratio ($\sqrt{300}$, or 17-fold). The kinetic traces thus obtained are fitted to equations describing irreversible first-order or second-order reactions. The second order equation is given by:

$$\Delta ABS(t) = offset + Abs_{inf} + \frac{(B_0 - A_0) \cdot \epsilon \cdot b}{(B_0 - A_0) \cdot e^{(B_0 - A_0) \cdot t \cdot k_{2nd}} - 1} \quad (\text{Eq. 8})$$

in which *offset* is a free parameter, Abs_{inf} is absorbance at infinite time and ϵ the effective extinction coefficient of ferrocyanochrome c . A_0 and B_0 are initial concentrations of ferrocyanochrome c and sodiumferrihexacyanide in M, t is time in seconds, k_{2nd} the second order rate constant in $M s^{-1}$.

10.4 Kinetic experiments

The stopped-flow experiments were performed with an Applied Photophysics SX21 instrument for which the dead-time was determined at 2.5-2.6 ms. Experiments were performed in the SF photo-diode array mode, allowing absorbance spectral recording in the wavelength range from 195 nm to 740 nm. In all experiments, 2.96×10^{-5} M ferrocyanochrome c (reduced by 6×10^{-5} M of ascorbic acid) was mixed with sodiumferrihexacyanide at concentrations varying from $1-20 \times 10^{-6}$ M. Kinetic measurements were performed in 50 mM phosphate buffer at pH 7, at two different temperatures, 19.3°C and 34.4°C. Acquired kinetic absorbance spectra were analysed in two ways: 1) using the whole spectrum and applying Two-component analysis (**Eq. 8**) or 2) by extracting the single wavelength traces at 550 nm.

Continuous-flow kinetic measurements with the new setup were performed at a total flow rate of 20 mL min^{-1} , at 27.5°C, in the spectral range from 350 nm to 650 nm. A stock solution of 2.2×10^{-3} M ferrocyanochrome c (the oxidized form reduced by 4.4×10^{-3} M of ascorbic acid) was diluted to 0.96×10^{-3} M; this latter solution was mixed

with different sodiumferrihexacyanide concentrations varying from 1-100 mM. All solutions contained 50 mM phosphate buffer (pH 7.0). In separate experiments oxidized and reduced cytochrome *c* (0.96×10^{-3} M) were mixed versus buffer only. The data from these latter experiments served as the basis set for Two-component analysis. Optical reference solutions contained BSA (20 mg mL^{-1}) in 50 mM phosphate buffer (pH 7.0); these reference solutions were mixed with buffers containing the same ferrihexacyanide concentrations as in the oxidation experiments. HPTS (8-hydroxypyrene-1, 3, 6-trisulfonic acid, or pyranine) was supplied by Invitrogen, Molecular Probes. Cytochrome *c* from equine heart, sodiumferrihexacyanide, and ascorbic acid were from Sigma Aldrich.

11. References

1. Ballou, D. P. Freeze-quench and chemical-quench techniques. *Methods in Enzymology*, 1978, 54, 85-93.
2. Cherepanov, A. V.; De Vries†, S. Microsecond freeze-hyperquenching: development of a new ultrafast micro-mixing and sampling technology and application to enzyme catalysis. *Biochimica et Biophysica Acta*, 2004, 1656, 1-31.
3. Roder, H.; Maki, K.; Cheng, H. Early events in protein folding explored by rapid mixing methods. *Chemical Reviews*, 2006, 106, 1836-1861.
4. Ballou, D. P.; Palmer, G. A. Practical rapid quenching instrument for the study of reaction mechanisms by electron paramagnetic resonance spectroscopy. *Analytical Chemistry*, 1974, 46, 1248-1253.
5. Berger, R. L. Some problems concerning mixers and detectors for stopped flow kinetic studies. *Biophysical Journal*, 1978, 24, 2-20.
6. Berger, R. L.; Balko, B.; Chapman, H. F. High resolution mixer for the study of the kinetics of rapid reactions in solution. *Review of Scientific Instruments*, 1968, 39, 493-498.
7. Chance, B. *Journal of the Franklin Institute*, 1940, 229, 737-740.
8. Cherepanov, A.; de Vries†, S. bo3 oxidase studied by ultrafast mixing and freeze-quenching in the microsecond time domain. (Abstract oral presentation) in 6th European Conference on Biological Inorganic Chemistry (EuroBIC), 2002, p 35, July 29 - August 3, Lund, Sweden.
9. de Vries†, S.; Albracht, S. P.; Berden, J. A.; Slater, E. C. The pathway of electrons through QH2:cytochrome c oxidoreductase studied by pre-steady-state kinetics. *Biochimica et Biophysica Acta*, 1982, 681, 41-53.
10. de Vries†, S.; van Hoek, A. N.; Berden, J. A. The oxidation-reduction kinetics of cytochromes b, c1 and c in initially fully reduced mitochondrial membranes are in agreement with the Q-cycle hypothesis. *Biochimica et Biophysica Acta*, 1988, 935, 208-216.
11. Grigoryants, V. M.; Veselov, A. V.; Scholes, C. P. Variable velocity liquid flow EPR applied to submillisecond protein folding. *Biophysical Journal*, 2000, 78, 2702-2708.
12. Hartridge, H.; Roughton, F. J. W. The velocity with which carbon monoxide displaces oxygen from combination with haemoglobin. I. *Proc Royal Soc London, series B Biol Sci*, 1923, 94, 336-367.
13. Neltchev, V. Z.; Detchev, G. D.; Boyadjiev, L. A. Mixing device for investigating the kinetics of rapid reactions in solutions. *Journal of Physics E: Scientific Instruments*, 1970.
14. Paeng, K.; Paeng, I.; Kincaid, J. Time-resolved resonance raman spectroscopy using a fast mixing device. *Analytical Sciences*, 1994, 10, 157-159.
15. Regenfuss, P.; Clegg, R. M.; Fulwyler, M. J.; Barrantes, F. J.; Jovin, T. M. Mixing liquids in microseconds. *Review of Scientific Instruments*, 1985, 56, 283-290.
16. Roder, H.; Maki, K.; Latypov, R. F.; Cheng, H.; Shastry, M. C. R. Early events in protein folding explored by rapid mixing methods. *WILEY-VCH Verlag GmbH & Co. KGaA, Weinheim*, 2005, Vol. Part I.
17. Shastry, M. C.; Luck, S. D.; Roder, H. A continuous-flow capillary mixing method to monitor reactions on the microsecond time scale. *Biophysical Journal*, 1998, 74, 2714-2721.
18. Tanaka, M.; Matsuura, K.; Yoshioka, S.; Takahashi, S.; Ishimori, K.; Hori, H.; Morishima, I. Activation of Hydrogen Peroxide in Horseradish Peroxidase Occurs within approximately 200 micro s Observed by a New Freeze-Quench Device. *Biophysical Journal*, 2003, 84, 1998-2004.
19. Tang, J.; Gai, F. A millisecond infrared stopped-flow apparatus. *Applied Spectroscopy*, 2006, 60, 1477-1481.
20. White, A. J.; Drabble, K.; Wharton, C. W. A stopped-flow apparatus for infrared spectroscopy of aqueous solutions. *Biochemical Journal*, 1995, 306, 843-849.
21. Wiertz, F. G. M. Electron transfer and proton pumping pathways in cytochrome aa3. *PhD Thesis, Delft University of Technology, Delft, The Netherlands*, 2007.
22. Mitic, S., de Vries†, S. Rapid Mixing Techniques for the Study of Enzyme Catalysis. In: Edward H. Egelman, editor: *Comprehensive Biophysics*, Vol 1, Biophysical Techniques for Structural Characterization of Macromolecules, H. Jane Dyson. Oxford: Academic Press, 2012, 514-532.

Design and characterization of a continuous flow ultra-fast mixing instrument for the study of transient (bio)chemical reactions by optical spectroscopy

23. Roughton, F. J. W. The kinetic's of haemoglobin IV: General methods and theoretical basis for the reactions with carbon monoxide. *Proceedings of the Royal Society. of London*, 1934, 115B, 451-464.
24. Chance, B. The stopped-flow method and chemical intermediates in enzyme reactions: A personal essay. *Photosynthesis Research*, 2004, 80, 387-400.
25. Majumdar, Z. K.; Sutin, J. D. B.; Clegg, R. M. Microfabricated continuousflow, turbulent, microsecond mixer. *Review of Scientific Instruments*, 2005, 76, 1-11.
26. Avila, K.; Moxey, D.; de Lozar, A.; Avila, M.; Barkley, D.; Hof, B. The Onset of Turbulence in Pipe Flow, *Science*, 2011, 333, 6039, 192-196.
27. Chance, B.; Eisenhardt, R. H.; Gibson, Q. H.; Longberg-Holm, K. K., Eds. Rapid Mixing and Sampling Techniques in Biochemistry; *Academic Press*: New York, 1964.
28. Bray, R. C. Sudden freezing as a technique for the study of rapid reactions. *Biochemical Journal*, 1961, 81, 189-195.
29. Bray, R. C. Quenching by Squirtng into Cold Immiscible Liquids. In Rapid Mixing and Sampling Techniques in Biochemistry; Chance, B.; Eisenhardt, R. H.; Gibson, Q. H.; Longberg-Holm, K. K., Eds.; *Academic Press*: New York, 1964; 195-203.
30. Palmer, G.; Beinert, H. An experimental evaluation of the Bray rapid-freezing technique. In Rapid Mixing and Sampling Techniques in Biochemistry; Chance, B.; Eisenhardt, R. H.; Gibson, Q. H.; Longberg-Holm, K. K., Eds.; *Academic Press*: New York, 1964; 205-217.
31. Palmer, G.; Bray, R. C.; Beinert, H. Direct studies on the electron transfer sequence in xanthine oxidase by electron paramagnetic resonance spectroscopy: I. Techniques and description of spectra. *The Journal of Biological Chemistry*, 1964, 239, 2657-2666.
32. de Vries†, S. Freeze-Quench Kinetics. In *Encyclopedia of Inorganic Chemistry*; Wiley: Hoboken, NJ, 2007, 125-142.
33. de Vries†, S.; Albracht, S. P.; Berden, J. A.; Slater, E. C. The pathway of electrons through QH2: cytochrome c oxidoreductase studied by pre-steadystate kinetics. *Biochimica et Biophysica Acta*, 1982, 681, 41-53.
34. Wiertz, F. G.; Richter, O. M.; Ludwig, B.; de Vries†, S. Kinetic resolution of a tryptophan-radical intermediate in the reaction cycle of *Paracoccus denitrificans* cytochrome c oxidase. *The Journal of Biological Chemistry*, 2007, 282, 31580-31591.
35. Wiertz, F. G. M.; Richter, O. M.; Cherepanov, A. V.; MacMillan, F.; Ludwig, B.; de Vries†, S. An oxo-ferryl tryptophan radical catalytic intermediate in cytochrome c and quinol oxidases trapped by microsecond freezehyperquenching (MHQ). *FEBS Lett.* 2004, 575, 127-130.
36. Mojumdar, S. S.; Mondal, T.; Das, A. K.; Dey, S., and Bhattacharyyaa, K. Ultrafast and ultraslow proton transfer of pyranine in an ionic liquid microemulsion. *The Journal of Chemical Physics*, 2010, 132, 194505.
37. D. B. Spry, A. Goun, and M. D. Fayer. Deprotonation Dynamics and Stokes Shift of Pyranine (HPTS). *The Journal of Physical Chemistry A*, 2007, 111, 230-237.
38. Brand, K. G.; Parks. P. C.; Czerlinski, G. H.; Hess. G. P. On the Elucidation of the pH Dependence of the Oxidation-Reduction Potential of Cytochrome c at Alkaline pH. *The Journal of Biological Chemistry*, 1966, 241, 4180-4185.
39. Marcus, R. A.; Sutin, N.. Electron transfers in chemistry and biology. *Biochimica et Biophysica Acta*, 1985, 811, 265-322
40. Rosenberg, R. S.; Wherland, S.; Holwerda, R. A.; Gray, H. B. Ionic Strength and pH Effects on the Rates of Reduction of Blue Copper Proteins by Fe(EDTA)²⁻. Comparison of the Reactivities of *Pseudomonas aeruginosa* Azurin and Bean Plastocyanin with Various Redox Agents. *Journal of the American Chemical Society*, 1976, 98, 6364-6369.
41. Chance, B. The stopped-flow method and chemical intermediates in enzyme reactions - a personal essay. *Photosynthesis Research*, 2004, 80, 387-400
42. Malinowski, E. R. Factor Analysis in Chemistry, 2002, *Wiley-Interscience*, ISBN 0-471-13479-1

Chapter 5

An optically improved continuous flow ultra-fast mixing instrument for the study of transient intermediates

Sandra Mitić, Marc J.F. Strampraad, Wilfred Hagen
and Simon de Vries†

1. Summary

A continuous flow ultra-fast mixing device with a rectangular flow cell has been developed with similar advances in time resolution (dead-time of $3.8 \pm 0.3 \mu\text{s}$) as described in **Chapter 4**, but with greatly improved optical qualifications to record of UV-Vis spectra. The rectangular flow cell contains a ~ 30 mm long channel of $70 \pm 5 \mu\text{m}$ path length constructed from two parallel sheets of silver foil with a thickness of $109 \mu\text{m}$. The silver foil also acts as a shield for stray light thus producing a spectrophotometer that is linear up to at least 3.5 Absorbance. The noise in each spectrum has decreased from $\pm 0.001 \Delta A$ to $\pm 0.0003 \Delta A$. The new instrument was used to study the partial refolding kinetics of acid denatured cytochrome *c* in a pH-jump experiment. After a very rapid initial phase ($\tau = 4.7 \mu\text{s}$) not observed hitherto, partial refolding proceeds with life times of $83 \mu\text{s}$ and $345 \mu\text{s}$. Using singular value decomposition the complete spectra of three folding intermediates were determined. The spectra indicate a high spin to low spin change of the heme iron in the $345 \mu\text{s}$ folding phase. The newly detected phase of $4.7 \mu\text{s}$ is proposed to reflect formation of the heme-iron bond with His18, an event, which triggers amino-acid residues Trp59 and Ile75 to initiate the folding of the two distal α -helices that surround the porphyrin ring. Our experimental results show that this new instrument enables study of (bio)chemical reactions on the microsecond time scale including protein folding.

2. Introduction

In **Chapter 4** we indicated that a complete study of the catalytic mechanism of enzymes and of chemical reactions in general, requires that the reaction is initiated so rapidly that the subsequent formation and decay of all reaction intermediates can be monitored. A setup was designed that acquires UV-Vis spectra with a dead-time of 3.8 μs using the oxidation of cytochrome *c* by ferrihexacyanide as a test reaction. Here we report on the optical improvement of this setup and further provide a study of the refolding kinetics of acid denatured cytochrome *c*.

Globular proteins often display cooperative unfolding transitions in which mixtures of native and partially denatured molecules accumulate at equilibrium. The compact folded (native) structure is proposed to be stabilized by a great number of weak interactions that are cooperative in nature and consequently, the partially folded states are inherently unstable^{1,2}. A long-standing question is whether protein (un)folding proceeds via a series of specific intermediates that are partially folded or that compaction/denaturation of the protein chain are nonspecific condensation/unfolding processes, respectively.

Partially folded states – structures intermediate between or *en route* to the completely folded or unfolded state – accumulate under denaturing conditions, e.g. at extreme acidic or alkaline pH or in the presence of denaturants like >0.5 M guanidine HCl (GuHCl)^{2,3}. Although these partially folded states are often unstable they represent distinct thermodynamic states with well-defined secondary structures, which can be resolved kinetically¹⁻⁴. Protein folding studies provide evidence for the occurrence of kinetic intermediates even in small, single domain proteins^{5,6}. The study of structural, kinetic and thermodynamic properties of protein folding contributes to our understanding of many diseases such as Parkinson and Alzheimer caused by protein misfolding or aggregation of partially denatured proteins⁷. Cytochrome *c* is a polypeptide of 104-residues and synthesized as the apoprotein. The apoprotein folds into a stable globular structure only after covalent attachment of the heme, which occurs in the mitochondrial intermembrane space^{8,9}. Cytochrome *c* is bound to the mitochondrial innermembrane and serves as the electron shuttle between the cytochrome *bc*₁ complex and cytochrome *c* oxidase. Release of cytochrome *c* into the cytosol for example as a result of structural damage to the mitochondrion leads to apoptosis, programmed cell death¹⁰.

Cytochrome *c* has been used in many studies on electron transfer and more recently as a model system for the study of protein folding because unfolding and (re)folding are reversible processes that occur in the absence of chaperones and without protein degradation¹¹. At pH 2, cytochrome *c* is fully unfolded and it completely refolds upon neutralization. Oxidized cytochrome *c* exhibits five states between pH 1 and 12, labeled with Roman numerals I-V¹². State III is the fully folded native state, states IV and V have been populated under alkaline conditions. When the oxidized cytochrome *c* is exposed to alkaline conditions at pH 11.5 for a week, the protein undergoes a very slow conformational transition from state V to a partially unfolded state M. This state is very stable even under physiological conditions (pH 7 and room temperature)¹³.

Folding of cytochrome *cin vivo* is initiated by the covalent attachment of the heme group to two cysteine residues (Cys14 and Cys17). In, the fully folded native protein, His18 and Met80 serve as axial ligands to the low spin heme iron and a cluster of three α -helices is grouped around one edge of the heme. In horse heart cytochrome *c* a conserved tryptophan residue, Trp59, is located within 10 Å of the heme iron, and its fluorescence is almost completely quenched upon folding via energy transfer to the covalently bound heme³. Strong denaturing conditions result in a large increase in Trp59 fluorescence (up to ~60% of that of free tryptophan in water) indicative of a major increase in the average heme-tryptophan distance, greater than 35 Å, ref.¹⁴. However, excitation-wavelength-dependent fluorescence spectroscopy studies by Kleinermananns at al.¹⁵ show that upon excitation of cytochrome *c* at 280 nm actually both Trp59 and porphyrin fluorescence contribute to total fluorescence and that their relative contributions depend on pH. At pH 2 the fluorescence originates almost completely from the Trp59 residue. At pH 3-7, the porphyrin system contributes 80% to the total fluorescence.

In one of the first studies, Akiyama et al. using a continuous-flow CD instrument with a shortest time resolution of 400 μ s, were able to resolve the changes in the far-UV region of the spectra associated with the ($\tau = 500 \mu$ s) and ($\tau = 2$ ms) phase of folding of oxidized cytochrome *c*. Extrapolation to time zero, indicates that in the first 400 μ s of the refolding approximately 20% of the native α -helical structure is formed.

By using Trp59 heme Fluorescence quenching due to nonradiative energy transfer from the Trp to the heme and far-UV Circular Dichroism D. Elove et al.¹⁶ detected formation of a compact (loosely folded state) intermediate I_C with a native-like helix content, which accumulates during the first few milliseconds of refolding. Studies on the folding of cytochrome *c* by Roder and Elove¹⁷ have shown that the paring of the N- and C-terminal helices leads to formation of the partially folded I_{NC} intermediate that accumulates within 10-20 ms under refolding conditions (pH > 6). Thus, under the refolding conditions (pH 6.3, 0.7 M GuHCl), the folding mechanism is described by two sequential intermediates: I_C , which accumulates on the (sub)millisecond time scale and is in rapid equilibrium with the unfolded states, and I_{NC} , which is populated within 10-100 ms.

Using the continuous-flow capillary mixing instrument (dead-time of ~45 μ s) Roder^{2,18} investigated both, the fluorescence changes and heme absorbance changes in the Soret region (360-430 nm) during the refolding of oxidized cytochrome *c*. The reaction was initiated by a jump from pH 2, where the protein is completely unfolded, to pH 4.5 where partial refolding rapidly occurs. The data indicate a bi-exponential decay with a rapid phase (time constant of $59 \pm 5 \mu$ s) that accounts for 60% of the total fluorescence changes (indicative of the formation of an assembly of compact states) followed by a smaller change of ~435 μ s that contributes approximately 30% to the total amplitude. Combined continuous-flow and stopped-flow absorbance kinetic data indicated three time constants of 65 μ s, 500 μ s and 2 ms, and accumulation of two intermediates, I and M. The two intermediates show absorbance properties distinct from both the initial (unfolded, U) and the final (totally folded, native, N) state. In a recent study¹ NMR was used to observe H/D exchange of 50 backbone NH groups with 140 μ s time resolution allowing to directly detect hydrogen-bond formation in refolding cytochrome *c*. The results showed rapid folding

of two α -helical segments in the C-terminus. The N-terminal helix remained largely unstructured and folded in the millisecond time range. These findings were proposed to indicate that the initial folding steps occur through specific interactions ‘among a subset of α -helical segments’ rather than a general hydrophobic collapse¹.

Combining time-correlated single photon counting – TCSPC, which measures the distance between the heme of the protein and a covalently attached dye molecule – with fluorescence correlation spectroscopy – FCS, which measures changes in the overall physical dimensions of the protein over the range of pH values, Godwin et al. (2006)¹⁹ indicated that the acid-unfolded structure of cytochrome *c* is in a rapid (30 μ s) dynamic equilibrium with a compact intermediate structure.

Resonance Raman kinetic studies with \sim 100 μ s time resolution of cytochrome *c* folding by Rousseau et al.²⁰⁻²³ provide direct information on the ligation state of the heme iron. The authors suggest that at pH 2 in denatured cytochrome *c* the heme is five-coordinate high spin. None of the histidine residues (His18, the native ligand, or His26 and His33) are coordinated, the fifth ligand being water. During folding the heme iron becomes six-coordinate with water and His18 as ligands before folding proceeds to yield the native low spin His18/Met80 coordinated heme iron. It was further observed that non-native intermediates may form during folding or unfolding such as the six-coordinate low-spin bis-His intermediate where His18 and His26 (or His33) serve as ligands to the heme iron.

As indicated above, Raman, Fluorescence and UV-Vis spectroscopy are frequently-used techniques to study the (re)folding of cytochrome *c*. In spite of their good time resolution (\sim 30 μ s for TCSPS and FCS, \sim 50 μ s the capillary flow mixer) and the information on the heme iron ligation state, the protein structural information that one can obtain is limited. Circular Dichroism is more informative yielding the amount and type, but not location, of secondary structure. NMR is the most informative technique providing direct evidence for the position of secondary structure based on the C $^{\alpha}$ resonances, thus local rather than global information¹. It is important to establish the very first events in refolding and the recent NMR work¹ gives hints for structural changes occurring at rates of 150,000 s⁻¹ or higher. Our optically improved continuous flow ultra-fast mixing instrument can approach this latter time scale. Our results show that the initial refolding of denatured oxidized cytochrome *c* occurs very rapidly with $\tau = 4.7 \mu$ s, a phase not observed before, and is followed by partial refolding steps with time constants of 83 μ s and 345 μ s.

3. Results

3.1 Optical components and optical performance of the setup

The optically improved continuous-flow ultra-fast mixing setup uses the same type of instrumental components as the instrument described in the previous **Chapter 4, Fig. 1**, but instead of a cylindrical cuvette it employs a 30 mm long rectangular cuvette (**Fig. 1** and compare with **Chapter 4, Fig. 2**). The rectangular observation flow cell is constructed from two parallel sheets of silver foil with a thickness of 109 μ m (the optical path length) and separated by $70 \pm 5 \mu$ m. The silver sheets not only form a rectangular microchannel for fluid flow, but also act as an efficient shield for stray light. The high reduction in stray light is illustrated in **Fig. 2**. The UV-Vis

spectrometer is linear up to an absorbance value of at least 3.5 AU and superior to most commercial UV-Vis spectrometers that are linear up to an absorbance of 1-1.5 AU.

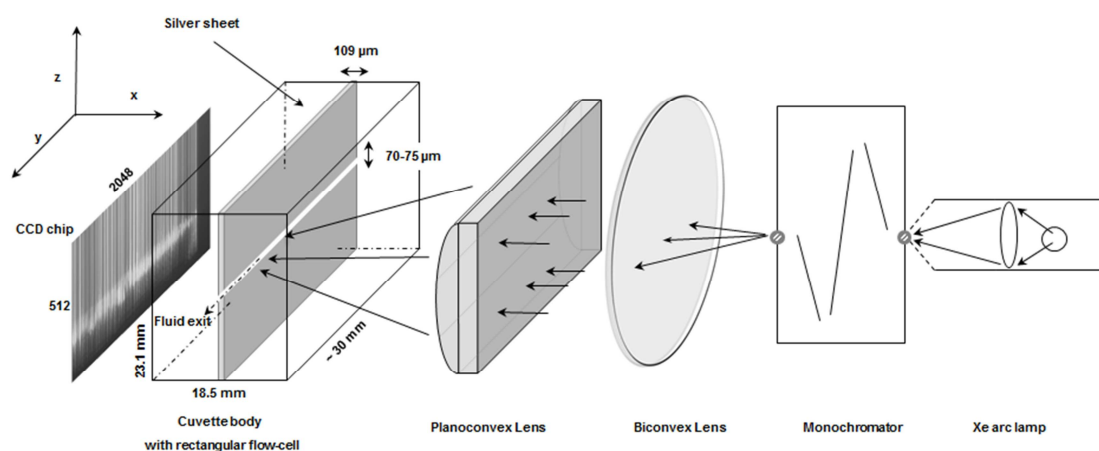


Figure 1. Schematic drawing of the lenses, the rectangular cuvette holder and the CCD chip. Monochromatic light is collimated by a bi-convex collimating lens (150 mm focal length, 50 mm diameter) and focused on the rectangular flow-cell by a plano-convex lens (100 mm focal length, 25 x 50 mm). The two halves of the plexiglass cuvette body are separated by two parallel sheets of silver (109 μm thickness, 11.515 mm height). The two sheets of silver are held in position by six horizontal screws (not shown in the drawing) that press together the two plexiglass halves that make up the cuvette body. The rectangular CCD chip measures 512 pixels x 2048 pixels (height x length, each pixel being 13.5 μm x 13.5 μm). The image of the rectangular cuvette recorded by the CCD camera in the 'Image Mode' is shown in the figure.

The spectra of ferrocytochrome *c* were arbitrarily zeroed at 650 nm; between ~580 and 650 nm the absorbance should be flat and close to zero, however, the spectra slightly deviate from zero (see also **Chapter 4, Fig. 10a**) proportional to the concentration of ferrocytochrome *c* yielding a curved negative absorbance profile. When low pass filters of 320 nm or 450 nm were used – placed at the exit slit of the monochromator, the absorbance between 580-650 nm was flat (not shown) suggesting that the negative absorbance is due to a second or higher order diffraction effect of the grating in the monochromator. Between 300 and 580 nm the spectra were found within experimental error to be the same to those determined in commercial spectrophotometers, including the ratio of the Soret-band to α -band absorbance of 5-5.3. The noise in each single spectrum, i.e. recorded in a vertically binned single pixel, equals ± 0.0003 AU under the specific conditions of recording (single scan at 50 nm s^{-1} , five cycles per data point, see also **Materials and Methods**).

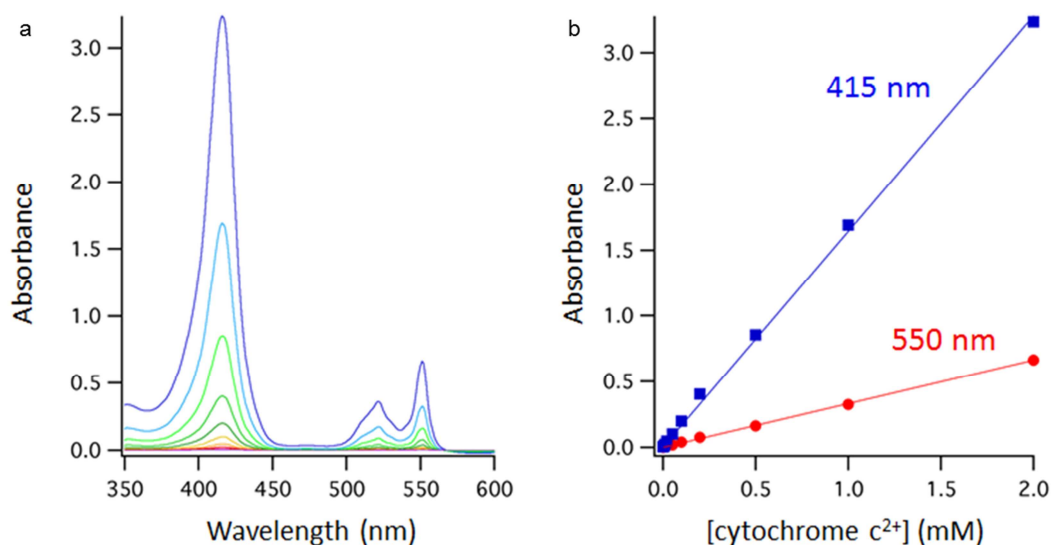


Figure 2. (a) Absorbance spectra of ferrocyanochrome *c* at various concentrations. (b) The relation between absorbance and concentration of ferrocyanochrome *c* at 415 nm and 550 nm. The straight lines (b) are fits to the data points. The ratio of the slopes for A416 and A551 of these lines equals 5.0, similar to the ratio of the extinction coefficients for the Soret- and α -band maxima determined in commercial UV-Vis spectrometers. Ferrocyanochrome *c* concentrations were (– to – traces): 0.001, 0.002, 0.005, 0.01, 0.025, 0.05, 0.1, 0.2, 0.5, 1.0 and 2.0 mM, respectively. The spectra are the average of the spectra recorded in pixels 0-1900, along the whole length of the rectangular flow-cell, and were put arbitrarily at zero at 650 nm.

3.2 Comparison between static absorbance spectra and spectra recorded during fluid flow

For kinetic experiments the fluid in the rectangular flow-cell moves at high speeds up to $40\text{--}45\text{ m s}^{-1}$ at the maximal volumetric flow rate of 20 mL min^{-1} . In spite of this high flow rate, spectra of ferricytochrome *c* recorded under static and flow conditions appear virtually identical (**Fig. 3** bottom spectra). For ferrocyanochrome *c* the intensity of the α -band slightly decreases while that for the Soret-band slightly increases. The reason for these small spectral changes remains unclear, but it is not due to the pressure in the system (maximum $\sim 260\text{ bar}$) since spectra of cytochrome *c* are unaffected by pressures up to 6 kbar or 600 MPa^{20} .

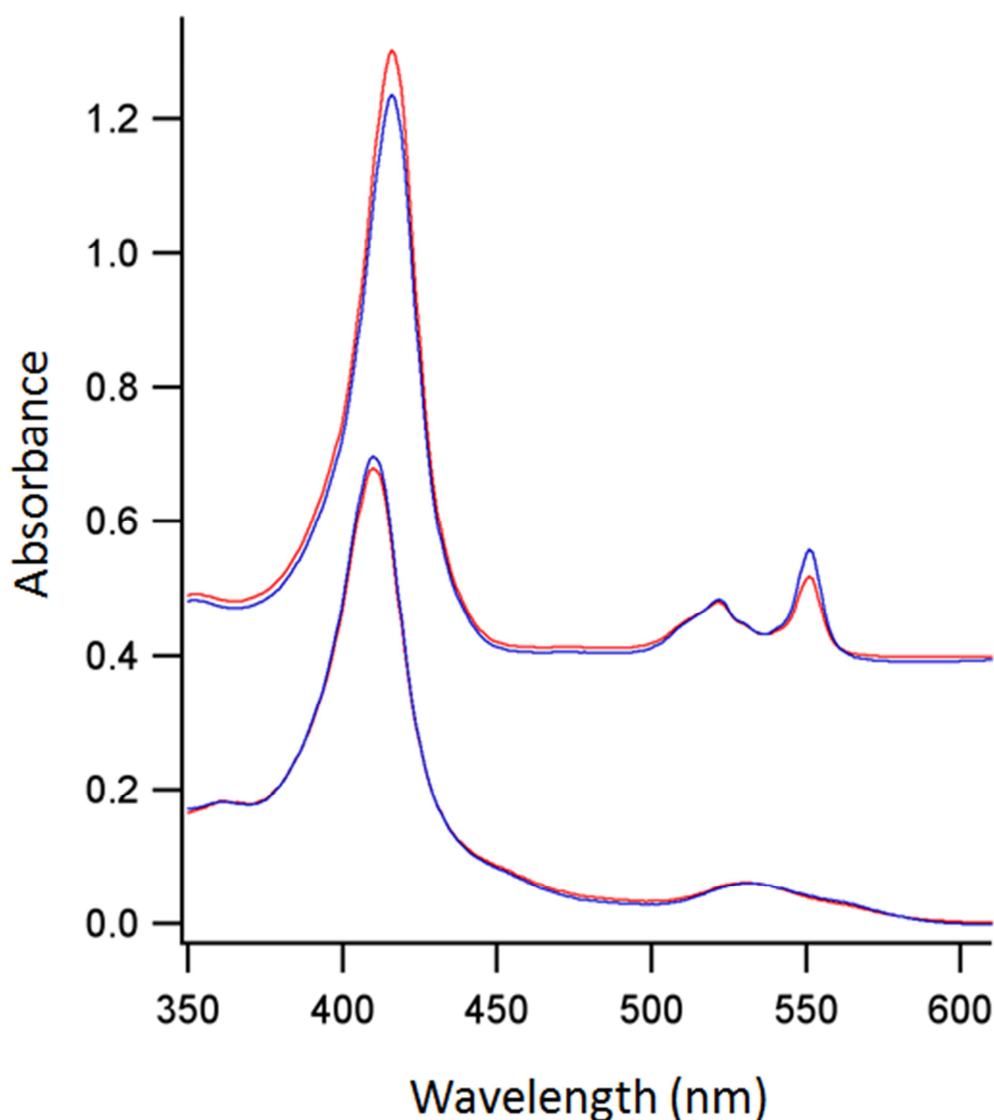
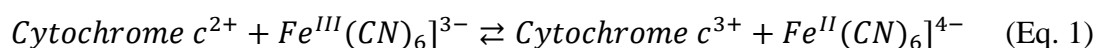


Figure 3. Absorbance spectra of ferro- and ferricytochrome *c* without fluid flow (–) and with a fluid flow rate (–) of 20 mL min⁻¹. Bottom spectra are ferricytochrome *c*. The spectra of ferrocytochrome *c* are offset by 0.5 A for clarity. The spectra are the average of the spectra recorded in pixels 0-1900, along the whole length of the flow-cell.

3.3 Calculation of the dead-time

To determine the dead-time of the set up, the reaction between ferrocytochrome *c* and sodiumferrihexacyanide was studied as in **Chapter 4**:



Spectra of cytochrome *c* in reaction with 20 mM ferrihexacyanide recorded in the time span from 3.8 μs (the first data point) to 70 μs after initiation of the reaction are shown in **Figs. 4** and **5**.

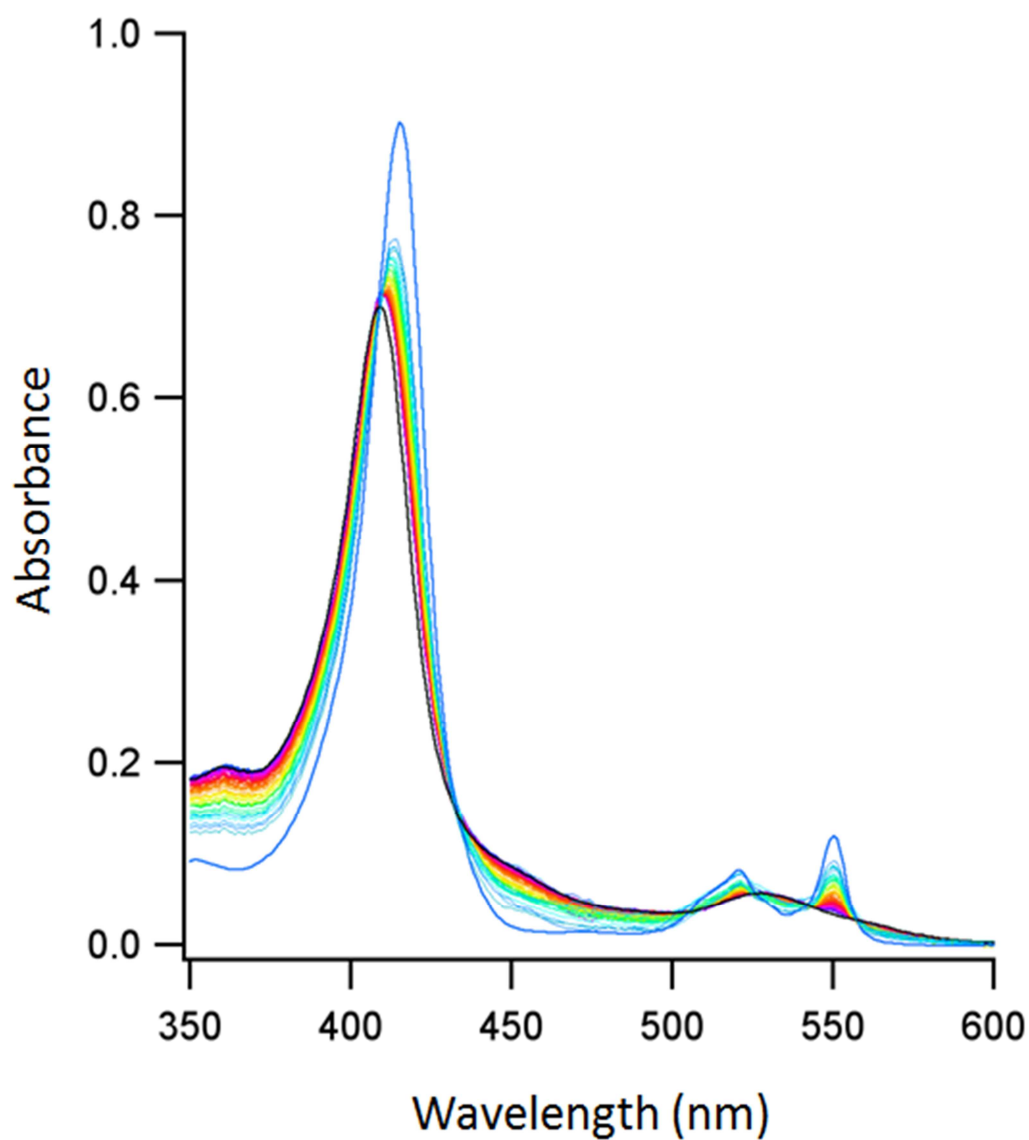


Figure 4. Spectra of cytochrome *c* (0.5 mM) in reaction with 20 mM ferrihexacyanide recorded in the time span from 3.8 μ s to 70 μ s after initiation of the reaction. The spectrum with the largest amplitude at 415 and 550 nm (\rightarrow) represents the $t = 0$ sample, recorded separately. The figure shows 190 spectra, i.e. the time resolution of the spectra is 350 ns.

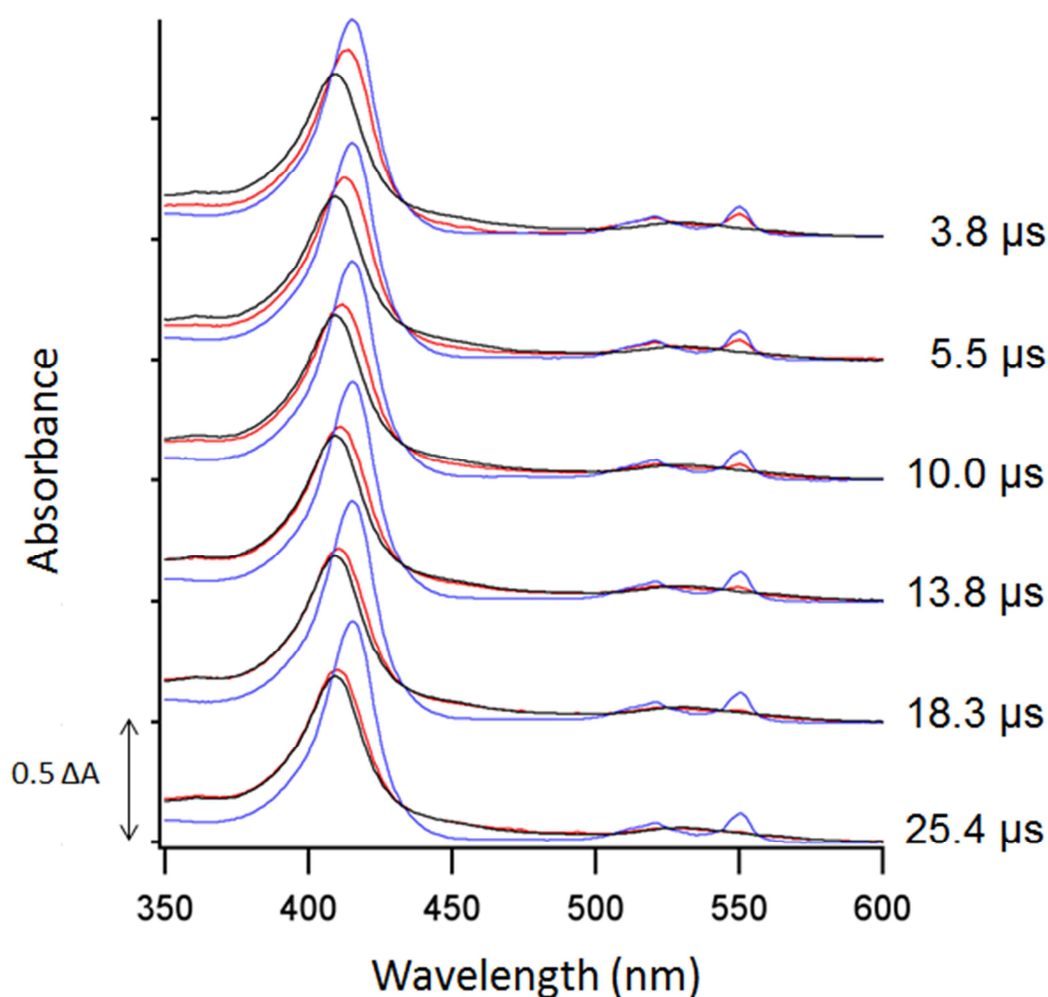


Figure 5. Selection of spectra of cytochrome *c* (0.5 mM) in reaction with 20 mM ferrihexacyanide (—) and comparison to the spectra of ferri- (—) and ferrocytochrome *c* (—) that both served as reference spectra to calculate the amount of conversion by component analysis.

The kinetic analyses (**Figs. 6** and **7**) were performed exactly as described in **Chapter 4**. Two-component analysis employed the spectra of ferri- and ferrocytochrome *c* as basis spectra (**Fig. 5**). Separate analyses were made for the Soret spectral region (352-450 nm, **Fig. 6a**) and for the α -band (500-600 nm, **Fig. 6b**); these latter analyses were combined to calculate the ionic strength (0.1 M) corrected second order rate constant (**Fig. 7**) yielding $k = 0.986 \pm 0.028 \cdot 10^7 \text{ M}^{-1} \text{ s}^{-1}$. The value determined here is in very good agreement with that determined in **Chapter 4** ($k = 0.96 \pm 0.03 \cdot 10^7 \text{ M}^{-1} \text{ s}^{-1}$). Also the dead-time of $3.8 \pm 0.3 \mu\text{s}$ indicated by the crossing of the simulated traces where the fraction of the reactant, ferrocytochrome *c*, equals 1.0 (**Fig. 6**) is the same as determined in **Chapter 4**. This is expected because the dead volume of the mixer channels and the *Pt* inlay are the same (1.2 and 1.3 nL) as well as the experimental fluid flow rate of 20 mL min^{-1} .

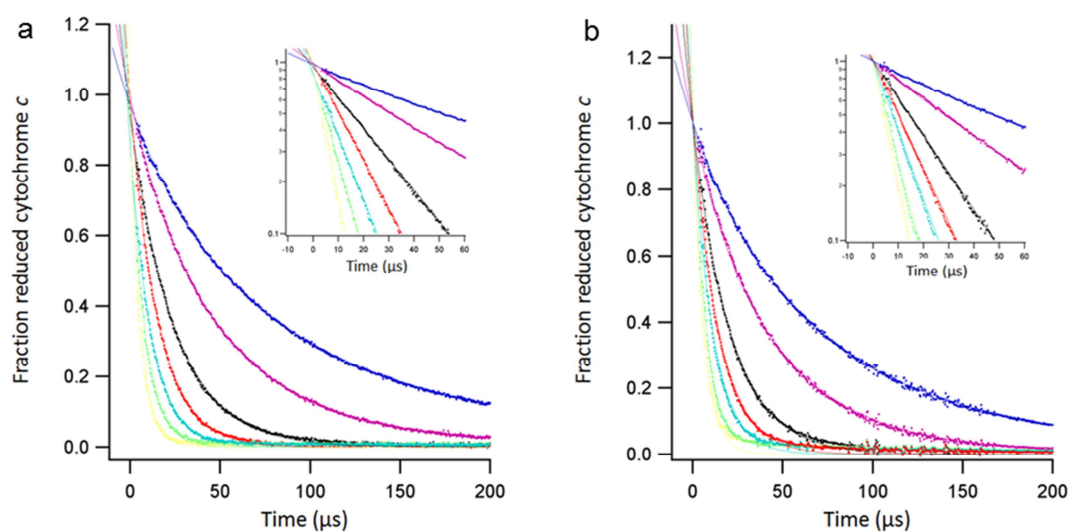


Figure 6. Kinetic traces of the reaction between ferrocyanide (0.48 mM) and various concentrations of sodium ferrihexacyanide at 27.5°C recorded with the improved continuous-flow setup. The graphs show the data after Two-component analysis as the fraction of ferrocyanide *c* vs time and after calculating the logarithm of this fraction (inset) for (a) the Soret region 352-450 nm and (b) the α -band region 500-600 nm. The buffer was 50 mM potassium phosphate (pH 7, Ionic strength is 0.1 M). Final ferrihexacyanide concentrations were: 1 mM (—), 2 mM (—), 5 mM (—), 10 mM (—), 20 mM (—), 50 mM (—) and 100 mM (—). The lines through the data points (b) are second-order fits (1 and 2 mM ferrihexacyanide) and first-order exponentials. The fits all cross in a single point (± 1 pixel or 318 ns) where the fraction of reduced cytochrome *c* equals 1. Kinetic traces (dotted) are shown from a time of 3.8 μ s (the determined dead-time). From this time onwards, the experimental data follow the fits.

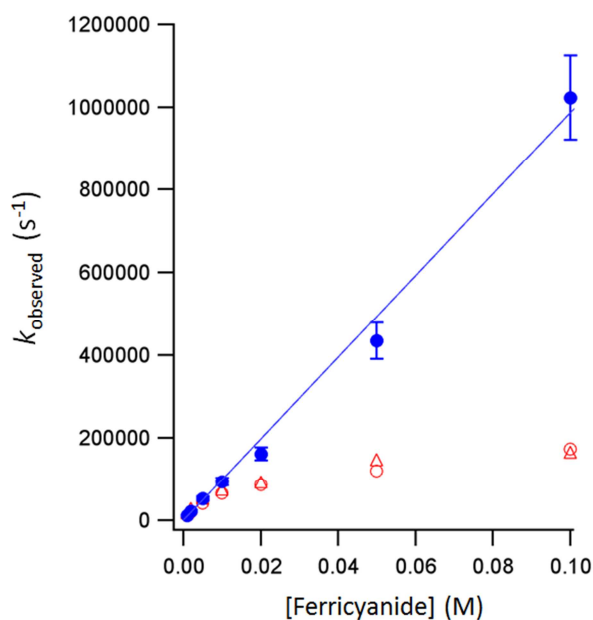


Figure 7. Observed rates (k_{observed}) as a function of the ferrihexacyanide concentration. (Δ) are from analysis of the Soret band, (\circ) of the α -band. (\bullet) are the observed rate constants after corrections for the ionic strength (see **text** and **Materials and Methods**) and the average of the analyses performed for the Soret band (**Fig. 6**) and α -band (**Fig. 7**); (—) is a linear fit through the origin and the data points yielding a second-order rate constant of $0.986 \pm 0.028 \cdot 10^7 \text{ M}^{-1} \text{ s}^{-1}$.

3.4. The refolding of denatured cytochrome *c*

Acid denatured cytochrome *c* at pH 2 refolds partially when the pH is rapidly changed to a final pH 4.5^{2,3,18}. Using Fluorescence spectroscopy to monitor changes in Trp59 or single wavelength UV-Vis absorbance spectroscopy in the Soret region two kinetic phases ($\tau = 59 \pm 5 \mu\text{s}$ and $\sim 435 \mu\text{s}$) were observed in the first few milliseconds of the refolding reaction^{2,3,18}. Although the rapid phase ($\tau = 59 \mu\text{s}$) is close to the instrumental dead-time (50 μs), Roder et al. concluded from extrapolation of the kinetic traces to time zero, that this phase was not preceded by an earlier (UV-Vis or Fluorescence observable) folding event.

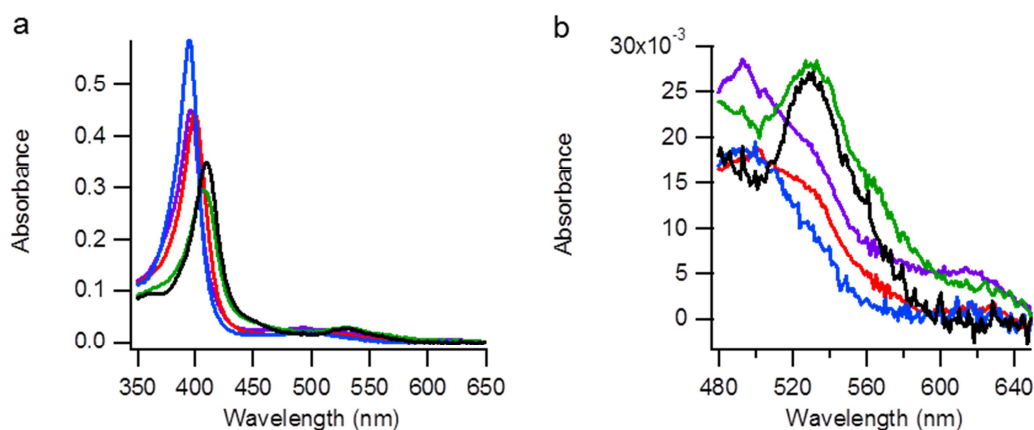


Figure 8. Spectral components obtained after SVD analysis. Unfolded - time zero, pH 2 (—), I_1 (—), I_2 (—), I_3 (—) and Folded - native, pH 6 (—). The spectral regions: (a) 350 – 650 nm and (b) 480–650 nm. The appearance of bands in the ‘so called’ Q region at 495 nm; and 530 nm and 560 nm are indicative for the formation of high spin (HS) and low spin (LS) species, respectively²⁴. The 500–580 nm region in I_3 is indicative for the presence of bis-His coordination (His18/His26 (or His33)), (Fig. 8 in²⁴). The appearance and disappearance of the band at 620 nm is considered to result from the formation of HS and LS ferric heme during the reaction, respectively (see also **Table 1**). The spectra were put arbitrarily at zero at 650 nm.

The new instrument was used to study the refolding kinetics of denatured cytochrome *c* by the same pH-jump technique as described by Roder. The experiment was performed at 20 mL min⁻¹ fluid flow rate providing a total reaction window of 0.65 ms (**Figs. 8** and **9**). Singular value decomposition (SVD) analysis of the spectra obtained during the reaction yielded four significant spectral components. Three rate constants and four spectra were calculated according to the following model: $U(\text{Unfolded}) \rightarrow I_1 \rightarrow I_2 \rightarrow I_3$. Herein I_3 is the final, partially folded, intermediate at pH 4.5. After a very rapid initial phase ($\tau = 4.7 \mu\text{s}$) not observed before, partial refolding proceeds with life times of 83 μs and 345 μs relatively close to the values quoted in ref.¹⁸. The uncertainty in these τ values was estimated as follows: the root mean square error (RMSE) values between the reconstructed and the modeled time traces for each of the four traces (cf. **Fig. 9**) were added to a single sum RMSE value. Then the three k -values in the model were modified by a certain percentage and the sum RMSE value was calculated between model and modified model. Correspondence between this and the previous sum RMSE value determined a general percentage uncertainty in the k values and therefore approximately so in the τ values. The found uncertainty was circa $\pm 20\%$. The Soret maxima of the three calculated spectral intermediates (I_1 , I_2

and I_3) progressively shift to the red during the reaction from 395 nm to 408 nm for I_3 (**Table 1**). In addition, appearance and disappearance of the absorbance at 620 nm indicates a change from HS to LS of the heme iron during the reaction, respectively (**Fig. 8, Table 1**). The calculated spectrum of I_3 differs from the fully folded native cytochrome *c* (**Fig. 8, Table 1**) indicating that the protein does not fold to the native state on this time scale (**Table 1**,^{18,20-22}).

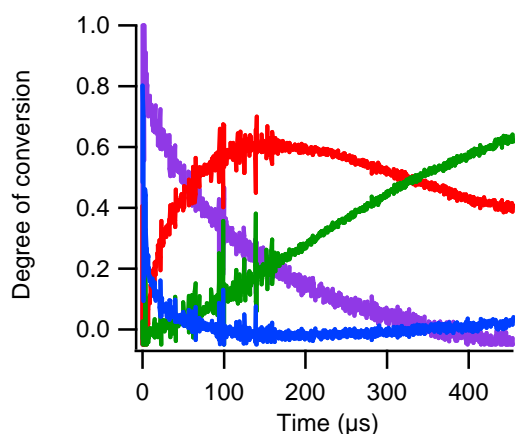


Figure 9. Kinetic traces of acid denatured cytochrome *c* in a pH-jump experiment obtained after SVD analysis. Unfolded - time zero, pH 2 (—), I_1 (—), I_2 (—) and I_3 (—).

Table 1. Kinetic and structural properties of native cytochrome *c* and folding intermediates

State	Heme Fe-ligation (Spin state)	Soret maximum (nm) ^{ab}	Q region (nm) ^b	Band at 620 nm ^b	Formation time constant, τ (μ s)
2^a	W and/or W-W (HS) H18-M80, H18-H26/33 (LS)	395 (HS)	495 (HS)	No intensity (LS)	
I_1	H18-W (HS, LS)	397 (HS, LS)		620 (HS)	4.7
I_2	H18-W (HS, LS)	400 (HS, LS)		No intensity (LS)	83
I_3^a	H18-M80 (LS) H18-H26/33 (LS) W, W-W (HS)	408 (LS)	530 and 560 (LS)	620 (HS)	345
Native	H18-M80 (LS)	410 (LS)	530 and 560 (LS)	No intensity (LS)	

^{a,b}Assignments of heme ligation based on^{24,25}, respectively). W is water as ligand. LS = predominantly low spin, HS = predominantly high spin; LS, HS = a mixture of low and high spin.

4. Discussion and conclusions

A rectangular flow cell was designed to reduce uncontrollable light scattering effects, which occur in the cylindrical flow cell described in **Chapter 4**. The microchannel of the flow cell is constructed from two parallel sheets of silver (**Fig. 1**). Both light loss and stray light are greatly reduced in the rectangular microcuvette compared to the cylindrical cuvette (**Fig. 2**). As a consequence, the absorbance is linear with concentration up to at least 3.5 AU. In contrast to the cylindrical cuvette, where the extinction coefficient is approximately halved (**Chapter 4**) the extinction coefficient determined for regular (e.g. 1 cm path length) rectangular cuvettes applies using a path length of 109 μ m, the thickness of the silver sheets. In addition, the spectra can

be referenced against buffer; using a calibrated BSA solution with the same density as that of the protein or buffer as reference produced the same spectra. The reduction in loss of light made it possible to average each data point five times and was the main determinant decreasing the noise level from $\pm 0.001 \Delta A$ to $\pm 0.0003 \Delta A$. The dead-time of the improved setup remained the same ($3.8 \pm 0.3 \mu s$) because the dead volumes of the mixer and *Pt* seal were the same as described in **Chapter 4**.

The refolding kinetics of acid denatured cytochrome *c* was studied using the pH-jump technique. Using SVD analysis three time constants and four spectra were calculated that represent the main components formed in the first 0.65 ms of the reaction. The reaction was previously assumed to consist of two irreversible steps as indicated above but actually three intermediates were found. A very rapid initial phase ($\tau = 4.7 \mu s$) not observed before significantly improved the analysis. The calculated life times (83 and 345 μs) are similar (59 and 435 μs , respectively) to those found by the group of Roder¹⁸. The process with a life time of 4.7 μs has not been observed previously and significantly improved the analysis.

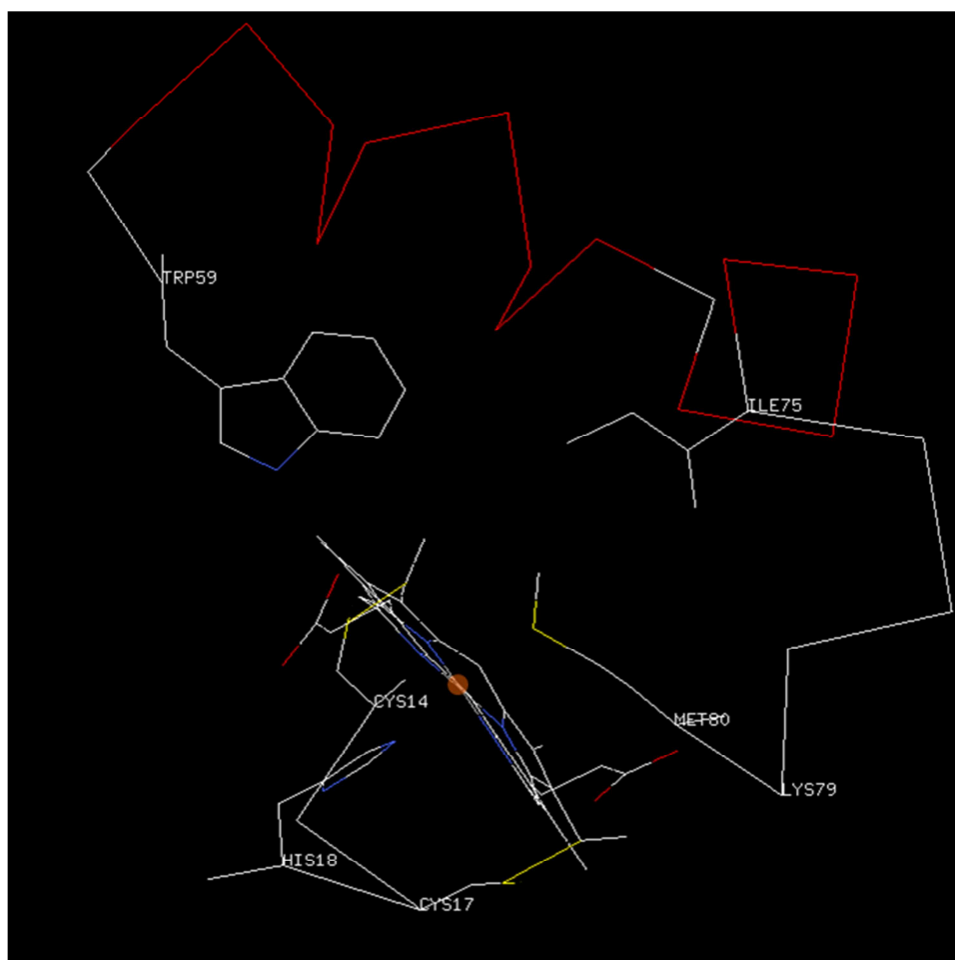


Figure 10. Structure of (native) cytochrome *c* around the heme. (●) Orange sphere Fe^{3+} . (—) The two α -helical stretches (Res61-69 and Res71-74) surrounding the heme. Trp59 and Ile75 are located at the beginning of the first and at the end of the second α -helical stretch, respectively. (—) Sulphur from Cys14 and Cys17 covalently linked to the porphyrin ring; sulphur from Met80 (not bonded to Fe^{3+}). The Fe-His18 bond and coordinating water are not shown. Drawing made with Swiss-PdbViewer from PDB 1HRC.

At the initial pH 2, the heme Fe^{3+} is high spin with one or more weakly coordinating ligands²⁵. Resonance Raman spectroscopic analysis indicated that at pH 2 a mixture of different components is present (**Table 1** in refs.^{22,25}). Progressive unfolding by lowering the pH leads to protonation of His18 and dissociation from the heme iron, which is then coordinated by one or two water ligands. The high spin form at pH 2 exhibits a Soret maximum at 395 nm and another band at 495 nm indicative of HS heme iron, suggesting coordination with two weak-field ligands according to ligand or crystal field theory. Shifts in the Soret maximum generally report both spin state and polarity changes. Coordination of one strong-field ligand and one weak-field ligand produces a mixture of high- and low-spin configurations having a Soret maximum between 396 nm and 400 nm²⁵. Therefore, I_1 and I_2 are both mixtures of high- and low-spin configurations and because I_1 spectrum contains the 620 nm band (**Table 1**). The shift in Soret maximum from 395 to 400 nm (I_1 to I_2) suggests a decreased polarity of the heme environment in I_2 . In the last intermediate, I_3 , Fe^{3+} is predominantly in the low spin state because the Soret maximum is above 400 nm and Q bands are found at 530 nm and 560 nm, suggesting coordination by two strong-field ligands²⁴.

Work described in²⁰⁻²² considers the His18 - Fe^{3+} - so called W intermediate central both to the formation of the native structure (His18 - Fe^{3+} - Met80) and to the misfolded state His18 - Fe^{3+} - His26 (or His33) where after ~1-2 ms both these states are formed²⁰⁻²². The spectrum of I_3 in terms of its Soret maximum at 408 nm and its intensity at ~530-560 nm (**Fig. 8** in²⁴) is consistent with a mixture of native and misfolded forms in the proportion given in **Table 1**.

The recent NMR H/D exchange study¹ showed rapid folding (in 0.6 M urea, pH 9.8) of the two α -helical segments that surround the heme (**Fig. 10**). Although the time resolution was 140 μs , the results indicated solvent shielding of the α -helical segments (61-69 and 71-74) with rates of the individual residues between 8-20 μs . Moreover, solvent shielding for W59 and Ile75 was even faster, estimated <6.7 μs (**Fig. 5** in¹). We therefore propose that the 4.7 μs phase observed here represents the very initial event of helix formation (I_1) triggered by residues W59 and Ile75. The formation of α -helical segments 61-69 and 71-74 and that of the C-terminal α -helix (89-120, with individual solvent shielding rates of 20-100 μs (**Fig. 5** in ref.¹), might collectively be represented by the 83 μs phase (I_2). Formation of these α -helical segments is expected to lead to loss of solvent water surrounding the heme and thus to a lowered polarity, consistent with the Soret maximum of I_2 at 400 nm. Formation of the C-terminal α -helix is important to bring Met80 into contact with the heme iron and to form the native structure. Production of the misfolded His18 - Fe^{3+} - His26 (or His33) state is probably due to the slow (1-2 ms) formation of the N-terminal α -helix (Res3-13). The formation of the native and misfolded low spin forms (I_3) takes 345 μs (**Table 1**). The misfolded and native states are in rapid (~30 ms) equilibrium via the His18 - Fe^{3+} - W state^{20,21}, which subsequently can fold to the native state.

Our results show that following a pH jump from pH 2 to pH 4.5, His18 deprotonates and ligates to the heme Fe^{3+} . Deprotonation and bond formation can actually occur well within 4.7 μs . The local structural change brought about by formation of the iron-histidine bond affects the local structure of Trp59 and Ile75, detected as a very fast protection against H/D exchange¹, which we propose is the first step (4.7 μs) in the

formation of the two α -helical segments 61-69 and 71-74 around the heme (**Fig. 10**) and in the formation of the C-terminal helix, collectively detected as the 83 μ s phase. At this stage the heme Fe^{3+} is HS and ligated by His18 and a water residue. From this intermediate the native and the misfolded bis-His states are formed, the latter equilibrating to the native state as the N-terminal helix progressively forms over time. Under *in vivo* conditions the Fe^{3+} - His18 bond is likely formed immediately following covalent linkage of the two Cys residues to the heme, i.e. the state seen here in the first few microseconds of the reaction. From there on the protein folds into its native conformation with the possible reversible formation of a misfolded intermediate His18 - Fe^{3+} - His26 (or His33).

5. Materials and methods

5.1 Instrumentation and construction of the rectangular flow-cell

The improved ultrafast mixing device employs the same parts as the Continuous Flow Ultra-Fast Mixing Instrument described in **Chapter 4** but instead of a cylindrical cuvette it employs a 30 mm long rectangular cuvette ($70 \pm 5 \mu\text{m}$ path length) integrated in the cuvette holder (**Fig. 1**). The rectangular flow channel is constructed from two parallel sheets of silver foil with a thickness of $109 \mu\text{m}$ separated by $70 \pm 5 \mu\text{m}$. The silver foil acts as a seal to prevent leakage of the pressurized fluid (up to ~ 400 bar) and also acts as an effective shield to reduce stray light thus producing a spectrophotometer that is linear up to at least 3.5 Absorbance Units.

The cuvette-holder is physically connected to the stainless-steel micro-mixer via a disc-shaped seal of soft material of Pt ($50 \mu\text{m}$ thick, with a central hole of $100 \mu\text{m}$). Light from a 75 W Xenon lamp was passed through an Optical Building Blocks monochromator with a $1,200 \text{ g mm}^{-1}$ 500 nm blaze grating. A collimating and a plano-convex lens were used to focus light on the flow channel as described in **Chapter 4**.

Alignment of the setup, spectral recordings, data acquisition, processing, analyses and graphical presentation of data were performed in the same way as in the **Chapter 4**. Monochromator entrance and exit slits were set at 0.1 mm (0.4 nm) and 0.95 mm (3.8 nm), respectively. Spectra were recorded in crop 200 mode of the CCD camera at a rate of 50 nm s^{-1} or 20 ms. The illumination time was 220 μs per cycle. In each scan of 20 ms five cycles were recorded and averaged, i.e. the total dark time was 18.9 ms, the total illumination time 1.1ms. SVD analyses were performed with home-written programs in IgorPro by S. de Vries† and later in LabView by W.R. Hagen following the guidelines in²⁶.

5.2 Kinetic experiments

Continuous-flow kinetic measurements with the improved setup were performed at a total flow rate of 20 mL min^{-1} , at 27.5°C , in the spectral range from 350 nm to 600-650 nm. A stock solution of 2.2 mM ferrocyanochrome *c* (the oxidized form reduced by 4.4 mM of ascorbic acid) was diluted to 0.96 mM; this latter solution was mixed with different sodiumferrihexacyanide concentrations varying from 1-102 mM. All solutions contained 50 mM phosphate buffer (pH 7.0). In separate experiments

oxidized and reduced cytochrome *c* (0.96 mM) were mixed versus buffer only. The data from these latter experiments served as the basis set for Two-component analysis. Refolding experiments of acid denatured cytochrome *c* were performed at flow rates of 20 mL min⁻¹. Ferricytochrome *c* (0.5 mM) was dissolved in water and adjusted to pH 2 with HCl. This solution was rapidly mixed with a buffer of 50 mM phosphate, 50 mM acetate (pH 6.08) yielding a final pH after mixing of 4.54 and a final concentration of 0.25 mM cytochrome *c*. The time zero spectrum used to calculate the reaction progress was prepared by mixing two solutions of 0.25 mM cyt *c* at pH 2.

References

1. Fazelinia, H.; Xu, M.; Cheng, H.; Roder, H. Ultrafast hydrogen exchange reveals specific structural events during the initial stage of folding of cytochrome c. *Journal of the American Chemical Society*, 2014, 136, 733-740.
2. Roder, H.; Maki, K.; Cheng, H. Early events in protein folding explored by rapid mixing methods. *Chemical Reviews*, 2006, 106, 1836-1861.
3. Shastry, M. C.; Roder, H. Evidence for barrier-limited protein folding kinetics on the microsecond time scale. *Nature Structural Biology*, 1998, 5, 385-392.
4. Shank, E. A.; Cecconi, C.; Dill, J. W.; Marqusee, S.; Bustamante, C. The folding cooperativity of a protein is controlled by its chain topology. *Nature*, 2010, 465, 637-640.
5. Roder, H.; Colon, W. Kinetic role of early intermediates in protein folding. *Current Opinion in Structural Biology*, 1997, 7, 15-28.
6. Roder, H.; Maki, K.; Latypov, R. F.; Cheng, H.; Shastry, M. C. R. *In Protein folding handbook*. Part I: Bucher, J.; J. Kiefhaber, T.; Eds.; Wiley-VCH: Weinheim, Germany, 2005.
7. Tapan K. Chaudhuri and Subhankar Paul. Protein-misfolding diseases and chaperone-based therapeutic approaches. *FEBS Journal*, 2006, 273, 7, 1331-1349.
8. Dumont, M. E.; Cardillo, T. S., Hayes, M. K. and Sherman, F. Role of cytochrome c heme lyase in mitochondrial import and accumulation of cytochrome c in *Saccharomyces cerevisia*. *Molecular and Cellular Biology*, 1991, 11, 5487-5496.
9. Gonzales, D. H. and Neupert, W. Biogenesis of mitochondrial c-type cytochromes. *Journal of Bioenergetics and Biomembranes*, 1990, 22, 753-768.
10. Jiang, X.; Wang, X. Cytochrome c-mediated apoptosis. *Annual Review of Biochemistry*, 2004, 73, 87-106.
11. Yeh, S. R.; Han, S and D. L. Rousseau. Cytochrome c folding and unfolding: A biphasic mechanism. *Accounts of Chemical Research*, 1998, 31, 727-736.
12. Theroell, H.; Akessen A. Absorption spectrum of further purified cytochrome c. *Science*, 1939, 90, 67.
13. Soffer, J. B.; Fradkin, E.; Pandiscia, L. A.; Schweitzer-Stenner, R. The (Not Completely Irreversible) Population of a Misfolded State of Cytochrome c under Folding Conditions. *Biochemistry*, 2013, 52, 1397-1408.
14. Tsong, T. Y. Ferricytochrome c chain folding measured by the energy transfer of tryptophan 59 to the heme group. *Biochemistry*, 1976, 15, 25, 5467-5473.
15. Lowenich, D.; Kleinermanns, K. Porphyrin Fluorescence Dominates UV Photoemission of Folded Cytochrome c. *Photochemistry and Photobiology*, 2007, 83, 1308-1312.
16. Elove, G. A.; Chaffotte, A. F.; Roder, H.; Goldberg, M. E. Early steps in cytochrome c folding probed by time-resolved circular dichroism and fluorescence spectroscopy. *Biochemistry*, 1992, 31, 30, 6876-6883.
17. Elove, G. A.; Bhuyan, A. K.; Roder, H. Kinetic Mechanism of Cytochrome c Folding: Involvement of the Heme and Its Ligands. *Biochemistry*, 1994, 33, 22, 6925-6935.
18. Shastry, M. C.; Luck, S. D.; Roder, H. A continuous-flow capillary mixing method to monitor reactions on the microsecond time scale. *Biophysical Journal*, 1998, 74, 2714-2721.
19. Werner, J. H.; Joggerst, R.; Dyer, B.; Godwin, P. M. A two-dimensional view of the folding energy landscape of cytochrome c. *PNAS*, 2006, 103, 30, 11130-11135.
20. Takahashi, S.; Yeh, S. R.; Das, T. K.; Chan, C. K.; Gottfried, D. S.; Rousseau, D. L. Folding of cytochrome c initiated by submillisecond mixing. *Nature Structural Biology*, 1997, 4, 1, 44-50.
21. Yeh, S. R.; Takahashi, S.; Fan, B.; Rousseau, D. L. Ligand exchange during cytochrome c folding. *Nature Structural Biology*, 1997, 4, 51-56.
22. Yeh, S.R.; Rousseau, D. L. Folding intermediates in cytochrome c. *Nature Structural Biology*, 1998, 5, 3, 222-8.
23. Yeh, S. R.; Rousseau, D. L. Ligand Exchange during Unfolding of Cytochrome c*. *The Journal of Biological Chemistry*, 1999, 274, 25, 17853-17859.
24. Santoni, E.; Scatragli, S.; Sinibaldi, F.; Fiorucci, L.; Santucci, R.; Smulevich, G. A model for the misfolded bis-His intermediate of cytochrome c: the 1-56 N-fragment. *Journal of Inorganic Biochemistry*, 2004, 98, 6, 1067-77.
25. Babul, J.; Stellwagen, E. Participation of the protein ligands in the folding of cytochrome c. *Biochemistry*, 1972, 11, 7, 1195-1200.

26. Henry, E. R.; Hofrichter, J. Singular value decomposition: Application to Analysis of Experimental Data, *Methods in Enzymology*, 1992, 210, 129-192.

Chapter 6

Conclusions and outlook

Understanding the chemical details of enzyme catalyzed reactions constitutes a main focus of current research in the fields of biochemistry and biocatalysis. Such fundamental knowledge is needed to more successfully employ enzymes for application purposes e.g. in drug discovery and medical science in general, and providing 'green catalytic' alternative solutions to current approaches in the chemical industry that in many cases produce too much waste or too many side products.

Fundamental insight in the function of (bio)catalysts requires knowledge of their three dimensional structure and a wide range of time resolved experiments aiming to unravel each and every chemical step of the overall reaction. This thesis has focused on the design, development and characterization of new rapidly mixing micro-mixers to perform time-resolved experiments. One such micro-mixer, a four-jet tangential micro-mixer, has been fully characterized for its flow and mixing properties and was integrated in a new kinetic instrument that enables monitoring (bio)chemical reactions by UV-Vis spectroscopy that can observe reactions in the microsecond timescale, with a dead time of 3-4 microseconds. This is close to the timescale ($\sim 0.1-1 \mu\text{s}$) for the fastest formation of enzyme intermediates involving bond-breaking and bond-making reactions and for the folding of (small) protein domains.

It was realized approximately ninety years ago that in order to study catalytic mechanisms of enzymes and chemical reactions in detail, the reaction should be initiated so rapidly that the subsequent formation and decay of all reaction intermediates can be detected. With this in mind rapid mixing equipment was developed that replaced the then current practice of mixing reagents by hand. The first instruments (between 1923-1930) were continuous-flow mixing set ups in which the reaction time increases along the observation cell; the best instrument had dead-time of ~ 2 ms. In the 1930's and early 1940's the stopped-flow instrument was developed (dead-time ~ 1 ms) and in the last twenty years instruments with a miniaturized mixer (dead-time ~ 0.5 ms). The consumption of reagents in the stopped-flow setup is greatly reduced compared to that in continuous-flow instruments, which is the main reason for the wide-spread use of the stopped-flow for research purposes. However, the dead-time of the stopped-flow instrument is limited by how fast the fluid flow can be arrested and hence, the dead-time of ~ 0.5 ms is not likely to be improved further.

With the advance of microsystem technology in the last twenty years it became possible to construct micro-mixers with microfluidic ($\sim < 500 \mu\text{m}$) channels. These micro-mixers are mostly used in continuous-flow 'lab-on-a-chip' devices for analytical purposes but can also be used in kinetic instruments. The fastest present-day continuous-flow mixing instruments with UV-Vis read out have mixing times of $\sim 11 \mu\text{s}$ and $\sim 45 \mu\text{s}$ and employ a T-mixer or co-axial ball mixer, respectively. We have previously designed a stainless-steel four-jet tangential micro-mixer that is used in a microsecond freeze quench set up. The mixing properties of this mixer are not known, except that it mixes solutions faster than $10 \mu\text{s}$.

Four-jet tangential mixers

In order to build a kinetic instrument with microsecond time resolution we first determined the premixing and mixing properties of the stainless-steel four-jet tangential micro-mixer using optically transparent glass-silicon micro-mixer chips of similar geometry. Employing acid-base reactions monitored by a pH-sensitive fluorescent dye the optical and stainless-steel mixers show very similar (unwanted) premixing and mixing profiles in the vortex chamber and after the mixing chamber in a free-flowing jet, respectively. The amount of premixing varies from ~9% (for 25 μm orifice chips) to a maximum of 15% (for chips of 70 μm orifice) and is even lower than 9% in the stainless-steel mixer (20 μm orifice) because the length of the vortex chamber is shorter. The ABAB configuration of the mixers in which the channels with the same reagents (A or B) are opposed (rather than side-by-side as in the AABB configuration) and offset by one-half to one channel diameter creates a vortex of four fluids that rotate around one another, which leads to a decrease in the diffusion distances and improves the mixing performance. As a result, (near) complete mixing occurs at $Re \sim 1000$ to 1500, which is well below the value of 2040 ± 10 for the onset of sustained turbulent flowing a pipe. For the stainless-steel mixer, we calculated a mixing time of only 160 ns (for a 20 μm orifice), which is at least 50 times shorter than estimated for other fast mixing devices.

Continuous flow ultra-fast mixing instrument

A continuous flow ultra-fast mixing instrument with major advances in time resolution was built with a dead-time of $3.8 \pm 0.3 \mu\text{s}$ which is 10-20 fold shorter than any other continuous-flow mixing instrument in the world and represents an improvement of at least factor of 300 in time resolution over commercially available stopped-flow instruments.

The instrument employs a four-jet tangential stainless-steel micro-mixer that completely mixes two liquids within 3.5 μs . This dead-time is solely determined by the dead volume of the four channels with $\sim 50 \mu\text{m} \times \sim 50 \mu\text{m}$ dimensions. These channel dimensions are determined by the dimensions of the optical path length ($\sim 100 \mu\text{m}$) to produce high quality – nearly free of stray light – UV-Vis spectra ($S/N > 50$) even when using a highly sensitive CCD camera. Each spectrum is recorded in a volume of only 106 pL with 10-90 femtomol of enzyme, which with a path length of $\sim 100 \mu\text{m}$ requires high concentrations of reagents ~ 0.2 -1 mM. The latter remains a general disadvantage of continuous-flow over stopped-flow methods. In a typical experiment, ~ 1900 UV-Vis spectra are recorded in a single scan of the monochromator between 300-700 nm and separated in time by only 318 ns for 600 μs at the highest flow rate of 20 mL min^{-1} . The new instrument was successfully used to study protein refolding of denatured horse heart cytochrome *c*. After a very rapid initial phase ($\tau = 4.7 \mu\text{s}$) not observed before, partial refolding proceeds with time constants of 83 μs and 345 μs . Using singular value decomposition the complete spectra of three folding intermediates were determined.

Final remarks

Four-jet tangential micro-mixers with an ABAB channel configuration described in this work are faster than any other mixing device design so far. The extension to 8 or 16 tangential fluid channels leads to more or even complete premixing in the vortex chamber⁹. This behavior is suitable for lab-on-a-chip applications where a 1-ms time resolution is adequate, but for the design of instruments with (sub)microsecond time resolution premixing should be prevented as much as possible. The research described in this thesis allowed us to formulate a set of guidelines in order to design fast mixing micro-mixers. To minimize the amount of premixing, the height (or length) of the vortex chamber should be as small as possible to reduce the retention time for diffusion across the fluid boundaries. On the other hand, the diameter of the vortex chamber should be as large as possible with respect to the diameter of the mixing chamber. This will maximize the ratio of the Re values in the mixing chamber and vortex chamber and, thus, minimize premixing resulting from turbulence at the fluid boundaries. In view of the quadratic relation between pressure and fluid flow rate, the micro-mixers described here could be used at approximately 2-fold higher flow rates before protein denaturation sets in, potentially decreasing the mixing time to less than 100 ns. Because the great majority of the glass-silicon micro-mixers that were used to study the premixing and mixing behavior were found to be stable at pressures up to 10 MPa, they themselves can be employed for large-scale production of nanosecond mixers.

The continuous flow ultra-fast mixing instrument is used for the study of transient (bio)chemical reactions by optical spectroscopy. Although an increase in temperature relative to ambient cannot be avoided due to the energy release during turbulent mixing, the micro-mixer plus cuvette holder could be provided with a thermostat expanding the applications of the current setup. The UV-Vis spectrometer can be used either in front-face or 90° fluorescence mode by placing a transparent plexiglass window within the black plexiglass body perpendicular to the capillary flow cell. The continuous flow ultra-fast mixing device described in this thesis fills the current gap in instrumentation to study (bio)chemical reactions on the microsecond time scale and enables detailed kinetic analyses of the very onset of substrate and ligand binding, biocatalysis and protein folding.

Curriculum Vitae

Sandra Mitić was born on the 12th of October 1976 in Belgrade, Serbia (at that time Yugoslavia). In 2002 she obtained her BSc degree (5 years university program, eqv. M.Sc./M.Eng.), in the department of Biochemical Engineering and Biotechnology, at the faculty of Chemical Engineering and Metallurgy of the University of Belgrade. After graduation she worked as a Sales Specialist in a commercial company which dealt with selling of laboratory supplies and chemicals, Megra in Belgrade. In 2003 she worked as a product technologist in quality-control and production of cosmetic-, medical-plant-based products, and baby products and chemicals in BeoLab Laboratories in Belgrade. Finally in 2004 she worked as process and product technologist, trouble-shooter regarding the production processes and packaging of 7 production lines. She was involved in the quality-control and stability tests of semi- and final- hygiene products. She took part in product innovation, design and development based on customers' desires and quality-price balance in Drenik ND, Belgrade, Serbia.

In 2005 she started her PhD in the Enzymology group, in the department of Biotechnology, at TU Delft, in the Netherlands, under the supervision of professor Simon de Vries†. During her doctoral studies she collaborated with the Mesa⁺ research institute at TU Twente in Enschede. Her main focus since she started her scientific career in the Netherlands, first as PhD student, later as a research scientist at VSL, Holland Metrology Institute in Delft, and recently again as a postdoctoral researcher in the department of Biotechnology, at TU Delft, has been instrumental method development of several micro- and nano-flow analytical innovative devices.

List of Publications

- Mitić, S.; van Nieuwkastele, J.; van den Berg, A.; de Vries†. S. 'Design of turbulent tangential micro-mixers that mix liquids on the nanosecond time scale', *Analytical Biochemistry*, 2015 Jan 15; 469:19-26
- Mitić, S.; de Vries†. S. 'Rapid Mixing Techniques for the Study of Enzyme Catalysis' *Comprehensive Biophysics*, Vol. 1, 2012. pp. 514-532

Acknowledgments

Every beginning has an end and the end of my thesis is here. All of it would not be possible without people whom I would like to thank for being part of my thesis in one way or the other.

First of all, I would like to express my deepest gratitude to my promoter, Prof.dr. Simon de Vries†. If it was not for Simon back in 2005 I would not have had the opportunity to become a member of Enzymology group, experienced and achieved everything I did in that time frame. Simon taught me how to face, feel and experience part of science and its challenges. His door was always open for me to discuss things, argue about science, agree and/or disagree about the progress of my thesis and when needed to talk about personal matters. Simon was as family to me for more than 10 years, I could always rely on him and I would always get a quick reply from Simon either in person or on each and every of my emails. He was always eager to inspire me to do the right thing in the right way. He was really a great scientist, what he knew he knew best, and rarely one could make him change his mind. Simon was always an optimist and through each and every step of building our instrument, he knew how to motivate me to reach our mutual goal. I truly appreciate how much knowledge, ideas, effort, optimism and love he put in our work. He gave himself totally (>100%) in whatever he did. Often enough he was a perfectionist as I am myself. All of it together was the reason why my thesis, and I am convinced ‘one of’ his life-time wishes to make such a great kinetic instrument took so long. Several times during my PhD career I had (work related and personal) setbacks but he always found a way to convince me to continue. It makes me very sad that he is not there anymore to promote one of his longest lasting PhD candidates in his career in person and to be there to see **Chapter 5** get published. I will never get to hear what he thought of me during those years in his end speech just before I would get the PhD title. Numerous times he told me that he had the speech ready in his head. But as it goes without saying, I can still hear and would always recognize Simon's typical sentences and his writing style, as much as I can predict a part of that speech. I am sure that my defense would make him proud of himself.

I am grateful to Prof.dr. Wilfred Hagen, because without a doubt, Fred, you put so much time and effort to understand and redo the SVD analysis, and without the Singular Decomposition Value analysis ‘SdV analysis’ the thesis will not have such an impact. Thank you Fred for your scientific contribution, support and help to finalize my thesis during the last 12 months and for all discussions during our group meetings which helped me to grow as a scientist.

I would further like to thank Dr. Peter-Leon Hagedoorn. Thank you Peter-Leon for your scientific contribution during our group discussions, your ideas and final minor thesis comments and remarks.

For enabling and funding this NanoNed project I thank Prof.dr. Albert van den Berg from the Mesa+ research institute at TU Twente in Enschede. Thank you Albert for your scientific contribution during our yearly NanoNed meetings, symposiums and conferences. Thank you Jan van Nieuwkastele for fabricating the four-jet tangential

ABAB glass-silicon micro-mixer chips at the Mesa+ research institute. Without the NanoNed fundings and the glass-silicon mixers the project would not have succeeded.

I am thankful to our previous and current head of the department Prof.dr. J.H. de Winde and Prof.dr. Isabel W.C.E. Arends. Thank you both for your help and creative support regarding organizational matters.

I am also thankful to Dr. Peter D.E.M. Verhaert and Gert van der Steen for making available to us the Nikon Eclipse inverted microscope.

Many thanks to my workshop colleagues Arno van den Berg and Marcel Langeveld. Thank you both for your daily, years long assistance in the workshop, and in the lab, in building numerous parts of the NanoSpec Instrument. Without your expertise we would not be able to build the instrument.

I want to take this opportunity to thank our secretary Mieke van der Kooij. Mieke thank you for your kindness, help and fast response regarding administrative matters

I would like to thank Marc Strampraad for his technical support, continuing the NanoSpec work after my contract finished and for performing the cytochrome c refolding experiment.

I would like to thank my paranymphs, Angela and Milja. Thank you Angela for being with me from the very beginning to the very end of my thesis. I enjoyed sharing my ideas, achievements and setbacks with you. Milja thank you for your support and friendship during the last 12 months.

Thanks a lot to my colleagues from the Enzymology group for their group discussions, comments and friendship at various times during my PhD: Laurice, Franky, Heidi, Alexey, Elena, Inga, Yana, Loes, Esengül, Marieke, Barbara, Laura, Emil, Peter, Ana (and Roeland), Marija, Nahid, Kourosh, Linda, Aida, Dubravka, Sinan and Eda (and Aksel). I would also like to thank Sjaak and Jos Lispet, Ginie Klumpers, Herman Frumau, Kees Boshuizen, Hans Kemper, Johan Knoll and Robert van Tuijll for their help over the years.

Last, but not least my gratitude and appreciations go to both my family in Serbia and here in Holland. Hvala ti mama što si mi omogućila uz Bongovu pomoć da završim V Beogradsku gimnaziju i tehnološki fakultet. Hvala ti što si mi pokazala put u svet i naravno hvala i tebi Minji što si zajedno sa mamom, kao i tetana Spoma jednim delom, uvek bili uz mene, pomagali mi i podržavali me u svim mojim odlukama i delima. Hvala vam mama i Minja što ste uvek uskakali i brinuli se o meni, Jurunu i našoj deci, što ste uvek uz nas kad god je to potrebno.

Thank you Jurune for all of your support, understanding and love from the very first day I came to Holland. You are the only one who knows how easy and/or difficult it had been for me during all these years The life path we chose has been exciting, unique, with some obstacles, that got me to the end of my thesis and gave us two precious sons. Hvala vam Jasone i Dione što postojite i za svu vašu ljubav.

I am sure there are many people who I did mentioned and who supported me over the years, to all of them I am very thankful as well.